KU LEUVEN

ARENBERG DOCTORAL SCHOOL
Faculty of Engineering Science

Modeling, optimal control and HVAC design of large buildings using ground source heat pump systems

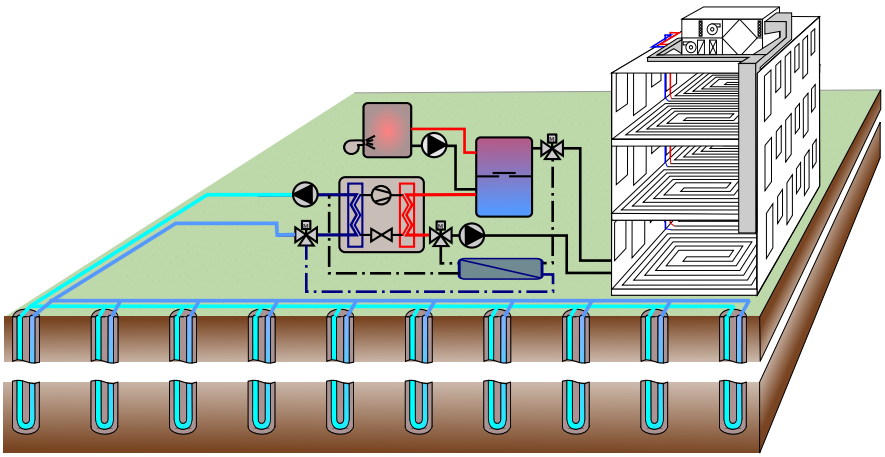

Damien Picard

Supervisor:
Prof. Dr. Ir. L. Helsen

Dissertation presented in partial fulfillment of the requirements for the degree of Doctor of Engineering Science (PhD): Mechanical Engineering

September 2017

Modeling, optimal control and HVAC design of large buildings using ground source heat pump systems

Damien PICARD

Examination committee:
Prof. Dr. Ir. Arch. H. Heynen, chair
Prof. Dr. Ir. L. Helsen, supervisor
Prof. Dr. Ir. Arch. D. Saelens
Prof. Dr. Ir. G. Pipeleers
Prof. Ir. W. Boydens
(University of Ghent, Belgium)
Dr. Ir. M. Wetter
(LBNL, Berkeley, CA, USA)

Dissertation presented in partial fulfillment of the requirements for the degree of Doctor of Engineering Science (PhD): Mechanical Engineering

September 2017

Preface

In November, 2011, I was working on my master thesis for just a few months, slowly grasping the concept of Model Predictive Control, when I went to my promotor, Lieve Helsen, seeking advice. I was considering doing a Ph.D. abroad and I asked Lieve whether she knew about good opportunities. And indeed, she knew about a very good one, except that it was not abroad but in her own team. I did not need long to make up my mind. The very interesting nature of the Ph.D. topic, the collaboration with a project composed of experts of the field and, also, the excellent contact I had with Lieve, with my daily coach Clara and even with my future office mate Dieter and future colleague Stefan all contributed to my YES!

Five years later, here I am, with a book in my hand, a bit wiser and knowledgeable than before, but still having so much to learn. These five years have been filled with the excitement of searching for satisfying answers and exploring a problem in great depth, the joy of imagining and creating new solutions and the fulfillment of learning constantly. These five years, and especially the last ones were also characterized by an increasing pressure I put on myself, by fights against my negligence or inaccuracy hampering the further construction of my work and, most of all, by making peace between my very ambitious self and what was feasible in the allocated time. And during all the joy and difficulties, a few people kept me going and always kept the balance positive. I would like to thank them heartily.

Eerst en vooral, mijn promotor, Lieve Helsen. Je hebt me een unieke kans geboden. Niet enkel heb je voor een zeer interessant doctoraatsonderwerp gezorgd maar ook voor een fantastische ploeg van medewerkers die stuk voor stuk, zoals jij, mensen vol van warmte, enthousiasme en humor zijn. Je was bovendien altijd beschikbaar voor productieve gesprekken, je steunde me in alles en je stapte in zeer interessante projecten. Ik was heel blij om met jou samen te werken en ik kijk ernaar uit om deze samenwerking verder te zetten.

I would further like to thank all members of the jury, not only for challenging me with interesting questions during my preliminary defense and enriching my text by their comments, but also for influencing me throughout my Ph.D. Thank you, Goele, for making time to discuss the subtleties of Kalman filtering and for accepting the role of assessor. I would also like to thank Prof. Van den Bulck for his guidance unfortunately suddenly interrupted by his unexpected parting. Thank you, Dirk, for the different discussions we had about modelling and systems and thank you for supporting the very rich and close collaboration between Building Physics and TME. Thank you, Wim, for all the interesting conversations about buildings in general, for sharing your knowledge from the practice and being one of these rare, extremely passionate people who want to excel at their work and constantly improve, without fearing to share their knowledge with others. Finally, thank you, Michael, for pushing the field of Building Energy Simulation forward with the help of your vision, your rigorous work and openness to collaborate – it has been a pleasure to work with you (despite our profound disagreement about chocolate quality).

Het eindresultaat van een doctoraat hangt vaak af van de invloed en hulp van andere mensen. Dit is zeker mijn geval. Ooit heb ik luid op gezegd: “Filip, je hebt mijn doctoraat gered!” en zo denk ik nog altijd. Hartelijk bedankt, Filip, voor uw diepgaande Modelica kennis en uw bereidheid tot helpen die zoveel bugs en problemen hebben opgelost. Bedankt ook voor de vruchtbare en fijne samenwerking doorheen de jaren. Ik kijk ernaar uit om die verder te zetten! Ook wil ik hier Roel bedanken. Roel, uw visie over Modelica, Python, Git en open-source programma’s en uw wil om kennissen te delen, hebben mijn doctoraat grondig beïnvloed. Dankzij jou heb ik zoveel over computers, programmeren en samenwerken geleerd en ik hoop om ooit opnieuw samen te kunnen werken. En als laatste collega met een wezenlijke invloed op mijn werk, wil ik graag Dieter bedanken. Dieter, bedankt voor de talrijke ontspannende pauzes die we hebben genomen, voor uw constante steun en aanmoediging, voor de uitwisseling van ideeën over ons onderzoek en onze levensprojecten en voor jouw openheid en warmte. Ik heb echt genoten om 5 jaar de bureau met je te delen.

There are still so many people I’ll like to thank. Thank you to the Sysi’s for all the good Sysi time. In particular, thank you Brecht for our philosophical and technical discussions, Maarten for sharing your extensive knowledge, Iago for knocking on my door every second day, Ján for the very nice collaboration and extensive philosophical discussions, Javier for your never ending enthusiasm, Clara for being such an excellent coach, Stefan for being the kindest colleague I have ever had, Arnout for being the most fidgety and at the same time such an excellent discussion partner, Mats for all the good time we had together on conferences and thank you to all the other sysi’s for being part of the team. I

would also like to thank Ruben Gielen for our discussions about heat transfer and religion, and for providing me with such excellent teaching materials, Ruben Baetens, Christina Protopapadaki, and Glenn Reynders for working together on IDEAS, Wout Parijs for all the work you did for Smartgeotherm and for me, and Joris Gielens for your punctual help with Casadi. I'm also grateful to all the co-workers of my project for the nice collaboration despite the delays with the planning.

Ook bedankt, Raf Schildermans, Jos Vansteenwinkel, David Simpson, Wim Dieltjens, Frederik Maertens, Jarno Tempelaere, Joost Verstraete en zoveel andere mensen van de praktijk, om jullie kennis met mij te delen. Bedankt ook, David Robben, voor uw deskundige advies over programmeren.

Merci aussi à mes parents. Bien que les subtilités d'ingénieur ne vous intéressent que moyennement, c'est grâce à vous que j'en suis arrivé ici. Merci de m'avoir poussé à bien faire, de m'avoir fait confiance dans mes choix et tout simplement d'être ma maman et mon papa.

As last but not least, I would like to thank you, Zsuzska. As we are not so good at onions and violins, I would just like to say the most important: Köszönöm a hatalmas ségitséged, köszönöm hogy itt vagy velem és Matyival, és köszönöm hogy továbbra is együtt leszünk. Szeretlek kedves!

Abstract

Since May 2010, the directive 2010/31/EU of the European Parliament compels its Member States to drastically decrease the energy use of buildings, to increase their energy efficiency and to increase the relative amount of renewable energy they use. One of the technologies recommended by the directive is the heat pump which efficiently uses electricity to extract thermal energy from a heat or cold source. In this work, buildings equipped with the particularly efficient *hybrid GEOTABS* system are considered, consisting of a ground source heat pump (GSHP) coupled to a thermally activated building structure (TABS) system and optionally extended with a gas boiler, radiators or other auxiliary systems. The main objective of this research is to *improve the thermal comfort and the energy efficiency of large hybrid GEOTABS buildings by applying model predictive control (MPC) and to improve their economic viability by optimizing the size of the GSHP and of the auxiliary systems as well as the type of the auxiliary systems to install.*

To this end, Building Energy Simulation (BES) models of an existing office building, a school, a retirement home and a block of flats were created using and extending the open-source Modelica library `IDEAS` to represent a wide set of hybrid GEOTABS buildings. The models include the building envelope, the heating, ventilation and air conditioning (HVAC) system, the occupancy and a default rule-based building climate controller (RBC). Additionally, a method to linearise the building envelope of the developed Modelica models was developed in order to obtain highly accurate controller models for MPC. The method automatically precomputes the non-linear equations which do not depend on the model states and linearises the other equations. The obtained controller models are then used by a toolchain which semi-automatically generates a linear MPC and tests its control performance on a full year simulation of the developed BES models. Finally, a python tool was created to optimize the economic viability and CO_2 emissions of hybrid GEOTABS systems.

As main results, it was found that hybrid GEOTABS systems were capable of

providing very high thermal comfort in all investigated buildings when controlled by MPC, showing that hybrid GEOTABS systems are suitable for a wide range of buildings when appropriate control is used. The developed MPCs could further save between 30 to 50% of the energy cost compared to standard RBC controllers while significantly improving thermal comfort when both the thermal powers to the TABS and the auxiliary emission system and the ventilation supply temperature were optimized simultaneously. However, current practice RBC were found not to always be able to provide the required comfort when, for example, the building was not equipped with a fast reacting system such as an air handling unit with heating and cooling coils to complement the TABS or when parts of the building with significantly different thermal needs were coupled to the same production system. Furthermore, the lack of correlation between the optimal control actions computed by MPC and the past or future ambient temperature indicates that the optimal behaviour achieved by MPC cannot be mimicked by RBC based on heating/cooling curves. Finally, the economic optimization and CO_2 emissions analysis of HVAC designs showed that GEOTABS systems without auxiliary production and emission systems are in general 1.0 to 1.8 times more expensive than conventional systems composed of a condensing gas boiler, a compression cooling machine and fan coil units but that properly sized *hybrid* GEOTABS systems (thus including an auxiliary production and emission system) have in general a lower present cost (PC) over the 20 years life time of the building while they emit between 20% to more than 50% less CO_2 than conventional systems. Hybrid GEOTABS systems are thus very advantageous both economically and for the environment and it is advised to always consider their installation for large buildings.

This work significantly contributed to the fields of building simulation and optimal control by developing new models and tools such as a novel borefield model, contributing to the development of the open-source libraries `IDEAS` and `Annex60`, and creating a highly automated method to generate accurate linear building models for MPC. Furthermore, the MPCs developed in this work achieved between 30 to 50% energy cost savings and significant thermal comfort increase compared to current practice rule-based-controllers which goes beyond the typical 15 to 25% cost savings found in the literature. This work also helped the industry forward by designing a tool to help design engineers to choose and optimally size the most appropriate HVAC system for a given building.

Beknopte samenvatting

Sinds mei 2010 verplicht de Europese richtlijn 2010/31/EN de lidstaten het energiegebruik van gebouwen drastisch te verminderen, hun energie efficiëntie te verhogen net als hun aandeel hernieuwbare energie. Een van de door de richtlijnen aanbevelen technologieën is de warmtepomp omdat deze elektriciteit efficiënt kan gebruiken om thermisch energie uit een warmte of koude-bron te extraheren. Dit werk beschouwt gebouwen uitgerust met het bijzonder efficiënte hybride GEOTABS systeem (bestaande uit betonkernactivering dat thermisch gevoed wordt door een grondgekoppelde warmtepomp (Eng. GSHP) en optioneel aangevuld met een condenserende gasketel, koelmachine en bijkomende afgiftesysteem). Het hoofddoel van dit onderzoek is dan om het thermische comfort en de energie efficiëntie van grote hybride GEOTABS gebouwen te verbeteren door Modelgebaseerde Predictieve Regeling (MPC) toe te passen en de rendabiliteit van zo'n systeem te verhogen door de grootte en de type van het verwarmings- en koelsysteem te optimaliseren.

Hiervoor werden energiesimulatiemodellen van een bestaande kantoorgebouw, een school, een rusthuis en een appartementsgebouw opgesteld, gebruik makend van en uitbreidend op de open source Modelica bibliotheek IDEAS, om over een brede waaier aan hybride GEOTABS gebouwen te beschikken. De modellen bevatten de gebouwschil, de verwarmings-, ventilatie en luchtbehandelingssystemen (Engl. HVAC), de bezetting en een regelgebaseerde regeling (Engl. RBC). Verder werd er een methode ontwikkeld om het gebouwschilmodel lineair te maken en zo een wiskundig eenvoudig maar toch zeer accuraat regelaarmodel voor MPC te bekomen. De methode laat toe om de niet-lineaire vergelijkingen die niet van de modeltoestanden afhangen, automatisch voor te berekenen terwijl de andere vergelijkingen lineair worden gemaakt. De bekomen regelaarmodellen kunnen dan door een toolchain worden gebruikt die lineaire MPCs op een semi-automatische manier genereert en hun regelprestatie op jaarbasis test. Als laatste werd er een Python tool ontwikkeld om de rendabiliteit en CO_2 uitstoot van hybride GEOTABS systemen te optimaliseren.

Als belangrijkste resultaat, bleek dat hybride GEOTABS systemen in staat waren om hoog thermisch comfort te halen in alle onderzochte gebouwen wanneer deze door MPC werden geregeld. Dit bevestigt dat hybride GEOTABS systemen voor een brede waaier van gebouwentypes geschikt zijn wanneer ze goed geregeld zijn. Bovendien halen de ontwikkelde MPCs een besparing in energiekosten van 30 tot 50% en een significante verhoging van het thermisch comfort ten opzichte van standaard RBC regelaars door zowel de thermische vermogens van de BKA, de bijkomende afgiftesysteem en de ventilatie aanvoertemperatuur tegelijkertijd te optimaliseren. Daarentegen bleken RBCs uit de huidige praktijk niet altijd in staat te zijn om voor het nodige comfort te zorgen, bijvoorbeeld wanneer het GEOTABS gebouw niet met een snel-reagerend systeem, zoals een ventilatiegroep met verwarmings- en koelbatterij, was uitgerust om het vermogen van BKA bij te vullen of wanneer delen van het gebouw met thermische behoeften die significant van elkaar verschillen door eenzelfde productiesysteem worden gevoed. Daarnaast toont dit werk dat, aangezien er geen sterke correlatie tussen de MPC regelacties en de buitentemperatuur van de vorige of toekomstige dagen bestaat, de regelacties van een MPC niet door stooklijn gebaseerde RBCs kunnen worden nagebootst. Ten laatste toont de economische optimalisatie en CO_2 uitstoot analyse van HVAC systemen dat GEOTABS systemen zonder bijkomende productie en afgiftesystemen typisch tussen de 1 tot 1.8 keer duurder zijn dan conventionele systemen (nl. condenserende gasketel en koelmachine gekoppeld aan ventilo-convectoren) maar dat goed ontworpen hybride GEOTABS systemen meestal de laagste huidige kost over de 20 jaar levensduur van een gebouw hebben, terwijl ze 20 tot 50% minder CO_2 uitstoot veroorzaken dan conventionele systemen. Hybride GEOTABS systemen kunnen dus beide economisch en ecologisch zeer voordelig zijn als ze over het hele gebouwlevensduur worden beoordeeld en het is dus aangeraden om de installatie van zo'n systeem voor grote gebouwen altijd te overwegen.

Dit werk brengt een significant bijdrage tot het vakgebied van energiesimulatie van gebouwen en optimale regeling door de ontwikkeling van nieuwe modellen en tools door het nieuwe boorveld model, de bijdrage tot de ontwikkeling van de open source bibliotheken IDEAS en Annex60, en het creëren van een grotendeels geautomatiseerde methode om accurate lineaire gebouwmodellen voor MPC te bekomen. De ontwikkelde MPCs halen bovendien een besparing in energiekosten van 30 tot 50% en een significante verhoging van het comfort, wat de typisch 15 tot 25% besparing in energiekosten die in de literatuur te vinden is, ver overschrijdt. De python tool uit dit werk helpt bovendien de industrie verder door een ontwerpingenieur te ondersteunen bij het kiezen en dimensioneren van HVAC systemen.

List of Abbreviations

ACH Air changes per hour. 57, 69, 79, 87, 166

AHU Air handling unit. 12, 50, 51, 56–58, 63, 64, 66–69, 71, 75–80, 82–86, 88, 91, 93, 135, 144

ATES Aquifer thermal energy storage. 13, 14, 17

BES Building energy simulation. 7, 96–98, 103, 108, 166, 184, 193, 220, 222, 225, 226

BHX Borehole heat exchanger. 27–30, 33, 35, 38, 41

BIM Building information modelling. 226

CCA Concrete core activation. 4, 5, 19, 200, 201, 204, 206–208, 212–214, 217, 224, 230

COP Coefficient of performance. 6, 17, 19, 26, 47, 146–148, 152, 154–157, 164, 165, 170, 175, 177, 228

DHW Domestic hot water. 70, 71, 73, 88, 89, 91–93, 167, 172

EER Energy efficiency ratio. 17, 19, 212

FH Floor heating. 58, 69–71, 73, 201, 204, 207

GSHP Ground source heat pump. v, vii, 3–6, 8, 11, 12, 17, 26, 45, 56, 57, 68, 69, 78, 79, 86, 88, 145–147, 154, 156, 157, 165, 204, 207, 208, 213, 216, 217, 220, 221, 224, 226, 228

HCF Heat carrier fluid. 15, 17, 26–31, 35, 36, 38, 39, 41, 58, 145–152, 155, 156

HEX Heat exchanger. 12, 17, 58, 70, 71, 75, 80, 83, 89, 167, 175, 205

HSRM Hybrid step response model. 33, 35, 38–42

HVAC Heating, ventilation and air-conditioning. v–viii, 5, 7–9, 12, 43, 44, 46, 49, 51, 55, 56, 64, 68, 74, 78, 87, 96, 97, 106, 109–111, 113, 160, 161, 164, 166, 170, 172, 182, 184, 196–205, 208, 209, 214, 216, 217, 220–224, 226–228, 230

LDC Load duration curve. 199–203, 207, 208, 212–214, 216

LTM Long-term model. 26, 28, 30, 33, 38, 39

MILP Mixed integer linear programming. 198, 199

MOR Model order reduction. 114–116, 119

MPC Model predictive control. v–viii, 5–9, 11, 20–23, 96, 97, 109–111, 113–116, 120, 123, 125, 126, 128–134, 137, 139, 140, 142–144, 159–166, 170–173, 175, 177, 180–185, 187–190, 193, 221–223, 225, 226

OCP Optimal control problem. 161

PC Present cost. vi, 196, 197, 202, 203, 207, 211, 212, 214, 216, 217, 221, 224

RBC Rule based controller. v–viii, 5–8, 52, 56, 68, 78, 87, 109, 114–116, 123, 128–132, 159–166, 170, 177, 180–185, 187–190, 193, 194, 222, 223

RES Renewable energy sources. 3, 197

ROM Reduced order model. 115, 116, 120–124, 126, 131, 132, 222

SPF Seasonal performance factor. 17

SSM State space model. 20, 97, 102, 103, 105–108, 110, 115, 116, 118–122, 126, 131, 135, 137, 142, 163, 164, 170, 171

STM Short-term model. 26, 28, 30, 31, 33, 38

TABS Thermally activated building structure. v, vi, 4, 5, 8, 9, 11, 12, 19, 46, 48, 49, 51, 57, 58, 61–64, 66–71, 73, 75–77, 86, 88, 89, 91, 93, 135, 159–162, 164–166, 170–173, 175, 177, 180, 181, 183–193, 197, 220–224

TES Thermal energy storage. 19

TRCM Thermal resistive-capacitive model. 29–31, 48, 135, 136, 161

List of Symbols

Roman symbols

P_{comp}	Compressor power	[W]
$\dot{Q}_{\text{cond}}$	Condenser power	[W]
$\dot{Q}_{\text{eva}}$	Evaporator power	[W]
R_b	Borehole fluid-to-ground thermal resistance	[(m.K)/W]
R_a	Borehole grout-to-grout thermal resistance	[(K.m)/W]
c_p	Specific heat capacity	[J/(kg.K)]
T_b	Borehole wall temperature	[K]
T_{Low}	Lower comfort bound for zone temperature	[K]
T_{Up}	Upper comfort bound for zone temperature	[K]
T_m	Average HCF temperature	[K]
T_0	Initial temperature	[K]

Greek symbols

α	Thermal diffusivity	$[(\text{m}^2)/\text{s}]$
λ	Thermal conductivity	[W/(m.K)]
Δt	Discrete time step	[s]

Contents

Part I

Introduction and concepts

Chapter 1

Introduction

1.1 Context and motivation

One of the major problems that humanity has to face nowadays beside wars, famine, inequality, terrorism, etc. is the energy crisis. Due to the finite resources of the earth and the climatic impact of (fossil) energy, energy use should be drastically reduced. Obviously, reduction should be firstly achieved by changing our behaviour to use and to need less: avoiding the use of cars, avoiding to eat meat, promoting local production, avoiding trash, etc. As a second step, energy can further be reduced by increasing the energy efficiency of the systems we use and by using more renewable energy as energy sources.

Therefore, in line with the Kyoto Protocol and its commitment to maintain global temperature rise below 2°C, the European Union (EU) has committed itself between 2007 and 2009 to reach the 20/20/20 target by 2020. This target corresponds to a reduction of the EU's energy use by 20%, a 20% increase of energy efficiency, and an increase of the share of renewable energy to provide 20% of the total EU's energy use. The European Union (EU) has now extended its ambition to, by 2030, reach a 40% reduction of green house gases emissions compared to 1990, to use at least 27% share of renewable energy use, and at least 27% energy savings compared to the business-as-usual scenerio. In order to reach these ambitious goals, improvements in the building sector are crucial as buildings accounts for 40% of the total energy use in the EU from which halve is due to heating and cooling [111]. EU's Directive 2010/31/EU proposes a concrete action plan having as goal that by 31 December 2020, all newly built buildings would be nearly zero-energy buildings and that new buildings

occupied and owned by public authorities would be nearly zero-energy already by 31 December 2018 [44]. *Article 4* of 2010/31/EU further stipulates that *minimum energy performance requirements for buildings have to be set with a view to achieving cost-optimal levels* and *Article 6* states that *before construction starts, the technical, environmental and economic feasibility of high efficiency alternative systems such as those listed below, if available, is considered and taken into account: (a) decentralised energy supply systems based on energy from renewable sources, (b) cogeneration, (c) district or block heating or cooling, particularly where it is based entirely or partially on energy from renewable sources, and (d) heat pumps* [44]. Finally, while the directives of 2010/31/EU are binding, each Member State has the freedom to develop its own legislation and its own tools to comply with them.

These goals and directives are in Flanders translated into increasingly strict energy requirements for residential and non-residential (excluding industrial) buildings and the obligation of using a minimum percentage of renewable energy sources (RES). For example, residential buildings built in 2017 are required to have an energy level below E-50 (E-30 by 2021) and to use at least 15 kWh/m^2/y of RES and the requirements for office buildings and schools are E-55 (E-40 by 2021) and 10 kWh/m^2/y [162]. The RES quota can be met by installing solar panels, an air-source or a geothermal heat pump, by using biomass or by being connected to a district heating network. This work focuses on buildings equipped with a geothermal heat pump and, in particular, how to increase the energy performance of such buildings, the thermal comfort they provide, and their economic viability.

Geothermal energy in the form of hot springs has been utilized by mankind since its existence to bath or for therapeutic purposes. Hot springs were also used already as early as the first Century AC by the Romans to heat buildings as testified by the ruins of the thermal spa of Baden-Baden (Germany). The spa was equipped with a floor heating system heated with the hot water coming from the ground [138]. Nowadays, beside the numerous spa's and other bathing facilities, geothermal energy is used to produce electricity, to supply heat to district heating networks, and to provide heat and cold to ground source heat pump (GSHP) systems. In Europe in 2015, 84 geothermal plants were installed which produce 2188 MW of electricity, 257 plants were coupled to district heating networks providing about 4.6 GW of thermal energy, and finally, about 1.3 million of GSHPs are currently in use and an increase to 2.0 million units by 2020 is expected [43]. GSHPs are thus a proven and viable technology which is popular for its high energy efficiency, earning the highest category A+++ according to the EU labelling system. GSHPs have a primary energy efficiency of 120 to 160% and produce between 0.2 and 0.27 kg-CO_2/kWh-heat compared to an efficiency of 70-80% for traditional gas boilers (100% if condensing) for a

CO_2 production of 0.26 to 0.31 (0.21 if condensing) kg-CO_2/kWh-heat [121]. However, the high investment cost required for GSHPs compared to more traditional solutions, the lack of clarity regarding legislation about geothermal energy (e.g. legislation about drilling, about thermal depletion of the ground, etc.), and the lack of know-how in most of the European countries keeps the market share of GSHPs still low.

Therefore, several research and development (R&D) projects sponsored by different countries and by the EU have been set up with the goals to alleviate the remaining barriers and to spread this interesting technology. Between 2009 and 2015, in Belgium, about 14.40 M€ has been invested in geothermal R&D through different Belgian and European projects in which Belgium was a partner [112]. GEOTRAINET (2008-2011) focussed on trainings for installers, designers and drillers [58]. GEOPOWER (2010-2012) proposed different action plans per country on technical and financial criteria of applying GSHP systems and suggesting legislative solutions to promote the use of geothermal energy [54]. GEOTABS aimed at improving the system design and control of office buildings equipped with a GSHP and a thermally activated structure (TABS) by using monitoring, comfort survey and simulation data [55]. GROUNDMED (2009-2014) aimed at the demonstration of GSHP systems for Mediterranean climate [63]. REGEOCITIES (2012-2015) worked on the integration of shallow geothermal energy at a local and regional level [121]. THERMOMAP (2010-2013) mapped the soil composition and other parameters necessary for designing very shallow (<10m) GSHPs across Europe [151]. ESTMAP (2014-2016) provided a view of available locations in Europe that could host geothermal energy storage facilities [42]. The objectives of CHEAP GSHPs (2015-2019) are to substantially reduce the total cost of ownership of GSHP systems, to increase its safety during installation and operation, and to increase awareness of this technology throughout Europe [29]. BRUGEO (2016-2020) aims at promoting GSHP systems in Brussels, Belgium [25]. Smartgeotherm (2011-2017) aims at developing integrated concepts using GSHPs, concrete core activation (CCA) and other techniques to design nearly-zero energy buildings [131]. GEOTECH (2015-2019) want to lower the investment cost by proposing new drilling and ground heat exchanger technologies and improving the control of hybrid heat pumps [57]. Finally, the project GEOTABS$^{\text{hybrid}}$ (2016-2020) intends to optimise the pre-design and operation of a building equipped with a combination of a GSHP coupled to TABS and an additional auxiliary system such as gas boiler, radiators, etc. [56].

In line with the Smartgeotherm project which has funded this PhD and with the EU objectives to strive for nearly-zero energy buildings by (among others) using highly energy efficient devices such as heat pumps, this work focuses on the improvement of low energy, (hybrid) GEOTABS buildings. A *GEOTABS*

building is a building which uses a GSHP and TABS such as CCA to heat and cool the rooms. When the building has an auxiliary production system to produce heat or cold beside the GSHP (e.g. a gas-boiler) and/or an auxiliary emission system to emit the heat or cold in the building (e.g. radiators), the building is called *hybrid GEOTABS*. As the performance of a (hybrid) GEOTABS buildings strongly depends on the interactions between the building envelope, the HVAC system and the users, between the different HVAC components themselves, and between the building and its control, an important feature of this work is its *integrated* approach which includes and strongly focusses on these numerous interactions. The following sections specify the goals and research questions, the methodology, and the main assumptions of this work.

1.2 Goals and research questions

The main objective of this work is:

> *To improve the thermal comfort, the energy efficiency and the economic viability of large hybrid GEOTABS buildings.*

Firstly, the thermal comfort and the energy efficiency of the building are improved by applying Model Predictive Control (MPC) to control its heating, ventilation and air-conditioning (HVAC) system. Secondly, this work aims at improving the economic viability of *hybrid GEOTABS* buildings by optimizing the type and the ratio between the size of the GEOTABS system and the size of the supplementary production/emission system while keeping the building envelope as it is. Four building types are considered: an office building, a school, a retirement home, and a block of flats.

Based on the main objective, seven specific research questions (RQ) are formulated focussing on the *feasibility* of *GEOTABS* systems, on its *control* and on its *design*:

A) Feasibility:

RQ1 : Are GEOTABS systems suitable for office buildings, schools, retirement homes, and block of flats in terms of thermal comfort?

B) Control:

RQ2 : How much energy can be saved and how much thermal comfort can be gained by applying MPC instead of traditional rule based controllers (RBC)?

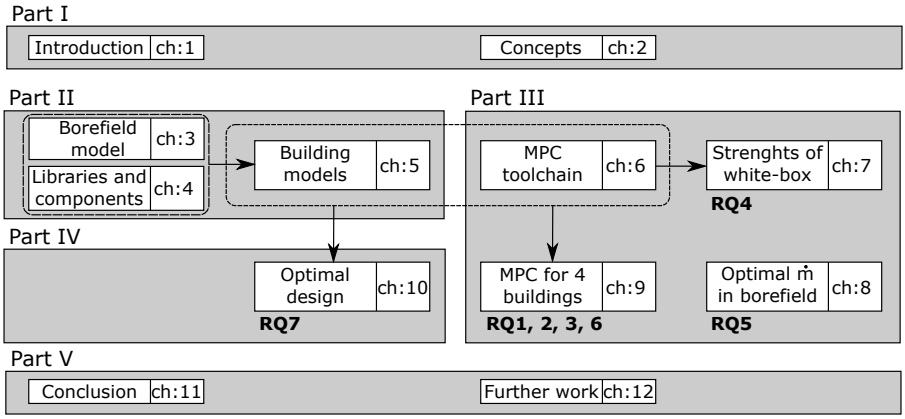

Figure 1.1: Methodology and PhD outline.

RQ3 : Is it possible for RBC to mimic the MPC behaviour?

RQ4 : What is the influence of the controller model complexity on the MPC performance?

RQ5 : What is the optimal flow rate in a borefield maximizing the coefficient of performance (COP) of the GSHP system?

C) Design:

RQ6 : Are supplementary emission systems necessary to achieve acceptable thermal comfort in (hybrid) *GEOTABS* buildings?

RQ7 : For which boundary conditions and which hybrid designs are *hybrid GEOTABS* buildings economically viable?

1.3 Methodology and outline

The methodology and the PhD outline are schematically represented in fig. 1.1. Figure 1.1 also draws the connections between the different chapters and it indicates in which chapter the different research questions (RQ1-RQ7) are answered.

The structure of this PhD text follows the methodology: firstly, **Part I** introduces and motivates the goals of this research (chapter 1) and explains its main concepts (chapter 2). Secondly, the buildings models used to answer the research questions and their component models are handled by **Part II**:

chapter 3 describes the new borefield model which has been developed to predict the fluid temperature returning from a vertical ground heat exchanger of arbitrary configuration; chapter 4 introduces the main component models that are used from the Modelica *Building Energy Simulation* (BES) libraries `IDEAS`, `IBPSA`, and `Buildings`, and some models specifically developed for this work; and finally, the four *GEOTABS* building models and their boundary conditions used to answer the research questions are elaborated on in chapter 5. **Part III** is then devoted to optimal control and is divided into four chapters: a *methodological* chapter (chapter 6) which focuses on the developed toolchain to enable the semi-automatic generation of linear MPC. The corner stone of the toolchain is the automatic generation of a white-box controller model for MPC by linearising the Modelica emulator model developed in `IDEAS`. *Emulator model* is used in this text to refer to the model used as the most accurate representation of the real building, while *controller model* refers to the (simplified) model used by the MPC to predict the behaviour of the building. The next chapter is *comparitive*: chapter 7 demonstrates the advantages of the linearisation method to obtain the controller model by comparing the MPC performance when using the linearised controller model and the MPC performance when using a *grey-box* model obtained by *system identification* instead. Chapter 7 also illustrates how the controller model complexity affects the MPC performance (**RQ4**). Chapter 8 is a side track: in its current stage, the MPC toolchain focuses on controlling the building inputs such as the supply temperature or the thermal power supplied to the emission system while the production system is not optimized. Chapter 8 partially solves this short-coming by proposing an analytical solution for the optimal mass flow rate in the borefield of a GSHP system (**RQ5**). The last chapter of the optimal control part is the core of this dissertation: using the building models and the MPC toolchain, chapter 9 applies different MPCs to each building and the obtained thermal comfort, the energy use and the energy cost are compared with those obtained by traditional RBC. The analysis of the results answers **RQ1, 2** & **3**. **RQ6** is also addressed by forcing the MPC not to use the supplementary system and then comparing the results with the normal MPC. Finally, **Part IV** closes the research part of the work by investigating the economic viability of *hybrid GEOTABS* buildings and by proposing a methodology to optimize the HVAC design (chapter 10, **RQ7**). **Part V** concludes and proposes further research tracks as a continuation of this work.

1.4 Main assumptions

The different assumptions made throughout this work are specified in each chapter where they are relevant. For the reader's convenience, they are all

summarized below.

Firstly, this work is entirely based on simulations. The building models are composed of models from the `IDEAS` (v1.0.0), `Annex60` (v1.0.0) (now continued under the name `IBPSA`), and `Buildings` (v3.0.0) Modelica libraries (see chapters 4 and 5). Each library has been (partially) validated and the building envelope of one of the building models has been successfully validated against measurement data of the real building (see section 5.1). It is therefore assumed that the developed building models are a realistic representation of reality. In order to limit the complexity of the models, a number of approximations were made:

- No pressure drops were modelled except in chapter 8. As a consequence, the electrical use of fans and pumps are not included and the pipes of the hydraulic system are not modelled dynamically. Instead, a rough estimate of the pipes water content is added and dispatched between the different HVAC components to account for its thermal inertia. Finally, two way-valves used to control the mass flow rate are replaced by ideal pumps which can directly regulate the flows.
- As the pipes are not modelled and the exact positions of the different HVAC components in the building is often not known, thermal losses of HVAC components are set to zero. The introduced approximation error is, however, expected to remain limited for the GSHP system as the TABS supply temperatures are low for heating (max 29 °C) and high for cooling (min 16 °C).
- The conversion efficiencies of production components are modelled dependent on sink and source temperatures but independent on mass flow rates and on the load ratio as such information is rarely available in manufacturer datasheets (except in chapter 8).
- The occupancy models are based on weekly profiles per zone which do not change throughout the year, except for the block of flats model which uses a yearly profile (see chapter 5).

The developed Modelica building models are further used to evaluate the performance of the controllers developed in this work (except for section 7.1 which uses a linearised version of the model). Two types of controller are developed: rule-based-controllers (RBC) and model predictive controllers (MPC). RBCs are modelled as they are typically implemented in current buildings and control the HVAC system in order to maintain good thermal comfort in buildings. They are thus tuned but not optimized. In contrast to the RBCs, the developed MPCs do not directly control HVAC components but

prescribe instead the thermal powers to the TABS and the supply ventilation temperature using a linear dynamic model of the building envelope and a linear static model of the HVAC system. MPCs assume thus the existence of subcontrollers which control the HVAC system. MPCs further use perfect weather and occupancy prediction and their states are updated using direct measurements (except in section 7.1 where a state observer is implemented).

Finally, the optimization of the HVAC design is based on a static method and no direct connection is made with the dynamic simulation models. Furthermore, the building envelope is not optimized.

Chapter 2

Concepts

This chapter provides the necessary background information about the different key concepts used in this work. Chapter 2 is meant to be understandable to any reader even if they are not familiar with the topic. Firstly, section 2.1 introduces the concept of *GEOTABS buildings* and the working principle of its different components such as ground heat exchangers (section 2.1.1), heat pumps (section 2.1.2) and thermally activated building structure (TABS) (section 2.1.3). Secondly, Model Predictive Control (MPC) is explained in section 2.2. Section 2.2.1 specifies the terminology used in this text, section 2.2.2 sketches the working principle of MPC using a simple example and finally, section 2.2.3 describes the different blocks of which a typical MPC framework is composed .

2.1 GEOTABS concepts

Ground source heat pumps (GSHP) are devices that extract heat or cold from the ground to heat or cool a building. A GSHP extracts heat or cold from the ground by using a geothermal system and rejects it in the building. GSHPs are the most efficient when the temperature difference between the ground and the supply water sent to the building is small. Therefore, buildings using a GSHP are typically equipped with a low temperature (or for cooling a high temperature) emission system such as floor heating or TABS.

Buildings using a combination of GSHP and TABS are called *GEOTABS* which is an acronym for **GEO**thermal heat pump combined with **TABS**. When the

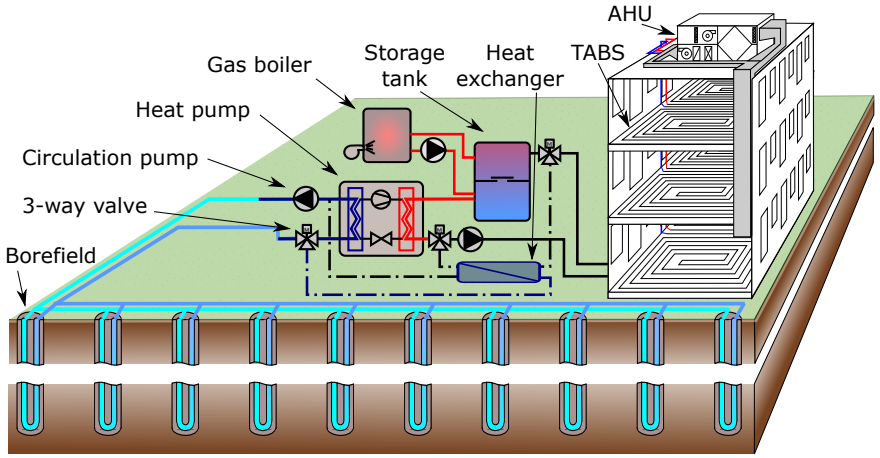

Figure 2.1: Hybrid GEOTABS building.

building is also equipped with more traditional systems such as a gas boiler, radiators or fan coil units, or if its *air handling unit(s)* (AHU) can heat and cool, the building is called *hybrid GEOTABS*. Figure 2.1 illustrates such a building with its heating, ventilation and air-conditioning system (HVAC). The following sections describe its main components: section 2.1.1 describes typical geothermal systems for buildings, section 2.1.2 explains the working principle of a heat pump, and section 2.1.3 introduces the TABS concept.

2.1.1 Geothermal systems for buildings

GEOTABS buildings use the ground as a heat and cold source in order to maintain thermal comfort in the building. In Belgium, the undisturbed ground temperature is not influenced by the weather from a depth of 15 m where the temperature remains constant (10 to 12°C) throughout the year. The ground temperature further increases with the depth, with 2 to 3°C every 100 m due to the geothermal heat flux (see fig. 2.2) [52]. Despite its relatively low temperature, heat can be efficiently extracted from the ground by using a geothermal system such as a GSHP. For cooling, the ground temperature is generally cold enough to allow passive cooling where a simple heat exchanger (HEX) is used between the ground and the building. The first paragraph present the common geothermal systems used by buildings while the second paragraph

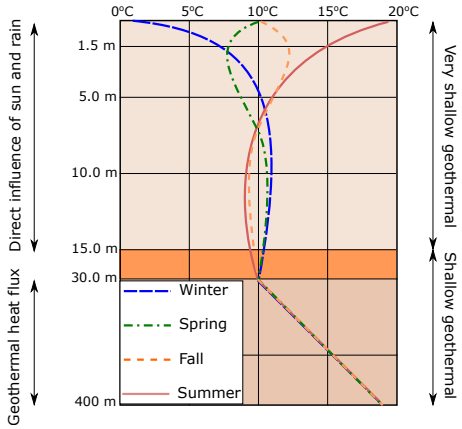

Figure 2.2: Undisturbed ground temperature as a function of the depth for the different seasons (inspired from [52]).

focuses on the most commonly used system (the vertical ground heat exchanger) which is also the one considered in this dissertation.

Shallow and very shallow geothermal systems

Typically, only *shallow* (up to 400 m deep) and sometimes *very shallow* (up to 15 m deep) geothermal systems are used to heat and cool buildings. The most common (very) shallow geothermal systems are summarized in fig. 2.3. The systems can be divided into two groups: *open* systems such as *Aquifer Thermal Energy Storage* (ATES) and *closed* systems such as *vertical* or *horizontal ground heat exchangers*, *energy piles*, *pond loop* and *standing column well*.

Open systems such as ATES extract ground water from an *extraction* well and reject it into the *recharge* well after the heat pump (or heat exchanger) has extracted the desired heat (or cold) energy (see (1) in fig. 2.3). ATES systems are characterized by a very high efficiency as water is an excellent heat carrier fluid. However, their installation is complex and such systems cannot be installed anywhere as they require an underground aquifer. Figure 2.4 indicates which regions are suitable for ATES in Flanders, Belgium.

The most commonly used closed system is the vertical ground heat exchanger which consists of holes (called *boreholes*) vertically drilled in de ground and in which a pipe is installed to circulate a mixture of water and glycol (see (2) in fig. 2.3). The system is described in detail in the next paragraph. When

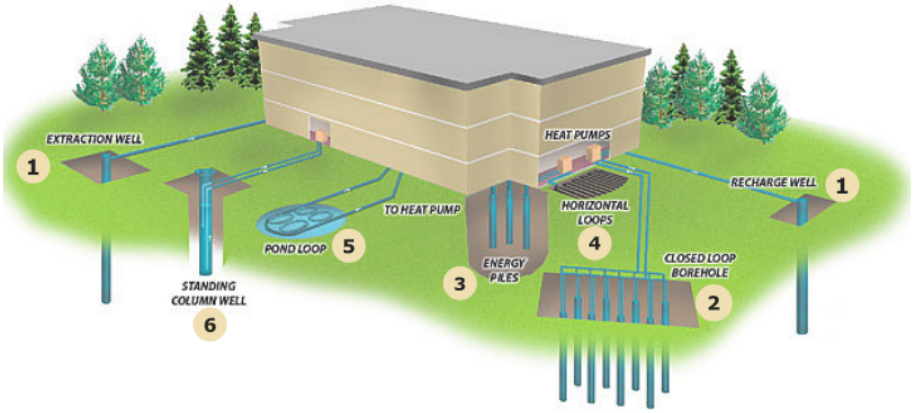

Figure 2.3: Most common (very) shallow geothermal systems. Source: `http://www.geoexanalytics.com`.

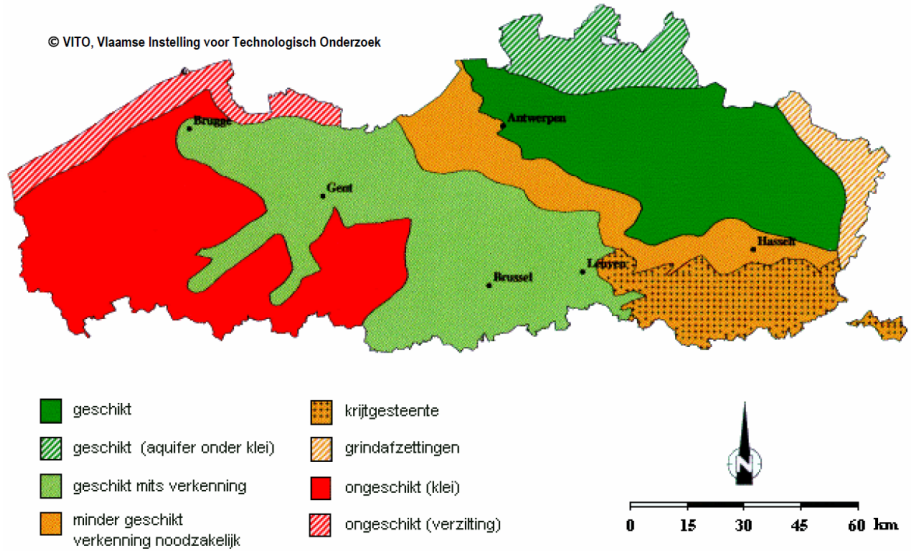

Figure 2.4: Suitability map for ATES systems in Flanders, Belgium. Dark green means *suitable*, light green *probably* suitable, orange *probably not* suitable and dark red *not suitable*. Source: `http://www.smartgeotherm.be/open-systemen/`.

the boreholes are very short (5 to 20 m) and when they are initially installed for geotechnical purposes, the system is called an *energy piles* system (③ in fig. 2.3). Energy piles are generally not sufficient to cover the thermal needs of the building but they can be a cheap additional energy source. Instead of installing the pipes in vertical boreholes, horizontal systems can be used where pipes are buried 1.2 to 2 m under the ground surface (④ in fig. 2.3), or where pipes are placed in a pond (⑤ in fig. 2.3). Such systems are unusual for large installations because they require a large ground surface area. Finally, in the case of rocky soil, a standing column well system is sometimes used. The system consists of a vertically drilled hole filled with water which can be pumped and re-injected by the heat pump (⑥ in fig. 2.3).

Vertical ground heat exchanger (borefield)

Vertical ground heat exchangers (also called *borefields*) are the most commonly installed closed-loop geothermal systems. A borefield is a heat exchanger in the ground composed of one or multiple vertically drilled holes (called *boreholes*) as illustrated by fig. 2.1. Boreholes are drilled in the ground to a depth typically between 15 and 180 m [6] with a diameter between 76 and 178 mm [30]. A single U-shaped, double U-shaped or (less frequent) coaxial pipe is inserted in the borehole in order to circulate the heat carrier fluid (HCF). Figure 2.5 gives a schematic representation of these different borehole heat exchanger types. The HCF is typically a mixture of water and antifreeze and it is often called *brine*. The pipe diameter varies between 20 and 40 mm [6] and the mass flow rate of the HCF is usually chosen so that the flow is slightly turbulent, or a more conservative flow rate of 0.1 l/s per pipe may be used. The borehole is filled with *grout*, which is usually a mixture of bentonite and sand. The *grout* and the ground thermal conductivities and thermal capacities, as well as the borehole diameter, the pipe arrangement and material, and the mass flow rate determine the so-called *borehole fluid-to-ground resistance* R_b. R_b is defined by Hellström [69] as the thermal resistance per borehole length between the average temperature of the HCF T_m and the borehole wall temperature T_b. According to ASHRAE [6], R_b values for single U-pipe boreholes range from 0.08 to 0.4 K.m/W but typical values rather range from 0.09 to 0.16 K.m/W for single U-pipe and from 0.05 to 0.08 K.m/W for double U-pipe boreholes [70]. The average thermal conductivity of the ground up to a depth of 100 m or up to the bedrock for Flanders and Brussels can be found in fig. 2.6 and it can be measured using a so-called Thermal Response Test (TRT) [52].

The design and sizing of a borefield depend on the thermal needs of the building (peak powers, balance between heating and cooling energy, supply temperature

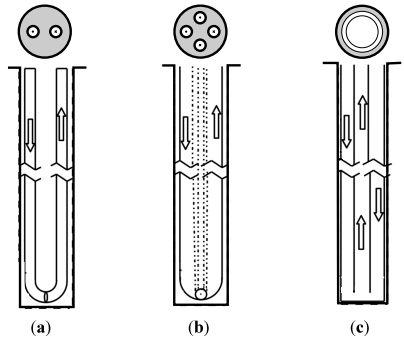

Figure 2.5: Single U-tube (a), double U-tube (b) and coaxial (c) borehole heat exchangers. Source: adapted from Sliwa and Rosen [130].

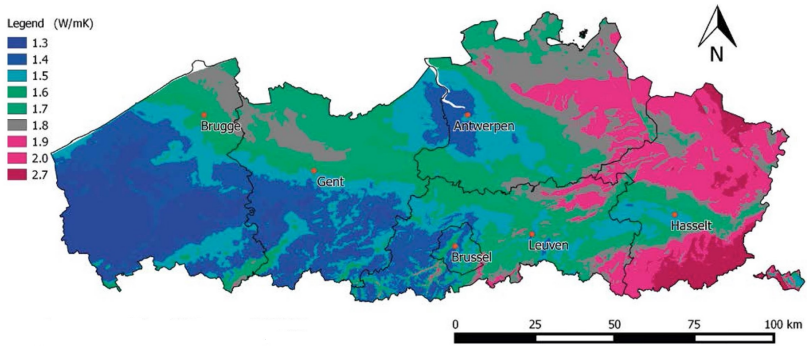

Figure 2.6: Minimum ground thermal conductivities for Flanders and Brussels up to 100 m deep or up to the bedrock [52].

of the heating and cooling system), the thermal properties of the grout and those of the ground, the distance between the boreholes and their diameter, the type of borehole heat exchanger, the type and percentage of antifreeze used in the brine, the initial ground temperature and some technical or legal restrictions regarding the drilling depth and the minimum and maximum ground temperature. For small installations with a maximal thermal power of 30 kWth and less than 2400 full load hours per year, the simple design method described by standard NBN EN 15450 [147] is sufficient. For larger systems, the use of dedicated standards such as the Dutch standard ISSO73 [77] and the Swiss standard SIA 384/6 [128], or design software such as Energy Earth Design (EED) [70] and Ground Loop Heat Exchanger Pro (GLHEPro) [59] are advised.

2.1.2 Heat pump

An electrical heat pump is a device that extracts heat from a low temperature heat source and rejects it in a heat sink at a higher temperature, by compressing a refrigerant typically with the help of an electrical compressor. Such a device can be, for example, found in a fridge where heat is extracted from a cold environment (inside the fridge) and is rejected in a warmer environment (the room). Figure 2.7 sketches the working principle of a heat pump for buildings and fig. 2.8 represents the same cycle in a T-s diagram. Firstly, the refrigerant evaporates in a first heat exchanger (called *evaporator*, (2) in fig. 2.7), by extracting heat at a low temperature. This heat is provided by a *heat source* such as the ground in case of a GSHP, by air for *air source heat pumps* or by ground water in ATES systems (see (1) in fig. 2.7). The fluid used to transport the heat from the heat source to the heat pump is called the *heat carrier fluid* (HCF) or more generally, the *brine* (see section 2.1.1). The refrigerant is then compressed (state *a* in fig. 2.8) to a higher pressure and temperature (state *b*). Once compressed, the refrigerant condenses to a liquid state (state *c*, in fig. 2.8) while rejecting heat at a higher temperature in the second heat exchanger (called *condenser*, (4) in fig. 2.7). At the other side of the condenser, heat is transported by water and rejected in a *heat sink* (the building heating system ((5) in fig. 2.7)). Finally, the refrigerant expands over an expansion valve ((6) in fig. 2.7) and re-enters the evaporator (state *d*).

Heat pumps can also cool by inverting their heat source and sink. In this case the ground, air or ground water becomes the heat sink and the building becomes the heat source. However, in the case of ground or ground water as a source, the source is usually cold enough to be directly used for cooling without using the reversed heat pump to cool it further. In that case, a simple heat exchanger can be used instead. Figure 2.1 represents a *GEOTABS* building equipped with both a GSHP for heating and a HEX for passive cooling. Threeway valves are used to switch between the two devices.

The energetic performance of the heat pump is described by its *coefficient of performance* (COP) which is defined as the ratio between the useful delivered heat ($\dot{Q}_{\text{cond}}$, the heat rejected by the condenser) and the electrical power used by the compressor (P_{comp}) (see eq. (2.1)). In case of cooling, the performance coefficient is called the *energy efficiency ratio* (EER) which is the ratio between the heat extracted ($\dot{Q}_{\text{eva}}$) and P_{comp} (see eq. (2.2)). Both the COP and the EER depend on the source and sink temperatures which can fluctuate with the time of the year. Therefore, the efficiency of a heat pump system is also often described by its *seasonal performance factor* (SPF) which is the ratio between the yearly heat delivered to the heating system of the building and the electrical consumption of both the heat pump compressor and the auxiliary systems such

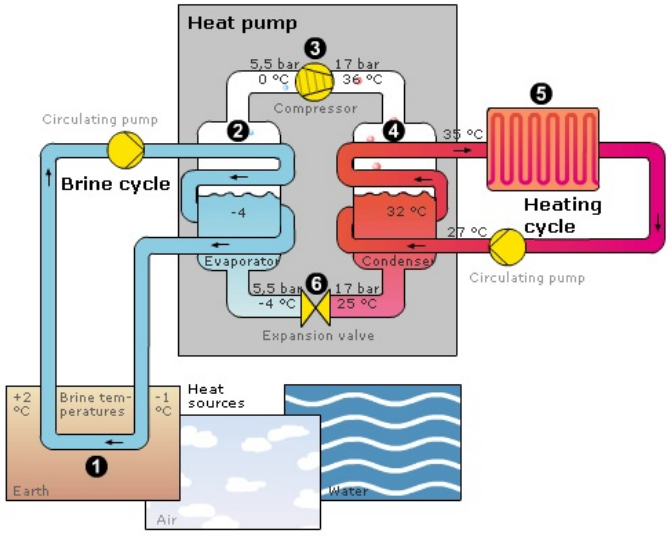

Figure 2.7: Schematic representation of a heat pump. Source: `http://www.geothermal-solar.com`.

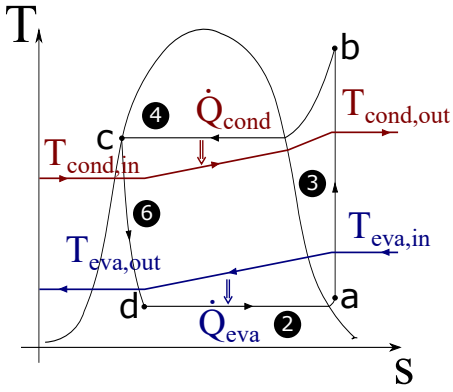

Figure 2.8: T-s diagram of a heat pump cycle. The circled numbers correspond to those from fig. 2.7.

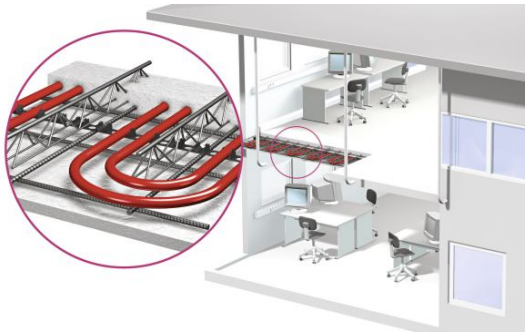

Figure 2.9: Example of a TABS system using concrete core activation. Source: `https://www.specifile.co.za/`.

as circulation pumps.

$$\mathrm{COP} = \frac{\dot{Q}_{\mathrm{cond}}}{P_{\mathrm{comp}}} \tag{2.1}$$

$$\mathrm{EER} = \frac{\dot{Q}_{\mathrm{eva}}}{P_{\mathrm{comp}}} \tag{2.2}$$

2.1.3 Thermally activated building structure

Thermally activated building structure (TABS) is an emission system where the building structure itself is used to deliver or extract heat to/from the building. Different systems exist: the water pipes in which warm or cold water is circulated can be integrated in different components: in the screed at the floor surface (for floor heating systems), in the concrete between two floors of the building (for concrete core activation (CCA) systems), close to the ceiling surface (for cooling ceiling systems) or even in the walls. Figure 2.9 is an example of a TABS system using CCA.

The large heat transfer surface and the high thermal capacity of concrete make TABS ideal for thermal energy storage (TES) and heat transfer with low temperature difference. Heat pump systems are often coupled to TABS to avoid the need of a high supply water temperature which would result in a drop of the heat pump efficiency.

2.2 Model predictive control

Model Predictive Control (MPC) is an optimal controller which computes the optimal value of the *control inputs* of a system so that the system would behave as required and in the *best possible way*. In the case of a building, the desired behaviour is, for example, that the temperature inside the building remains above 20°C and under 24°C. The *best possible way* can mean *using as little energy as possible*, or *using the energy of the solar panels as much as possible and the electricity from the grid as little as possible*. Finally, the *control inputs* can be the water temperature and mass flow rate sent to the radiators. The following sections describe the used terminology, the MPC working principle and the different MPC components.

2.2.1 Terminology

The following list gives an overview of the different terms used for MPC.

1. **Models**:
   (a) **Controller model**: a model used by the MPC to predict the behaviour of the system. The complexity of the controller model is typically kept low as it is used by the MPC optimization algorithm.
   (b) **Emulator model**: a model of the system used to mimic the behaviour of the real system. Emulator models can be used as a virtual testbed.
   (c) **State space model (SSM)**: a mathematical representation of a physical system written as a set of first order differential equations composed of inputs, outputs and states. In this work, only *linear, time invariant* SSMs are used.
2. **Variables**:
   (a) **Control variable/input**: a variable which the MPC can optimize in order to bring the system to its desired state. Examples: supply temperature and mass flow rate of a radiator.
   (b) **Disturbance variable**: a variable which is not controllable but which influences the system. Example: ambient temperature (= temperature outside the building).
   (c) **Input variable**: an input of the controller model. Typically, the control variables and the disturbances constitute the inputs.

   (d) **State variable**: a differentiated variable from the controller model. The state variables are loosely speaking the *memory*, or the *inertia* of the system.

3. **Horizons**

   (a) **Prediction horizon**: a time window for which the MPC receives predictions and optimizes the control variables.

   (b) **Effective horizon**: a subset of the prediction horizon during which the optimal value of the control variables is applied to the system before the MPC re-measures the system and re-computes the optimal values.

4. **Objective function**: a function which the MPC minimizes by finding the optimal value of the control variables for the entire prediction horizon while fulfilling the constraints.

5. **Constraints**:

   (a) **Equality constraint**: a constraint which obliges a variable to be equal to a (time varying) value.

   (b) **Inequality constraint**: a constraint which obliges a variable to be larger or smaller than a (time varying) value. Example: the temperature inside the building must remain higher/lower than the lower/higher comfort temperature.

   (c) **Hard/soft constraints**: the constraint is called *hard* if it needs to be respected at all times. If the constraint is *soft*, the constraint violation is caught by a *slack* variable which is penalized in the MPC objective function.

2.2.2 Working principle

The MPC algorithm computes the optimal value of the control variables based on predictions of the disturbances, predictions of the system behaviour and on the constraints of the system. In order to compensate for the error due to predictions inaccuracy, the MPC measures the system on regular basis and recomputes the optimal values.

Figure 2.10 illustrates the MPC working principle for an example building. The considered disturbances are the solar heat gains (orange) and the ambient temperature (dark green). The MPC controls the amount of heat to the building (lower graph, light green) and its objective is to keep the building temperature (red) above the minimum comfort temperature, called the *comfort constraint*

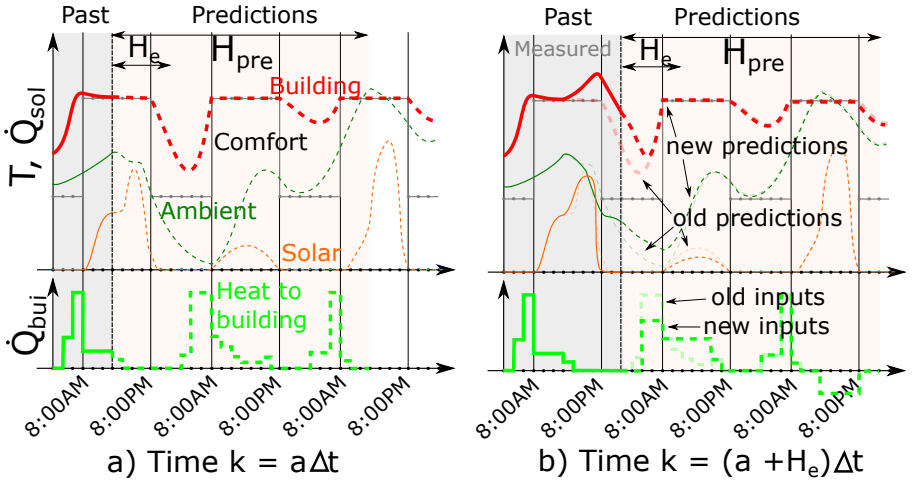

Figure 2.10: Illustration of the working principle of Model Predictive Control.

(black). Notice that the comfort constraint varies between day and night. At time $k = a\Delta t$, the MPC receives the measurement of the current building temperature, the prediction of the disturbances, and the comfort constraint for the coming $H_{pre} \times \Delta t$ hours, with H_{pre} the *prediction horizon* and Δt the discrete time step. In fig. 2.10, $H_{pre} \times \Delta t$ corresponds to 2 days. The MPC objective function which needs to be minimized is the amount of used energy. The MPC then optimizes the amount of heat to the building at each time step of H_{pre} so that the comfort constraint is respected and that a minimal amount of energy is used. The computed optimal values of the first H_e time steps are applied to the system. At time $k = (a + H_e)\,\Delta t$, the actual temperature of the building is measured and new predictions are received for the next H_{pre} steps. Due to prediction errors (differences between faded and solid lines in fig. 2.10 (b)) of both the disturbances and the building's behaviour, the new optimal values of the control variable are different from the values computed at time $k = a\Delta t$. The same procedure is repeated every $H_e \times \Delta t$ hours resulting in the optimal control of the building. The MPC performance depends on the accuracy of the prediction of the disturbances and of the building's behaviour, but also on the prediction and effective horizon lengths.

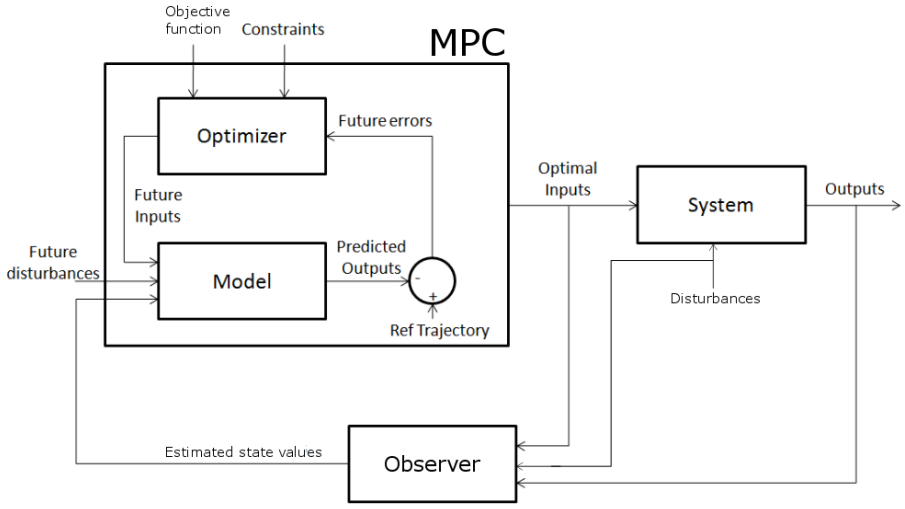

Figure 2.11: Model predictive control structure.

2.2.3 MPC components

Figure 2.11 sketches the different components of an MPC controlling a system. On the right of fig. 2.11, the system controlled by the MPC is represented. As shown by its connection, the state of the system depends on the disturbances and on the value of its control inputs. The state of the system can further be (partially) measured resulting in a number of *outputs*. The system is controlled by the MPC block which is composed of an *optimizer* which minimizes the objective function while respecting the constraints, and of a *controller model* used to predict the system's behaviour.

As described in section 2.2.2, the MPC has a feedback mechanism by which it reinitializes the state values of its controller model every H_e time steps in order to match the measurements of the system. As the measurements of the system generally do not coincide directly with the states of the controller model, an *observer* is used to estimate the controller model state values based on the system inputs/outputs.

Part II

Models

Chapter 3

Borefield

This chapter merges two papers previously published as:
Picard, D. and Helsen, L. A new hybrid model for borefield heat exchangers performance evaluation. In *Proceedings of the American Society of Heating, Refrigeration and Air Conditioning Engineersm, Inc.* (Seattle, USA, 2014), vol.120.

Picard, D. and Helsen, L. Advanced hybrid model for borefield heat exchanger performance evaluation, an implementation in Modelica. In *Proceedings of the 10th International Modelica Conference.* (Lund, Sweden, 2014).

Ground source heat pump (GSHP) systems are gaining importance for heating and cooling of buildings. To assess their performance, detailed simulation models are required with both short-term (to calculate the instantaneous coefficient of performance (COP) of the heat pump) and long-term (to calculate the ground temperature evolution) accuracy. In this chapter, a borefield model is developed, based on a step response which uses a combination of a short-term response model (STM) which takes into account the transient heat transfer in the heat carrier fluid (HCF), the grout and the immediately surrounding ground, and a long-term response model (LTM) which calculates the boreholes interactions.

Sections 3.1 and 3.2 firstly summarize the characteristics of existing borefield models available in different BES software and those of analytical models available in the literature. Secondly, a new model is proposed (section 3.3) together with the implementation of an aggregation method to speed up the

calculations (section 3.3.3). Finally, sections 3.4 and 3.5 validate the model and show a simulation example.

3.1 Introduction

Energy system simulations for design or performance evaluation of buildings and communities have gained significant importance in the last decades resulting in several dynamic simulation platforms such as EnergyPlus [139], TRNSYS [84] or Modelica [40]. These simulation tools should comprise libraries containing every important building system component including for example accurate and computationally efficient borefield models. TRNSYS already comprises different borefield models, i.e. the Superposition Borehole Model (SBM), the Duct Heat Storage model (DST) and the *type 451a* based on a previous version of the EWS (ErdWärmeSonde) program. The first two models allow simulating single or multiple boreholes but the dynamics of the borehole heat exchanger (BHX) (i.e. the thermal inertia of the borehole material from the heat carrier fluid (HCF) to the borehole wall) is not taken into account and the computation time might be high. The type 451a model takes the transient heat flux in the ground, in the filling material, and in the HCF into account. The model also handles multiple boreholes simulations using numerical and analytical *g-functions* and superposition. The analytical *g-functions* are calculated with Eskilson's line-source approach or with the Cylindrical Source model [73].

To the author's knowledge, no borefield model was implemented in Modelica so far. The open-source Modelica `Buildings` library [169] developed by the Lawrence Berkeley National Laboratory (LBNL, US) is the only freely available library which has a single-U-pipe single borehole model. The borehole model is similar to the EWS model implemented in TRNSYS. The HCF and the grout (i.e. the filling material of the borehole) are simulated dynamically but their capacities are lumped. A triangle thermal resistance network is used to describe the heat transfer into the BHX. In the vertical direction, the borehole and the surrounding ground are divided into adiabatic horizontal layers. The model is not suited for multiple boreholes simulations. The E.ON Energy Research Center (Germany) [74] also developed a single borehole model for single-U-pipe and coaxial type. The pipe model is connected to an axially and radially discretized cylindrical ground model. A fixed temperature boundary condition is used for the ground model. However, the model does not take the dynamics of the grout into account and multiple boreholes simulation is not possible.

The aim of this chapter is to implement a borefield model in Modelica which (i) is able to simulate any arbitrary configuration of boreholes, (ii) allows coaxial,

single-U- or double-U-tube type BHX, (iii) has short- and long-term accuracy for minute-based year-long simulations, (iv), and which has a low computation time. The impact of ground water flow is not included.

3.2 Existing models

In general, borefield models can be divided into two groups, i.e. the short-term models (STM) which focus on the transient heat transfer within the grout and the immediate ground (see section 3.2.1) and the long-term models (LTM) which describe the transient heat transfer in the surrounding ground (see section 3.2.2). The models of both groups can be classified as (1) analytical models, (2) numerical models using finite-volumes and (3) empirical models.

3.2.1 Short-term models

STMs describe the transient heat flux in the BHX and the immediate surrounding ground. For the steady state case, Hellström [69] defined two thermal resistances to describe the heat flux, i.e. the *fluid-to-ground resistance* R_b, and the *grout-to-grout resistance* R_a. R_b is defined as the resistance from the HCF in the pipes (with each pipe having an equal HCF temperature) to the borehole wall with uniform equivalent temperature. A correction factor can be used to calculate the *effective fluid-to-ground thermal resistance* R_b^* which includes the effects of the varying HCF temperature along the flow channels (extrapolation from the 2D resistance to 3D) and the thermal interaction between them. R_a represents the thermal interaction between the different grout parts of the borehole. Hellström calculated both resistances using the complex *multipole* method developed by Bennet and Claesson [16]. Many authors proposed alternative and simplified methods to calculate these resistances, so did Hellström himself [69], using a line-source in composite region approximation, or Paul with his experimentally determined shape factor coefficients which depend on the shank spacing [30]. Lamarche et al. [90] concluded in their review paper that the multipole method of Claesson and Bennet gives the most accurate results except when the borehole is lined with a high conductivity steel casing, for which the method of Sharqawy et al. is a better choice. In the latter the borehole resistance is indeed decreased by the fin effect of the steel casing. In order to describe the transient behaviour of the borehole, the dynamics of the HCF, of the pipe wall and mainly of the grout should be taken into account. Numerical models have been developed using finite volume formulation to validate simplified approaches. However, these models are very computationally expensive due to the high number of grid cells. Several authors have developed

analytical or empirical transient borehole models to speed up calculations. So far, analytical solutions exist only for boreholes with equivalent pipe diameter, i.e. the borehole is approximated as a single (lumped) pipe in the middle of the grout. Different formulations exist to compute the equivalent diameter as shown by Lamarche [89] or by Chiasson [30]. Lamarche [89] found the exact solution of the borehole with equivalent diameter in the Laplace domain. The solution does not take the HCF into account. Javed and Claesson [78] developed an analytical solution including the HCF capacity. Both analytical models approximate the behaviour of single- or double-U-type only and their accuracy depends on the grout and soil properties as well as on the equivalent diameter correlation. Bauer et al. [12] proposed a different method by setting up thermal resistive-capacitive models (TRCM) for coaxial, single- and double-U-tube (with one, two and four capacities, respectively). The resistances are calculated such that R_b and R_a of the BHX correspond to their respective values from the multipole method of Claesson and Bennet and the sum of the capacities equals the total grout thermal capacity. A very good agreement between the numerical models and the TRCMs is observed after 15 minutes when the capacities are placed at the grout area centers (see section 3.3.1).

3.2.2 Long-term models

The STMs described in section 3.2.1 cannot accurately simulate the transient heat transfer into the ground and the interactions between the different boreholes. The STMs need the borehole wall temperature T_b as an input. LTMs are designed to calculate T_b accurately over periods longer than decades. Most models are based on the step response of the heat transfer rate and use the superposition principle to compute the response to an arbitrary load profile. Long-term behaviour of multiple boreholes systems has been investigated firstly by Eskilson and Hellström [41, 69]. Eskilson developed a two-dimensional finite difference model in radial-axial coordinates for vertical or inclined boreholes. The model allows calculating the heat flux $q(t)$ through the borehole wall for a given uniform $T_b(t)$, or $T_b(t, z)$ for a given $q(t)$, with z the axial coordinate. This is an approximation of reality in the case of a non-coaxial borehole where T_b is not radially-uniform. Eskilson used this model to compute the famous *g-functions* defined as $g(t/t_s, r_b/H) = (2\pi\lambda(T_b - T_0))/q'_0$ with $t_s = H^2/(9\alpha)$, H the depth of the borehole, α and λ the thermal diffusivity and the conductivity of the ground, r_b the diameter of the BHX, T_0 the initial uniform ground temperature, and q'_0 the heat flow rate per meter. The *g-functions* are valid for $t > (5r_b^2)/\alpha$. The response to an arbitrary load is then obtained by approximating the load as a sum of time-shifted step-loads and taking the sum of their responses (see section 3.3.3). The *g-functions* are time-consuming to calculate and configuration specific.

Several authors developed analytical solutions to approximate these functions. The most recent contributions are the analytical solutions of Lamarche and Beauchamp [88] and of Claesson and Javed [32]. Both solutions use a finite line source approach to calculate the mean borehole temperature and the authors spent considerable effort to mathematically simplify the solutions in order to allow fast computing. The analytical solutions are extended to multiple boreholes models using spatial superposition approximation. As mentioned by Eskilson and Claesson [126], the superposition does not respect the exact boundary condition. Indeed, the superposition introduces a non-zero heat flux which is not due to heat injection, at each borehole location. Furthermore, contrary to numerical models, analytical models assume that the heat injection/extraction is the same for each borehole. This is obviously not the case because the temperature field within the borefield is usually non-uniform and the convective-diffusive heat transfer from each borehole is driven by the temperature difference. The injected/extracted heat of a borehole in the middle of the configuration differs from the one at the edge. This has been illustrated by Malayappan and Spitler [97], who showed that it can cause a serious deviation from the numerical *g-functions* for compact configurations. For example, if $\lambda = 2\ W/mK$, $q'_0 = 50\ W/m$ and a square borefield configuration with $a \times b$ boreholes with $B/H = 0.0625$ is used, the analytical solution of Claesson and Javed overestimates the temperature rise due to the step input with 0.25 K (for 4x4), 0.5 K (for 6x6) and 1.76 K (for 8x8) after 44 years [97]. The error for a variable load will be substantially lower.

3.3 New hybrid borefield model

This section proposes a new model that combines a STM with a LTM to obtain accurate g-functions. Sections 3.3.1 and 3.3.2 describe the implementation of the STM and the LTM and section 3.3.3 deals with their combination to a single hybrid model and the aggregation method.

3.3.1 Short-term model

The short-term model (STM) should be able to calculate the transient thermal response of the HCF, the grout and the surrounding ground accurately for time periods ranging from minutes to $t = 5R_b^2/\alpha$ (typically $10\ h < t < 200\ h$). The interaction between the boreholes for these short times can be neglected; therefore a single borehole model is used. Bauer et al.'s TRCM is chosen for the BHX of the STM [12]. Its steady state resistances (R_b and R_a) are indeed calculated with the most accurate method (i.e. the multipole method of Bennet

and Claesson [16]), it includes the dynamics of the grout and the authors proposed models for coaxial, single- and double-U-type systems. The position of the capacities was calculated to be at the area center of the borehole with an equivalent single pipe. The dynamics of the HCF is calculated using the *Fluid* base classes of the open-source `Buildings` library [169] and the *Media* library from the Modelica Standard Library [40]. The convective resistance between the HCF and the pipe is calculated by the correlation for smooth pipes in turbulent flow regime of Dittus-Boelter in the case of single- and double-U-tubes [69]. For the circular-tube annulus, the correlation of Petuhkov and Roizen is used [69]. Vertical discretization is also possible but no vertical heat transfer is computed except through the HCF. Finally, the heat transfer from the borehole wall to the surrounding ground is calculated by discretizing the ground using a TRCM. The mesh is generated according to Eskilson's guidelines [41]:

$$\Delta r = \left[\Delta r_{min}, \Delta r_{min}, \Delta r_{min}, \beta\Delta r_{min}, \beta^2\Delta r_{min}, \cdots\right] \quad ,$$

$$\Delta r_{min} = \min(\sqrt{\alpha\Delta t_{min}}, H/5) \quad ,$$

with α the diffusivity of the ground, H the depth of the borehole, Δt_{min} the minimum resolution time and Δr the size of the cell. The discretization has been tested with the analytical Cylindrical Source Model developed by Carslaw and Jaeger [28] and it shows very good agreement when the mesh is chosen fine enough (i.e. around 10 states for a layer of 3 meters). The width of the ground layer is by default equal to three meters but it can be adapted. The external part of the ground layer is connected to a constant undisturbed ground temperature. Figure 3.1 illustrates the STM structure for a single borehole with a single-U-tube configuration.

3.3.2 Long-term model

The long-term temperature response of the borefield is calculated using the model of Javed and Claesson [78]. Their model is preferred for its accuracy and efficiency and the analytical approach is chosen to enable the simulation of arbitrary borefield configurations.

The model is based on the spatial superposition of finite line-sources of equal length, each representing one borehole of the borefield. The finite line-source is calculated from the convolution of a point source of constant power along the depth of the borefield. The mirror of the solution at z=0 is subtracted to ensure that no heat transfer occurs between the ground and the ambient air. After several mathematical manipulations to simplify the calculation, Javed and Claesson obtained the following compact expression for the mean borehole wall temperature:

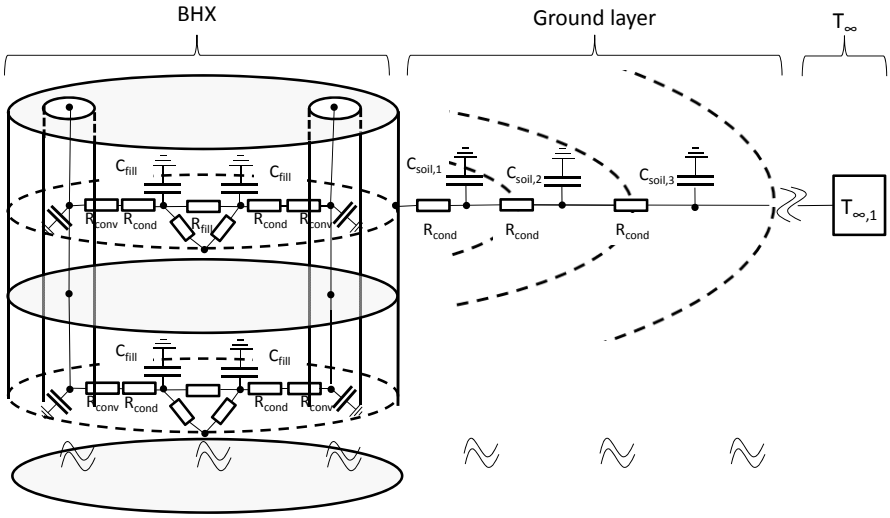

Figure 3.1: Structure of the short-term model for a single borehole with a single-U-tube configuration. The rectangles and the double lines represent thermal resistances and capacities, respectively, and $T_{\infty,i}$ is the undisturbed ground temperature in layer i.

$$\bar{T}_{mbhw}(t) = \frac{q_0}{4\pi\lambda} \int_{1/\sqrt{4\alpha t}}^{\infty} \left(\sum_{i=1}^{N} \sum_{j=1}^{N} e^{-r_{i,j}^2 s^2} \right) \frac{\mathrm{I_{ls}}(Hs)}{Hs^2} ds \tag{3.1}$$

where q_0 is the heat flux per meter length assuming that each borehole extract the same amount of heat, λ is the ground heat conductivity, α is the ground heat diffusivity ($\lambda/(\rho c_p)$), N is the number of boreholes and H is the depth of the borefield. $\mathrm{I_{ls}}$ is defined by eqs. (3.2) and (3.3) and $r_{i,j}$ by eq. (3.4):

$$\mathrm{I_{ls}}(h) = 4 \ \mathrm{ierf}(h) - \mathrm{ierf}(2h) \tag{3.2}$$

$$\mathrm{ierf}(x) = \int_0^x \mathrm{erf}(u) du = x \ \mathrm{erf}(x) - \frac{1}{\sqrt{\pi}} (1 - e^{-x^2}) \tag{3.3}$$

where *erf* is the error function,

$$r_{i,j} = \begin{cases} r_b & \text{if } \ i = i \\ \sqrt{(x_i - x_j)^2 + (y_i - y_j)^2} & \text{if } \ i \neq j \end{cases} \tag{3.4}$$

where r_b is the BHX radius and (x_i, y_i) are the spatial coordinates of the center of each borehole from an arbitrary reference point.

Equation (3.1) is valid for $t > \frac{5r_b^2}{\alpha}$, i.e after the transient part of the heat transfer through the BHX is completed [41]. The model also makes an important approximation by assuming an uniform heat flux for all boreholes. The (long-term) accuracy of the model decreases for long simulation times for configurations with non-uniform heat fluxes, e.g. a densely packed rectangular grid (see section 3.2.2).

3.3.3 Computation of the response function and aggregation method

The STM gives an accurate step response of the borefield as long as the diffusion length of the thermal process is small compared to the radius of its ground layer model or to the distance between the boreholes. The LTM is able to correctly compute the step response of the ground for a long time horizon as well as the interaction between the boreholes. It does not calculate, however, the borehole thermal resistance and its transient behaviour, contrary to the STM. The full response function is then obtained by lifting the LTM response to the STM response in the time interval where both models are still valid as shown in fig. 3.2 a. As Javed mentioned in his work [78], this interval is rather large (default value in model = 200 hours). Physically, this interval begins when the transient behaviour of the BHX is over and it lasts until the interactions of the boreholes start to appear. The combination of both STM and LTM leads to an hybrid step response model (HSRM) which is accurate for both short- and long-term.

The response-function can be calculated at the start of each simulation or it can be priorly saved with a sample time equal to the time resolution of the model. The STM is connected to a pump and a prescribed heater/cooler from the `Buildings` library (see fig. 3.3). A script-function automates the simulation of the STM and it writes the sampled values of its temperature response in the `Data` package of the model as .txt file. At the initialization of the model, a script checks whether the short-term response has already been calculated for the particular borefield parameter values of the model and loads it if it is the case in order to build the full response function of the HSRM.

As described above, g-functions and most of the analytical models give only a step response solution for the borefield. In order to model arbitrary input signals, the inputs need to be represented by a sum of time-shifted step signals and their responses should be superposed (see fig. 3.2 b).

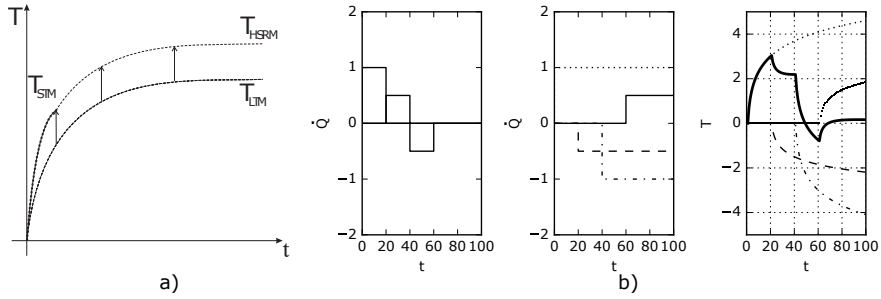

Figure 3.2: (a) Combination of the long-term borehole wall temperature step response (T_{LTM}) with the short-term fluid temperature step response (T_{STM}) to compose the hybrid fluid temperature step response (T_{HSRM})). (b) Left: initial discrete load; center: decomposition of the load into a sum of time-shifted step loads; right: temperature response to the load obtained by superposition.

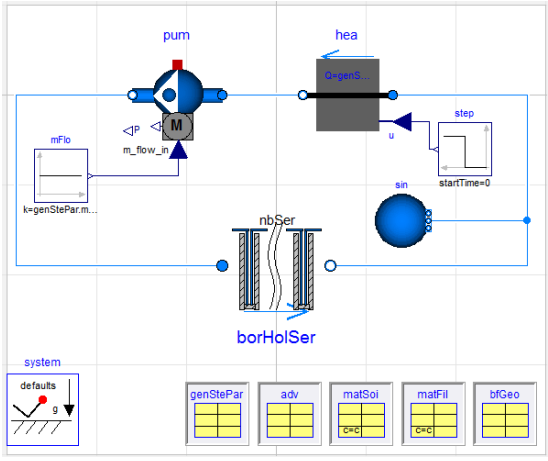

Figure 3.3: Model for the short-term temperature step response. The boreholes in series (*borHolSer*) are connected to a pump (*pum*) and to an ideal heater (*hea*). All parameter values are stored in the records (bottom of the figure).

For minute-based multi-year simulations where the individual step responses of each input step should be summed, this approach leads to enormous calculations. This problem is solved by using an aggregation method. The following paragraphs describe the technique of Claessons and Javed [78]. The notation has been adapted to gain clarity.

Assume that the discrete load input to the borefield is $\dot{Q}$ and the HCF temperature is T_f. $\dot{Q}$ and T_f can be written as:

$$\dot{Q}_{\nu}^{(n)} := \begin{cases} \dot{Q}\left[(n+1-\nu)h\right], & \text{if } \nu \leq n. \\ 0, & \text{otherwise.} \end{cases} \tag{3.5}$$

$$T_f(nh) - T_f(0) = \sum_{\nu=1}^{\nu_{\max}} \frac{\dot{Q}_{\nu}^{(n)}}{\dot{Q}_{\text{step}}} \left[T_{f,\text{step}}(\nu h) - T_{f,\text{step}}(\nu h - h)\right] \tag{3.6}$$

with $\nu_{\max} \geq n$, h the discrete time-step, Q the discrete load and $T_{f,\text{step}}$ the response function from HSRM with step load $\dot{Q}_{\text{step}}$. Notice that the model assumes a uniform temperature at time 0.

The idea behind this aggregation is the following: the HCF temperature difference of the borehole system (from an initial steady state) at $t = nh$ depends on the n load pulses which have been applied to the borehole system from $t = 0$ to nh. However, the influence of the pulses on the HCF temperature decreases the further they are from the observation time nh. If the pulses happened long before the observation time, the transient behaviour of the BHX has faded out, and only the net energy injection or extraction of the pulse is important. This net energy injection or extraction indeed increases or decreases the global temperature of the borefield. An accurate profile of the load, far away from the observation time, is therefore not necessary. On the contrary, the load profile at times close to the observation time is important because they still influence the transient behaviour of the borefield and immediate surrounding ground.

Claesson and Javed proposed an aggregation algorithm grouping (i.e. taking the average of) the load pulses and their coefficients into cells of exponentially increasing size. The cells are themselves grouped into q levels. Each level has a given number of cells $p_{\max}$ and each cell of a same level contains the same amount of load pulses R_q. Javed and Claesson proposed to double the size of the cells at each level, in order to have the same number of cells in each level and in order to choose this number of cells per level according to the desired accuracy (a higher number of cells per level gives a more detailed load profile but penalizes the computational time).

Equation (3.6) is now rewritten to implement the aggregation method. Notice that the temperature difference of the HCF between two time steps in eq. (3.6) divided by the amplitude of the step load $\dot{Q}_{\text{step}}$ can be considered as the transient thermal resistance of the borehole for that particular time. Let us define the transient thermal resistance R_ν and the dimensionless factor κ_ν as:

$$R_\nu = \frac{T_{f,\text{step}}(\nu h) - T_{f,\text{step}}(\nu h - h)}{\dot{Q}_{\text{step}}} \tag{3.7}$$

$$\kappa_\nu = \frac{T_{f,\text{step}}(\nu h) - T_{f,\text{step}}(\nu h - h)}{T_{f,\text{step}}(\infty)} = \frac{R_\nu}{R_{ss}}. \tag{3.8}$$

Equation (3.6) can now be rewritten as:

$$T_f(nh) - T_f(0) = R_{ss} \sum_{\nu=1}^{\nu_{\max}} \dot{Q}_\nu^{(n)} \kappa_\nu \ . \tag{3.9}$$

with R_{ss} the steady state thermal resistance.

As explained above, the aggregation is consisting of $q_{\max}$ levels, each composed of $p_{\max}$ cells which have a level-dependent width R_q defined as:

$$R_q := 2^{q-1} \quad \text{for} \quad q = 1, ..., q_{\max} \ . \tag{3.10}$$

The number of pulses covered by the aggregation is then:

$$\nu_{\max} := \sum_{q=1}^{q_{\max}} R_q \ p_{\max} \qquad \geq n_{\max} \ . \tag{3.11}$$

Define $\nu_{q,p}$ as the number of pulses covered from cell 1 at level 1 till (including) cell p at level q:

$$\nu_{q,p} := p \ R_q + \sum_{i=1}^{q-1} R_i \ p_{\max} \ . \tag{3.12}$$

Define the function $\nu(q, p, r)$ numbering each pulse, starting from pulse 1 in cell 1 at level 1:

$$\nu(q, p, r) := \nu_{q,p} - R_q + r \quad \text{for} \quad q = 1, \ldots, q_{\max}, p = 1, \ldots, p_{\max}, r = 1, \ldots, R_q \ .$$

These different definitions are illustrated in fig. 3.4.

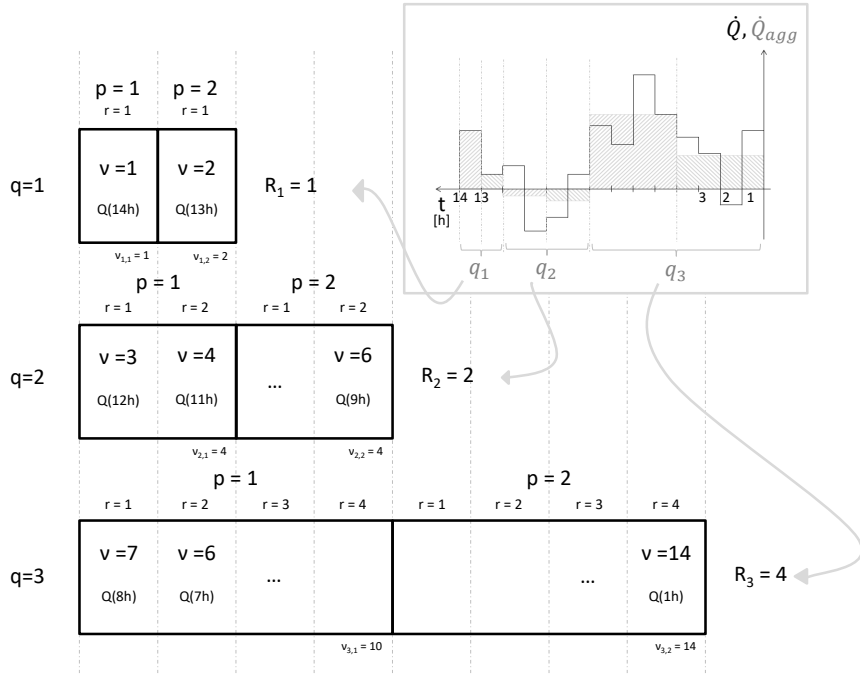

Figure 3.4: Illustration of the aggregation method for a load of 14 hours with time steps (pulses) of one hour. The number of levels is three and each level has two cells. The size of the cells is doubled at each level.

Using these definitions, eq. (3.9) can be rewritten as:

$$T_f(nh) - T_f(0) = R_{ss} \sum_{q=1}^{q_{\max}} \sum_{p=1}^{p_{\max}} \sum_{r=1}^{R_q} \dot{Q}^{(n)}_{\nu(q,p,r)} \kappa_{\nu(q,p,r)} \tag{3.13}$$

Now we apply the aggregation technique by approximating the last sum of eq. (3.13) by

$$\sum_{r=1}^{R_q} \dot{Q}^{(n)}_{\nu(q,p,r)} \kappa_\nu \approx \left[\frac{\sum_{r=1}^{R_q} \dot{Q}^{(n)}_\nu}{R_q} \right] \sum_{r=1}^{R_q} \kappa_{\nu(q,p,r)} := \bar{\dot{Q}}^{(n)}_{\nu(q,p)} \bar{\kappa}_{\nu(q,p)} \tag{3.14}$$

Finally the aggregation of eq. (3.9) gives:

$$T_f(nh) - T_f(0) \approx R_{ss} \sum_{q=1}^{q_{\max}} \sum_{p=1}^{p_{\max}} \bar{\dot{Q}}^{(n)}_{\nu(q,p)} \bar{\kappa}_{\nu(q,p)} \ . \tag{3.15}$$

The term $\bar{\kappa}_{\nu(q,p)}$ is a matrix with the transient thermal resistance of each cell of the aggregation which is independent of the load. At the initialization of the model, a script checks whether the aggregation matrix for the given parameter values has already been calculated and loads it if it already exists instead of recomputing it. The term $\overline{\dot{Q}}^{(n)}_{\nu(q,p)}$ is a vector with a length equal to the number of aggregation cells and which is composed of the aggregated past load pulses. At each new discrete simulation time, a new load pulse needs to be added and the previous pulses need to be shifted in the $\overline{\dot{Q}}^{(n)}_{\nu(q,p)}$ vector. This means re-calculating the whole vector. Claesson and Javed developed a method which avoids this time consuming re-calculation by updating instead the load vector from the previous time step. The method is based on the shift of each cell to the next one and it has been applied to our model. An error, however, is introduced due to mixing in the cells. Claesson and Javed concluded after a detailed study that the error can be neglected. For example, in the case of a simulation of 20 years using the aggregation method with each level having 5 cells, the error compared to the non-aggregated solution was lower then 0.1 K (for more information about the method and accuracy, see Claesson and Javed [33]).

Note that the left-hand term of eq. (3.15) is only an approximation of its right-hand term due to the approximation made in eq. (3.14). The error, however, is negligible if the number of cells is sufficiently high. By default, the number of cells by level is five and the sizes of the levels increase exponentially with base two.

3.4 Model validation

The STM and the LTM have been verified by their respective developers. To avoid coding error and to check and generalize the validity of the hybrid step response model (HSRM), an extensive model verification is carried out.

The STM is compared to the widely used sandbox experiment of Beier et al. [14]. These authors have carefully performed a thermal response test using a U-tube BHX. The U-tube is grouted into an aluminium pipe of 18 meters long which is placed into a box filled with homogeneous sand. An electrical heater injects a constant power to the HCF and a pump ensures a constant flow rate. All ground and grout properties are presented in their paper, except the heat capacities. The ground capacity has been estimated by Beier [13] using a best fit method (c = 1.6 kJ/kgK). For the grout a heat capacity of 2 kJ/kgK is used. The HCF temperature is measured at the in- and outlet as well as the BHX wall and sand temperatures at various depths. It should be noted that

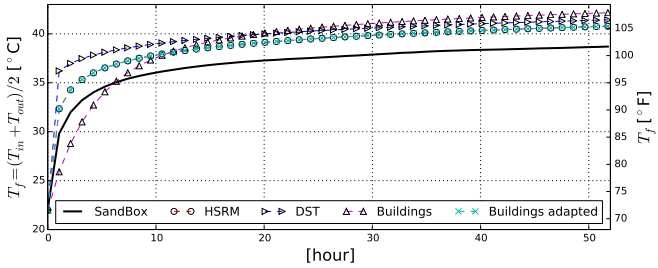

Figure 3.5: Comparison between the heat carrier fluid temperature from the sandbox experiment [14], the borehole model from the `Buildings` library, type 557a of TRNSYS (DST) and the new hybrid model (HSRM).

the aluminium pipe around the grout acts as a thermal fin which reduces the borehole thermal resistance by flattening out its wall temperature. Consequently the HCF temperature should be lower for the experiment compared to the models which do not take this fin effect into account (see [90]). Figure 3.5 compares the average of the in- and outlet temperatures of the HCF for the case of the experiment, the `Buildings` model, TRNSYS models (type 557a (DST)) and the implemented HSRM. The `Buildings` model dynamics is clearly too slow. This is due to the position of the lumped capacity of the grout, as illustrated by Bauer et al [12]. In the `Buildings` model, the grout capacities are positioned at the pipe wall instead of the area center of each grout zone. Adapting the capacity location (which requires also the adaptation of the resistances), the problem is solved (`Buildings` adapted). TRNSYS DST model and HSRM give similar results. DST, however, does not incorporate the short-term thermal dynamics of the fluid, contrary to the new model HSRM. The experiment results were also compared with the HSRM using the R_b formulation of Sharqawy et al. (see [90]) instead of the multipole method. No significant improvements could be seen, as the R_b value differed only by 1 % from its original value.

The LTM is verified using the well known g-function developed by Eskilson and the infinite cylindrical heat source (CHS) solution for different configurations (the data are taken from the paper of Bertagnolio et al. [18]). Figure 3.6a illustrates the case of a 110 m deep single borehole. The error of the implemented model compared to the g-function never exceeds 0.11 K during the 25 year-long simulation (relative error of 1.7 %). The difference is caused by the so-called end effect of the borehole, i.e. the axial heat transfer due to the finite length of the borehole. The analytical solution uses a finite line-source approximation whereas the Eskilson finite volume model is three-dimensional (different boundary condition at the foot of each borehole). The CHS model is

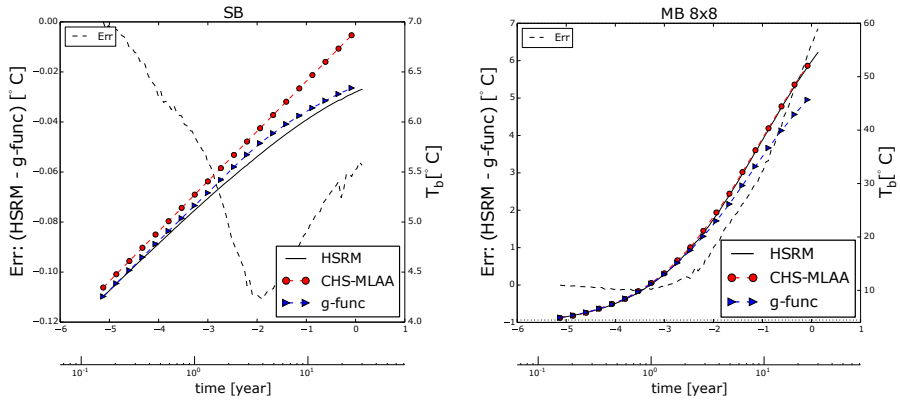

(a) Single borehole.

(b) 64 boreholes in filled square configuration (B/H=0.05).

Figure 3.6: Step response temperature of the borehole wall of the borefield calculated by the g-function (*g-func*), the infinite cylindrical source with aggregation method (*CHS-MLAA*) and the new hybrid model (*HSRM*).

logically unable to model the end effect. Figure 3.6b illustrates the case of a borefield with a square 8x8 configuration. The length of the boreholes is 110 m (328 ft) and the distance between the boreholes to length ratio equals 0.05. Due to the very compact configuration, high ground conductivity and low heat injection, a large error appears, as Malayappan and Spitler [97] warned for (see section 3.2.2). The end effect error is negligible compared to the large error (> 7 K after 25 years for this case, relative error of 17.5 %) introduced by the homogeneous heat source approximation. However, if the borefield is dissipative enough, the model shows very good results (e.g. for a line configuration of eight boreholes with the same parameter values, the error is lower than 0.1 K). For simulations with small yearly thermal ground imbalance (amount of injected heat equals amount of extracted heat), the configuration error is partly counteracted and it will not cause significant accuracy issues.

3.5 Example

This section presents an example of a borefield subjected to a varying non-symmetric load proposed by Bernier et al. [18]. The CPU time and the fluid temperature of the `Buildings` model and those of the HSRM are compared for a simulation of one year in the case of a single borehole and the case of

three boreholes in series (fig. 3.7). The `Buildings` model is composed of the `Buildings` component `Boreholes.UTube`, an ideal heater and a pump. The interaction between the boreholes is taken into account by the HSRM but not by the `Buildings` model. As observed in fig. 3.5, the `Buildings` model overestimates the time constant of the BHX which is also visible in fig. 3.7 where the fluctuations of the HCF temperature of the `Buildings` model have a smaller amplitude than those of the HSRM model. The analysis of the CPU times illustrates very clearly the difference between the models. In the case of a single borehole, the HSRM is about twelve times faster than the `Buildings` model. The HSRM has a longer initialization time due to the calculation of the aggregation matrix, but it calculates the temperature response very fast. In the case of three boreholes in series, the HSRM is about 60 times faster. The initialization time is longer than for a single borehole because the superposition of the temperature field of the boreholes needs to be calculated. However, once the aggregation matrix is calculated, the calculation time is the same for any configuration. This is not the case for the `Buildings` model.

3.6 Conclusion

A new hybrid model for borefields with arbitrary configuration having both short-term (minutes) and long-term accuracy (decades) has been successfully developed and implemented in Modelica. The state-of-the-art of both short-term and long-term models from the literature has been combined into a hybrid model to calculate accurate step-responses (or so-called *g-functions*). The step-responses are superposed to get the fluid temperature response to an arbitrary load. Thanks to its aggregation method, the implemented model is about twelve times faster than the borehole model of the `Buildings` library for the case of a single borehole and about 60 times faster for the case of three boreholes in series. The long-term accuracy of the model decreases for compact borefield configurations. This can be solved by plugging a g-function in the model instead of calculating the temperature step response.

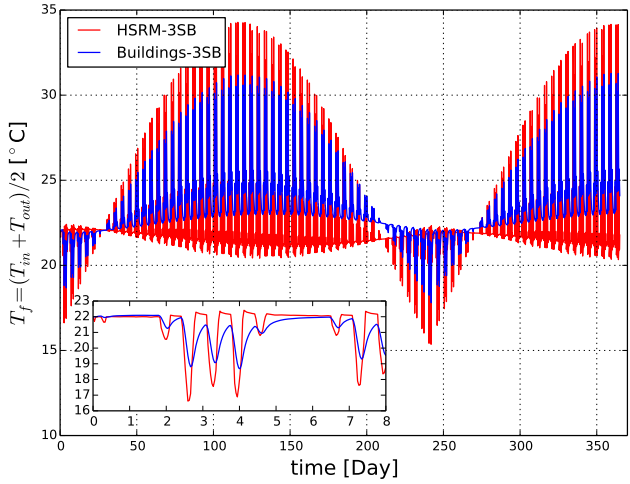

(a) Heat carrier fluid temperature for HSRM-3SB and Buildings-3SB.

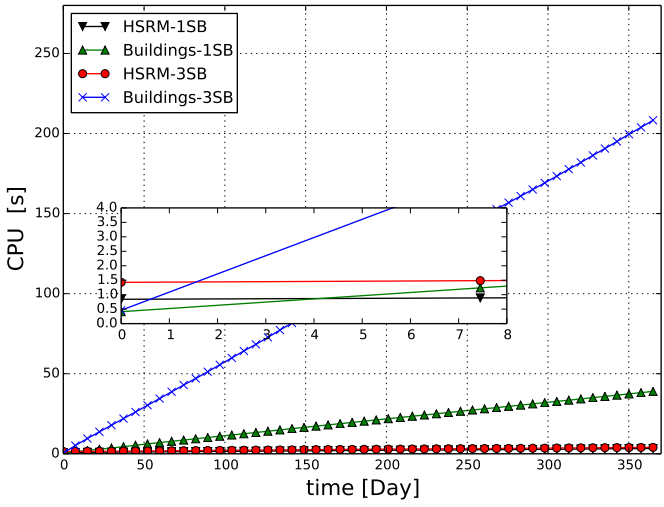

(b) CPU time comparison.

Figure 3.7: Comparison between between the new model (HSRM) and the model from the `Buildings` library (Buildings) for a single borehole (1SB) and for three boreholes in series (3SB).

Chapter 4

IDEAS, IBPSA, and Buildings libraries, and other component models

The building models developed in this work are built upon different Modelica libraries. Section 4.1 summarizes the characteristics and assumptions of the libraries and shortly describes the main components used by the building models presented in chapter 5. It has been strived to include most of the code development, which was necessary to model the different buildings and their HVAC systems, to the libraries themselves. However, some models which were either too specific or which did not meet the libraries requirements, are not included in the libraries yet. These models are described in section 4.2. Finally, section 4.3 lists the measures taken to speed up the simulations.

4.1 Modelica libraries

In 2013, the Annex 60 project (conducted under the umbrella of the International Energy Agency's Energy in Buildings and Communities Programme (IEA EBC)) started with the aim to create a free, open-source library for building and community energy systems. The Annex 60 project resulted in the development of a library which is now used as the core of the `IDEAS` [10], the `Buildings` [169], the `AixLib` [99], and the `BuildingSystems` [102] libraries. The Annex 60 project is continued under the umbrella of the International Building Performance

Simulation Association (IBPSA) and the library has been renamed to `IBPSA`. Therefore, the main assumptions, the design principles and the key component models of `IBPSA` are firstly described in section 4.1.1 as they form the base of `IDEAS` and `Buildings` whose components are used in this work. Secondly, `IDEAS` (section 4.1.2) and the few models used from `Buildings` (section 4.1.3) are presented.

4.1.1 IBPSA (Annex 60) library

`IBPSA` is a Modelica library containing more than 300 classes (models, functions, etc.) which are compatible with models of the *Standard Modelica Library* and, in particular, with the models from `Modelica.Fluid` and `Modelica.Media` [168]. The library currently contains the following main packages: `BoundaryConditions` dealing, among others, with weather data, `Controls` containing simple controllers such as PIDs, timers and hysteresis, `Fluid` gathering all HVAC components which use water or air, and `Media` in which the *water* and the *moist air* packages are implemented.

`IBPSA` is developed following strict restrictions. Firstly, all physical models must have a continuous first derivative to ensure the existence of a unique solution of the system. Secondly, the level of idealization of the models can be conditionally chosen. For example, all mass flow rates are pressure driven to allow simulation of piping network. However, the pressure drop calculations can be conditionally removed to simplify the equations. Another possible conditional simplification is to switch from a dynamic model of first or higher order to a quasi steady-state model. Finally, the library makes extensive use of *inheritance* with many different levels of `BaseClasses` from which all component models are extended such that code duplication is limited.

In the following paragraphs, the main models used for the building models developed in this work are briefly described.

Weather and solar irradiation The package `BoundaryConditions` contains the models which compute the boundary conditions related to the weather data such as the ambient temperature, the air humidity, the solar irradiation, the sky temperature, etc.. The weather information is read from a TMY3 weather data file of a given location by `ReaderTMY3` and the solar irradiation is calculated based on the latitude and longitude of the location, the time of the year, and the orientation and inclination of the surface (for a detailed description of the equations, see Wetter (2004) [164]).

Fans and pumps In `IBPSA`, fans and pumps are modelled by the same models as their physics is similar. The models use the affinity laws and/or performance curves that compute pressure rise, electrical power draw and efficiency as a function of the volumetric flow rate and the speed, depending on the control signal type. The different control signals are i) pressure head, ii) mass flow rate, iii) speed (in revolution per minutes) or normalized speed. The dynamics of the fan or pump are further influenced by the volume of fluid in the model, the heat losses to the surroundings, whether the heat losses of the motor are added to the fluid, and finally, by the raise time of the model input filter used to mimic the inertia of the rotor and the fluid. The model equations have further been adapted to make sure that the model has a unique solution for any pressure boundary and control signal (see Wetter (2013) [165] for a complete description).

Heat exchangers `IBPSA` only contains a simple heat exchanger model (`ConstantEffectiveness`) which computes the transferred power $\dot{Q}$ as $\dot{Q} = \epsilon \dot{Q}_{\max}$ with ϵ a constant effectiveness and $\dot{Q}_{\max}$ the maximum power that can be transferred. This model will be used for the heat exchanger used for passive cooling in the GSHP system and for the recovery unit of the ventilation. In the case of heat exchange between water and moist air, the more complex model `DryCoilCounterFlow` of `Buildings` is preferred (see sections 4.1.3 and 4.2.1).

Radiators The radiator implementation is based on a slightly adapted version of the standard EN 444-2 [143]. The adaptation consists of the discretization of the transferred heat computation along the water flow path (in order to allow variable mass flow rates) and the use of an air (T_a) and a radiation (T_r) temperature instead of a single temperature. Assuming a discretization of N elements, the convective $\dot{Q}_{c,i}$ and the radiative heat $\dot{Q}_{r,i}$ transferred to the room from element i is computed as:

$$\dot{Q}_{c,i} = \operatorname{sign}(T_i - T_a)\,(1 - f_r)\frac{\mathrm{UA}}{N}\,|T_i - T_a|^n$$

$$\dot{Q}_{r,i} = \operatorname{sign}(T_i - T_r)\,f_r\frac{\mathrm{UA}}{N}\,|T_i - T_r|^n$$

where T_i is the water temperature of element i, $f_r \in [0, 1]$ is the fraction of radiant to total heat transfer, UA is the heat transfer value of the radiator, and n is the exponent for heat transfer. The values $n = 1.33$, $f_r = 0.35$ and $N = 4$ are used in this work.

Media: air and water IBPSA contains its own *moist air* and *water* models. The models are simpler than the implementation proposed by the Standard Modelica Library leading to faster and more robust computations while maintaining a good accuracy for the typical temperature ranges present in HVAC systems. The *air* package uses a simplification of the gas law where pressure and temperature are independent. The specific heat capacities c_p and c_v are further assumed constant. The *water* package models liquid water with a constant density (995.586 kg/m^3) and a constant specific heat capacity (4184 J/(kg.K)). The thermal conductivity and viscosity are also assumed constant. For a complete description of the models, see the model documentation (to be found in http://www.iea-annex60.org/releases/modelica/1.0.0/help/Annex60_Media.html#Annex60.Media).

4.1.2 IDEAS library

All building models described in chapter 5 have been modelled using IDEAS v1.0.0, a Modelica Library developed by KU Leuven and 3E which allows simultaneous transient simulation of thermal and electric systems with their controls at the building or at the district level. The library is free and open-source and it is available at https:github.com/open-ideas/IDEAS.

IDEAS is built upon IBPSA and thus contains all IBPSA models. Additionally, IDEAS integrates models required to define the thermal response of a building and to model occupancy, internal gains, and thermal comfort. Jorissen et al. (2017) [80] and Baetens (2015) [9] described the implemented equations of those models and most of the equations are repeated in section 6.1 to explain the developed linearisation methodology. IDEAS further includes HVAC components such as a borefield (see chapter 3), air/water and water/water heat pumps, boilers, a thermal storage tank with stratified layers, etc., and the package IDEAS.Electric allows the simulation of the electricity system. Finally, OpenIDEAS [10] extends IDEAS with stochastic residential occupant behaviour models [11] and with the FastBuildings library which is used by a grey-box toolbox meant to identify buildings with low order models (see De Coninck et al. (2016) [36]). The following paragraphs describe the heat pump, gas-boiler and TABS models of IDEAS as they are the main models used to develop the building models beside the models which define the thermal response of the building.

Heat pump and gas-boiler models In this work, the heat pump and gas-boiler models of a development branch of IDEAS (https://github.com/open-ideas/IDEAS/tree/issue45BoilerModel) are used instead of the models of IDEAS

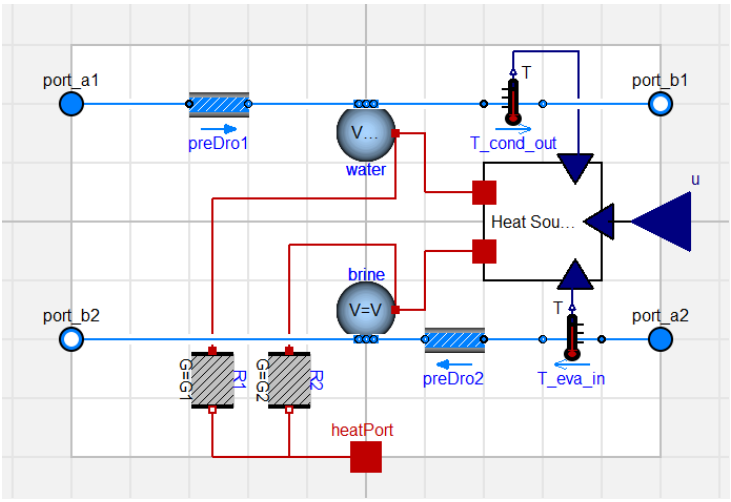

Figure 4.1: Schematic representation of the heat pump model.

v1.0.0. The model assumptions of both versions are the same but in the development version, code duplication is avoided by merging the water/water heat pump, the air/water heat pump and the gas-boiler models to a same base class as they have similar physics. This section firstly describes the water/water heat pump and then specifies the characteristics of the air/water heat pump and of the gas boiler.

The heat pump model is a dynamic model based on typical performance maps that can be found in manufacturer data-sheets. The dynamics are modelled by two *mixing volumes* which represent all water and all brine contained in the condenser and in the evaporator, respectively (see fig. 4.1). Each *mixing volume* is assumed well mixed and it has therefore a unique temperature. Instead of modelling the refrigerant cycle, a *heat source* model based on performance maps computes the thermal powers delivered to the evaporator ($\dot{Q}_{\mathrm{eva}}$) and condenser ($\dot{Q}_{\mathrm{cond}}$) mixing volumes as well as the electrical power used by the compressor (P_{comp}). The performance maps typically return the heat pump COP and P_{comp} as a function of the condenser outlet and the evaporator inlet temperature (*T_cond_out* and *T_eva_in* in fig. 4.1). The *heat source* model also allows 3-D performance maps which are used when, for example, the heat pump powers are also given for different part load ratio's. For examples of performance maps, see chapter 5

The heat pump model further accepts different types of control input. The heat pump can be on/off controlled or use a temperature or a thermal power set point

in which case the device is ideally modulated to reach it if possible. Moreover, the user can directly control the heat pump modulation level. A security feature can also be conditionally added which automatically switches the heat pump off if it reaches its maximum or minimum allowed temperature and turns it back on based on a hysteresis controller. In order to avoid a large number of events (= discrete changes of the model equations which can potentially slow down the solver), the hysteresis controller can be replaced by a direct modulation control which overrules the user control. Finally, the pressure drops in both the evaporator and condenser (*preDro1* and *2* in fig. 4.1) and their heat losses to the surroundings (through *R1* and *R2* in fig. 4.1) can be conditionally added or removed.

The air/water heat pump and the gas boiler models have the same features as the water/water heat pump model except that they have only a water circuit and no brine circuit. The performance maps typically depend on the ambient air conditions for the heat pump and the efficiency of both the heat pump and the (condensing) gas boiler depend on the supply temperature.

TABS The TABS model in `IDEAS` is composed of two parts: the building structure itself which is modelled by a multi-layer internal wall in which heat can be injected at some given positions, and the water circuit which is modelled by the `EmbeddedPipe` model. The internal wall assumes one-dimensional heat diffusion through a succession of homogeneous layers, each modelled by a TRCM. The heat delivered by the water circuit to the TABS can be injected between two layers which implies the assumption of a uniform temperature in the water circuit plane. For the `EmbeddedPipe` model, the work of Koschenz and Lehman (2000) [85] is used. Koschenz and Lehman approximated the three dimensional heat diffusion in TABS by a one dimensional TRCM as described below (see fig. 4.2).

A first resistance (R_z) transforms the supply temperature into a *pipe-average* temperature to take the temperature gradient along the pipe length into account. Secondly, the resistances R_w and R_r are defined to model the convective resistance between the water and the inner pipe wall and the conductive resistance of the pipe wall, respectively. Finally, a resistance R_x computes the resistance between the outer pipe wall and the fictive uniform temperature of the TABS core. R_x can then be connected to the internal wall model. Koschenz and Lehman successfully validated their model against Finite Element models and against experimental measurements. The `IDEAS` model has further been verified with the measurements provided by Koschenz and Lehman's publication [85].

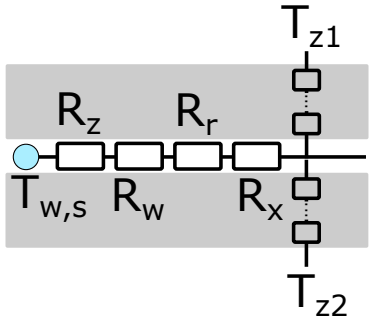

Figure 4.2: Thermal resistances in TABS model according to Koschenz and Lehman [85].

4.1.3 Buildings library

The Modelica `Buildings` library is a free, open-source library based on the `IBPSA` core library and available at `https://github.com/lbl-srg/modelica-buildings`. `Buildings` provides models for HVAC systems, controls, heat transfer between rooms and the outside, multizone airflow, single-zone computational fluid dynamics coupled to heat transfer and HVAC systems, data-driven load prediction for demand response applications, and electrical DC and AC systems with two- or three-phases which can be balanced or unbalanced. The library hierarchical structure and the implementation decisions are described by Wetter et al. (2014) [169], while the library scope is presented in Wetter et al. (2014) and by Wetter et al. (2015) [167]. The following paragraphs elaborate on the models used from this library in this PhD work: the storage tank model and a heat exchanger model.

Stratified storage tank In this work, a slightly adapted version of the `Buildings.Fluid.Storage.StratifiedMultipleInlet` model is used. The model represents a storage tank with stratified layers and multiple in- and outlets. The model is adapted such that the in- and outlet positions in the tank can be freely chosen. The stratified storage tank is modelled by a series of *mixing volumes* (each representing a different layer) which can exchange heat with each other through mass transport, through heat conduction through the fluid and through the vessel wall, and through buoyancy if a temperature inversion occurs. Each layer can further exchange heat with the surroundings through the insulated vessel wall. It should be noted that the buoyancy model is here highly simplified and it just ensures that mixing occurs when a layer is

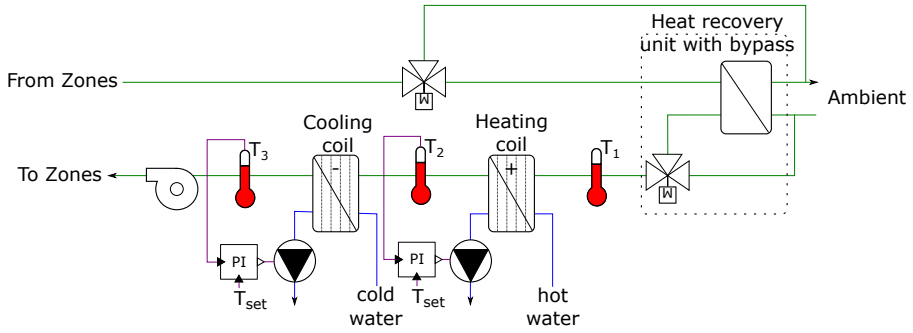

Figure 4.3: Schematic representation of the air handling unit model.

colder than the layer underneath. The time constant of this mixing process is a parameter defined by the user.

Dry coil heat exchangers For the AHU (see section 4.2), an air to water heat exchanger is required. For simplicity and since the AHU of the modelled buildings rarely have to actively cool, no water vapour condensation is considered. The model `Buildings.Fluid.HeatExchangers.DryCoilCounterFlow` proposes an implementation where the heat transfer in the heat exchanger is discretized into n elements. Each element is composed of two heat convection terms for water and air which (conditionally) depend on the mass flow and/or the temperature of the fluids. The two fluids are further separated by a metal plate which is modelled by one state per element.

4.2 Additional models

This section describes the most important component models which have been additionally developed but not included in the libraries.

4.2.1 Air handling unit

Three of the four buildings presented in chapter 5 have an air handling unit (AHU) composed of a heat recovery with bypass, a heating and a coiling coil. Figure 4.3 depicts the developed AHU model which is based on sub-components from `IDEAS` and from `Buildings`.

The top of fig. 4.3 represents the air flows returning from the different zones of the building which are mixed into a single flow. In order to model the fact that only a fraction of the air volume which is supplied in the building, is also extracted, a three-way-valve is used. Through the valve, a constant fraction of air (95%) is lead to the heat recovery unit which is modelled by a simple heat exchanger with constant efficiency (the `ConstantEffectiveness` model as described in section 4.1.1), before being rejected to the *ambient* air. The remaining 5% which represents the fraction lost due to infiltration is rejected to the ambient air. At the other side of the heat exchanger, from right to left, ambient air is circulated with a mass flow rate that depends on the opening of the by-pass valve. The pre-heated or pre-cooled air emerging from the recovery unit is then further conditioned by a heating and a cooling coil which are both modelled using the `DryCoilCounterFlow` model as described in section 4.1.3. Notice that water vapour condensation is neglected. At the water side of the heat exchangers, hot and cold water from the production unit are circulated by a pump whose mass flow rate is controlled by a *PI-controller*. Finally, one fan per zone is used to supply each of the zones with their nominal flow rate (the pressure drop is disregarded).

4.2.2 Building model interface

Modelica is an object-oriented language and the inheritance principle is applied at every level of the libraries and of the models developed in this work. That means that most of the models extend from *base classes* and from *interface classes* to avoid code duplication. Figure 4.4 illustrates the interface class used for all buildings modelled in this PhD work.

The interface is composed of six components which interact with each other using *fluidPort* (), *heatPort* (), *input/ouput* (), and *propsBus* () connectors. The *Weather* component computes all weather-related boundary conditions and propagates this information to all components by using an *inner/outer* structure. The *Building envelope* contains all elements related to the building envelope. These are zones, walls, roofs, floors and windows but also solar shadings and TABS. However, the controller of the solar shadings is included in the *RBC* block which contains the controllers of each element of the building, and the water circuit of the TABS is included in the *HVAC* block which contains the heat/cold production and emission systems except the air handling unit which is included in the *AHU* block. Each building zone can further exchange air with the AHU block and convective and radiative thermal powers with the HVAC block. Heat can further be directly injected in TABS at the position(s) of the water circuit(s) and measurement and control signals are exchanged through

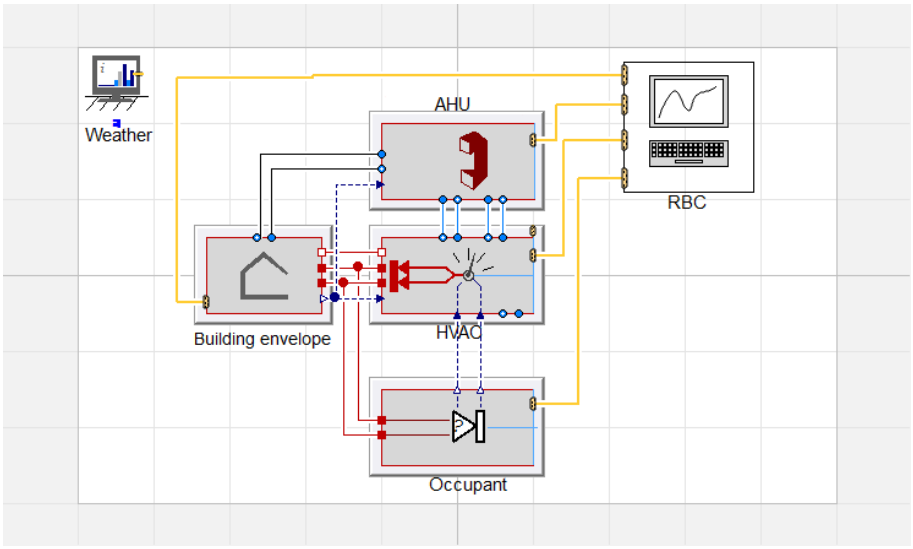

Figure 4.4: Interface used for all building models using RBC.

propsBus and input/output connectors. Finally, the *occupant* model includes all gains, schedules and set points related to occupancy.

4.3 Computational aspects

The Modelica language allows the simulation of multidisciplinary problems. In this work, both thermal and hydraulic physics of the building are (partially) modelled as well as its control. This results in large models ($>$ 1000 states) with a large variety of time constants and of events. In order to keep tractable simulation times, a number of guidelines advised by Jorissen et al. (2015) [81] are followed and they are briefly summarized in this section. The simulation time could be drastically reduced by improving four aspects: the size of the non-linear systems of equations, the number of events, the removal of too small time constants, and the type of integrator used in Dymola.

Size of non-linear systems of equations Typically, a Modelica model can be expressed as a set of ordinary differential equations potentially coupled to each other by algebraic equations. When the algebraic equations cannot be simplified by computer algebra, an *algebraic loop* is created forcing the solver to solve

the equations involved in the loop simultaneously. The cost to solve such loops increases with the number of equations it contains and whether the equations are linear or non-linear. The algebraic loop can be broken by introducing a state variable which decouples the different variables present in the loop and by giving additional information to the solver such as the direction of the flow. This technique is part of the design decisions of `IDEAS` (see Jorissen et al. [80]) and it is also applied to the different building models of chapter 5 such that only three systems of non-linear equations of size 1 are left in the most complex building.

Number of events *Events* are discrete changes of the equations. They can be either *time events* if the change is related to the simulation time (e.g. ON/OFF switch of the ventilation based on an occupancy schedule) or *state events* if the change depends on the value of a state variable (e.g. ON/OFF switching of the heat pump based on a set point). While events are avoided in most of the `IDEAS` and `IBPSA` physical models (see Wetter et al. (2016) [168]), they are unavoidable in controllers. In this work, the number of time events due to occupancy schedules is reduced by trying to synchronize them as much as possible. However, the number of events remains very high.

Small time constants Small time constants create fast dynamics which need to be tracked by the solver and its integrator. In the case of an adaptive step solver, fast dynamics will result in smaller integrator steps and thus longer computation time. In the case of a fixed step solver, the integrator will return erroneous values if its step size is larger than the smallest time constant of the model. Therefore, time constant smaller than one minute are systematically removed from the model by either lumping different elements together (e.g. air volumes in pipes are lumped into one single volume) or by removing the dynamics of the too fast reacting elements and simulating their steady state behaviour instead.

Type of integrator In Dymola, the user can choose which integrator to use to simulate the model. In line with the conclusions of Jorissen et al. (2015) [81], using an explicit integrator such as Euler with integrator step of 30 seconds instead of an implicit and higher order integrator such as Dassl or LSolar resulted in a decrease of the simulation times by a factor 200 or more without significant changes in the precision of the results. However, the use of the Euler integrator is only possible after all time constants smaller than one minute were removed from the model.

Chapter 5

Office, school, retirement and residential buildings: emulator models and simulation results

This chapter is based on the report published as:
Picard D. and Helsen L. Report on the building energy simulation models of an office building, a retirement home, a school, and a block of flats. Tech. rep., KU Leuven, Leuven, Belgium, May 2017.

This chapter describes the office building (section 5.1), the retirement home (section 5.2), the school (section 5.3), and the block of flats building (section 5.4) models on which section 7.2 and chapter 9 are based. Each of the building models is inspired by an existing Belgian building. However, due to lack of information and/or the complexity of the real buildings, some assumptions and simplifications both about the building layout and HVAC design and about its boundary conditions are made as described in the respective sections. The two major simplifications are i) that pressure drops are disregarded in all models and the mass flow rates are controlled by ideal circulation pumps, and ii) that the HVAC components are assumed perfectly insulated (i.e. no heat losses are considered). Start-up behaviours are also not simulated as the building (and all its construction elements) starts the simulation at a temperature of 20°C. Each model is further simulated using a typical meteorological year from Uccle, Belgium [98].

The two additional building models used in section 6.1 and in section 7.1 and developed by Maarten Sourbron ([132]) and Arnout Aertgeerts, respectively, will be briefly described in their own chapters.

5.1 Office building: Hollandsch Huys

The case study building, called *Hollandsch Huys* is located in Hasselt, Belgium. Its construction was finished in 2007. Designed to be a low-energy, innovative office building, the building is a hybrid *GEOTABS* building. The AHU is composed of a recovery wheel with by-pass, a heating and a cooling coil and the supply and extraction fans are on-off controlled. The heat and cold are produced by a GSHP.

5.1.1 Model description

The building consists of five floors: an underground parking, three floors and a roof apartment (the latter not modelled). The following sections describe the building envelope, the HVAC, the occupancy and internal gains assumed for the model, the RBC, and the model validation.

Building envelope

The general parameters of the building envelope are summarized in table 5.1. In order to simplify the model, the building is divided in 12 thermal zones as depicted by fig. 5.1. All transparent parts of the façade are equipped with triple glazing. The window surface lies 40 cm deeper than the façade. Each of them is equipped with an external slat shading device whose angle is adjusted automatically to the solar radiation intensity: the shading device is controlled by a hysteresis controller which closes the shading when the horizontal solar radiation exceeds 150 W/m^2 and re-opens it when the solar radiation is lower than 80 W/m^2.

Table 5.1: General building parameters. The U-value is an average value for the whole building and ACH stands for *air changes per hour*.

Floor area	[m^2]	3760	U-value	[$W/m^2/K$]	0.216
Conditioned volume	[m^3]	10526	Loss area	[m^2]	4438
Window-to-wall ratio	[-]	34%	ACH (n50)	[1/h]	0.9

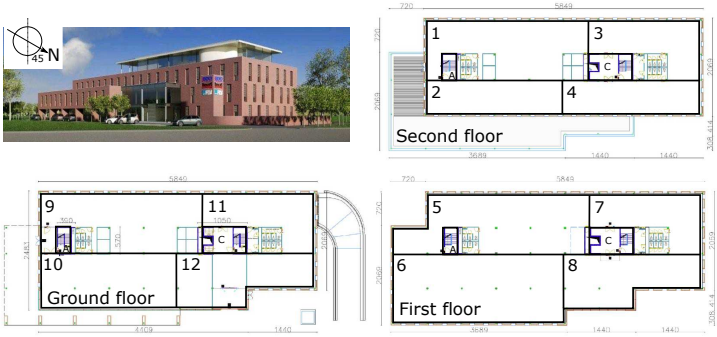

Figure 5.1: Zone layout.

HVAC System

The building is a *hybrid GEOTABS* building. Its emission system is composed of TABS (for the second and third floors) and floor heating (for the ground floor) and the production system is a GSHP. An additional gas-boiler is installed in the real building to back up the heating of the ventilation air but it is not included in the model as it is not needed when proper control is used. The AHU is composed of a recovery wheel which can be by-passed, a heating and a cooling coil and the supply and extraction fans are on-off controlled.

Heat/cold production and emission Figure 5.2 shows the hydraulic scheme of the building. The emission system is composed of floor heating at the ground floor, of TABS with a floor and a ceiling circuit between the different floors of the building, and of TABS with a ceiling circuit in the roof. The nominal mass flow rates are listed in table 5.2. The production system is composed of a borefield, two buffer tanks of 2 m^3 each, three heat exchangers, some circulation pumps and a heat pump of 181 kWth. Notice that the heat pump of the real building is a Daikin EWWP145 KAW1M which consists of three modules that can be separately controlled. In the model, this heat pump is simplified as a perfectly modulating heat pump with characteristics given by fig. 5.3 (scaled

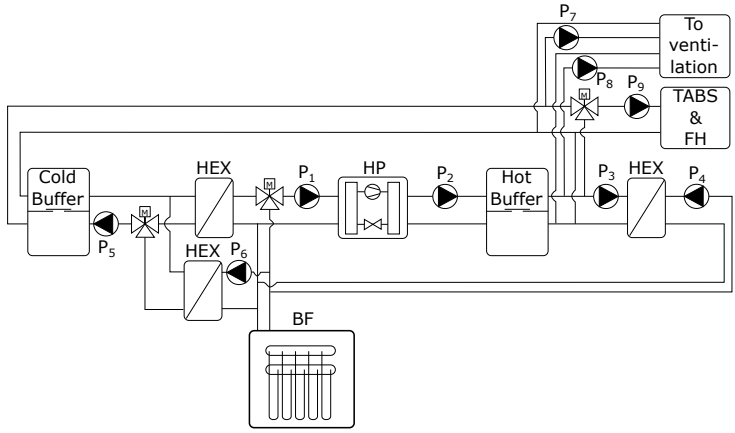

Figure 5.2: Hydraulic scheme. The components are: a borefield (BF), heat exchangers (HEX), buffers, a heat pump (HP), TABS and floor heating (FH) and 9 circulation pumps P_i.

Table 5.2: Nominal mass flow rates for TABS and floor heating.

Emission	Nominal mass flow rate			
TABS-ceiling	7	[l/h/m^2]	0.0019	[kg/s/m^2]
TABS-floor	6	[l/h/m^2]	0.0017	[kg/s/m^2]
Floor heating	4	[l/h/m^2]	0.0011	[kg/s/m^2]
Entire building	47600	[l/h]	13.22	[kg/s]

data from the Viessmann heat pump VitoCal300GBWS301.A45 as the Daikin data was not found). The borefield characteristics are summarized in table 5.3 and fig. 5.4 shows its layout. The HCF in the borefield of the real building contains 34% of ethylene. In the model, the fluid is simplified to 100% water as the temperature never drops below the freezing point. The nominal mass flow rates of the different pumps are given in table 5.4. Notice that in the model, pump P_9 is actually a set of 29 pumps in parallel which control each individual TABS and floor heating circuit. In reality, the mass flow in each circuit is controlled by a valve and two pumps to ensure the pressure head.

Air handling unit The air handling unit is composed of a heat recovery with by-pass, a heating and coiling coil, a supply and an extraction fan and the AHU is modelled as described in fig. 4.3. In the real building, the heating coil can be connected to a gas boiler in the case the heat pump cannot deliver the necessary

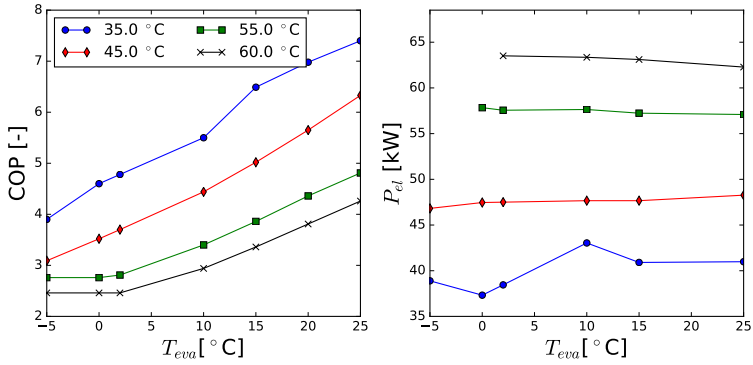

Figure 5.3: Heat pump characteristics as a function of the evaporator inlet and different condensor outlet temperatures, scaled from the characteristics of the heat pump VitoCal300GBWS301.A45 of Viessmann [161] (45kWth) to 181kWth.

Table 5.3: Borefield parameters.

Layout			Borehole			Ground / Grout		
# bh	14+8	[-]	D_{bh}	160	[mm]	λ	2.2/0.6	[W/(m.K)]
Type	1U	[-]	D_{pipe}	32	[mm]	ρ	$10^3/10^3$	[kg/m^3]
H	75	[m]	e_{pipe}	2.9	[mm]	c_p	2.5/1.7	[kJ/(kg.K)]
T_0	11.3	[°C]	λ_{pipe}	0.38	[W/(m.K)]	R_b	0.266	[(m.K)/W]

Table 5.4: Nominal mass flow rates of the different pumps indicated in fig. 5.2.

		P_1	P_2	P_3	P_4	P_5	P_6	P_7	P_8	P_9
$\dot{m}_{\text{nom}}$	[m^3/h]	49.0	49.0	49.0	49.0	49.0	49.0	1.4	1.4	47.6
	[kg/s]	13.6	13.6	13.6	13.6	13.6	13.6	0.4	0.4	13.2

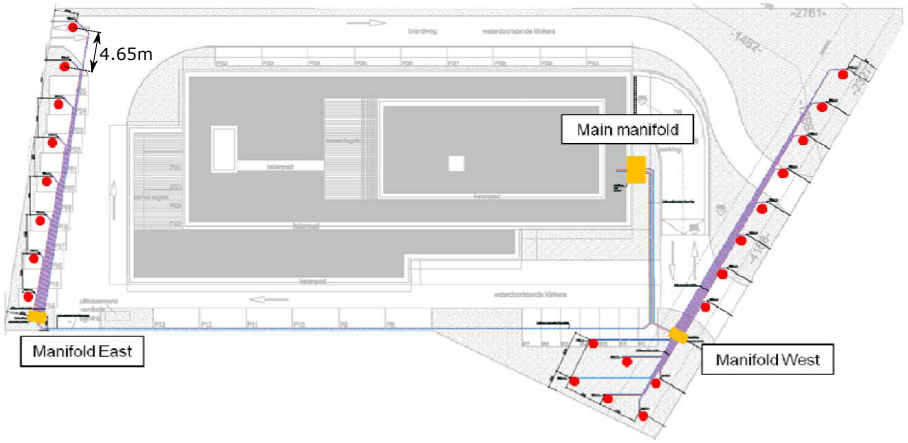

Figure 5.4: Borefield layout.

Table 5.5: Nominal ventilation flow rates.

Type of room	Nominal mass flow rate			
Office area	1.80	$[m^3/h/m^2]$	6.01E-4	$[kg/s/m^2]$
Technical room	0	$[m^3/h/m^2]$	0	$[kg/s/m^2]$
Entire building	6787.50	$[m^3/h]$	2.26	[kg/s]

heat power. For simplicity, the model only has a supply fan, the coil is split into a heating and a cooling unit and the gas boiler is omitted. Furthermore, no air humidity is simulated. The ventilation works at nominal condition when occupancy is non-zero and it is turned off otherwise (see nominal conditions in table 5.5 and occupancy in fig. 5.5).

Occupancy and internal gains

The internal gains are computed by the stochastic behavioural model of Parys et al. [109]. Their nominal values are listed in table 5.6. In the model, the nominal values are multiplied by the stochastic coefficients of fig. 5.5.

Table 5.6: Nominal internal heat gains. The actual heat gains are obtained by multiplying the nominal values with the coefficients of fig. 5.5.

		People *			Light		Appliances	
Type of room		Conv	Rad	Lat	Conv	Rad	Conv	Rad
Office area	[W/m^2]	1.63	1.63	2.75	3.50	3.50	6.23	8.60
Technical room	[W/m^2]	0	0	0	0	0	0	0

* (assuming 20 m^2 / person as the building is only partially occupied)

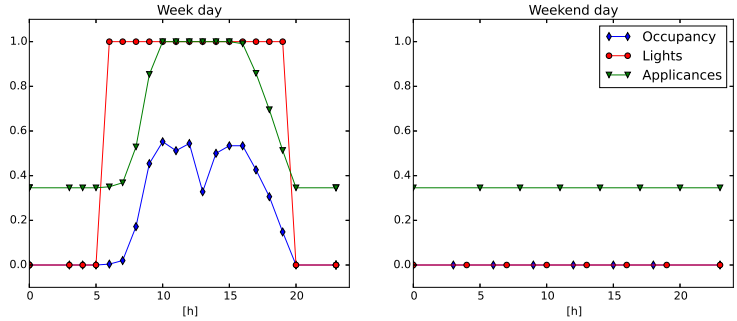

Figure 5.5: Time-dependent coefficients for internal gains. Profiles taken from Parys et al. [109].

Rule based control

The building control is based on three different modes: the heating (H), the passive cooling (PC) and the active cooling (AC) mode. The controller can switch from mode to mode according to the finite state machine as described in fig. 5.6. The transitions are only evaluated at the start of each hour in order to avoid a too fast switch between the modes. Depending on the mode, the production system can either heat, cool using the passive cooling or cool using the active cooling function of the heat pump. The working principle of the production system is shown for each mode in fig. 5.7.

In H mode, the temperature of the hot storage tank is controlled using a PI-controller which modulates the heat pump. Its measured input is the temperature of the highest layer of the hot buffer tank and its set-point is the maximum of the heating/cooling curve for the TABS and the one for the floor heating (see fig. 5.8). The circulation pumps P_1 and P_2 are turned on at nominal condition for non-zero modulation of the heat pump. During the PC mode and the AC mode, the temperature of the cold storage is controlled using

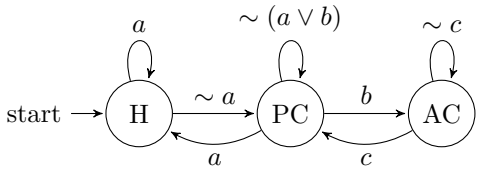

$$a = T_{e3d} \ < 12°C$$

$$b = (T_e \ > 30°C) \ \wedge \ (T_{\text{cold,storage,top}} > T_{\text{cold,storage,set}} + 10°C)$$

$$c = (T_{\text{cold,storage,top}} < T_{\text{cold,storage,set}}) \vee (T_{e3d} < 30°C)$$

Figure 5.6: Mode selection between the heating (H), the passive cooling (PC) and the active cooling (AC) mode. T_e and T_{e3d} are the ambient temperature and its 3-day average, respectively. $T_{\text{cold,storage,top}}$ is the temperature in the highest layer of the cold storage tank and $T_{\text{cold,storage,set}}$ its set-point. $\vee$ is the logical conjunction (and), $\wedge$ the logical disjunction (or), and $\sim$ the negation (not).

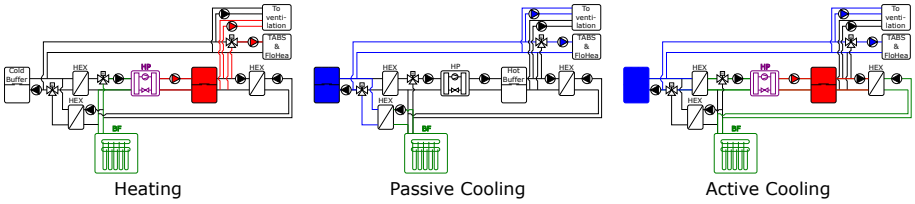

Figure 5.7: Working principle of the production system as a function of the mode.

a PI-controller which modulates pump P_5. The temperature of the lowest layer of the cold buffer tank is used and the set-point is set by the TABS cooling curve (see fig. 5.8). In the case of the PC-mode, P_6 is turned on for non-zero modulation of P_5. In the case of AC-mode, the heat pump is controlled with the same signal as P_5, P_1 and P_3 are turned on for non-zero modulation and P_4 is only turned on if the temperature of the hot buffer tank reaches its maximum allowed temperature.

The TABS and floor heating circuits are controlled as follows: each hour, the water is circulated in each circuit for 10 minutes. Depending on the difference between its supply temperature and its return temperature, the re-circulation is continued for a given amount of time (see table 5.7). It should be noted that the starting time of the different circuits is shifted by 10 minutes relative to

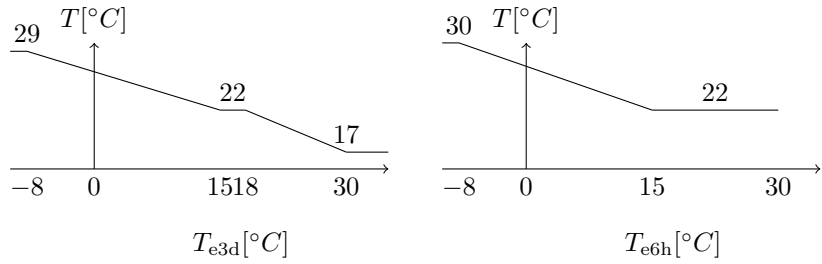

(a) Heating/cooling curve for TABS.

(b) Heating/cooling curve for floor heating.

Figure 5.8: Heating/cooling curves for the supply water to the TABS (a) and to the floor heating system (b) as a funcion of respectively the previous three days (3d) and previous 6 hours (6h) average ambient temperature (T_e).

Table 5.7: Re-circulation times for TABS and floor heating as a function of the difference between the supply temperature (T_{sup}) and the return temperature (T_{ret}).

T_{sup}-T_{ret}	[K]	3	5	7	9	9+
Extra re-circulation time	[s]	0	600	1200	2000	3000

each other in order to smooth the thermal demand loads.

Finally, the ventilation is *on* from 6:00 AM to 8:00 PM. Its supply set-point temperature is set equal to the lower temperature of the comfort range. The supply air is firstly conditioned by the heat recovery and the by-pass of the AHU. If necessary, the air is further conditioned by the heating or the cooling coil controlled by a PI-controller. The water to the coils is coming from the hot and cold buffer tank. The AHU can therefore not cool during the H-mode or heat during the PC-mode.

Model validation

This section is based on Picard et al. [116].

The following paragraphs describe the building monitoring data, the weather data, the tuning of the model and the model validation.

Measurement data. The Modelica model of the Hollandsch Huys building has been validated using 5 sets of measurement data. The first data set was

obtained from an experiment conducted in the building during the Christmas holidays of 2012. The building was not or only partially occupied during 11 consecutive days and this opportunity was used to excite the HVAC system with several step inputs: two sequences of whole building cooling down (all HVAC off) and heating up (resp. TABS on and TABS+ AHU on), and sequences of active cooling down (TABS cooling on) and heating up (TABS on or TABS+ AHU on) of specific zones. These last step inputs were generated to evaluate the intra-zone effect of thermal conditioning. During these experiments, extra zone temperature sensors were installed in addition to the Building Management System (BMS) zone temperature sensors, allowing a more accurate validation for each of the 12 zones.

The other four data sets each contain approximately one month of measurement data during the year 2014: Jan 14-Feb 10; May 9-June 2; June 13-July 7; Aug 23-Sept 16. These periods were the only error-free data sets for zones 1, 2 and 4 (fig. 5.1) and reflect a winter, a mid-season and two summer periods. Due to corruption or failure of many sensors of the BMS, no data during 2014 is available to validate the 9 other zones.

Weather data. The building does not have a local weather station, although during the Christmas experiment the ambient temperature was measured using a dedicated temperature sensor. Therefore, the identification and validation data sets from the BMS are extended with historical data of a weather station in Hasselt obtained from the website `darksky.net`. In order to verify this data, the Christmas ambient temperature from the weather station in Hasselt (F-Hasselt) was compared with those from the airport of Maastricht from both `darksky.net` (F-Maastricht) and `www.wunderground.com` (WG-Maastricht). The comparison shows that the weather data are similar except between the 31st of December and the first of January. The data F-Hasselt is chosen because it is the closest match and because no solar information is available for historical data from `www.wunderground.com`. The direct normal irradiation and the diffuse irradiation on a horizontal surface are computed using the cloud coverage factor from the weather data and the theoretical cloudless solar radiation, which depend on the position of the sun and on the geographical location [119, 24]. Using this conversion, the ambient temperature, direct normal and diffuse horizontal irradiation are known. The Modelica model then makes a geometrical projection on the building surfaces.

Model parameter tuning and validation results. The data obtained during the Christmas experiment (D-Xmax) are used to fine-tune the Modelica model, while the data sets of the year 2014 (D-Y14) are used as validation data. In order to obtain a good temperature fit on D-Xmax, the following tuning is done: the insulation thickness is increased below the apartment (to have a better fit for the effective insulation created by the (non-modelled) apartment on

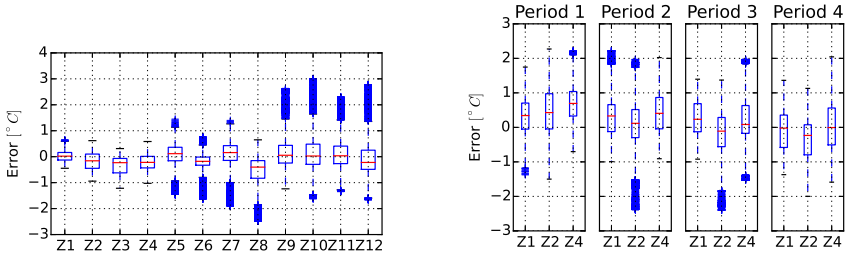

(a) Christmas experiment. (b) Year 2014.

Figure 5.9: Boxplot of the air temperature error for each zone for the tuning data-set (a) and for zones 1, 2 and 4 using the four validation data sets of one month each (b).

the roof) and decreased for all roof surfaces that are not below the apartment.

For the validation using the D-Y14 data sets, the tuning made with D-Xmas is kept unchanged and only the internal gains are reduced by 40% compared to their theoretically estimated values. Figure 5.9 shows boxplots of the air temperature error for each validated zone. The horizontal line corresponds to the median, the box to the first and third quartiles, the whiskers to the 95% confidence interval and the crosses to the outliers. Figure 5.9b shows that the errors on the validation data mostly stay below 1 K for the entire data set, which indicates that the Modelica model is a realistic representation of the real building. The other building types are modelled in a similar way. As the goal of this work is not to mimic the exact behaviour of particular buildings but rather to use realistic building models, the validation of only one of the four buildings was considered sufficient and the validation exercise has not been repeated.

5.1.2 Simulation results

This section discusses the simulation results. Figure 5.10 shows the operative temperature (i.e. the weighted sum between radiative and air temperatures) of each zone for the whole year and the black lines indicate the comfort range. The heating and the passive cooling mode (active cooling mode is not needed) are indicated with the red and blue background, respectively. Figure 5.11 presents the thermal discomfort computed as number of Kelvin hours outside the comfort range and the maximum and minimum temperature deviation from the comfort range. Figures 5.10 and 5.11 show that the comfort level is good with the

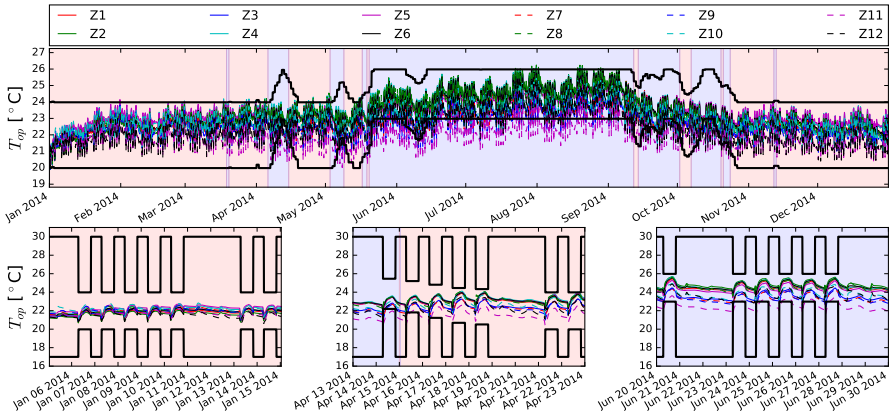

Figure 5.10: Operative temperature of each zone Z_i. The *heating* and *passive cooling mode* are indicated by the red and blue background, respectively.

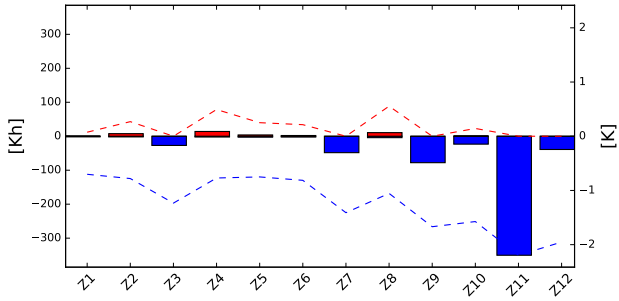

Figure 5.11: Thermal discomfort per zone measured in number of Kelvin hours per year (bars) and yearly maximum temperature deviation from comfort boundaries (dashed lines).

exception of zone 11 which shows some undercooling due to its higher heat losses (zone 11 is above the underground parking entrance).

Figure 5.12 depicts the heat and cold emission of the AHU and TABS per floor area, and the figure shows that the ventilation always cools (around 5 W/m^2). This is due to the fact that the ventilation set-point corresponds to the lower comfort temperature and the ventilation air is therefore not pre-heated up to the zone air temperature. Notice that the ventilation air is rarely actively

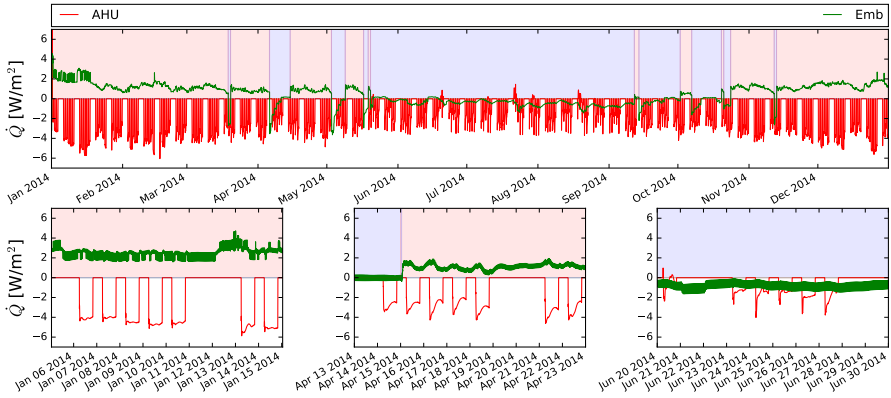

Figure 5.12: Average heating and cooling power per unit floor area delivered by the different emission systems: the AHU and the TABS (Emb). The *heating* and *passive cooling mode* are indicated by the red and blue background, respectively.

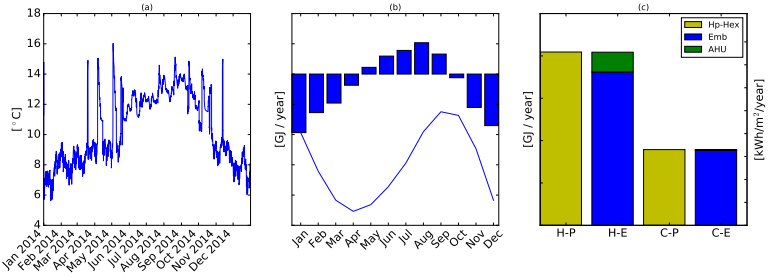

Figure 5.13: (a): borefield return temperature. (b): bars: energy to the borefield (positive = injection), line: cumulative energy. (c): yearly energy used by production systems (P) for heating (H) and cooling (C) and energy delivered by the emission systems (E). The right axis gives the energy in kWh per unit floor area per year.

cooled (see fig. 5.13). Figure 5.13 gives the borefield return water temperature, its heating and cooling loads per month and the heat and cold produced and delivered to the building. Figure 5.13 (b) shows that the building is heating dominated with a net 80 GJ/year of energy extracted from the borefield. The building is mostly conditioned by its TABS and about 11% of the produced heat is used to pre-heat the ventilation air flow (see fig. 5.13 (c)). The building only uses 15 kWh/m^2/year for heating and 6.5 kWh/m^2/year for cooling (compared to 15 kWh/m^2/year for the total energy used by a passive house).

5.2 Retirement home: Ter Potterie

The case study building, called *Ter Potterie*, is an retirement home (10738 m^2 floor area) of 121 beds in Brugge, Belgium. The building is a so-called *hybrid GEOTABS* building which uses a combination of a GSHP to heat and cool through TABS and a gas-fired boiler used to provide the high temperature water used by the radiators and for domestic hot water. The AHU is composed of a recovery wheel with by-pass, a heating and a cooling coil and the supply and extraction fans are on-off controlled.

5.2.1 Model description

The *Ter Potterie* model is composed of three conditioned floors, an attic and an underground garage. The following sections describe the building envelope (section 5.2.1), the HVAC (section 5.2.1), the occupancy and internal gains assumed for the model (section 5.2.1), and the RBC (section 5.2.1).

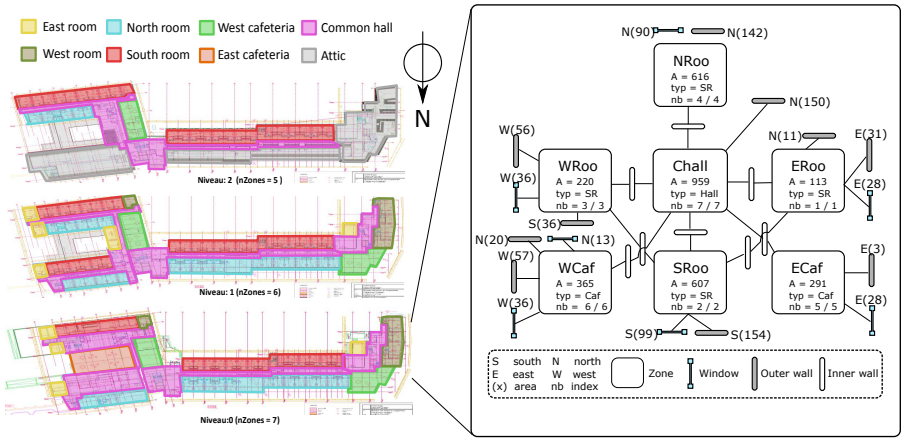

Figure 5.14: Left: Zone layout. Right: zones, walls and windows interconnections for the ground floor model.

Building envelope

The general parameters of the building envelope are summarized in table 5.8. In order to limit the model size, rooms with similar function and orientation are lumped together. The resulting model is composed of 18 conditioned zones, the garage and the attic (see fig. 5.14).

Table 5.8: General building parameters. The U-value is an average value for the whole building and ACH stands for *air changes per hour*. The U-value of the ground is computed as described by ISO 13370.

Floor area	[m^2]	10135	U-value	[$W/m^2/K$]	0.51
Conditioned volume	[m^3]	41326	Loss area	[m^2]	7913
Window-to-wall ratio	[-]	36%	ACH (n50)	[1/h]	1

HVAC system

The building is a *hybrid GEOTABS* building, i.e. the emission system is composed of a combination of TABS, floor heating (FH) and radiators and the production system is composed of a GSHP and a gas-fired boiler. The AHU is composed of a recovery wheel with by-pass, a heating and a cooling coil and the supply and extraction fans are on-off controlled.

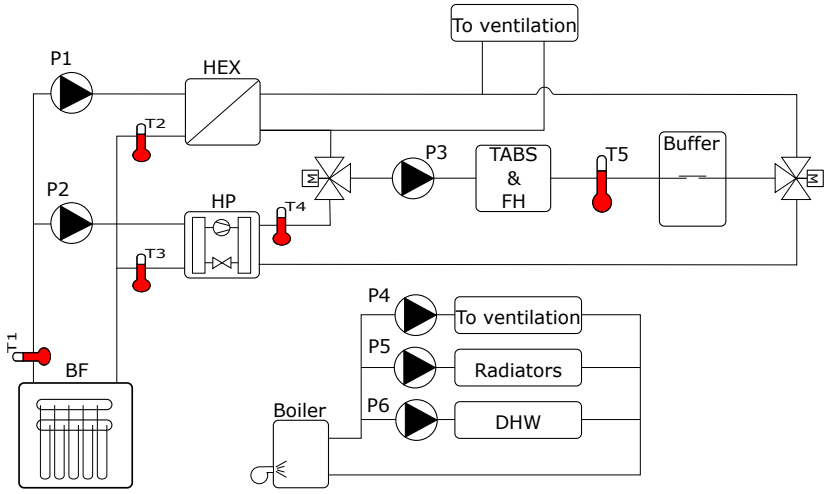

Figure 5.15: Hydraulic scheme. The components are: a borefield (BF), a heat exchanger (HEX), a buffer, a heat pump (HP), a gas-fired boiler, radiators, TABS and floor heating (FH), circulation pumps and domestic hot water (DHW).

Heat/cold production and emission Figure 5.15 depicts the hydraulic scheme of the building. The emission system is composed of floor heating at the ground floor, of TABS with the water circuit in the middle of each floor, and of radiators in each room. The nominal mass flow rates and thermal powers of the TABS, floor heating and radiators are listed in table 5.9.

Table 5.9: Nominal mass flow rates, heating powers and cooling powers of TABS, floor heating (FH) and radiators.

Emission	Mass flow rate		Heating power		Cooling power	
TABS	6	[l/h/m^2]	27.9^{*,a}	[W/m^2]	34.8^{*,b}	[W/m^2]
FH	4	[l/h/m^2]	23.2^{*,b}	[W/m^2]	NA	[W/m^2]
Radiator	0.86^{*,c}	[l/h/m^2]	20	[W/m^2]	NA	[W/m^2]
TABS + FH (tot)	54468	[l/h]	267.7	[kW]	242.6	[kW]
Radiators (tot)	8716	[l/h]	170	[kW]	NA	[kW]

* Assuming an inlet-outlet temperature difference of 4 K (a), 5 K (b), and 20 K (c).

The production system is composed of a borefield (BF) consisting of 90 boreholes of 75 m depth each. All borefield parameters are summarized in table 5.10 and

the borehole positions are indicated in fig. 5.16. The borefield is used as a heat source by two heat pumps (Carrier type 61WG 090, 110 kWth) operated in parallel which is approximated in the model by a perfectly modulating single heat pump (HP) of 220 kWth with characteristics given by fig. 5.17. The borefield is used as the cold source by a heat exchanger (HEX) of 260 kW. While in reality the borefield and the heat pump and heat exchanger are supplied by two pumps in parallel with some valves to control the distribution, the model uses a simplified approach where two independent pumps (P1 & P2) are used in parallel for each production component. The cold water coming from the HEX or the warm water coming from the HP is fed to the AHU and to the TABS and FH and the return water is collected in a buffer tank of 1.5 m^3 in order to stabilize the inlet temperature of the heat pump. The building is further equipped with a condensing gas boiler which supplies the domestic hot water (DHW), the hot water for the radiators and the heating load of the AHU. The efficiency of the boiler as a function of its set-point temperature is shown in fig. 5.18.

Table 5.10: Borefield parameters.

Layout			Borehole			Ground/Grount		
# bh	90	[-]	D_{bh}	160	[mm]	λ	2.5/0.8	[W/(m.K)]
Type	2U	[-]	D_{pipe}	32	[mm]	ρ	$10^3/10^3$	[kg/m^3]
H	75	[m]	e_{pipe}	2.9	[mm]	c_p	2.4/1.7	[kJ/(kg.K)]
T_0	12.6	[°C]	λ_{pipe}	0.38	[W/(m.K)]	R_b	0.1	[(m.K)/W]

Air handling unit The AHU is composed of a heat recovery with by-pass, a heating and coiling coil, a supply and an extraction fan and the AHU is modelled as described in section 4.2.1. The heating coil is connected to the gas-boiler and the cooling coil to the heat exchanger. The ventilation works at nominal condition during the day and at 50% during the night (see nominal conditions in table 5.11 and occupancy in fig. 5.19). For the cafetaria's and common rooms, the ventilation is set to zero during the night. The nominal ventilation flows are taken from the real building and the European standard EN 13779 [144].

Occupancy and internal gains

The modelled occupancy and internal gains are given by fig. 5.19. The convective, radiative and latent heat production are estimated using the European standard EN 13779 [144] and the detailed description of the appliances and lighting of the

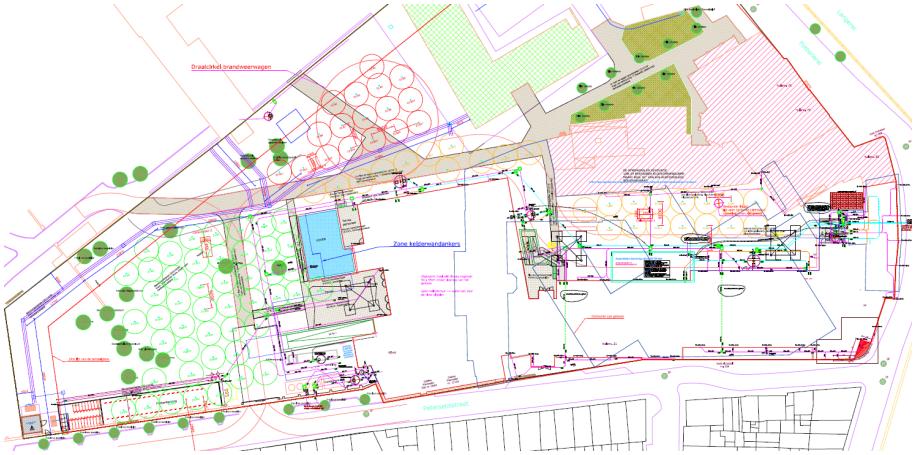

Figure 5.16: Borefield layout. The borefield is divided into three fields around the building (green, red, orange). A minimum distance of 6 m is kept between adjacent boreholes.

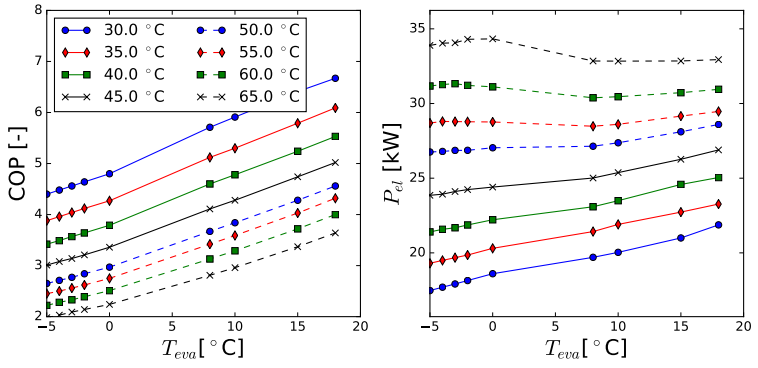

Figure 5.17: Heat pump characteristics (COP and electrical power of the compressor) of *Carrier type 61WG 090* (110 kWth) from its technical description [27].

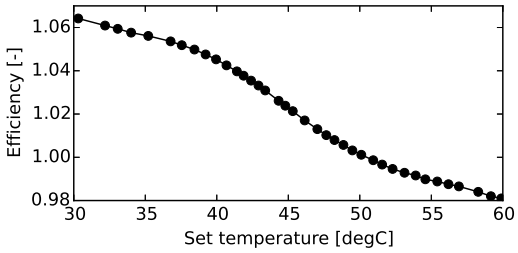

Figure 5.18: Efficiency as a function of the set-point temperature for condensing gas boiler *Riello Tau N 290* (270 kWth) from its technical description [123].

Table 5.11: Nominal occupancy and ventilation flow rates for the three room types of the building.

Type of room	Nominal occupancy		Nominal flow rate	
Bedroom	28	[m^2/ pers]	75*a	[m^3/ h / pers]
Hall	28	[m^2/ pers]	45*b	[m^3/ h / pers]
Cafetaria / common	8	[m^2/ pers]	25*c	[m^3/ h / pers]

* based on real building. Equivalent to standard EN 13779 (a: IDA1, b: IDA2, c: IDA3) [144] .

bedrooms of the real building. The occupancy percentage varies as a function of time and activity of the residents. The domestic hot water (DHW) consumption is based on a similar retirement home (WZC De Vliedberg, [103]) which uses on average 0.6 m^3/month/bed of DHW at 60°C.

Rule based control

Figure 5.20 sketches the building control: a top level controller (General) decides on the control mode (heating (H), neutral (N) or cooling (C) mode), the lower and upper zone temperature of the comfort range (T_{Low}, T_{Up}), and the water supply temperature $T_{\mathrm{wat,sup}}$ to the TABS. The modes are calculated according to the state-machine described by fig. 5.21. The transition between the modes is evaluated only at the start of each hour to avoid fast switching. The comfort ranges are prescribed by the standard EN ISO 7730 [150]. The comfort range varies according to the time of the year (see fig. 5.22).

The action of the TABS and FH depends on the mode. During the N mode,

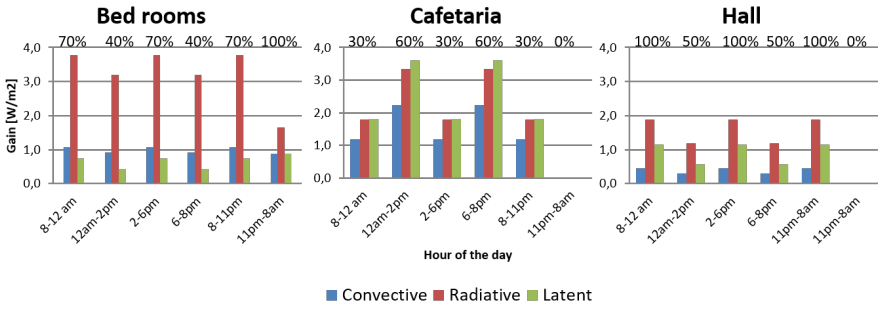

Figure 5.19: Time-dependent internal gains for the three room types of the building. The percentage values given for each time interval correspond to the occupancy compared to the values given by table 5.11 (Nominal occupancy).

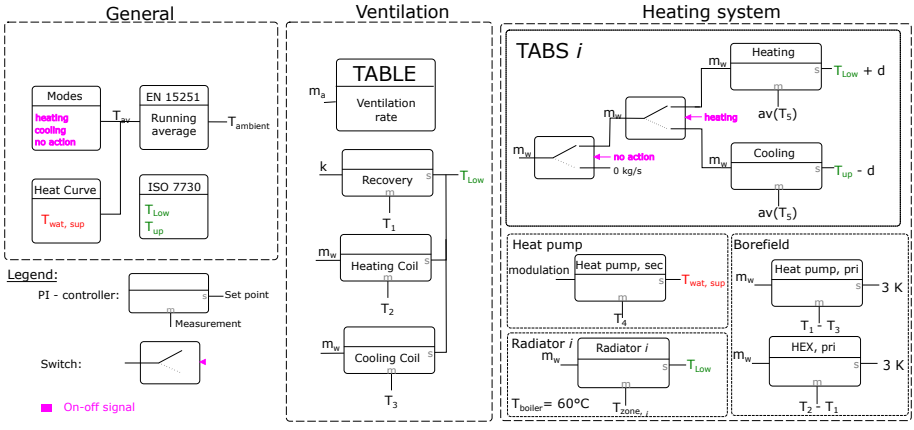

Figure 5.20: Schematic view of the HVAC control. The temperature sensors T_1 to T_3 of the *Ventilation* block refer to section 4.2.1 and T_1 to T_5 from the *Heating/cooling system* block refer to fig. 5.15.

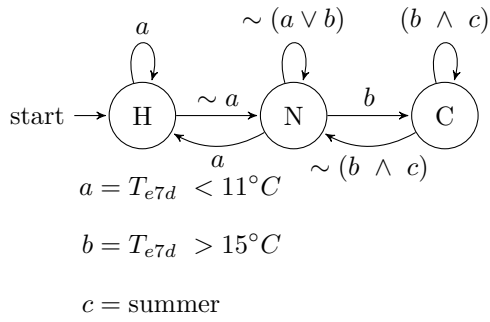

Figure 5.21: Mode selection between heating (H), neutral (N) and cooling (C) modes. T_{e7d} is the weighted 7-days average ambient temperature according to EN 15251 [145], $\vee$ is the logical conjunction (and), $\wedge$ the logical disjunction (or), and $\sim$ the negation (not).

no water is circulated. In H or C mode, the water flow is controlled by a PI-controller. The PI tries to set the TABS average return temperature equal to $\mathrm{T_{Low}}$ plus an offset d in heating mode and to $\mathrm{T_{Up}}$ minus an offset d in cooling mode. The water flow rates to the radiators are also controlled by a PI with the zone temperature as measured input and $\mathrm{T_{Low}}$ (without offset) as set-point. The modulation of the heat pump is also controlled by a PI controller such that it delivers water at $T_{\mathrm{wat,sup}}$. Finally, two PI controllers ensure that the temperature difference between the in- and outlet of the primary side of the HEX and the HP equals 3 K.

The ventilation is *on* when occupancy is non-zero. Its supply set-point temperature is equal to $\mathrm{T_{Low}}$. The supply air is firstly conditioned by the recovery unit and the by-pass of the AHU. If necessary, the air is further conditioned by the heating and the cooling coil controlled by a PI-controller. The water to the coils is coming from the boiler and the heat exchanger. The AHU can therefore heat or cool in any mode.

5.2.2 Simulation results

This section discusses the simulation results. Figure 5.22 shows the operative temperature of each zone for the whole year and the black lines indicate the comfort range. Figure 5.23 gives the thermal discomfort computed as number of Kelvin hours outside the comfort range and the maximum and minimum temperature deviation from the comfort range. According to figs. 5.22 and 5.23 the thermal comfort level is good with the exception of zones *1Hall* and *2Hall*

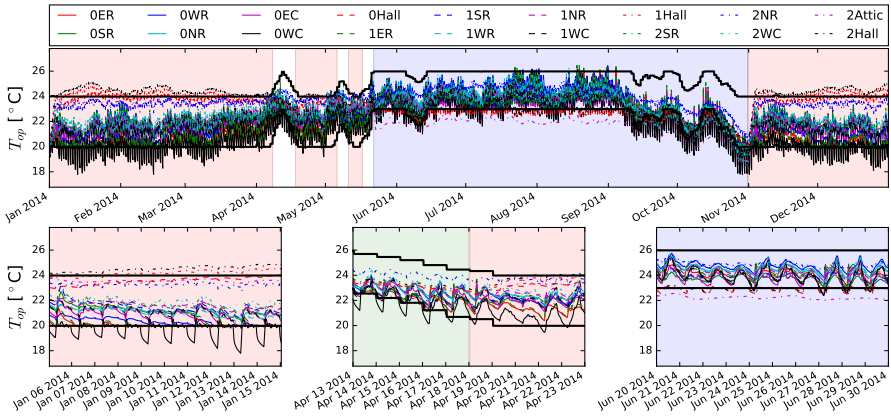

Figure 5.22: Operative temperatures. The *heating, neutral*, and *cooling mode* are indicated by the red, green, and blue background, respectively.

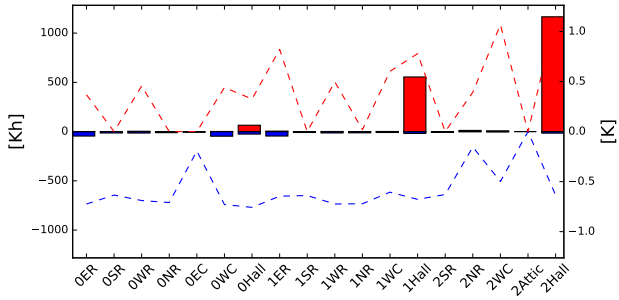

Figure 5.23: Thermal discomfort per zone measured in number of Kelvin hours per year (bars, left y-axis) and yearly maximum temperature deviation from comfort range (dashed lines, right y-axis).

(the corridors on the first and second floors) which suffer from some overheating. Notice that the cafetaria temperature is allowed to drop below the lower comfort temperature during the night as they are then not occupied.

Figure 5.24 summarizes the heat and cold emission powers of the AHU, TABS and radiators per unit floor area and shows that the ventilation always cools (around 2.5 $\mathrm{W/m^2}$). Figure 5.24 also indicates that the radiatiors are on average not much used (< 1 $\mathrm{W/m^2}$) but some of the zones use occasionally up to 15

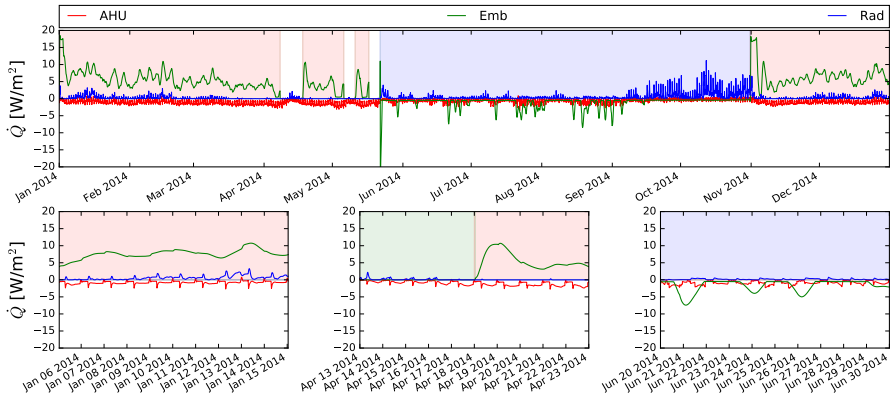

Figure 5.24: Average heating and cooling power per unit floor area delivered by the different emission systems: the AHU, the TABS (Emb), and the radiators (Rad). The *heating, neutral*, and *cooling mode* are indicated by the red, green, and blue background, respectively.

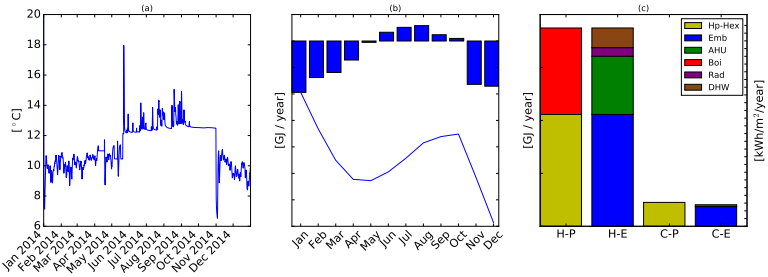

Figure 5.25: (a): borefield return temperature. (b): bars: energy to the borefield (positive = injection), line: cumulative energy. (c): yearly energy used by production systems (P) for heating (H) and cooling (C) and energy delivered by the emission systems (E). The right axis gives the energy in kWh per floor area per year.

W/m^2, especially during the cooling season. Figure 5.25 (c) shows that the radiators deliver about 15% of the heating load. Figure 5.25 gives the borefield return water temperature, its heating and cooling loads per month and the heat and cold produced and delivered to the building. Figure 5.25 (b,c) illustrate that the building is heating dominated with a net 700 GJ/year of energy extracted from the borefield and that the building uses 50 kWh/m^2/year for heating and 14 kWh/m^2/year for cooling (compared to 15 kWh/m^2/year for the total energy used by a passive house).

5.3 School: KTA Veurne

The case study building, called *KTA Veurne*, is a secondary school (1800 m^2 floor area) located in Veurne, Belgium. The building is a *hybrid GEOTABS* building, i.e. the heat and cold are generated by a GSHP and a gas-fired boiler and delivered to the building by floor heating and fan coil units. The AHU is composed of a recovery wheel with by-pass, a heating and a cooling coil and the supply and extraction fans are on-off controlled.

5.3.1 Model description

The building model of *KTA Veurne* is composed of 2 floors and 15 zones. The zones are of five types depending on their function: class room, teachers room, corridor, sanitary room, and technical room. The following sections describe the building envelope (section 5.3.1), the HVAC system (section 5.3.1), the occupancy and internal gains assumed for the model (section 5.3.1), and the RBC (section 5.3.1).

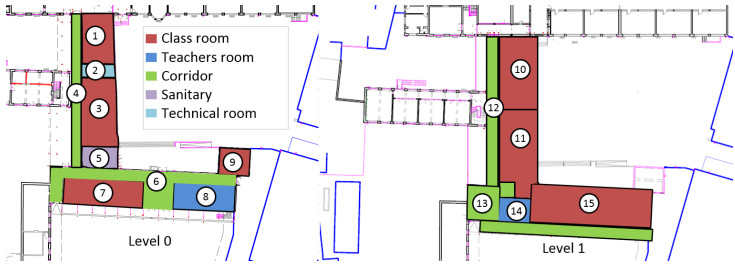

Figure 5.26: Zone layout for the model with the ground floor (left) and the first floor (right). Each number corresponds to the zone number and each color indicates the zone function. Zones 5 to 9 are equipped with fan coil units while the other zones are conditioned using floor heating. While zones 1-5 and 10-15 are newly built, zones 6-9 are kept from the old building.

Building envelope

The general parameters of the building envelope are summarized in table 5.12. In order to limit the model size, identical class rooms are lumped together. The resulting 15 zones layout is shown by fig. 5.26.

Table 5.12: General building parameters. The U-value is an average value for the whole building and ACH stands for *air changes per hour*. The U-value of the ground is computed as described by ISO 13370.

Floor area	1800	[m^2]	U-value	0.49	[$W/m^2/K$]
Conditioned volume	6250	[m^3]	Loss area	2160	[m^2]
Window-to-wall ratio	19.4%	[-]	ACH (n50)	1 (2.5)*	[1/h]

* The value between brackets is for the old part of the building (zones 6-9).

HVAC system

The building is a *hybrid GEOTABS* building, i.e. the heat and cold are generated by a GSHP and a gas-fired boiler and delivered to the building by floor heating and fan coil units. The AHU is composed of a recovery wheel with by-pass, a heating and a cooling coil and the supply and extraction fans are on-off controlled.

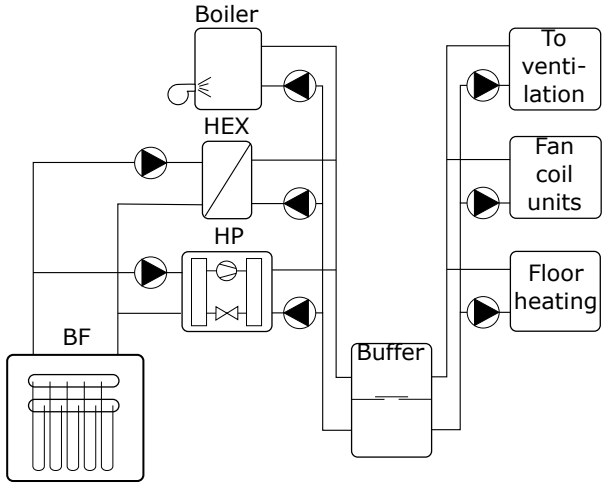

Figure 5.27: Hydraulic scheme. The components are: a borefield (BF), a heat exchanger (HEX), a gas-boiler, a heat pump (HP), circulation pumps, floor heating, and fan coil units.

Heat/cold production and emission Figure 5.27 sketches the hydraulic scheme of the building. The emission system is composed of fan coil units for the zones 5 to 9 and of floor heating for the other zones.

Heat is produced by a gas-fired boiler *Remeha Gas 210 ECO* (85 kWth) and by a heat pump of unknown type (50 kWth). The efficiency of an equivalent boiler (*Riello Tau N 290*) and the COP of an equivalent heat pump (VitoCal300GBWS301.A45) are used by scaling the nominal powers. Their characteristics are given in fig. 5.28 and fig. 5.29. Passive cooling is done by a HEX (*ALFA LAVAL CB76-40H*). The heat pump and the HEX are connected to a borefield consisting of 16 boreholes (100 m deep) at the primary side and to a buffer tank of 1 m^3 at the secondary side. The gas-boiler is connected to the same buffer tank and it can be used in parallel with the heat pump. All borefield parameters are listed in table 5.13 and the borehole positions are indicated in fig. 5.30.

Air handling unit The AHU system is composed of a heat recovery with by-pass, a heating and coiling coil, a supply and an extraction fan and the AHU is modelled as described in section 4.2.1. Both the heating and cooling coil are connected to the buffer. The AHU can therefore only heat or cool when the

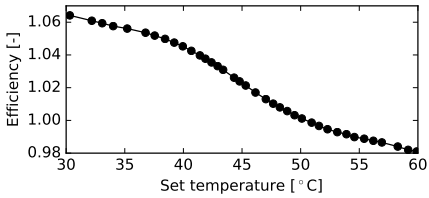

Figure 5.28: Boiler characteristics of the boiler *Riello Tau N 290* from its technical description [123].

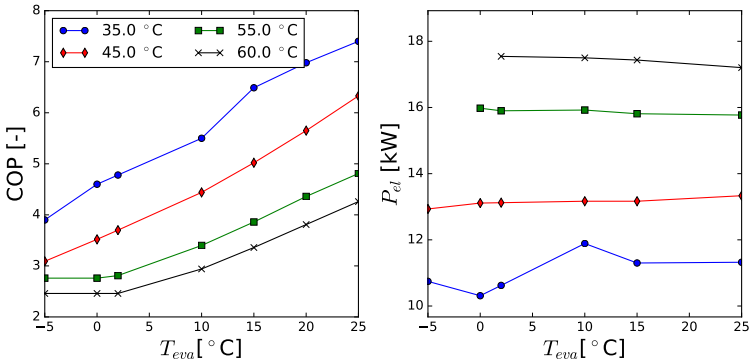

Figure 5.29: Heat pump characteristics of *VitoCal300GBWS301.A45* scaled to 50 kWth from its technical description [161].

Table 5.13: Borefield parameters.

Layout			Borehole			Ground/Grout		
# bh	16	[-]	D_{bh}	160	[mm]	λ	1.8/0.3	[W/(m.K)]
Type	2U	[-]	D_{pipe}	32	[mm]	ρ	$10^3/10^3$	[kg/m^3]
Depth	100	[m]	e_{pipe}	2.9	[mm]	c_p	2.4/1.7	[kJ/(kg.K)]
T_0	12.3	[°C]	λ_{pipe}	0.38	[W/(m.K)]	R_b	0.320	[(m.K)/W)]

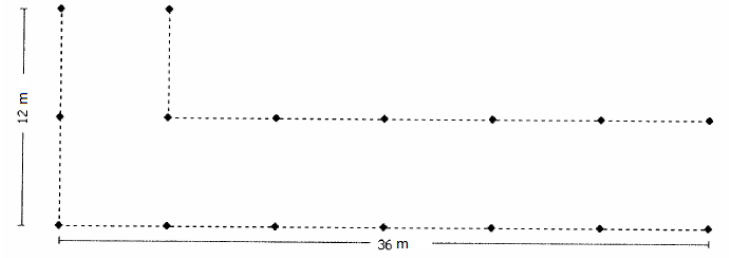

Figure 5.30: Borefield layout. The boreholes are at least 6 m from each other.

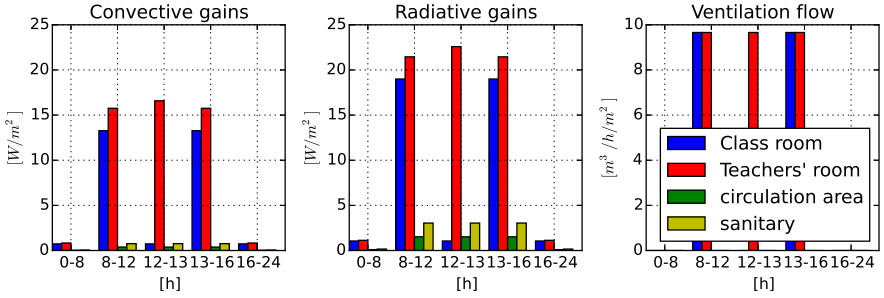

Figure 5.31: Time-dependent convective and radiative heat gains and ventilation flow rate per unit floor area.

emission system is in the same mode. The nominal ventilation flow rates and occupant density are taken from Wauman et al. [163]. The ventilation works at nominal condition when occupancy is non-zero and is turned off otherwise (see fig. 5.31). Note that the ventilation is turned on one hour before the students arrive in order to allow pre-heating or pre-cooling by the AHU.

Occupancy and internal gains

The convective and radiative gains and the ventilation flow rates are taken from Wauman et al. [163]. The room-type and time dependent gains are summarized in fig. 5.31.

Rule based control

The building control is composed of: i) a top level controller which decides on the control mode (heating (H), neutral (N) or cooling (C) mode), ii) a time varying lower and upper comfort zone temperature bound (T_{Low}, T_{Up}) and iii) a heating/cooling curve which sets the hot and cold water supply temperature $T_{wat,sup}$ for the floor heating and the AHU (eq. (5.1)).

$$T_{wat,sup} = \begin{cases} -0.22T_{e,av,^\circ C} + 28.1 & \text{(heating)} \\ -0.16T_{e,av,^\circ C} + 20.3 & \text{(cooling)} \end{cases} \tag{5.1}$$

with $T_{e,av,^\circ C}$ the average ambient temperature expressed in °C and computed according to the standard EN15251 [145].

The modes are calculated according to the state-machine described by fig. 5.21. The transition between the modes is evaluated only at the start of each hour to avoid fast switching. The system is further only turned on from Monday to Friday and not on Wednesday afternoon or during July and August. The floor heating is scheduled to only work between 0 AM to 4 PM and the fan coil units from 7 AM to 4 PM. The comfort ranges are prescribed by the standard EN ISO 7730 [150]. The lower and upper bounds vary according to the time of the year (e.g. [20,23]°C in winter and [24,26]°C in summer, see fig. 5.32).

In heating mode, the temperature of the buffer is kept at the temperature prescribed by the heating/cooling curve by a PI controller which controls the HP modulation and the mass flow rate from the borefield to the HP. When the HP is used at 99% of its maximum power, the boiler is turned on to help loading the buffer tank for a period of minimum 15 minutes. In cooling mode, the buffer tank temperature is maintained by the PI-controlled HEX. Both the primary and secondary sides of the HEX are controlled by the same PI.

The circulation pump of each floor heating and each fan coil unit is controlled by its own PI-controller with set-point temperature equal to $T_{Low} + \Delta_h$ in heating mode and $T_{Up} - \Delta_c$ in cooling mode. The measured temperature is the return water temperature for the floor heating and the zone air temperature for the fan coil units.

5.3.2 Simulation results

This section discusses the simulation results. Figure 5.32 plots the operative temperature of each zone for the whole year and the black lines indicate the comfort range (notice that for the full year plot, only the comfort range for

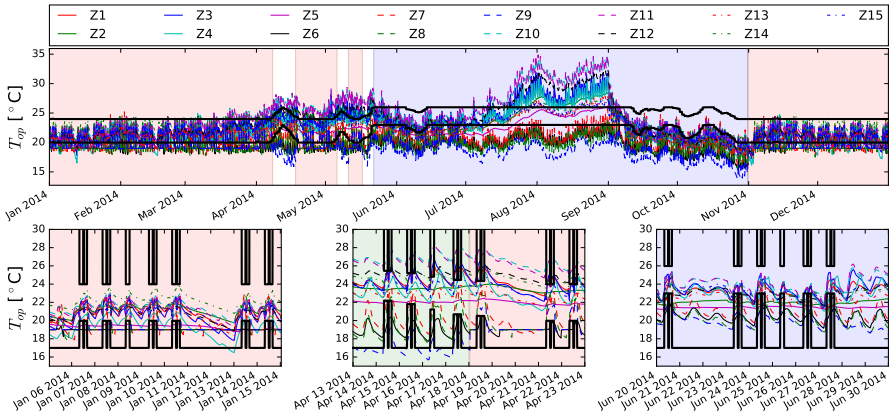

Figure 5.32: Operative temperatures. The *heating*, *neutral*, and *cooling mode* are indicated by the red, green, and blue background, respectively.

occupancy periods is shown while for the 10-days plots, the range for non-occupied periods is also plotted). Notice that the school is not conditioned during July and August as the building is not occupied. Figure 5.33 displays the thermal discomfort computed as number of Kelvin hours outside the comfort range and the maximum and minimum temperature deviation from the comfort range. Figures 5.32 and 5.33 show that the comfort level is good with the exception of zone *Z9* which shows some undercooling. The undercooling only happens during the N or the C mode during which this zone still needs heating due to its larger area of external walls and poor insulation.

Figure 5.34 summarizes the heat and cold emission of the AHU, floor heating and fan coil unit per unit floor area. Note that the ventilation part includes the fan coil unit powers. Figure 5.35 gives the borefield return water temperature, its heating and cooling loads per month and the heat and cold produced and delivered to the building. Figure 5.35 (b) demonstrates that the building is heating dominated with a net 65 GJ/year of energy extracted from the borefield. Figure 5.35 (c) shows that the building uses 26 kWh/m^2/year for heating and 10 kWh/m^2/year for cooling (compared to 15 kWh/m^2/year for the total energy use of a passive house). Most of the heat load is covered by the heat pump.

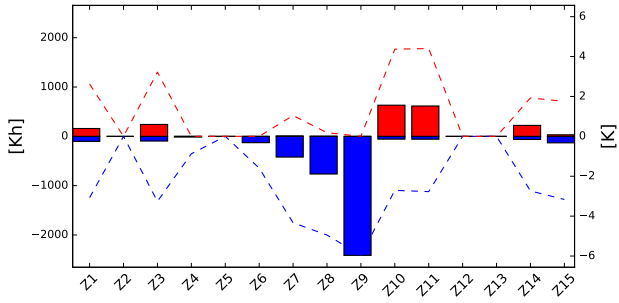

Figure 5.33: Thermal discomfort per zone measured in number of Kelvin hours per year (bars) and yearly maximum temperature deviation from the comfort range (dashed lines).

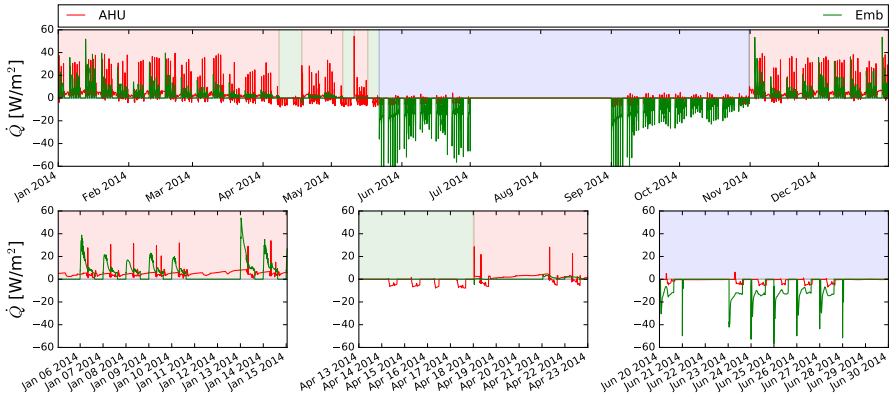

Figure 5.34: Average heating and cooling power per unit floor area delivered by the different emission systems: AHU and floor heating (Emb). The *heating*, *neutral*, and *cooling mode* are indicated by the red, green, and blue background, respectively.

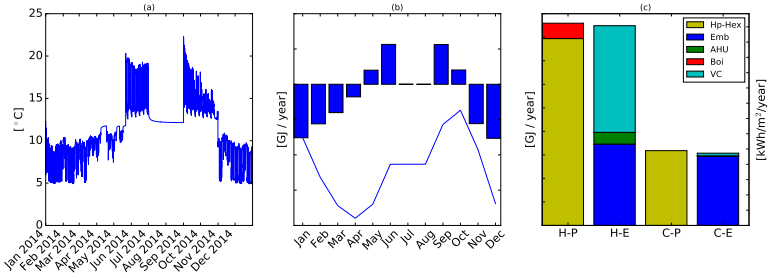

Figure 5.35: (a): borefield return temperature. (b): bars: energy to the borefield (positive = injection), line: cumulative energy. (c): yearly energy used by production systems (P) for heating (H) and cooling (C) and energy delivered by the emission systems (E). The right axis gives the energy in kWh per unit floor area per year.

5.4 Residential building: Evolution

The case study building, called *Evolution*, is a residential building of 10 apartments (820 m^2 total floor area) located in Maldegem, Belgium. The building is a pure *GEOTABS* building, i.e. the heat and cold are generated by a set of GSHPs and delivered to the building by TABS. The AHU is composed of an extraction fan which is controlled according to the CO_2 concentration in the flat, but is not equipped with a heating or cooling coil.

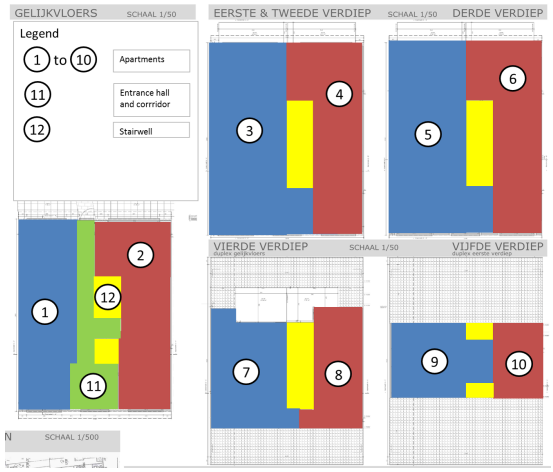

Figure 5.36: Zone layout of the model.

5.4.1 Model description

The *Evolution* building model is composed of five floors, each composed of 2 zones (1 zone = 1 apartment). The following sections describe the building envelope (section 5.4.1), the HVAC (section 5.4.1), the occupancy and internal gains assumed for the model (section 5.4.1), and the RBC (section 5.4.1).

Building envelope

The general parameters of the building envelope are summarized in table 5.14. In order to limit the model size, each flat is lumped into a single zone. An extra zone is used for the staircase and the lift and a last zone is used for the entrance hall. The resulting 12 zones layout is presented in fig. 5.36.

Table 5.14: General building parameters. The U-value is an average value for the whole building and ACH stands for *air changes per hour*. The U-value of the ground is computed as described by ISO 13370.

Floor area	[m^2]	818	U-value	[$W/m^2/K$]	0.36
Conditioned volume	[m^3]	2005	Loss area	[m^2]	585
Window-to-wall ratio	[-]	18.4%	ACH (n50)	[1/h]	2

HVAC system

The *Evolution* building is a pure *GEOTABS* system, i.e. the emission system is composed of TABS and the heat and cold are produced by GSHPs. The building is further equipped with a AHU composed of an extraction fan which is controlled according to the CO_2 concentration or humidity level in the flat.

Heat/cold production and emission Figure 5.37 sketches the hydraulic scheme of the building. The emission system is only composed of TABS with a ceiling circuit. Each apartment has its own heat pump which can heat, cool passively and produce DHW. The heat pumps are all the same (*Alpha InnoTec WZS31HKS* (4 kWth)) and their characteristics are depicted in fig. 5.38. Each heat pump is connected to one common borefield composed of 9 boreholes (125 m deep). All borefield parameters are listed in table 5.15 and the borehole positions are shown in fig. 5.39.

Table 5.15: Borefield parameters.

Layout			Borehole			Ground/Grout		
# bh	9	[-]	D_{bh}	130	[mm]	λ	2/0.8	[W/(m.K)]
Type	2U	[-]	D_{pipe}	32	[mm]	ρ	$10^3/10^3$	[kg/m^3]
H	125	[m]	e_{pipe}	2.9	[mm]	c_p	2.5/1.7	[kJ/(kg.K)]
T_0	11.3	[°C]	λ_{pipe}	0.38	[W/(m.K)]	R_b	0.12	[(m.K)/W]

Air handling unit The AHU is a *Renson C+ system*, which means that the air extraction is adapted to the measured CO_2 concentration or to the humidity level. The AHU is modelled as an ON/OFF extraction system which is turned ON when a minimum of 50 W of convective gain (as a measure for CO_2 concentration as CO_2 production is not modelled) is present. The nominal condition corresponds to an air change of 0.4 per hour.

Occupancy and internal gains

The convective and radiative gains and the DHW use are taken from the stochastic model StROBe [11]. Each flat and each day have a different profile. Figure 5.40 shows a snippet of one day for the 10 flats. Averaged over a year, each flat uses between 35 and 99 L per day of DHW at $60°C$ and has on average per day between 82 to 134 W of convective power and between 75 to 118 W of radiative power as internal gains.

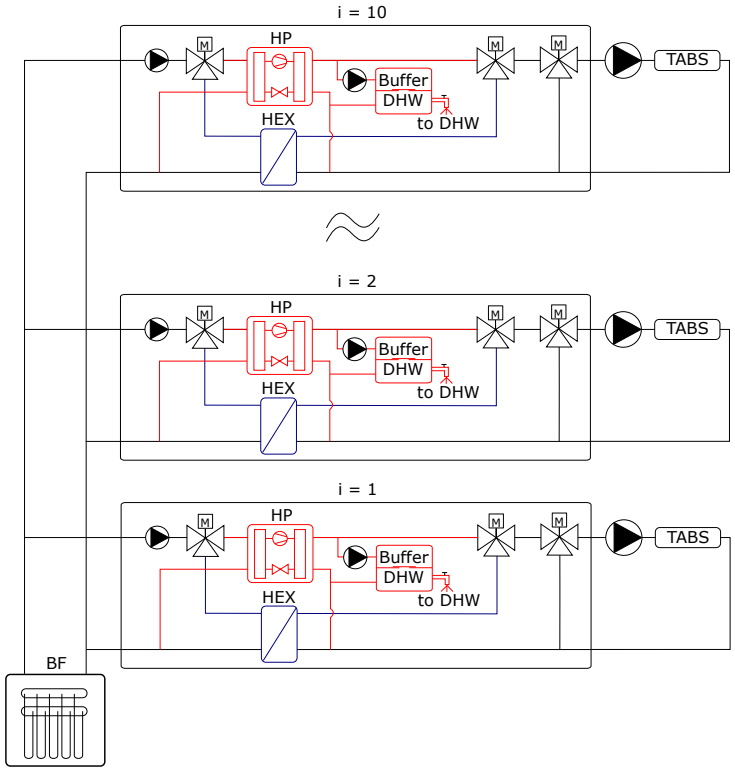

Figure 5.37: Hydraulic scheme. The components are: a borefield (BF), heat exchangers (HEX), a buffer for DHW, a heat pump (HP), three-way-valves, circulation pumps and TABS.

Rule based control

The building control is composed of: i) a top level controller which decides on the control mode (heating (H), neutral (N) or passive cooling (C) mode), and ii) a flat dependent heating/cooling curve which sets the hot and cold water supply temperature $T_{\mathrm{wat,sup}}$ for the TABS (eq. (5.2), with Δ_i a tuning parameter for each flat and $T_{\mathrm{Low}}, T_{\mathrm{Up}}$ the lower and upper bounds of the comfort range). The modes are calculated according to the state-machine described by fig. 5.21. The transition between the modes is evaluated only at the start of each hour to avoid fast switching. In H-mode, the supply temperature is delivered by the heat pump (perfect modulation assumed) while in cooling mode a PI controller mixes the return temperature with the water coming from the HEX using the

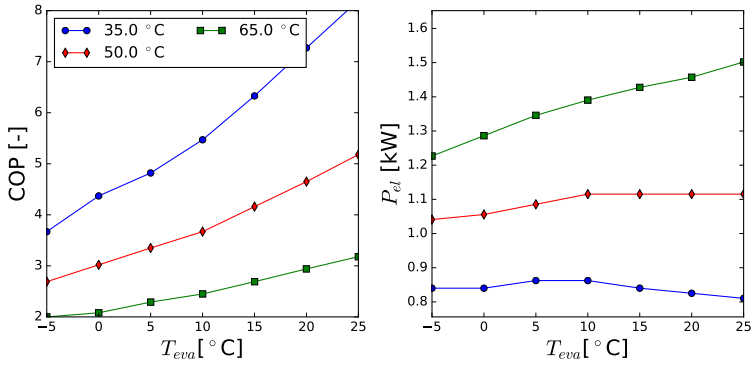

Figure 5.38: Heat pump characteristics of *Alpha InnoTec WZS31HKS* (4 kWth) from its technical description [2].

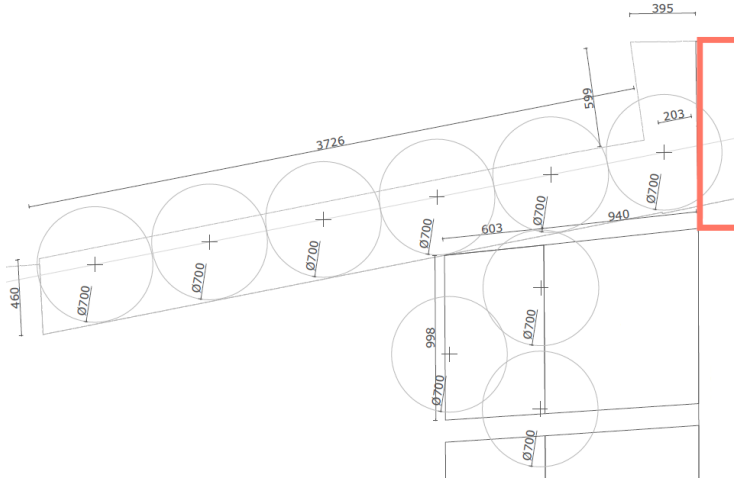

Figure 5.39: Borefield layout with distances given in cm. The distance between two boreholes is minimum 7 m.

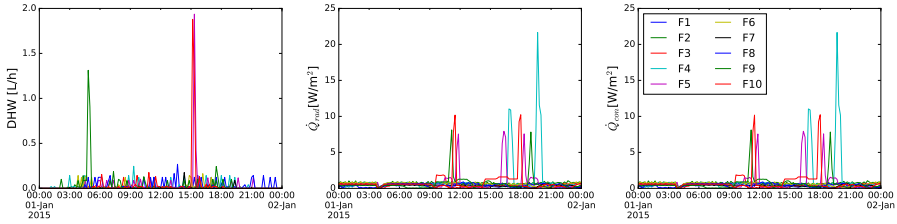

Figure 5.40: Time-dependent domestic hot water (DHW) use, radiative ($\dot{Q}_{rad}$) and convective ($\dot{Q}_{con}$) internal gains illustrated for 1 day for the 10 flats (F_i) based on Baetens and Saelens [11].

by-pass three-way-valve (see fig. 5.37). In N-mode, no water is circulated in the TABS and in the other modes the nominal mass flow rate is kept constant. When the temperature of the DHW tank of the HP drops below 50°C, the supply to the TABS is by-passed and the HP starts loading the DHW tank with water at 55°C. A second state-machine is used to define the HP working state (see fig. 5.41).

$$T_{\text{wat,sup}} = \begin{cases} 0.3(T_{\text{Low}} - T_{e7d}) + T_{\text{Low}} + \Delta_i & \text{(heating)} \\ T_{\text{Up}} - 0.3(T_{e7d} - T_{\text{Low}} + 20) + \Delta_i & \text{(cooling)} \end{cases} \tag{5.2}$$

5.4.2 Simulation results

This section discusses the simulation results. Figure 5.42 displays the operative temperature of each zone for the whole year. The comfort range plotted on the lower part of the figure is from flat 1 and it follows the flat occupancy. Figure 5.43 gives the thermal discomfort computed as number of Kelvin hours outside the comfort range and the maximum and minimum temperature deviation from the comfort range. Figures 5.42 and 5.43 show that the comfort level is not high for most of the flats, despite the tuning of the heating/cooling curve of each flat individually. The obtained comfort should be compared with the comfort reached by model predictive control to distinguish the limits of the system from the limits of the controller (see chapter 9).

Figure 5.44 summarizes the heat and cold emission of TABS and the AHU per unit floor area. Note that the AHU is not conditioned. Figure 5.45 gives the borefield return water temperature, its heating and cooling loads per month and the heat and cold produced and delivered to the building. Figure 5.45 (b) demonstrates that the building is heating dominated with a net 11 GJ/year

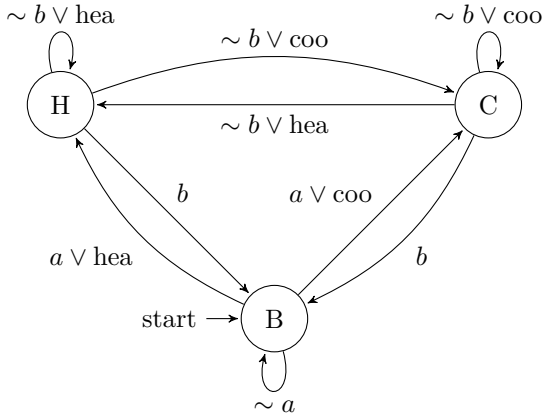

with $\begin{cases} a = T_{\text{Buf}} >= 55°C \\ b = T_{\text{Buf}} < 50°C \end{cases}$

Figure 5.41: State machine for mode selection between heating (H), loading buffer (B) and passive cooling (C) mode for the heat pump operation. T_{Buf} corresponds to the DHW buffer tank temperature, *hea* and *coo* indicates the heating and cooling mode as defined in fig. 5.21, $\vee$ is the logical conjunction (and), and $\sim$ is the negation (not).

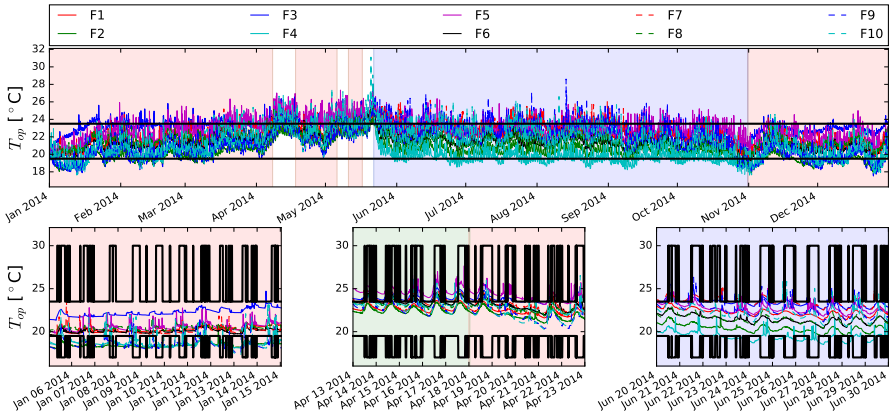

Figure 5.42: Operative temperatures. The *heating*, *neutral* and *cooling mode* are indicated by the red, green and blue background, respectively.

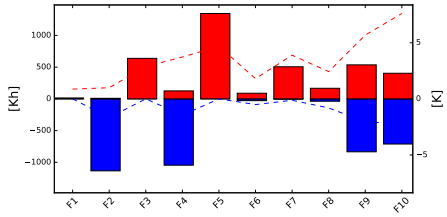

Figure 5.43: Thermal discomfort per zone measured in number of Kelvin hours per year (bars) and yearly maximum temperature deviation from comfort range (dashed lines).

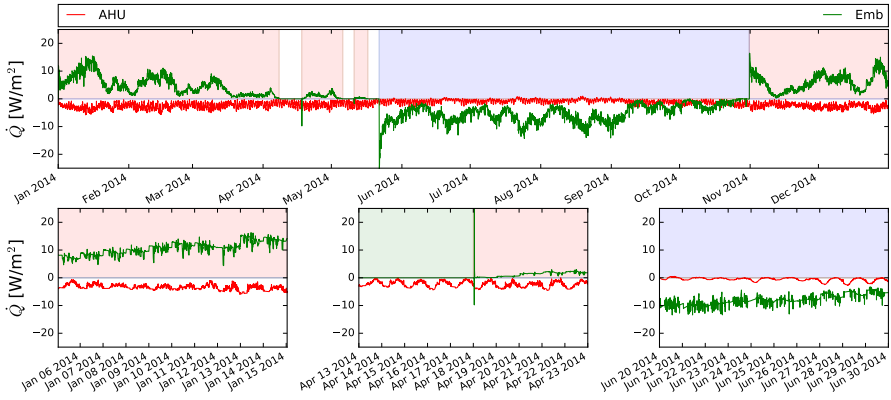

Figure 5.44: Average heating and cooling power per unit floor area delivered by the different emission systems: the AHU and TABS (Emb). The *heating*, *neutral* and *cooling mode* are indicated by the red, green and blue background, respectively.

of energy extracted from the borefield, despite the non-negligible cooling load of the building. The unbalance is due to the DHW production. Figure 5.45 (c) shows that the building uses 14 kWh/m^2/year for space heating and 13 kWh/m^2/year for cooling (compared to 15 kWh/m^2/year for the total energy use of a passive house).

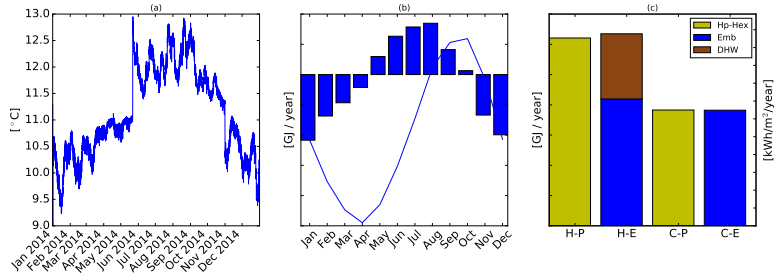

Figure 5.45: (a): borefield return temperature. (b): bars: energy to the borefield (positive = injection), line: cumulative energy. (c): yearly energy used by production systems (P) for heating (H) and cooling (C) and energy delivered by the emission systems (E). The right axis gives the energy in kWh per unit floor area per year.

Part III

Optimal control

Chapter 6

MPC toolchain

In this PhD work, different MPCs are formulated for the four different buildings which are each modelled in detail using the Modelica BES library `IDEAS`. This chapter presents the toolchain which has been developed around `IDEAS` to semi-automatically generate linear MPCs to control the HVAC system of the building and to simulate the building including its MPC in order to evaluate the controller performance. As a first step, the toolchain generates a controller model by linearising the building model (section 6.1). Secondly, it creates an MPC block written in C++ and callable from Modelica which automatically connects the controller model inputs and outputs to the Modelica building model and which performs the optimization (section 6.2). This toolchain has been used to generate all MPCs presented in section 7.2 and chapter 9 and the controller models from section 7.1. The toolchain has been developed as a joined effort with Filip Jorissen and the contribution of this work focusses on the linearization of the building enveloped while the MPC c-code has nearly been entirely written by Filip Jorissen.

6.1 Methodology for obtaining white-box controller models

This section is based on the paper previously published as:
Picard, D., Jorissen, F., Helsen, L. Methodology for obtaining linear state space

building energy simulation models. In *11th International Modelica Conference* (Paris, France, 2015), pp. 51–58.

Optimal climate control for building systems is facilitated by linear, low-order models of the building structure and of its HVAC. However, obtaining these models in a practical form is often difficult, which greatly hampers the commercial implementation of model predictive controllers. This work describes a methodology for obtaining a linear State Space Model (SSM) starting from Building Energy Simulation (BES) models, consisting of walls, windows, floors and the zone air. The methodology uses the Modelica library `IDEAS` to develop a BES model (see section 4.1.2), including its non-linearities, and automates its linearisation. The Dymola [38] function `linearise2` is used to generate the SSM formulation, facilitating further mathematical manipulations, or simulation in different environments.

This section is structured as follows: firstly, section 6.1.1 summarizes the existing studies about MPC controller models for building control. Secondly, section 6.1.2 describes the non-linearities of BES models together with common simplifications and section 6.1.3 explains the linearisation technique. Finally, section 6.1.4 develops the linearisation methodology in `IDEAS` and section 6.1.5 shows a validation of the methodology.

6.1.1 Introduction

Recent research has shown that (near) optimal controllers such as Model Predictive Control (MPC) can greatly improve the energy efficiency of buildings compared to traditional rule-based-controllers [66, 159]. The number of papers about Model Predictive Control (MPC) for building in several journals is increasing every year exceeding more than 100 new papers in the journal Energy and Buildings in 2015. Despite these intensive research efforts the commercialization of MPC is still in its early stages. This is partially due to the lack of direct comparison (i.e., for the same scenario) of different optimization algorithms, of different controller models and their prediction performance, of the simulation parameters such as sampling time, prediction horizon and of climate forecast, as pointed out in the review paper by Hilliard et al. [72]. The main difficulty remains, however, to obtain a good controller model of the whole building that is simple enough to allow optimization within a reasonable computation time but still accurate enough to correctly predict the building behaviour and this with a minimum of (manual) effort [129, 136, 118, 93]. Detailed building energy simulation software (BES) such as EnergyPlus [139],

TRNSYS [84] or Modelica (`Buildings` [169], `IDEAS` [10]) allow accurate building modeling but generate models which are too complex to be used in efficient optimization algorithms [129, 136]. Low order linear models are usually preferred due to their computational tractability [68]. Therefore, simplified models need to be generated by means of grey-box [117, 136, 8, 122] or black-box system identification such as auto regressive [171], subspace [118] and artificial neural network methods [125] or by simplified white-box modeling [66, 91, 115, 60, 50, 83].

While black-box identification has the advantage that no prior knowledge of the system is required and that it can deal more efficiently with large sets of data, its prediction performance for longer time horizons is not sufficiently accurate [117]. Grey-box system identification is more suitable for long time horizons but the method becomes very costly for large multiple-input multiple-output (MIMO) systems. As shown by [8, 122, 35] a good choice of the structure of the grey-box model, i.e., its order, its inputs and its states, is crucial for its performance but this choice is very case specific. Therefore authors involved in the opti-control project [66, 91, 142], and others [115, 60, 50, 83] opted for a linear white-box approach where the model is set up based on geometrical and on physical data of the building and simplified physical laws. The authors all showed that this simplified approach could mimic the results (typically expressed as operative temperatures) of the more complex models obtained with BES software within an error margin of $\pm$ 0.5 to 1 K. Linear models are further preferred since efficient optimization algorithms can then be used [87, 141]. However, setting up white-box models is a time consuming task as they require a large amount of information needs to be gathered, reason why it is important to automate the process as much as possible.

In this work, we propose an automated way of obtaining accurate linear BES models based on a non-linear model implementation in Dymola [38] using the `IDEAS` library [10].

6.1.2 Non-linearities in Building Energy Simulation Models and Common Simplifications

Typically, BES models contain three major sources of non-linearities. The first is longwave radiation, which is typically described using the Stefan-Boltzmann law. The second is the absorption of incident solar radiation by windows, which is a function of the incidence angle. The third is convective heat transfer, which is usually described using correlations for the convective heat transfer coefficient. These non-linear equations are first described in this section, then a linearisation technique is proposed. Other non-linearities in real buildings exist

(e.g temperature dependent emissivity, pressure dependent air leakage, ...) but they are rarely modelled. They will not be treated in this work.

Radiation Radiation is described by the non-linear Stefan-Boltzmann law which is given by eq. (6.1) for two grey-bodies with surface areas A_1 and A_2.

$$\dot{Q}_{1\to2}(t) = \sigma F_{1\to2}\, A_1 \left(T_1^4(t) - T_2^4(t)\right) \tag{6.1}$$

$\dot{Q}_{1\to2}$ and $F_{1\to2}$ are the heat transferred from surface 1 to 2 and their view factor respectively, $\sigma = 5.670373 \times 10^{-8}$ W/(m^2.K^4) is the Stefan-Boltzmann constant, and T_i is the temperature of body i.

Radiative heat transfer between room surfaces is often approximated using the Mean Radiant Temperature model (e.g. in TRNSYS TYPE 56 [84]) or using the Radiant Star Temperature model (e.g. in `IDEAS` [10]) since it greatly simplifies the computations without a significant loss in accuracy [94]. This radiant star temperature T_{star} is derived from the energy conservation equation in the radiant node and the temperature of each surface A_k is calculated using a distribution coefficient R_k:

$$\dot{Q}_{k\to\text{star}}(t) = \frac{\sigma A_k}{R_k} \left(T_k^4(t) - T_{\text{star}}^4(t)\right) \tag{6.2}$$

Equation (6.2) is often linearised around nominal temperatures $T_{k,nom}$ and $T_{star,nom}$ (eq. (6.3)), which is an accurate approximation for small temperature differences. Figure 6.1 shows the approximation error for the heat exchange between two black bodies with view factor equal to one.

$$\dot{Q}_{k\to\text{star}}(t) \simeq c\,(T_k(t) - T_{\text{star}}(t)) \tag{6.3}$$

$$c = \frac{\sigma A_k}{R_k} \left((T_{k,nom} + T_{star,nom})(T_{k,nom}^2 + T_{star,nom}^2\right) \tag{6.4}$$

The longwave radiation heat flow $\dot{Q}_{lw,k}(t)$ between exterior surface k of the building with longwave emissivity $\epsilon_{lw,k}$ and the environment can be modelled as:

$$\begin{aligned} \dot{Q}_{lw,k}(t) &= \sigma \epsilon_{lw,k} A_k \left(T_{s,k}^4(t) - F_{ce,k} T_{ce}^4(t) - (1 - F_{ce,k}) T_{db}^4(t)\right) \\ F_{ce,k} &= \frac{1 + \cos i_k}{2} \end{aligned} \tag{6.5}$$

with $T_{s,k}(t)$, $T_{ce}(t)$, $T_{db}(t)$ the surface, celestial dome and dry bulb temperature respectively, $F_{ce,k}$ the view factor between the surface k and the celestial dome,

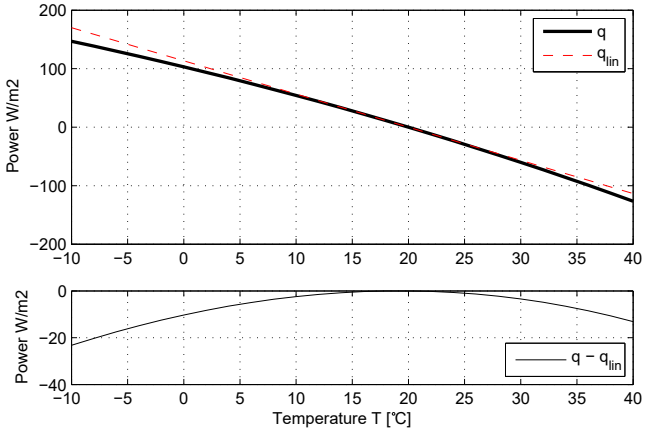

Figure 6.1: Error made by the linearisation of the radiative heat transfer equation around $T = 20°C$ between two black bodies with view factor one.

and i_k the inclination of the surface. This equation is linearised by default in `IDEAS` as:

$$\dot{Q}_{lw,k}(t) \simeq c\left(T_{s,k}(t) - \left(F_{ce,k}T_{ce}^4(t) + (1 - F_{ce,k})T_{db}^4(t)\right)^{0.25}\right) \tag{6.6}$$

with c a parameter defined similar to eq. (6.4).

Finally, the shortwave solar irradiation absorbed by exterior surface k equals:

$$\dot{Q}_{sw,k}(t) = \epsilon_{sw,k}A_k E_{e,k}(t) \tag{6.7}$$

with $E_{e,k}(t)$ the incident solar irradiation on surface A_k as a function of time.

Absorption and transmission through glazing Heat absorbed or transferred through windows is typically highly non-linear as it depends on the spectral properties of the window, on the angle of incidence of the sun and on possible shading. Typically, the window properties are precomputed using specialized software and delivered as an input to the BES software. `IDEAS` uses the software `Window 4.0` [49] to precompute window spectral properties but it computes the amount of absorbed and transmitted light during the simulation, requiring trigonometrical transformations and lookup tables, which are non-linear functions.

Convective heat transfer Two types of convective heat transfer are present in buildings: exterior, forced convection by the wind, and interior, natural convection when forced ventilation is absent.

In IDEAS, the external convective heat transfer rate $\dot{Q}_{cv}(t)$ between an exterior surface with area A_k and the outdoor air is based on [37]:

$$\begin{aligned} \dot{Q}_{cv,k}(t) &= h_{cv}(t) A_k \left(T_{db}(t) - T_{s,k}(t)\right) \\ h_{cv}(t) &= \max\left\{5.01(v_{10}(t))^{0.85}, 5.6\right\} \mathrm{W/m^2K} \end{aligned} \tag{6.8}$$

with convective heat transfer coefficient $h_{cv}(t)$, dry bulb ambient temperature $T_{db}(t)$, surface temperature $T_{s,k}(t)$ and the undisturbed wind speed at 10 meters above the ground $v_{10}(t)$.

Equation (6.8) is non-linear even if the convection coefficient is an input due to the multiplication of input with input $(h_{cv}(t)T_{db}(t))$ and input with state $(h_{cv}(t)T_{s,k}(t))$. If the nominal values of $T_{db}(t)$ and $T_{s,k}(t)$ are equal, eq. (6.8) can be linearised as:

$$\dot{Q}_{cv,k}(t) \simeq \bar{h}_{cv} A_k \left(T_{db}(t) - T_{s,k}(t)\right) \tag{6.9}$$

with $\bar{h}_{cv}$ the yearly average of the exterior convection coefficient. Note that the linearisation of the exterior convection coefficient can cause a heat flow rate error of more than 150 W/m^2 due to the wide range of h_{cv} (from 7 to 55 W/m^{2}K) and the potentially large difference between the ambient dry bulb temperature and the surface temperature. For the given example (see section 6.1.5), the maximum deviation is 141 W/m^2. This error culminates when both wind speed and solar radiation are high, which causes both a high heat transfer rate and a high surface temperature.

The interior convective heat transfer rate between a wall, ceiling or floor with surface area A_k and an air node is computed as:

$$\begin{aligned} \dot{Q}_{cv,k}(t) &= h_{cv,k}(t) A_k \left(T_{db}(t) - T_{s,k}(t)\right) \\ \bar{h}_{cv,k}(t) &= n_{1,k}\ D_k^{n_{2,k}} \left|T_{db}(t) - T_{s,k}(t)\right|^{n_{3,k}} \end{aligned} \tag{6.10}$$

with D_k the hydraulic diameter, and coefficients $n_{i,k}$. The value of the coefficients are $n_{1:3} = \{1.823, -0.121, 0.293\}$ for vertical surfaces, $n_{1:3} = \{2.175, -0.076, 0.308\}$ for heated floors and cooled ceilings and $n_{1:3} = \{0.704, -0.601, 0.133\}$ for cooled floors and heated ceilings [7].

These interior convection equations can be linearised in IDEAS using an average value for h_{cv}:

$$h_{cv,k} \simeq n_{1,k}\ D_k^{n_{2,k}} \left|\Delta T_{nom}\right|^{n_{3,k}} \tag{6.11}$$

with ΔT_{nom} the nominal temperature difference.

Heat transmission through walls and floors Heat transfer through walls and floors is characterized by convective and radiative heat transfer at the surfaces and conduction through the solid layers. The latter is governed by a partial differential equation (PDE). It extends in three spatial dimensions and in time. However, the heat transfer through walls and floors can often be approximated using a one dimensional PDE due to the small thickness to height and width ratio. The equations can then either be solved using discrete Laplace transform (e.g. TRNSYS) or using a finite volume method (e.g. EnergyPlus [139]). In `IDEAS`, the finite volume method is used, leading to a set of linear equations.

6.1.3 Linearisation Technique

The linearisation of a function consists of the first order term of the Taylor expansion of this function around a working point. Given a deterministic non-linear dynamic system:

$$\begin{aligned} \dot{x} &= f(x,u) \\ y &= g(x,u) \end{aligned} \tag{6.12}$$

where $x \in \mathbb{R}^{n_x}$ are the states, $\dot{x}$ are their derivatives, $u \in \mathbb{R}^{n_u}$ the inputs, and $y \in \mathbb{R}^{n_y}$ the outputs. The linearisation of eq. (6.12) around point $p_\star \triangleq (x_\star, u_\star)$ is defined as:

$$\begin{aligned} \dot{x} &= f(p_\star) + \left.\frac{\partial f}{\partial x}\right|_{p_\star} (x - x_\star) + \left.\frac{\partial f}{\partial u}\right|_{p_\star} (u - u_\star) \\ &\triangleq f(p_\star) + \mathbf{A}\tilde{x} + \mathbf{B}\tilde{u} \\ y &= g(p_\star) + \left.\frac{\partial g}{\partial x}\right|_{p_\star} (x - x_\star) + \left.\frac{\partial g}{\partial u}\right|_{p_\star} (u - u_\star) \\ &\triangleq g(p_\star) + \mathbf{C}\tilde{x} + \mathbf{D}\tilde{u} \end{aligned} \tag{6.13}$$

where $\mathbf{A}, \mathbf{B}, \mathbf{C}, \mathbf{D}$ are constant matrices.

The Dymola built-in function `linearise2` of the Modelica Linear System2 library provides the possibility of linearising Modelica models [108]. The hybrid differential-algebraic equation system is treated as an ordinary differential equation system at the linearisation point and the partial derivatives of the functions f and g are obtained by evaluation of the analytical Jacobian if it is available. Otherwise a central difference method is used. The function can also be used to transform a linear model into a SSM.

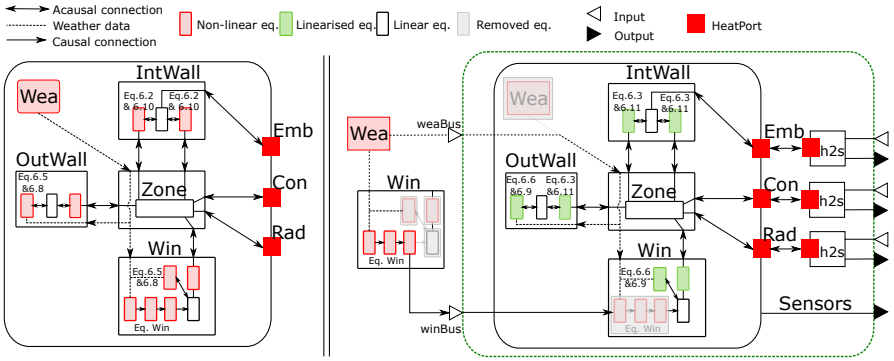

Figure 6.2: Left: original model with non-linear equations. Right: Adjusted model structure with moved and/or linearised non-linear equations. Component models are outer wall 'OutWall', interior wall 'IntWall', Window 'Win', weather model inputs 'Wea' and HeatPorts embedded (Emb), convective (Con) and radiative (Rad). White triangles represent inputs to the model, whereas black triangles represent outputs of the model.

It should be noted that even for a linear system, the linearisation point $p_\star$ used by the function `linearise2` should be chosen carefully to avoid numerical noise. The states $x_\star$ can be set using initial equations or `start` values. The inputs $u_\star$ can be set using `start` values. The default `start` value for the inputs in Dymola is zero which can lead to significant error when evaluating the derivatives using the central difference method.

6.1.4 Linearisation Methodology in IDEAS

This section describes how `IDEAS` was adapted to automatically obtain a state space formulation of a BES model in Dymola. Firstly the linearisation of the equations is discussed, followed by the model structure requirements for SSM's. Finally the SSM structure is described.

Linearisation of the equations

Here we describe how the non-linear equations of the Modelica BES models are conditionally linearised or moved outside the model and replaced by model inputs. Note that the moved equations should not depend on any state variables.

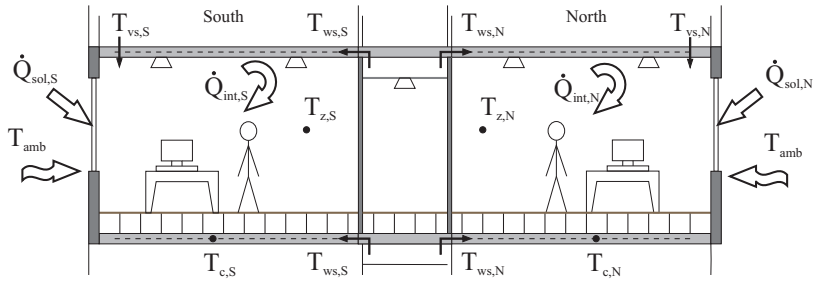

Figure 6.3: Illustration of the office building section, ([136], p 5).

Radiation As described in the previous section, all longwave radiation equations can be linearised accurately. If `linearise = true`, eq. (6.2) and eq. (6.5) are replaced by eq. (6.3) and eq. (6.6), respectively, where the square root term is transformed into a model input for each different orientations and inclination. The solar irradiation $E_e^{(k)}(t)$ required for the shortwave absorption is also converted into a model input per orientation and inclination.

Window models Window models contain equations for calculating the solar irradiance, the impact of shading and the amount of heat that is absorbed and transmitted through the window. These are non-linear equations indicated in fig. 6.2 by 'Eq. Win'. Linearising these equations would introduce large errors. Linearising them at noon may for instance have the consequence that the solar position and corresponding incidence angles become fixed, which can cause a large underestimation of the solar gains for windows. Therefore the absorbed and transmitted heat flow rates are calculated outside of the model and they are inputs to the linearised model, as indicated in the right part of fig. 6.2. Each window model is instantiated twice, once inside and once outside of the linearised model. The grey boxes in fig. 6.2 indicate which equations are removed and replaced by inputs. Note that the window model is thereby split into two parts. A bus connector `winBus` for each of the n_{win} windows is used for connecting the inputs.

Convective heat transfer The interior convective heat transfer is linearised using eq. (6.11). ΔT_{nom} was chosen equal to the mean absolute temperature difference between the window or wall and the zone air temperature. The exterior convective heat transfer coefficient is simplified by using the yearly average convective heat transfer coefficient $\bar{h}_{cv}$. These linearisations are indicated on

fig. 6.2 using green rectangles.

The remaining model equations, like thermal conduction equations, are already linear and they are retained.

State space formulation

In the previous paragraphs all remaining non-linear equations are removed from the building envelope model. The resulting linear model needs to be converted into state space format. This requires that all exterior connections are either inputs or outputs, otherwise Dymola does not detect the connections. However, `HeatPort` connections `Emb`, `Con` and `Rad` contain variables `T` and `Q_flow` that do not specify whether they are inputs or outputs. Each `HeatPort` for the room thermal gains is therefore connected to an input-output block `h2s`, which either sets heat flow rate `Q_flow` to a fixed input and temperature T to an output or the other way around.

In order to propagate weather data inputs to all sub-models, one weather bus `weaBus` with prefix `input` is connected to each zone. The zone further propagates this data to all its connected surfaces (walls, windows, ...) as indicated by the dotted lines in fig. 6.2.

State space model structure

All non-linear equations are now removed and all connections are either defined as an input or as an output. The state space formulation can now be obtained by using the `linearise2` function on the model containing all components of the dotted green box in fig. 6.2. This function returns matrices $\mathbf{A}$, $\mathbf{B}$, $\mathbf{C}$ and $\mathbf{D}$. The SSM inputs u are the heat flow rates or temperatures for thermal gains of the zones, the weather bus and n_{win} window buses. Outputs are either the temperatures or the heat flow rates of the transformed `HeatPorts`. Additional outputs can be defined in the linearised model by adding `RealOutput` components.

6.1.5 Validation

In this section, the linearisation methodology is applied to a test case. The case is firstly described after which the methodology is validated.

Case description The validation uses the cut-out of a typical office building with South and North oriented façades described by Sourbron et al. [132] (see fig. 6.3). We only consider the building structure, which consists of three zones (a corridor, a south-oriented and a north-oriented zone) each equipped with a thermally activated ceiling and floor composed of multiple layers (floor tiles, air layer, screed, and reinforced concrete), two external walls composed of multiple layers (plaster, concrete blocks, mineral wool, and bricks), and two windows. Each zone has a convective and a radiative heat gain input and heat can also be injected in the core of the thermally activated building parts.

The model is implemented with all details above in Modelica using the `IDEAS`library [10]. The model has 8434 variables and 50 differentiated states. Once linearised, the model has 52 inputs. The model uses the weather data of Uccle (Belgium).

Each of the heat flow rate inputs is set equal to the sum of the two sinusoids of eqs. (6.14) and (6.15), with $t = 0$ at new year. The sinusoids with a period of one day and one year, respectively, represent internal gains, and heating or cooling delivered by the HVAC system. The sinusoid parameters are tuned such that the zone temperature remains around 22 °C.

$$sin_1 = 4 + 4 \sin\left(\frac{2\pi\, t}{86400} - \frac{\pi}{2}\right) \tag{6.14}$$

$$sin_2 = 13 \sin\left(\frac{2\pi\, t}{31536000} - 1.4\right) \tag{6.15}$$

Model description In order to validate the methodology, the zone temperatures of three models are compared. The reference model is the `IDEAS` model with non-linear radiative heat transfer (eqs. (6.3) and (6.6)), temperature-dependent interior convection (eq. (6.11)) and wind speed dependent exterior convection (eq. (6.8)).

The second model is identical to the reference model but it uses the linearised equations for the radiation and interior and exterior convection. The model is then fully linear except for its inputs.

The third model is the state space version of the second model. The SSM is loaded into Dymola using `Modelica.Blocks.Continuous.StateSpace`. Note that the difference between the third and the second model should be around the solver tolerance.

Table 6.1: Comparison between three models based on equation types and equation formats.

	Ref	Lin	SSM
Convection	non-linear	linear	linear
Radiation	non-linear	linear	linear
Model inputs	non-linear	non-linear	non-linear
Other equations	linear	linear	linear
SSM formulation	no	no	yes

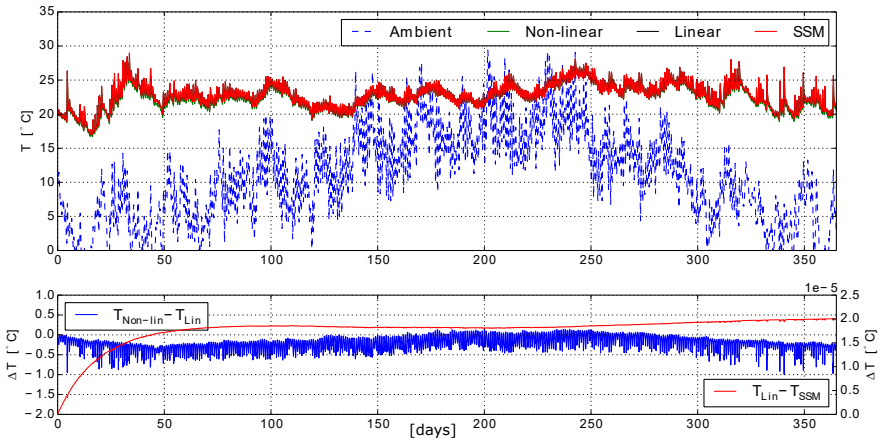

Figure 6.4: Result comparison between three model types for a one year simulation. The top graph shows absolute temperatures, while the other two graphs show absolute temperature differences.

A comparison of the equation types and formats for the three models is presented in table 6.1.

Model comparison The three model versions are simulated for a whole year using solver Dassl with a tolerance of 10^{-6}. The zone air temperatures are then compared. Figure 6.4 plots the southern zone temperature of the different models, the average error of the three zone air temperatures for the reference model and the linear model, and this average error for the linear model and its SSM. The zone air temperatures are then compared. Figure 6.4 shows that the zone temperature is excited over a realistic range. The CPU time is also

compared [1]. Normalized CPU times t_{norm} are computed by subtracting the 'CPUtime' required for a simulation that only computes the building model inputs. The CPU time ratio r_i is computed based on the non-linear reference case: $r_i = \frac{t_{norm,ref}}{t_{norm,i}}$. The total computation time for the reference case is 290 s.

Figure 6.4 confirms that the linear model is a good approximation of the non-linear model as the absolute error remains smaller than 1K and its average is close to zero. This justifies the often made linear approximations in building modelling. Figure 6.4 also shows that the transformation of the linear model into a SSM does not introduce significant errors, as expected. This indicates that the model equations were successfully extracted by the `linearise2` function.

The linear model is faster than the non-linear model with $r_{lin} = 1.8$. This is expected because linear equations typically require less operations and do not require non-linear algebraic loops to be solved. Interestingly, the SSM is much faster with an $r_{SSM} = 8.5$. This is because the state space model contains only 50 states and therefore only 50 equations. The linear model contains 50 states and 453 additional[2] algebraic variables, which also need to be computed, often requiring the analytical solution of linear systems of equations.

These results demonstrate that the symbolic processing can be improved, resulting in faster models.

6.1.6 Conclusion

Section 6.1 presents an approach for deriving linear state space models from BES models using the `IDEAS` library and Dymola. To this end, weakly non-linear equations are linearised. The remaining non-linear equations can be evaluated outside of the model since they do not depend on the model states. The resulting model is linearised using the Dymola function `linearise2`, which derives the state space matrices. The errors made by linearising the models are found to be acceptable. An important advantage of the presented methodology is that it automates the conversion of `IDEAS` BES models into state space formulation which can then be used for different purposes or by different programs. It should be noted that the zone and the window models allowing the conditional linearisation of the equations or their transformation into inputs are currently removed from `IDEAS` and included to a separate library called `LIDEAS`. This was

[1] Simulations are performed using Dymola 2016 and Euler integration using a fixed time step of 10 s and a duration of 10^7 seconds. Euler integration is chosen to ensure that the same number of time steps is performed.

[2] The translated linear model contains 453 'time-varying variables' more than the translated SSM model.

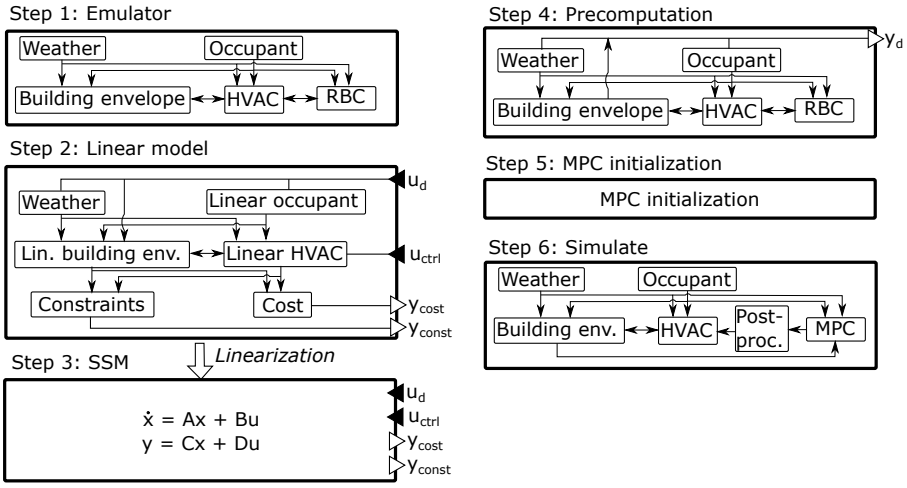

Figure 6.5: Schematic representation of the semi-automatic MPC toolchain.

done both for intellectual property reason and to avoid unnecessary complexity in the open-source `IDEAS` models.

6.2 MPC toolchain

The toolchain used for implementing linear MPCs is described in detail by Jorissen and Helsen [79] and is represented in fig. 6.5. The following paragraphs briefly explain the different steps assuming that the building is modelled using `IDEAS` and that Dymola is used as simulation environment.

Step 1: Emulator model The first step is to create an emulator model of the building using `IDEAS` and to replace the zone and window models by their equivalent from the `LIDEAS` library. The `LIDEAS` library only contains these two models which are the same as the `IDEAS` models but they contain additional conditional equations to automatically switch to a linear formulation of the models and to create the necessary precomputed variables by using a single flag. As represented by step 1 in fig. 6.5, it is convenient to split the building into different blocks: *weather*, *occupant*, *building envelope*, *HVAC*, and *controller* (which is here an *RBC*).

Step 2: Linear model The second step consists of making the emulator model *linear* by replacing the non-linear equations by their linear approximations or by precomputing them if they do not depend on the model states. For the building envelope and the weather block, this can be automatically done by setting a single flag (see section 6.1). The occupant block typically defines the boundary conditions of the model due to occupancy. Therefore, it does not depend on the model states and it can also be precomputed and replaced by an input vector (u_d in fig. 6.5). The linear occupant model is then reduced to a pass-through model. Finally, the HVAC block also needs to be linearised and the optimisation variables should become inputs of the model (u_{ctrl} in fig. 6.5). This often means that the optimization variables must be heat flow rates since the explicit modelling of mass flow rates and temperatures can lead to bi-linear equations.

In this framework, the cost function and the (in)equality constraints are also added to the linear model such that they can be automatically retrieved by the toolchain. They should be connected to output connectors called `cost` (y_{cost}) and `ineq` (y_{const}), respectively, and they should also be linear.

Step 3: State space model Once the linear Modelica model is ready, step 3 automatically converts the linear model into a SSM formulation by using the Dymola built-in function `linearise2` as described in section 6.1. This function linearises the model equations around a given working point and it returns the SSM $\mathbf{A}$, $\mathbf{B}$, $\mathbf{C}$, $\mathbf{D}$ matrices as well as the Modelica name of the input and output variables. The inputs are composed of the optimization variables (u_{ctrl}) and of the disturbances (u_d) and the outputs represent the cost function (y_{cost}) and the constraints (y_{const}).

Step 4: Precomputation The linearisation of the model requires the precomputation of a large set of variables. This can be done by extending the emulator model from step 1 with a `preComputed` output (y_d) to which all weather and building envelope precomputed variables will be automatically connected and to which additional precomputed variables such as the occupancy variables can be manually connected (step 4 in fig. 6.5). The model is then simulated for a full year and its output is saved with a fixed sampling time. The produced *.mat* file just needs to be converted to a format more easily readable by the MPC block (see next paragraph) and this is done either by a python or by a matlab script.

Step 5&6: MPC initialization and simulation All information and data necessary for MPC are produced by step 1 to 4. The last step uses a C++

library that performs the actual optimization and that can be called by an *MPC block* in Modelica. The C++ library firstly reads the input and output variable names to automatically detect the optimization and disturbance inputs, the constraints, and the cost function(s). Furthermore, the user can select different options in the Modelica MPC block such as the control horizon and the size of each control time step of the horizon, the frequency of the states update and of the MPC update, the type of solver, etc. Based on all this information, the code then automatically generates the optimisation problem using CasADI [3] and CPLEX and saves the different matrices in a text file if this has not been done previously. This significantly improves the simulation time as the MPC initialization is costly due to the used *single-shooting approach*. As explained in section 7.1.4, *single-shooting approach* (also called *dense approach*) is a good choice as it makes the optimization problem size independent of the number of states, which is an interesting feature since each building model described in chapter 5 has more than 700 states.

The emulator model can now be simulated with the Modelica MPC block which periodically calls the library to retrieve the optimal control results and to provide data for the states update algorithm within the controller. By default, *perfect states update* is used, which means that all state values of the Modelica model are measured and directly used to update the controller model states. These optimal control results are used to provide set points for the building HVAC model, after which the simulation can advance in time. Notice that the actual control signals required by the HVAC system (e.g. valve set points, modulation or ON/OFF signals, etc.) may not correspond to the MPC control variables, as mentioned previously. In that case, an additional *post-processing* block should be added between the MPC and the HVAC blocks to perform the translation as illustrated by step 6 in fig. 6.5. The *post-processing* block can either be composed of sub-controllers or of algebraic equations.

To summarize, the toolchain automates the process from an existing building model developed with `IDEAS` and `LIDEAS`, to the simulation of the building model controlled by its linear MPC controller. The only manual steps are: i) creating the building model, ii) creating a linear HVAC model containing the cost function and the constraints, and iii) (optionally) developing sub-controllers which translate the MPC control variables into actual control actions for the HVAC system.

Chapter 7

Strengths of white-box controller models

Model predictive control (MPC) for heating, ventilation and air conditioning (HVAC) in buildings requires accurate controller models of the building envelope and its HVAC systems. Controller models are typically obtained by means of black- or grey-box system identification or using a white-box modelling approach. However, the necessary level of model complexity used by each method in order to obtain good MPC performance remains a priori unknown and no systematic method or examples showing the optimal complexity are available.

This chapter firstly investigates the influence of the controller model complexity (and accuracy) on the MPC performance for a given building (section 7.1) and, secondly, compares the performance of some grey-box MPCs with a white-box MPC obtained using the toolchain from chapter 6. The controller performances are evaluated using four performance keys: energy use, thermal discomfort, 1-step (and more-steps) ahead prediction error and CPU time.

7.1 Controller model accuracy versus MPC performance

This section is based on the paper previously published as:
Picard, D., Drgoňa, J., Kvasnica, M. and Helsen, L. Impact of the controller

model complexity on model predictive control performance for building. *Energy and Buildings* (August, 2017).

This section systematically investigates the required controller model complexity necessary to obtain optimal MPC performance for a given building and shows that optimal MPC performance can only be achieved when the controller model contains a sufficiently high number of states which is typically higher than the number of states used by black or grey-box models. The methodology used is explained in section 7.1.2.

For this purpose, a six room house is modelled using `IDEAS` which is then linearised and reduced to a set of linear, time invarient (LTI) reduced order models (MOR) using a model order reduction technique (see section 7.1.3). Different types of building climate controllers (BCC) are developed (section 7.1.4): a traditional rule-based-controller (RBC), MPC in standard form (S-MPC) and MPC using an off-set free approach (OSF-MPC). Section 7.1.4 further describes the controller objectives, the state observer and the quadratic cost function of the MPCs as well as the state condensing approach which is used to improve the computational tractability of the simulations. The tuning and the performance evaluation of the different controllers for a full year simulation are described in section 7.1.5.

7.1.1 Introduction

The linearisation methodology described in section 6.1 generates accurate controller models but it leads to complex (i.e. high number of states) models. By applying model order reduction methods, the complexity of the obtained linear model can be further reduced [142, 83, 50, 61]. Both for the grey-box and for the white-box approach, the necessary level of model complexity in order to obtain a good MPC remains unknown and no systematic method to determine this optimal model complexity is available [93, 67].

Some studies have investigated the influence of the model order on the model off-line prediction performance [86]. At the building component level, Gouda et al. [61] applied a non-linear optimization technique to optimally reduce higher order building component models to second order models. Xu and Wang [170] also reduced their model complexity to a second order model by minimizing the error between the frequency response of a higher order model and their model. Fraisse et al. [51] concluded that a wall should be represented by a fourth order model. At the multi-zone building level, Sturzenegger et al. [142] and Kim

and Braun [83] created a linear model with a large number of states and they reduced the order by applying Model Order Reduction (MOR). Foucquier et al. [50] also started from a high order building model but they reduced the complexity by merging different walls together. However, to the author's best knowledge, no work was presented yet which focuses on the investigation of the influence of the controller model accuracy on the performance of building climate controllers. The studies mentioned above only considered the off-line prediction errors without quantifying their impact on the controller performance. The main contribution of this section is the performance comparison of an MPC which uses the same controller model as the emulator model such that no model mismatch is present, with MPCs using controller models of different orders. This section is the first to systematically assess the performance of MPCs for a given building using controller models of different orders without relying on system identification but using linearisation and model order reduction techniques instead. This means that each reduced order model is *the best possible linear representation* of the building with that given number of states as each remaining state is optimally chosen by the model order reduction technique.

7.1.2 Methodology

The methodology is graphically represented in fig. 7.1. Firstly, an existing small house is modelled using `IDEAS` and subsequently linearised (see section 7.1.3). The existing building is used to ensure reasonable parameter values but no validation has been performed between the reference building model and the real building. In contrast with the rest of this PhD work, the obtained SSM is used in this section as emulator model instead of the non-linear Modelica model such that no model mismatch between controller model and emulator model is present when the MPC uses the (not reduced) SSM as controller model. This case is the theoretical benchmark. Secondly, in order to artificially vary the complexity and accuracy of the controller models, the obtained SSM is reduced to different orders (i.e. different number of states) (see section 7.1.4). The model order reduction (MOR) decreases the complexity of the model as well as its ability to predict the thermal behavior of the building. The obtained ROMs are thus used to mimic the best possible low order controller models which can be obtained for these orders by means of system identification, for example. Finally, the influence of the controller model complexity is investigated by evaluating the thermal comfort, the energy use, the computational effort (CPU) and the prediction error of the different MPCs, each using a controller model with a different complexity while the building emulator model is kept unchanged. Additionally, MPC performance is compared with a traditional thermostat RBC and in order to generalize the results, the same methodology is

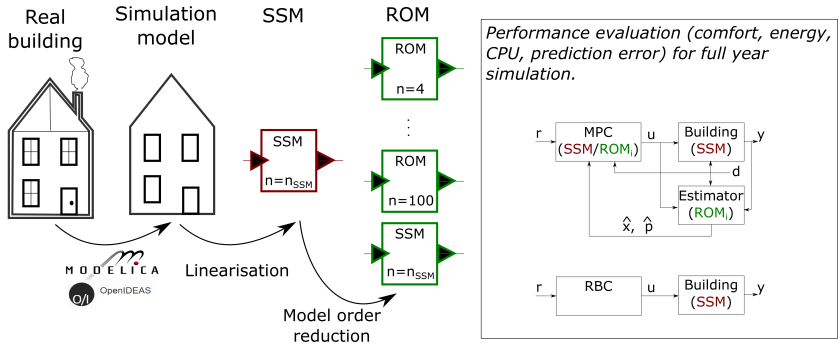

Figure 7.1: Schematic view of the methodology. From left to right: a 6-room house is modelled using `IDEAS`. The obtained model is then linearised and converted to a time-invariant SSM. Balanced truncation MOR technique is used to obtain ROMs of different orders. Finally, the upper bound of the controller performance is computed by using the SSM model both as controller and emulator model (theoretical benchmark). The performances of the MPC using the different ROMs as controller model are compared with the upper bound and with an RBC.

repeated for three different scenarios (see section 7.1.3): 1) the original building, 2) the same building but with an improved insulation level (Renovated building), and 3) the same building but with light weight wooden walls instead of concrete walls (light weight building).

7.1.3 Building modeling

This section describes the model of an existing house, its linearisation in order to obtain a SSM, and the applied model order reduction technique to obtain different ROMs from the SSM.

Building and building model description

The emulator model is based on an existing small 6-room terraced house in Bruges, Belgium (see fig. 7.2) with general parameter values given by table 7.1. The heating system is composed of one radiator per room fed by a central gas-boiler. The original building is poorly insulated and it has a low air-tightness.

Figure 7.2: Picture of the modelled house (Bruges, Belgium).

Table 7.1: General building parameters

Floor area	[m^2]	56
Conditioned volume	[m^3]	130.6
Total exterior surface area	[m^2]	195
Window to wall ratio	[-]	19%
Windows orientation	[-]	North-East

The column *original* of table 7.2 gives its overall heat transfer coefficient (U-value), its maximum volume air change per hour (ACH) and the composition of its outer walls, floors, windows and roof. For the renovated case, the U-value is decreased by adding insulation to the outer walls (see column *Renovated* in table 7.2). The thickness of the insulation layer varies for the different outer walls, respecting the actual renovation plans of the building. Finally, the case of a light weight building is considered by replacing all outer walls and the roofs by an insulated wooden structure which leads to a better insulation and a lower building mass. The last row of the table indicates the number of state variables of each model.

In this work, `IDEAS` is used as modelling tool and only the building envelope, consisting of 6 thermal zones, 5 windows, 11 outer walls, 5 boundary walls with neighboring buildings, 6 roof surfaces, 3 floor surfaces on the ground, 3 floor surfaces between the ground floor and the first floor, and 6 internal walls between the zones, is considered. The heating system is idealized as a perfectly controllable, limited heating power which can directly be supplied in each room (both convective and radiative). The radiators and the gas boiler are thus not modelled but they are replaced by one heat input per zone.

Table 7.2: Parameter values and number of states for the emulator models of the original, renovated and light weight buildings.

		Original/Renovated	Light weight	
Av. U-value	[W/m^2/K]	1.28/0.65		0.36
ACH	[1/h]	8.7/4.1		4.1
Composition		[m]		[m]
Outer Walls	Concrete	0.268/0.2	Wood + insulation	0.15
	Insulation	0/0.015-0.115		
	Plaster	0.01/0.01		
Floors	Reinforced concrete	0.12/0.12	Reinforced concrete	0.12
	Insulation	0/0.02		
	Screed	0.04/0.06	Insulation	0.02
	Topping	0.06/0	Screed	0.06
	Tiles	0.03/0.03	Tiles	0.03
Windows	Doubble glas (g=0.75/0.75, U=1.4/1.4 [W/m^2/K])		Doubble glas	
Roof	Fibre-cement	0.18/0.18	Wood + insulation	0.2
	Insulation	0.08/0.08		
	Plaster	0.01/0.01		
nStates		283/286		250

Linearisation and model order reduction

The house model is linearised using the methodology presented in section 6.1 resulting in a SSM in continuous time domain of following form:

$$\frac{\partial x(t)}{\partial t} = A_c x(t) + B_c u(t) \tag{7.1a}$$

$$y(t) = C_c x(t) + D_c u(t) \tag{7.1b}$$

with x the states representing temperatures, u the control inputs and the disturbances and A_c, B_c, C_c, D_c the SSM matrices where the subscript c refers to the continuous time domain.

Figure 7.3 gives the temperature errors between the non-linear `IDEAS` models for the three building types and the obtained SSM. The errors are computed for a full year open-loop simulation, i.e. the SSMs are never re-initialized with the non-linear models. A standard weather file of Uccle, Belgium [98] is used to

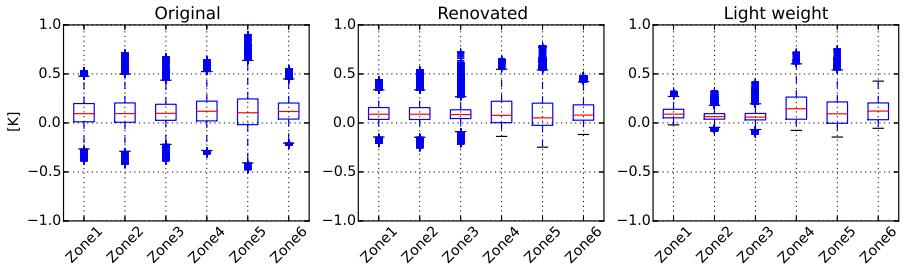

Figure 7.3: Boxplot of the temperature errors between the non-linear `IDEAS` models and their linear state space models for a full year open-loop simulation. The errors are given for each building type. The centered line gives the median, the box gives the first and third quartiles, the wiskers contain 99.5% of the data, and the crosses are the outliers.

represent the weather conditions and each zone temperature is kept within its comfort range using a PID-controller. All inputs of the non-linear and the linear models are exactly the same. As fig. 7.3 shows, all outlier errors are below $\pm$ 1K and the median of the error is close to zero for each zone. This confirms that the obtained SSMs with precomputed inputs are accurate approximations of the non-linear `IDEAS` models.

The complexity of the obtained SSMs can now be reduced using a model order reduction algorithm. In this work, the MATLAB function `reduce` with its default settings (square root balanced truncation algorithm) is used. However, when applying MOR, the initial state values also need to be transformed in their reduced form but the function `reduce` does not provide this transformation matrix. As the physical meaning of the initial states for the reduced models is lost by MOR, the initialization of reduced models is done as follows.

Assume a LTI SSM in continuous time domain with a given initial states value $x_0 = 293.15$ K. Because x_0 is a constant the SSM (7.1) is equivalent to:

$$\frac{\partial\left(x(t) - x_0\right)}{\partial t} = A_c\left(x(t) - x_0\right) + B_c u(t) + A_c x_0 \tag{7.2a}$$

$$y(t) = C_c\left(x(t) - x_0\right) + D_c u(t) + C_c x_0 \tag{7.2b}$$

By substituting $\bar{x}(t) := (x(t) - x_0)$, the model can be compactly rewritten as follows.

$$\frac{\partial \bar{x}(t)}{\partial t} = A_c \bar{x}(t) + \begin{bmatrix} B_c & A_c x_0 \end{bmatrix} \begin{bmatrix} u(t) \\ 1 \end{bmatrix} \tag{7.3a}$$

$$y(t) = C_c \bar{x}(t) + \begin{bmatrix} D_c & C_c x_0 \end{bmatrix} \begin{bmatrix} u(t) \\ 1 \end{bmatrix} \tag{7.3b}$$

The new SSM with state variables $\bar{x}$ has an initial states vector $\bar{x}_0 = 0$. The reduced model can now also be initialized at zero.

Finally, the SSM is discretized with a sampling time of 15 minutes to correspond with a reasonable control time step and for convenience, the inputs u_c and corresponding matrices B_c and D_c are splitted into the control inputs u_k with matrices B and D, the disturbances d_k with matrix E and the constant terms G and H.

$$x_{k+1} = Ax_k + Bu_k + Ed_k + G, \tag{7.4a}$$

$$y_k = Cx_k + Du_k + H. \tag{7.4b}$$

Off-line analysis of the ROMs

This section compares the behavior of the original SSM with the different ROMs. The temperatures obtained by an open-loop simulation are compared, the prediction performance is computed for different horizons and the frequency response of each model is analyzed using bode-plots.

Figure 7.4 shows the temperatures of each zone obtained by the SSM (dashed-line) and by the ROMs for the renovated building case. These profiles are obtained by a four days open-loop simulation with realistic control inputs (taken from a previous MPC simulation using the SSM as controller model) and disturbances. From fig. 7.4, one can see that ROMs of order below 20 cannot describe the temperature of each zone accurately. The ROM of order 15 shows, for example, a good fit for all zones except for zone 1 and zone 2 with a maximum temperature error of 1 K. The fact that only some zone temperatures are predicted accurately by low order ROMs while other zones are not, illustrates that the zones are not strongly correlated with each other. Therefore, each zone needs to be modelled by a minimum set of states which describe its own dynamics, as its temperature cannot be expressed by a linear combination of the neighboring zone temperatures. While the thermal interaction between the zones is weak, fig. 7.5 indicates that the interaction is not negligible for low

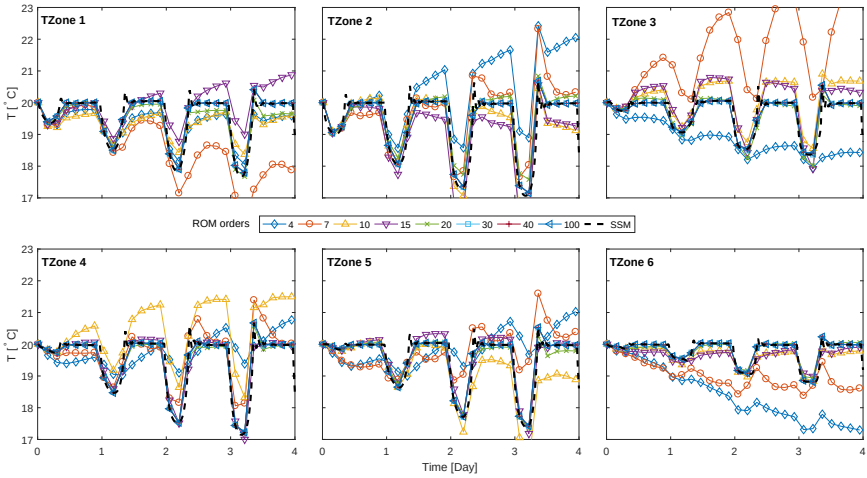

Figure 7.4: Zone temperatures for four days open-loop simulation. The same inputs are applied to the SSM (dashed-line) and to the ROMs (colored lines).

frequency excitations. Figure 7.5 presents the frequency response of the zone temperatures 1 and 2 as a function of the heat inputs to zones 1 to 6 for the SSM (solid black line) and the different ROMs for the renovated building case. The graph (1,1) of fig. 7.5 shows that zone 1 acts as a low pass filter on the heat injected in the same zone (Q(1)). The graphs (1,2) to (1,6) show that the temperature of zone 1 is also influenced by the heat inputs of the neighboring zones if the heat input frequencies are lower than 10^{-5} Hz (i.e., 1 day). Higher frequencies are damped out by the internal walls between the zones. The frequency responses of the ROMs order, however, differ from the SSM. They are overestimating the influence of the heat inputs on the neighboring zones for high frequencies. This is due to the lack of states available to physically separate the zones from each other. The ROMs of order 4 and 10 show large errors even for low frequencies due to the inaccurate zones representations. The frequency responses to solar gains are similar as the heat is injected in a similar way to the zone as the controlled heat inputs. The frequency response to the ambient temperature is plotted in fig. 7.6 for zone 5 and 6. From fig. 7.6, one can see that the responses of all ROMs except the one of order 4 are accurate. This means that the building insulation is correctly modelled by all ROMs of order above 10.

Figure 7.7 shows a boxplot of the 1, 10 and 40-step ahead prediction errors of all zones for the different ROMs for the original building (fig. 7.7a) and

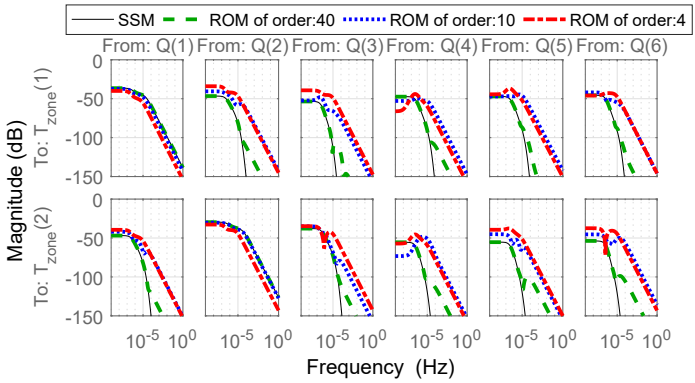

Figure 7.5: Frequency responses of zone 1 and zone 2 to the heat inputs of zone 1 to 6 for the renovated building.

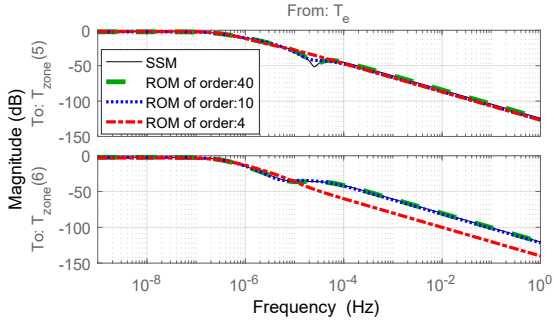

Figure 7.6: Frequency responses of zone 5 and zone 6 to the ambient temperature for the renovated building.

the light weight building (fig. 7.7b). Note that each box is computed with all prediction error points of each zones. The N-step ahead prediction error at time k (ϵ_k^N) is defined as the difference between the SSM outputs and the ROM outputs at time $k+N$ when the same inputs $u = [u_k, \cdots, u_{k+N}]$, disturbances $d = [d_k, \cdots, d_{k+N}]$ and equivalent initial state values x_k and $\tilde{x}_k$ are fed to the models:

$$\epsilon_k^N = F(x_k, u, d) - f_i(\tilde{x}_k, u, d) \tag{7.5}$$

with F and f the transfer function of the SSM and the ROM, respectively.

The errors for the renovated building scenario are not given as they are very similar to the original building. Comparing fig. 7.7a with fig. 7.7b shows that

ROMs of the same order have a lower prediction error for the light weight building than for the heavier original building. This is due to the higher mass content of the heavy building which requires a finer discretization of this mass to model the heat diffusion accurately. Remarkably, while fig. 7.4 shows that the error per zone is high for the ROMs of order below 20, all medians of fig. 7.7 are very close to zero. This means that the average building temperature (i.e., the average of all zone temperatures) is still correct for all ROMs.

7.1.4 Building climate controller

The objective of the building climate controller (BCC) in this work is to guarantee good thermal comfort by using as little energy as possible. The thermal comfort objective is achieved by maintaining each room temperature y_i of the house in the comfort range as defined by the European standard ISO-7730 [150]. The lower and upper temperature bounds (lb, ub) vary between $[20, 23]°C$ and $[24, 26]°C$, respectively, as a function of the 7-days average of the ambient temperature. The comfort objective corresponds thus to the constraint:

$$lb_k - s_k \leq y_{i,k} \leq ub_k + s_k \tag{7.6}$$

with s the relaxation variable which should be minimized and index k the sampling time.

In this section, the RBC and the MPCs are described.

Rule Based Controller (RBC)

The most commonly used controller for residential buildings with central heat production and radiators is a hysteresis rule based controller (RBC) also called central thermostat controller. Its working principle is as follows: a temperature sensor is placed in the main room, typically the living room. Based on this temperature and a comfort range, the central heating is turned on or off. Hot water can only flow to the radiators when the central heating is on. All radiators are equipped with thermostatic valves, except those in the room of the thermostat. The valve acts as a proportional controller by controlling the water mass flow rate through the radiator and so controlling its power.

The supply temperature T_{sup} is for all radiators the same and it is calculated using a typical heating curve equation:

$$T_{sup} = r + \left(\frac{T_{sup,n} + T_{ret,n}}{2} - y_{j,n} \right) q^{1/m} + \frac{T_{sup,n} - T_{ret,n}}{2} q \tag{7.7}$$

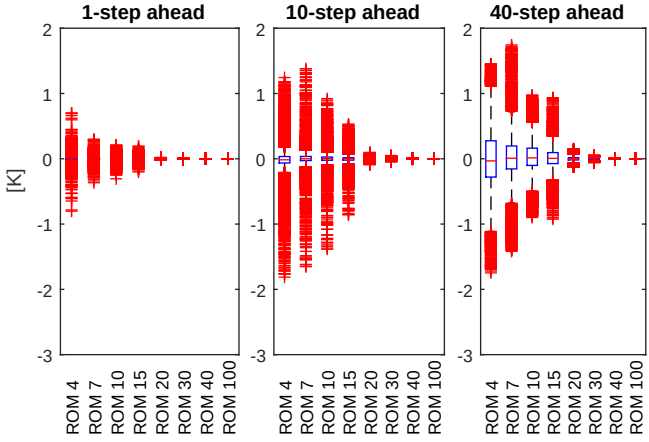

(a) Original.

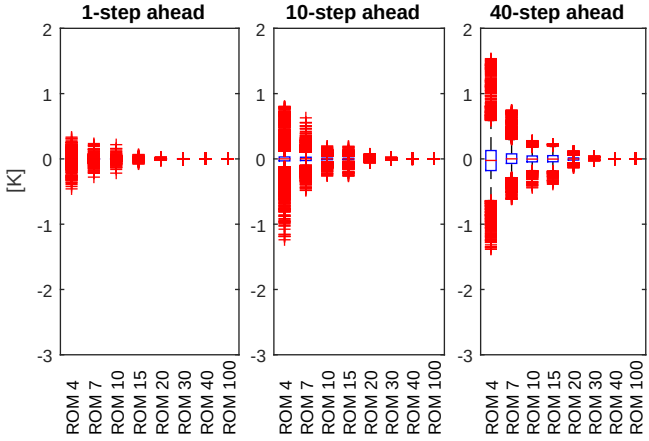

(b) Light weight.

Figure 7.7: Box-plot of the n-step ahead prediction error of all zone temperatures for different ROMs for the original building (top) and the light weight building (bottom). The centered line gives the median, the box gives the first and third quartiles, the whiskers contain 99.5% of the data, and the crosses are the outliers.

Table 7.3: Maximum heating power of the radiators (per zone).

Model Type	Maximum Radiator Gains $\overline{u}$ $[W]$
Original	$[2940\ 960\ 300\ 1400\ 460\ 253]^T$
Renovated	$[1680\ 685\ 154\ 1000\ 320\ 232]^T$
Light Weight	$[840\ \ 343\ \ 77\ \ 500\ \ 160\ 116]^T$

$$q = \frac{r - (T_{e,6h} + \epsilon)}{y_{j,n} - (T_{e,n} + \epsilon)} \tag{7.8}$$

where *sup* and *ret* stand for supply and return water temperatures, the subscript n refers to the nominal conditions ($T_{sup,n} = 70°C$, $T_{ret,n} = 50°C$, $T_{e,n} = -10°C$), and the index j refers to the room with the thermostat. The exponent m depends on the heating system (for radiator, $m = 1.3$). A correction term $\epsilon = 8$ K on the outside temperature $T_{e,6h}$ (averaged over 6 hours) is added to take the solar gain into account.

The binary control action z_k of the central heating in *k-th* time step, based on the temperature measurement in *j-th* (central) room $y_{j,k}$ and given reference temperature r_k is defined by a switching rule of the relay based thermostat given by following equation

$$z_k = \begin{cases} 1 & \text{if} \quad (z_{k-1} = 1 \ \wedge \ (y_{j,k} \leq r_k + \gamma)) \vee \\ & \qquad (z_{k-1} = 0 \ \wedge \ (y_{j,k} \leq r_k - \gamma)) \\ 0 & \text{otherwise} \end{cases} \tag{7.9}$$

where $\wedge$ is the logic conjunction and $\vee$ denotes the logic disjunction. The parameter 2γ here represents the width of the hysteresis. The values of the control action represent the heating mode if $z_k = 1$ and not heating if $z_k = 0$.

Finally the actual power $u_{i,k}$ delivered by the *i-th* radiator to the *i-th* zone at the *k-th* time step is given by:

$$u_{i,k} = \begin{cases} G_i z_k (T_{sup,k} - y_{i,k}), & \text{if } i = j \\ \alpha_i G_i z_k (T_{sup,k} - y_{i,k}), & \text{otherwise} \end{cases} \tag{7.10}$$

with $\alpha_i \in [0, 1]$ the proportional gain of the thermostatic valve and G_i the total thermal conductance of the radiator. Each radiator is sized such that its maximum power is required to maintain the indoor temperature to 20 °C when the outside temperature drops to −10°C (see table 7.3). The same thermal power bounds are used for MPC.

Model Predictive Building Control (MPC)

Two different types of MPC are considered: a standard MPC (S-MPC) and an off-set free MPC (OSF-MPC). In the OSF-MPC case, a set of extra states p is added to the controller model to take into account the mismatch between the controller model and the building model. In this work, 6 additional states are used (one per output). Equation (7.4) becomes thus eq. (7.11) for the OSF-MPC case.

$$\underbrace{\begin{bmatrix} x_{k+1} \\ p_{k+1} \end{bmatrix}}_{\tilde{x}_{k+1}} = \underbrace{\begin{bmatrix} A & \mathbf{0} \\ \mathbf{0} & I \end{bmatrix}}_{\tilde{A}} \underbrace{\begin{bmatrix} x_k \\ p_k \end{bmatrix}}_{\tilde{x}_k} + \underbrace{\begin{bmatrix} B \\ \mathbf{0} \end{bmatrix}}_{\tilde{B}} u_k + \underbrace{\begin{bmatrix} E \\ \mathbf{0} \end{bmatrix}}_{\tilde{E}} d_k + \underbrace{\begin{bmatrix} G \\ \mathbf{0} \end{bmatrix}}_{\tilde{G}}, \tag{7.11a}$$

$$y_k = \underbrace{\begin{bmatrix} C & F \end{bmatrix}}_{\tilde{C}} \begin{bmatrix} x_k \\ p_k \end{bmatrix} + \underbrace{\begin{bmatrix} D \\ \mathbf{0} \end{bmatrix}}_{\tilde{D}} u_k + \underbrace{\begin{bmatrix} H \\ \mathbf{0} \end{bmatrix}}_{\tilde{H}} u_k \tag{7.11b}$$

For the clarity of notation, only the S-MPC equations will be used further. The equations for the case of OSF-MPC are obtained by replacing the matrices (A,B,C,D,E) by their augmented equivalent $(\tilde{A}, \tilde{B}, \tilde{C}, \tilde{D}, \tilde{E})$. For the observer, the gain L is also recomputed using the augmented matrices (see following paragraph).

As the states of the ROMs do not correspond to those of the SSM, an observer is designed to estimate their state values. In this work, a standard Luenberger observer is used in the following form:

$$\hat{x}_{k|k} = \hat{x}_{k|k-1} + L\left(y_{m,k} - \hat{y}_{k|k-1}\right) \tag{7.12a}$$

$$\hat{x}_{k+1|k} = A\hat{x}_{k|k} + Bu_{k|k} + Ed_{k|k} + G \tag{7.12b}$$

$$\hat{y}_{k|k} = C\hat{x}_{k|k} + Du_{k|k} + H \tag{7.12c}$$

where the estimator gain L, given as a discrete stationary Kalman filter, is computed by the discrete Riccati equation using the `dlqe` MATLAB function. The subscript $k|k-1$ means that the value is estimated for time k based on the observed value of time $k-1$. The vector y_m denotes the vector of the measured outputs and the vectors $\hat{x}_k$ and $\hat{y}_k$ stand for the estimated states and outputs of the controller model, respectively.

Finally, The MPC optimization problem used in this work is formulated in linear way for the energy use and in a quadratic way for the slack penalties s

and the difference in control action δu as follows:

$$\min_{u_0,\ldots,u_{N-1}} \sum_{k=0}^{N-1} \left(||s_k||^2_{Q_\mathrm{s}} + ||\Delta u_k||^2_{Q_\mathrm{du}} + Q_\mathrm{u} u_k \right) \tag{7.13a}$$

$$\text{s.t. } x_{k+1} = Ax_k + Bu_k + Ed_k + G, \tag{7.13b}$$

$$y_k = Cx_k + Du_k + H, \tag{7.13c}$$

$$lb_k - s_k \leq y_k \leq ub_k + s_k, \tag{7.13d}$$

$$\Delta u_k = u_k - u_{k-1}, \tag{7.13e}$$

$$\underline{u} \leq u_k \leq \overline{u}, \tag{7.13f}$$

$$x_0 = \hat{x}(t), \tag{7.13g}$$

$$\forall k \in \{0, \ldots, N-1\}. \tag{7.13h}$$

where x_k, u_k and d_k represent the values of states, the inputs and the disturbances, respectively, predicted at the k-th step of the prediction horizon N. The predictions are obtained from the LTI prediction model given by equations (7.13b) and (7.13c). The lb_k and ub_k parameters represent the comfort range given by the constraints (7.13d), where the variables s_k are used as the indicators of a comfort violation. The min/max constraints for the control input amplitude are given by (7.13f). Equation (7.13e) defines the difference of the control action for two subsequent time steps which is used to limit peak powers. Note that for $k = 0$, (7.13e) becomes $\Delta u_0 = u_0 - u_{-1}$ where u_{-1} is the control input applied in the previous sampling instant. The initial conditions of the problem (7.13g) are given as the state estimates from the estimator, desired comfort boundaries, predicted disturbances and previous control input. For particular initial conditions, the optimization computes the sequence $u_0^*, \ldots, u_{N-1}^*$ of control inputs that is optimal with respect to the quadratic objective function (7.13a) and the constraints. The term $\|a\|_Q^2$ in the objective function represents the weighted squared 2-norm, i.e., $a^T Q a$, with the weighting matrices Q_s, Q_u, and Q_du given as positive definite diagonal matrices. The first term of the cost function minimizes the square of the comfort violations, the second term minimizes the fluctuations of the control input while the third term minimizes the energy used. The problem is defined in discrete time, for all time indices k acquiring integer values (7.13h).

In the problem formulation (7.13), each input and each state is considered as an optimization variable. However, the computation cost to solve a linear-quadratic control problem is $\mathcal{O}\left(N^3(n_x + n_u)^3\right)$, with N the control horizon,

n_x the number of states and n_u the number of inputs [53]. If the solver makes use of the sparsity of the problem, the complexity of the problem becomes $\mathcal{O}\left(N(n_x+n_u)^3\right)$. Another approach is to use the so-called *state condensing* method which rewrites the large and sparse system into a smaller but denser form. In this method only the inputs are considered as optimization variables and the computation cost becomes $\mathcal{O}\left(N^3 n_u^3\right)$. Due to the large number of states and relatively small horizon, the condensing method is the most appropriate method for this study.

The states can be eliminated by straightforward linear algebra substitutions as follows:

$$x_1 = Ax_0 + Bu_0 + Ed_0 \tag{7.14a}$$

$$x_2 = A\left(Ax_0 + Bu_0 + Ed_0\right) + Bu_1 + Ed_1 \tag{7.14b}$$

$$\vdots$$

$$\begin{aligned} x_{k+1} = {} & A^{k+1}x_0 + \dots \\ & \left[A^k B \dots AB\ B\right]\left[u_0^T \dots u_k^T\right]^T + \dots \\ & \left[A^k E \dots AE\ E\right]\left[d_0^T \dots d_k^T\right]^T \end{aligned} \tag{7.14c}$$

$$\begin{aligned} y_k = {} & CA^k x_0 + \dots \\ & C\left[A^{k-1}B \dots AB\ B\right]\left[u_0^T \dots u_{k-1}^T\right]^T + \dots \\ & C\left[A^{k-1}E \dots AE\ E\right]\left[d_0^T \dots d_{k-1}^T\right]^T + Du_k + Fp_0 \end{aligned} \tag{7.14d}$$

The state variables from the previous time instants are substituted into the subsequent state prediction equations. Recursively adopting this procedure an explicit formula (7.14c) is obtained for calculating the state update in the $(k+1)^{\text{th}}$ time step based only on the initial state condition and predicted control actions. The output equation (7.14d) with condensed states can now replace equations (7.13b) and (7.13c) of the controller model in the original MPC problem formulation (7.13).

7.1.5 Simulation case study

The different buildings are now simulated for a full year with their RBCs and their S-MPCs and OSF-MPCs using the different controller model complexities.

This section presents the general controllers tuning and the results. The controller performances are evaluated using four performance keys: energy use, thermal discomfort, 1-step ahead prediction error and CPU time. The energy use corresponds to the heat delivered by the radiators and is expressed in kWh. The thermal discomfort is evaluated as the number of Kelvin hours that the operative zone temperatures are outside the comfort range, i.e. the sum of each violation computed as its magnitude times its duration. This discomfort is further divided by the number of zones to be comparable to any building. The 1-step ahead prediction error is the error between the prediction of the zone temperatures made by the Luenberger observer and the outputs of the building model at the next time step. Finally, the CPU time corresponds to the overall simulation time.

Controllers Tuning In order to improve thermal comfort satisfaction of RBC and as such ensuring a fair comparison with MPC, the reference temperature r_k is shifted slightly above the lower boundary of the comfort range lb_k. The reference is now given as: $r_k = lb_k + 2.5°C$, while the width of the switching hysteresis (2γ) is equal to $0.5°C$. As shown by fig. 7.9, this shift was necessary to avoid too many comfort violations by the hysteresis controller.

In case of MPC, the values of the prediction horizon N and the weighting factor ratio $\frac{Q_s}{Q_u}$ are chosen based on the dependence of the MPC performance on the parameter values, as shown in fig. 7.8. With emphasis on thermal comfort satisfaction the choice of the prediction horizon is set to $N = 40$ steps (i.e., 10 hours), and weighting factor ratio $\frac{Q_s}{Q_u} = 10^8$.

In order to demonstrate the behavior and to verify the tuning of the investigated controllers the control profiles over a representative time window of 7 winter days are shown in figs. 7.9 and 7.10. for the RBC and the MPC, respectively. For the sake of brevity, only the profiles of the second zone of the original building are plotted as the behavior of the other zones and buildings is similar.

The MPC is constructed in the MATLAB environment, using the modeling and optimization toolbox YALMIP [95]. The closed-loop simulation is performed by applying the optimal control inputs $u^\star(t)$, computed at each sampling instant T_s by MPC to the building emulator model. The objective function (Eq. (7.13a)) is quadratic and all constraints are linear, therefore the problem (7.13) can be solved as a strictly convex quadratic program (QP). In this study the state of the art optimization solver GUROBI [65] is used.

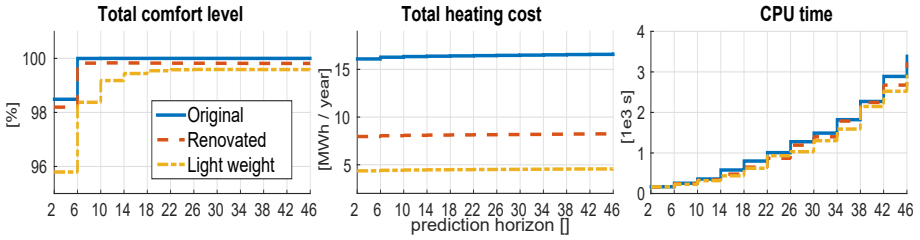

(a) Effect of the prediction horizon N.

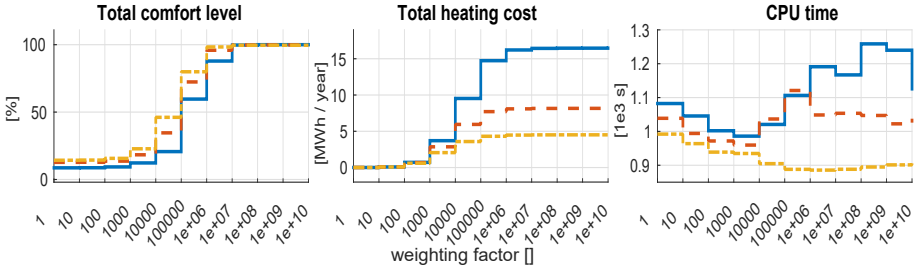

(b) Effect of the weighting factor $\frac{Q_s}{Q_u}$.

Figure 7.8: Analysis of the MPC performance based on the change of the parameters N and $\frac{Q_s}{Q_u}$, while fixing the rest of the parameters.

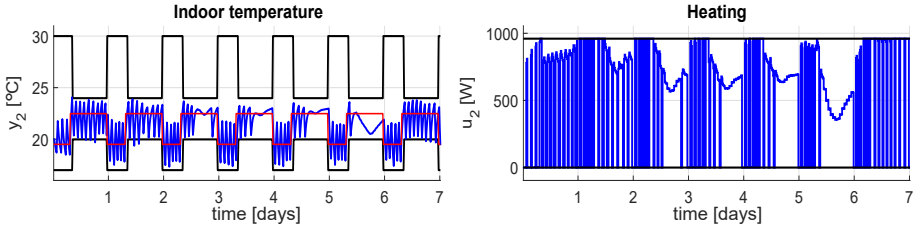

Figure 7.9: 7 days RBC profiles for the original building model. Left figure: closed-loop response of the indoor temperature (blue) in the second building zone w.r.t. the reference (red) and the comfort constraints (black). Right figure: corresponding profile of the control action (blue) w.r.t. the control boundaries (black).

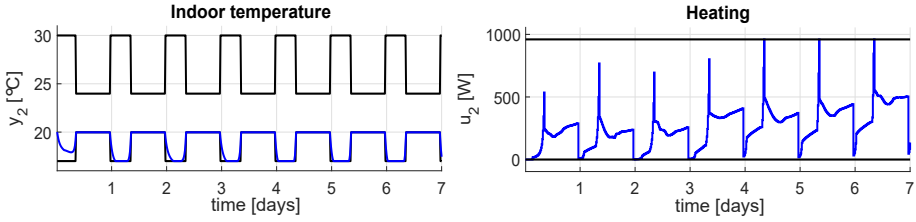

Figure 7.10: 7 days MPC profiles for the original building model. Left figure: closed-loop response of the indoor temperature (blue) in the second building zone w.r.t. the comfort constraints (black). Right figure: corresponding profile of the control action (blue) w.r.t. the control boundaries (black).

Results

Figure 7.11 presents the performance key values for the full year simulations and for the three building types using different controllers. The bars represent the RBC and the MPCs with different ROMs as controller models. The stars represent the results for the equivalent OSF-MPCs. Figure 7.11a shows that the comfort of MPC using the SSM as controller model is excellent with less than 30 Kelvin hour per year per zone (Kh/y/z) of discomfort for all buildings. These minimal comfort violations are caused by small overheating of the well insulated buildings during the hot days (no cooling is available). This confirms that the radiators are sized properly and that the prediction horizon is long enough. The RBCs are also well tuned as they show a discomfort smaller than 300 Kh/y/z. The high comfort satisfaction achieved by RBCs, however, is coupled to an additional energy use of 13, 15, and 12% compared to the highest order MPCs for the original, renovated and light weight building, respectively (see fig. 7.11b).

Figure 7.7 shows a decrease of the one-step ahead prediction error with an increase of the controller model complexity. Here the ROMs with $n_x \geq 20$ have negligible prediction error for all three building types. From fig. 7.11 it appears that MPCs using a ROM of order lower than 30 score significantly worse than MPCs using a higher order ROM. This is due to the prediction error made by the observer, as shown in fig. 7.11c. Figure 7.7 showes that even with perfect initialization, the ROMs of order lower than 30 have non-negligible prediction errors. Figure 7.11 confirms that the prediction errors directly influence the MPC results as the optimal controller is typically working near the comfort bounds. Even the very small error difference of 0.2-0.3K on the 40-steps ahead prediction between ROM 20 and ROM 30 (see fig. 7.7) results in a significant difference in thermal discomfort with a factor between 2 and 6

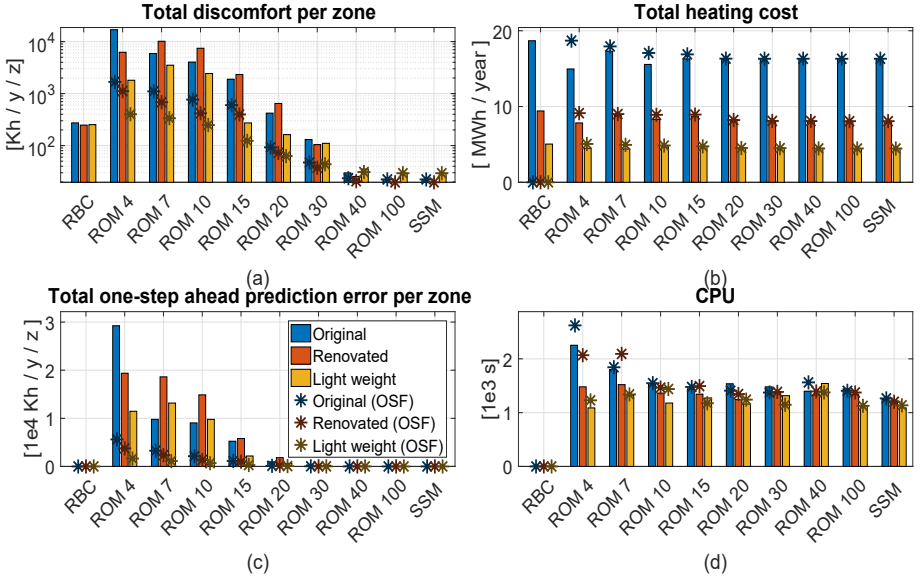

Figure 7.11: Comparison of performance keys evaluated for the RBC, S-MPC and the OSF-MPC approach for different controller model orders.

for the number of Kh/y/z between the two MPCs. Good controller models are thus effectively crucial for multizone control. Note that obtaining an accurate 30 states controller model for a 6-zone building using system identification is a challenging task [117].

Figure 7.11a shows that OSF-MPCs using low order ROM achieve a significantly better comfort than S-MPC with the same model complexity. This comfort improvement, however, comes with an increase in energy use (fig. 7.11b) for the OSF-MPCs using very low order ROMs ($n_x \leq 15$). For ROMs with $n_x > 15$, the comfort improvement comes with a small or negligible increase in energy use. This can be explained by the prediction errors shown in fig. 7.11c. The OSF approach adds one constant dynamic variable per output to the controller model, compensating the initialization error at each sampling instant, rather than improving the dynamical behavior of the ROM on the whole prediction horizon. Therefore when the model mismatch between controller model and building model is too large, the OSF method will not guarantee a good performance. By correcting the initialization value at each time step, oscillations may appear on the controller inputs. Overall, in the case of a sufficiently small model mismatch, the OSF method will improve the MPC results.

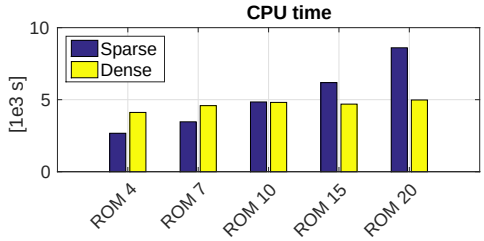

Figure 7.12: Comparison of the computational demands of the sparse and dense formulation of the control problem.

Finally, a reason to limit the controller model complexity is the computational effort required to solve the optimization problem. Figure 7.12 shows, however, that when applying the dense approach as explained in section 7.1.4, the CPU time becomes independent of the number of states. The CPU times for full year simulation scenarios and all building types using the dense approach have an average of 23.8 minutes with the maximum equal to 43.7 minutes and the minimum equal to 18.1 minutes (see fig. 7.11 (d)) with all computations performed on a 2.8 GHz machine with 2 CPU units each with 6 cores, under a GNU/Linux 64-bit Debian 3.16.7 operating system. As shown by fig. 7.12 the sparse approach leads to intractable CPU times for a large number of states.

7.1.6 Conclusion

This work systematically investigates the required controller model complexity necessary to obtain optimal control performance for a given building.

This work shows that the controller model should contain a minimum of states to model each zone separately, and that the walls and floors separating the zones should also have enough states to act as a low pass filter with correct cut-off frequency. The minimum number of states further increases with the building mass content. In the case of the investigated 6-room house, the thermal comfort achieved by MPC using a controller model with a minimum of 30 states instead of 20 states was improved with a factor 2 to 6 without significant increase of the energy use, showing that good MPC performances require controller models with a significantly higher number of states than the order used by most of the black- and grey-box system identification techniques. The minimum required number of states might be chosen lower when offset-free MPC (OSF-MPC) is used instead of conventional MPC. However, OSF-MPC might significantly increase the energy use when poor controller models (high model mismatch)

are used. Finally, the work shows that the computational effort required to solve the optimization problem becomes independent on the number of states of the controller model when a dense approach is used. The controller model can thus be as complex as necessary to generate accurate predictions without increasing the solving time. Note, however, that the more complex the model is, the less likely it will be observable. This drawback should also be considered. It should also be noted that interzonal air exchange through open doors was not considered which could significantly affect the results as significant heat can be transported through bi-directional buoyancy-driven air flow and as this heat transport is highly non-linear.

7.2 A comparison of MPC performance using white and grey-box approach

This section is based on the paper previously published as:
Picard, D., Sourbron, M., Jorissen, F., Cigler, J., Ferkl, L. and Helsen, L. Comparison of model predictive control performance using grey-box and white-box controller models. In *4th International High Performance Buildings Conference* (West-Lafayette, Indiana, USA, 2016), pp. 1–10.

This section compares the performance of different MPCs for which two different approaches to obtain the MPC controller model are used: (1) the white-box model approach as described in section 6.1, and (2) a system identification method using a grey-box model approach. The study is performed for the office building described in section 5.1.

This section is organized as follows: firstly section 7.2.1 gives an overview of the different controller models and their prediction accuracy. Secondly, section 7.2.2 describes the MPCs set up and finally, the performance of the different MPCs is analyzed (section 7.2.3).

7.2.1 Controller models

This section describes the different controller models and their prediction accuracy.

White-box model

The white-box controller model is obtained by using the linearisation method described in section 6.1. The resulting model is a SSM of the building envelope and it is composed of 821 states. The SSM inputs are: the thermal powers injected in the water circuit of the TABS, the supply ventilation temperature to the zones, the convective and radiative occupancy heat gains, the various ambient conditions, and the solar radiation through each window. As illustrated by fig. 7.15, the obtained white-box controller model (further referred as *LinMod*) is able to predict the zone temperatures of the emulator model with an error mostly smaller than ± 0.1 K.

Grey-box Model

Grey-box system identification is a technique which pre-defines the model structure based on physical knowledge but which optimizes its parameter values such that the model response fits some measurement data.

In this study, a method based on the simplified discretization of the continuous model structure is used, as described by Privara et al. [117] in the *deterministic semi-physical modeling* section of their paper. The method boils down to parameter estimation of a linear SSM. The SSM structure is constructed based on physical knowledge about the building and its discretization is then approximated by its first order Taylor expansion. The model parameters are estimated by solving a quadratic programming problem in which the one step ahead prediction error is minimized and the parameter values are constrained within physically meaningful bounds defined by the user. By keeping the model linear, the identification procedure can be formulated as a convex optimization problem.

For the considered office building, the model structure is chosen to be the so-called TRCM depicted in fig. 7.13. The model is composed of thermal resistances (representing thermal conduction, convection and radiation resistances) and capacitances (representing the heat capacity of the building mass). Each zone is represented by 3 nodes (zone temperature $T_{z,i}$, floor concrete temperature $T_{f,i}$, ceiling concrete temperature $T_{c,i}$) and a total of 12 zones are identified. The thermal power delivered by the AHU $\dot{Q}_{AHU,i}$, internal gains from occupants $\dot{Q}_{occup,i}$ and the solar radiation entering the zone through its windows $\dot{Q}_{solar}$ are injected in the zone capacity while the thermal power delivered to the TABS is injected in the floor and ceiling capacities. Thermal resistances exist between each zone and i) the ambient temperature $T_{ambient}$, ii) all neighboring zones

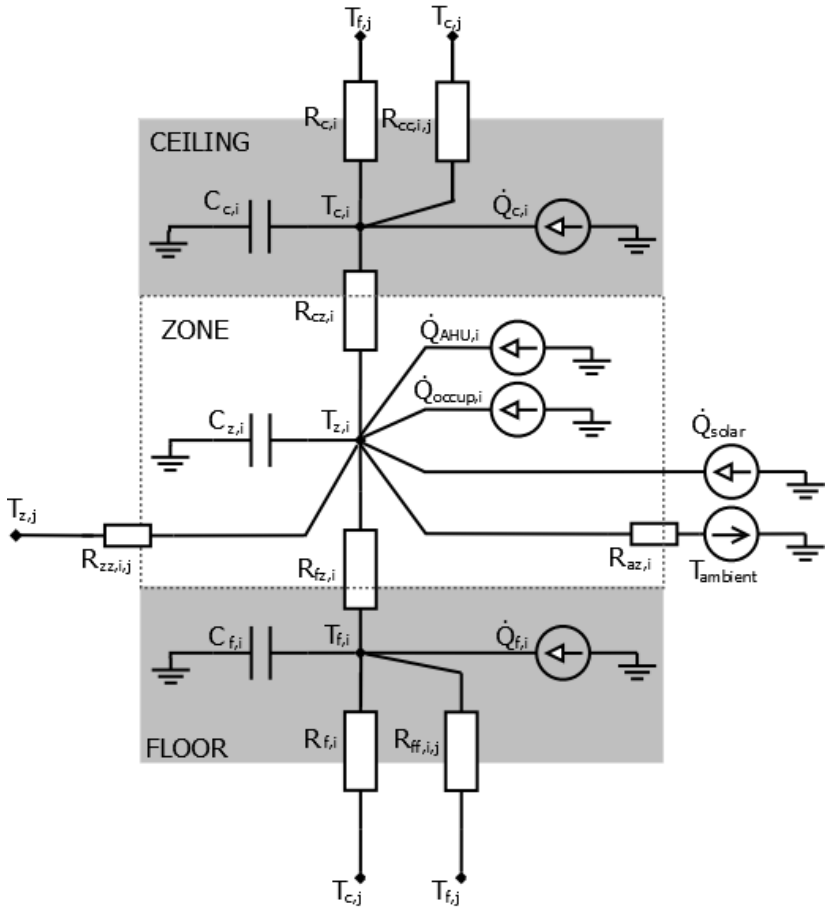

Figure 7.13: TRCM network of a zone. Subscripts f,z,c stand for floor, zone, ceiling respectively, and subscripts i and j stand for zone number. T stands for temperature (analogous to voltage) and $\dot{Q}$ stands for heat flux (analogous to electric current). The sources represent the inputs to the model – either temperatures or heat fluxes. Note that subscript j may represent more than one zone – it covers all neighboring zones.

$T_{z,j}$, iii) its ceiling and its floor. Ceilings (and floors) are coupled both to the zone above (under) and the adjacent zones.

Two controller models with the same structure (36 states) are identified: *IS-Mod* is identified using data obtained by simulation using the emulator building

with a reference controller from January to July, and *IE-Mod* is identified using measurement data of the real building collected during an experiment at Christmas time (see D-Xmas from section 5.1.1). The identification data is sampled every $T_s = 320s$ and the inputs are converted such that all inputs are either expressed in kW or $°C$. This ensures that the estimation problem is not ill-posed. The global solar radiation on the horizontal plane, available in the identification data set, is transformed into solar radiation per façade taking the solar blinds into account. This is possible as the solar blinds have a fixed control based on the intensity of the solar radiation on a horizontal surface. Window area and window properties are considered only in the case of identification from real data. For this model, the coupling between neighboring zones is not considered as it increases the number of parameters to estimate and information contained in the identification data is insufficient to identify all parameters correctly.

Validation of Controller Models

In this section, the controller models are validated against the reference emulator model (*Ref-Mod*) as the measurement data are incomplete for the validation of all 12 zones. The operative temperatures (i.e. a weighted temperature composed of the air temperature and the zone surface temperatures) of *Ref-Mod* are compared to the values of the linearised model (*Lin-Mod*), the identified model using simulation data (*IS-Mod*), and the identified model using experimental data (*IE-Mod*). The controller models are excited with the same (or the equivalent) inputs as the ones applied in *Ref-Mod*. *Ref-Mod* is simulated over a full year using a typical meteorological year from Uccle, Belgium [98] and typical control inputs. The simulation integrator step for *Ref-Mod* is 30 seconds and the outputs are sampled each 900 seconds. The controller models, however, are transformed to discrete SSM with the same sampling time as the MPC ($T_s = 3600$s) and the inputs are sampled accordingly using zero-hold. For model consistency, *IS-Mod* and *IE-Mod* are transformed such that their inputs and outputs are in Watt and Kelvin instead of kilo-Watt and degrees Celsius. Further, as only the global supply ventilation temperature ($T_{sup,ven}$) can be controlled and not the ventilation thermal powers to each zone ($\dot{Q}_{ven,i}$), the controller models are extended to use $T_{sup,ven}$ and the nominal ventilation mass flow rates instead of the $\dot{Q}_{ven,i}$'s. As explained in section 7.2.2, this transformation introduces a model mismatch for each zone but it becomes zero when the average is taken over all zones.

Figures 7.14a and 7.14b show 3-day winter and summer validation sets for the average operative temperature $T_{op,av}$ of the 12 zones. *Lin-Mod* and *IS-Mod* are able to accurately predict $T_{op,av}$. The error made by *Lin-Mod* is mainly

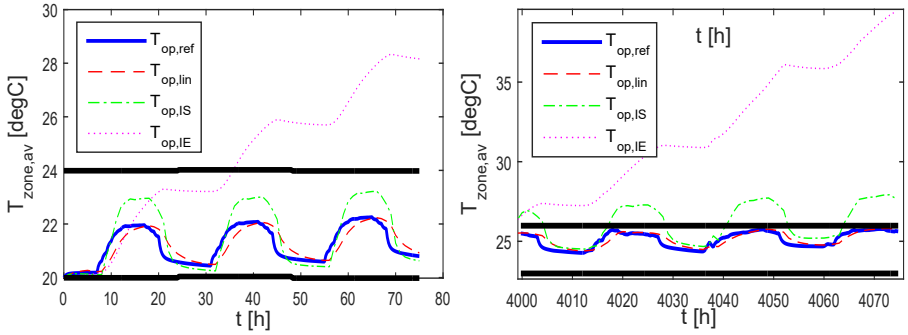

(a) Winter period.

(b) Summer period.

Figure 7.14: Average operative temperature of all zones for the reference model ($T_{op,ref}$), the linearised model ($T_{op,lin}$), the identified model using simulation data ($T_{op,IS}$), and the identified model using experiment data ($T_{op,IE}$) for a winter period (a) and for a summer period (b).

due to its zero-hold discretization as decreasing T_s significantly improves the predictions. For the *IS-mod* and *IE-mod*, no operative temperature is available and the temperature of the zone is used instead. This is the main cause of model mismatch for the *IS-mod* as its zone temperatures do coincide better with the air temperature of the reference model. However, both *IS-mod* and *IE-mod* show a temperature drift causing a serious prediction error for *IE-mod*. The drift probably originates from the system identification procedure which is carried out in the discrete time domain. An estimation error on the parameters can then lead to an integration error, which means the numerical creation of energy within the model. Simulating *IS-Mod* and *IE-Mod* with zero heat inputs and constant temperature input does indeed not result to convergence of the states to the temperature input value.

Figure 7.15 shows a boxplot of the prediction error of *Lin-Mod*, *IS-Mod* and *IE-Mod* for the prediction horizons of 3, 12 and 24 hours. The prediction errors are obtained by taking 1000 points from the reference simulation, evenly spaced over the whole year. For each point, the controller models are initialized with the corresponding state values of the reference simulation and the temperatures at the end of the prediction horizon are computed. Figure 7.15 gives the errors between these prediction temperatures and the reference temperatures for all zones together. Figure 7.15 shows that the *Lin-Mod* predictions are for 95% within ± 0.5 K for all horizons and the average prediction error is zero. The medians for *IS-Mod* and *IE-Mod* are positive which indicates a systematic overestimation of the temperature. However, *IS-Mod* is still able to predict the

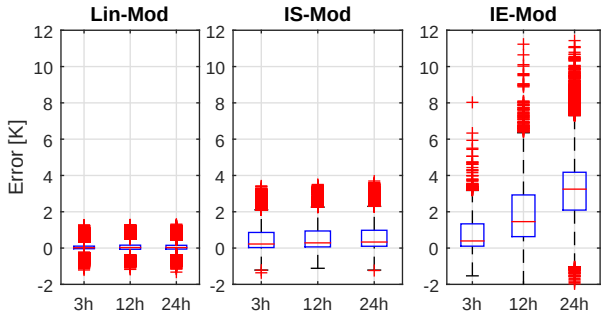

Figure 7.15: Prediction error for horizons of 3, 12 and 24 hours for the linearised model (*Lin-Mod*), the identified model using simulation data (*IS-Mod*), and the identified model using experiment data (*IE-Mod*).

temperature with an error range of $[0, 1]$ K for 75% of the time. This is not the case for *IE-Mod* which shows an average prediction error of 3 K for a horizon of 24 hours.

7.2.2 MPC cost function, constraints and parameters

In this work, the MPC optimization problem boils down to minimizing the heating and cooling TABS energy ($\dot{\mathbf{Q}}_{T,H,i} \times \Delta_t$, $\dot{\mathbf{Q}}_{T,C,i} \times \Delta_t$), and the ventilation energy $\dot{\mathbf{Q}}_{V,i} \times \Delta_t$, while the operative zone temperature $T_{op,i}$ stays within the time varying comfort range $[T_{\text{lb}}^{(k)}, T_{\text{ub}}^{(k)}]$ by minimizing the slack variable $\mathcal{S}_c^{(k)}$ (eq. (7.15a)). $\dot{\mathbf{Q}}_T$ denotes a vector containing the N tabs powers for zone i, with N the number of steps contained in the MPC horizon, Δ_t the discrete time step, $\dot{\mathbf{Q}}_{V,i}$ the ventilation thermal power to zone i for the full horizon and the subscript H and C for *heating* and *cooling*, respectively.

The sampling time in this work is 1 hour and the horizon is 1 day. The MPC uses perfect state update every 4 hours. Note that using perfect state updates is not possible in reality as not all states (such as the TABS core-temperature) are measurable and, moreover, sensors are not perfect. In order to limit the influence of the state update, the update only takes place every 4 hours, while the typical sampling time for building measurements is between 5 to 30 minutes.

Equation (7.15) formulates the MPC cost function and constraints. The optimization variables are $\dot{\mathbf{Q}}_{T,H,i}$, $\dot{\mathbf{Q}}_{T,C,i}$, and the unique ventilation supply temperature $T_{\text{sup,ven}}$. It should be noted that the current ventilation system imposes nominal ventilation flow rate for each zone when the building is occupied

and zero otherwise. $T_{\text{sup,ven}}$ is furthermore the same for all zones, which means that the $\dot{Q}_{V,i}^{(k)}$ (with (k) refering to the time index) computed by the MPC can not be exactly delivered to each zone. The exact value of $\dot{Q}_{V,i}^{(k)}$'s cannot be formulated in the linear MPC as it is bilinear (multiplication of the time varying ventilation mass flow rate $\dot{m}_{\text{i}}^{(k)}$ with $T_{\text{sup,ven}}$ or $T_{\text{air,i}}$). $\dot{Q}_{V,i}^{(k)}$ is approximated in this MPC by assuming that $\dot{m}_{\text{i}}^{(k)}$ is equal to its nominal value (eq. (7.15b)) and that the supply temperature equals the average of all air zone temperatures $\bar{T}_{\text{air}}$ when $\dot{m}_{i}^{(k)}$ is zero (eqs. (7.15i) and (7.15j)). Note that all $\dot{m}_{i}^{(k)}$ are turned on or off at the same time. This forces the MPC to limit $\dot{Q}_{V,i}^{(k)}$ as much as possible when the ventilation is off as the real ventilation system can then not supply the $\dot{Q}_{V,i}^{(k)}$'s to the zones. Due to this approximation, the MPC makes a prediction error on the amount of ventilation power injected when the ventilation is off. **This approximation will be solved in chapter 9 but it was not included in the paper on which this chapter is based.**

The global cost function and constraints can now be formulated as:

$$J = \min_{T_{\text{sup,ven}}, \dot{Q}_{T,H,i}, \dot{Q}_{T,C,i}} \sum_{k=0}^{N-1} \left[\sum_{i=1}^{12} \left(\underbrace{\dot{Q}_{T,H,i}^{(k)} + \dot{Q}_{T,C,i}^{(k)}}_{\text{TABS}} + \dots \right.\right.$$

$$\left.\left. \underbrace{\mathcal{A}_i^{(k)}}_{\text{Ventilation}} \right) + \underbrace{10^6 \mathcal{S}_c^{(k)}}_{\text{Discomfort}} + \underbrace{10^6 \mathcal{S}_v^{(k)}}_{\text{Soft ven.}} \right] \tag{7.15a}$$

$$s.t. \quad \dot{Q}_{V,i}^{(k)} = \dot{m}_{\text{nom,i}} c_p \left(T_{\text{sup,ven}} - T_{\text{air},i}^{(k)} \right) \tag{7.15b}$$

$$\mathcal{A}_i^{(k)} - \dot{Q}_{V,i}^{(k)} > 0 \ , \ \mathcal{A}_i^{(k)} + \dot{Q}_{V,i}^{(k)} > 0 \tag{7.15c}$$

$$\dot{Q}_{T,H,i}^{(k)} > 0 \ , \ \dot{Q}_{T,C,i}^{(k)} > 0 \ , \ \mathcal{S}_c^{(k)} > 0 \ , \ \mathcal{S}_v^{(k)} > 0 \tag{7.15d}$$

$$\begin{cases} \sum_{i=1}^{12} \dot{Q}_{T,H,i}^{(k)} < \dot{Q}_{\text{H,nom}} \\ \sum_{i=1}^{12} \dot{Q}_{T,C,i}^{(k)} < \dot{Q}_{\text{C,nom}} \\ \sum_{i=1}^{12} \dot{Q}_{V,i}^{(k)} < \mathcal{V}_{\text{H,nom}} \\ \sum_{i=1}^{12} \dot{Q}_{V,i}^{(k)} > -\mathcal{V}_{\text{C,nom}} \end{cases} \tag{7.15e}$$

$$\dot{Q}_{T,H,i}^{(k)} < \dot{Q}_{\text{H,i,nom}} \ , \ \dot{Q}_{T,C,i}^{(k)} < \dot{Q}_{\text{C,i,nom}} \tag{7.15f}$$

$$\begin{cases} T_{\text{ub}}^{(k)} - T_{\text{sup,ven}}^{(k)} + \epsilon + \mathcal{S}_v^{(k)} > 0 \\ T_{\text{sup,ven}}^{(k)} - T_{\text{lb}}^{(k)} + \epsilon + \mathcal{S}_v^{(k)} > 0 \end{cases} \tag{7.15g}$$

$$T_{\text{ub}}^{(k)} - T_{\text{op},i}^{(k)} + \mathcal{S}_c^{(k)} > 0 \ , \ T_{\text{op},i}^{(k)} - T_{\text{lb}}^{(k)} + \mathcal{S}_c^{(k)} > 0 \tag{7.15h}$$

$$\frac{\dot{m}_i^{(k)}}{\dot{m}_{\text{nom,i}}} \mathcal{V}_{\text{nom,H,i}} - \dot{m}_{\text{nom},i} c_p \left(T_{\text{sup}} - \bar{T}_{\text{air}} \right) > 0 \tag{7.15i}$$

$$- \frac{\dot{m}_i^{(k)}}{\dot{m}_{\text{nom},i}} \mathcal{V}_{\text{nom,C},i} + \dot{m}_{\text{nom},i} c_p \left(T_{\text{sup}} - \bar{T}_{\text{air}} \right) > 0 \tag{7.15j}$$

$$T_{\text{air}}^{(k)} = f \left(x^0, [T_{\text{sup,ven}}, \dot{Q}_{T,H,i}, \dot{Q}_{T,C,i}]^{(0)\cdots(k)} \right) \tag{7.15k}$$

with nominal working condition indicated by subscript *nom*, ventilation mass flow rates $\dot{m}_{\text{i}}^{(k)}$, air heat capacity c_p, maximum TABS powers $\dot{Q}_{T,H,\text{nom}}$, $\dot{Q}_{T,C,\text{nom}}$, $\bar{T}_{\text{air},i}$ the average of all zone air temperature and $T_{op,i}$ the operative temperature of each zone.

The minimization of $\mathcal{A}_i^{(k)}$ and eqs. (7.15b) and (7.15c) are the linear equivalent to the minimization of $|\dot{Q}_{V,i}^{(k)}|$ with $|\cdot|$ representing the absolute value. Equation (7.15e) constraints the total thermal powers such that the nominal production power of the heat pump is not exceeded. Equation (7.15f) limits the power of each TABS circuit, while eq. (7.15g) confines $T_{\text{sup,ven}}$ within a range ϵ broader than the comfort range. The relaxation ϵ is set to 1 K to avoid a too cold or too warm ventilation air flow. The constraint is furthermore relaxed by the slack variable $\mathcal{S}_v^{(k)}$ to improve the robustness of the algorithm. Finally, eq. (7.15k) represents the dynamics of the controller SSM.

7.2.3 Results

The MPC formulation presented by eq. (7.15) is used with the different controller models (*Lin-Mod*, *IS-Mod*, *IE-Mod*) to control the building climate during a full year simulation. Figure 7.16 shows the average of the 12 operative temperatures as calculated by the emulator for the different MPCs together with the lower and upper comfort temperature bounds. Table 7.4 summarizes the MPC performance factors for the whole building for each MPC, i.e. the yearly heating and cooling energy used by the TABS (TABS-Heat, TABS-Coo) and the ventilation (AHU-Hea, AHU-Coo) and the total discomfort (DC) together with the minimal and maximal deviation from the comfort range.

Figure 7.16 and table 7.4 show that the *Lin-Mod* MPC is able to keep the operative temperatures within the comfort bounds with only a negligible discomfort of 147 Kh/year and with a punctual maximal deviation of 1 K. The discomfort is mainly due to the model mismatch introduced by eq. (7.15b) which culminates when the air temperatures differ the most between the zones. When $T_{air,i}$ is higher than $\bar{T}_{\text{air}}$ and the ventilation is turned off (i.e. $\dot{m}_1 = 0$), the MPC constraints set $T_{\text{sup,ven}} = \bar{T}_{\text{air}}$. Equation (7.15b) becomes then negative and the MPC supposes that zone i is cooled by the ventilation while this is in reality not the case. Nevertheless, the discomfort caused by *Lin-Mod* MPC is only 7% and 0.4% of the discomfort caused by *IS-Mod* MPC and *IE-Mod* MPC, respectively, while its energy use is 41% and 8% of the energy used in the *IS-Mod* and *IE-Mod* approaches, respectively.

While less energy efficiency and comfort are guaranteed, *IS-Mod* MPC still achieves good comfort with only 2064 Kh /year of discomfort (172 Kh / zone / year) and its energy use is only 20% of the energy used in the case of *IE-Mod*. Due to the systematic overestimation of the temperatures as shown by fig. 7.15, *IS-Mod* MPC is not able to work close to the upper comfort temperature bound and therefore it cools more than necessary. Furthermore, the TABS control signals exhibit (not shown) too fast oscillations between heating and cooling

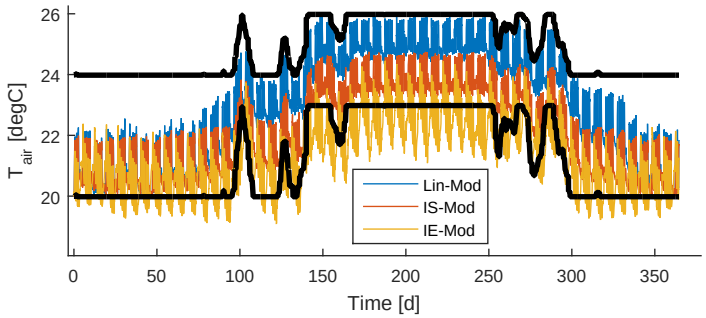

Figure 7.16: Comparison of the average of all operative zone temperatures for a full year simulation with MPC's using the *Lin-Mod*, the *IS-Mod* and the *IE-Mod* controller models.

actions which lead to an inefficient energy supply to the building. This bang-bang behavior is caused by the model mismatch and the linear formulation of the objective function. Adding a smoothing term on the inputs in the cost function as proposed by Cigler et al. [31] would probably significantly improve the MPC robustness against its prediction errors and so improve its global performance. Figure 7.15 also shows that errors on the 3 hours ahead prediction are non-negligible which causes regular discomfort when the MPC operates close to the bounds. The maximum deviation of -1.3 K remains, however, acceptable.

Finally, *IE-Mod* MPC shows poor comfort and a total energy use of 476 MWh while the energy use when the building model is controlled by the original rule-based-controller (not explained in the text) stays below 240 MWh. This confirms that due to the lack of 'rich' measurement data, the identified model *IE-Mod* is not reliable enough to be used in an MPC. The collection of 'rich' data (containing enough information for system identification) in real practice is thus a topic for further research, next to testing these approaches in real buildings.

7.2.4 Conclusion

In this study, two approaches to obtain a controller model for MPC were compared: a system identification method using a grey-box model approach and a white-box model approach for which a detailed building model is linearised. The MPC performance using both models is evaluated on a validated 12 zones emulator model of an existing office building. The results indicate that the MPC

Table 7.4: TABS and AHU energy use for heating (H) and cooling (C) and thermal discomfort (DC) obtained by MPCs for the three approaches (*Lin-Mod*, *IS-Mod*, *IE-Mod*)

	TABS H/C [MWh_{th}/y]	AHU H/C [MWh_{th}/y]	DC [kKh/y]	Min DC [K]	Max DC [K]
Lin-Mod	4.4 / 19.9	0.8 / 15.2	0.1	-0.4	1.0
IS-Mod	26.9 / 57.3	0.6 / 14.4	2.1	-1.3	0.0
IE-Mod	205.7 / 265.1	2.4 / 2.8	37.7	-3.6	0.0

performance is very sensitive to the prediction accuracy of the controller model. This work shows that both approaches can lead to an efficient MPC provided that very accurate identification data sets are available. For the considered simulation case, the white-box MPC results in a better thermal comfort and uses only 50% of the energy used by the best grey-box MPC. Tests in real buildings, however, are still needed to confirm the strength of the white-box approach in presence of all uncertainties (weather predictions, state measurement and estimations, user behaviour, ...).

Chapter 8

Optimal borefield flow rate

This chapter is based on the paper previously published as:
Picard, D., Jorissen, F. and Helsen, L. Analytical solution for optimal mass flow rate in primary circuit of ground-coupled heat pump systems. In *Proceedings of the International Ground Source Heat Pump Association* (Denver, CO, USA, March 2017).

Ground source heat pump (GSHP) systems extract heat or cold from the ground by circulating a heat carrier fluid (HCF) in a ground heat exchanger and inject this thermal energy in buildings (see section 2.1.1). This chapter firstly demonstrates that the mass flow rate of the HCF can significantly influence the total energy use of the GSHP system (section 8.1). Secondly, based on simple steady-state models (section 8.2), an analytical solution for the optimal mass flow rate is proposed as a function of measurable variables, system parameters and data that can easily be derived from manufacturer data sheets (section 8.3). Finally, the analytical solution is validated using a detailed simulation model (see chapter 3) representing an existing GSHP system of 99 boreholes with a depth of 30 m (section 8.4).

8.1 Introduction

Despite relatively high investment costs and thanks to their high energy efficiency, GSHP systems have proven their economic viability with about 10^5 units sold

every year in Europe between 2005 and 2013 [101]. Numerous studies and tools have been proposed to optimize the design of GSHPs in order to reduce the investment costs. Only a few of these studies propose (optimal) control strategies for the borefield mass flow rate in the installation, while ASHRAE [6] reports that pump energy represents 4 to 21% of the total energy demand of GSHP systems. This section firstly summarizes the findings from the literature about optimal flow in (ground source) heat pump systems and secondly, it describes the objective of this study and the chapter structure.

To the author's best knowledge, Li and Lai [92] were the first and only authors who proposed an analytical solution for optimal HCF flow rate in a borehole and for optimal borehole length. Li and Lai applied an entropy minimization technique to a ground heat exchanger with single U-tube but without considering the heat pump. In their case, an optimal flow rate exists due to 1) a rising entropy generation from pressure drops when the flow rate increases and 2) a decreasing entropy generation due to smaller ground and HCF temperature differences when the flow rate increases. A major drawback of their method is that the analysis does not include the heat pump performance which depends on the HCF flow rate and temperature, while it plays a crucial role in the system performance. Furthermore, an entropy optimum does not necessarily coincide with an energy or economic optimum since entropy generated due to pressure drops has a different energetic and economic value than entropy generated due to heat transfer.

Energy optimization of the air flow rate in heat pump systems was proposed by Granryd [62] for an air-to-air system. The author found an analytical solution that maximizes the COP_2 [1] by using simple (empirical) correlations to express 1) the heat transfer and the pressure drop in the heat pump heat exchangers and, 2) the heat pump thermal power ($\dot{Q}_{cond}$), as a function of the air velocity in the condenser and evaporator. The maximum COP_2 is then obtained by setting its derivative towards the air velocity to zero. A COP_2 optimum exists due to the increase of the heat pump COP_1 and the increase of pressure losses for increasing air flow rates in the evaporator. The author also showed that not only the COP_1 but also $\dot{Q}_{cond}$ depends on the flow rate and that the flow rate that maximizes $\dot{Q}_{cond}$ is not the same as the one maximizing COP_2. The simplified optimal solution shows good agreement with detailed simulations of the heat pump system.

The optimal HCF flow rate in borefield has also been investigated using simulation tools. Iolova and Bernier [76] performed a simulation-based comparative study for a school in TRNSYS between a GSHP system using a

[1] The coefficient of performance 2 (COP_2) is defined as the delivered useful energy (the condenser heat to the sink) divided by the electrical power use of the heat pump compressor and its fan or pump at both the source and sink sides.

variable speed drive (VSD) pump and one using constant flow rate. The system is composed of several heat pumps connected in parallel to a borefield. In case of the constant flow rate pump, the borefield pump is always on, regardless of whether the heat pump is on or off. In case of the VSD, each heat pump evaporator has a valve that blocks the flow when the heat pump is off. The VSD pump ensures a constant pressure drop over the system. They concluded that the variable flow system saves up to 82% of the pumping energy use and 18.5% of the total GSHP system energy use. The fact that inefficient systems with constant flow rate still exist today stresses the need of simple expressions to calculate the optimal HCF flow rate in GSHP systems.

This chapter proposes a simplified analytical solution for the optimal HCF flow rate of a GSHP system taking both the borefield and the heat pump into account. The optimal solution is a function of measurable variables and system parameters and data that can easily be obtained from manufacturer data sheets. Section 8.2 describes the steady state models used in section 8.3 to derive the analytical solution and section 8.4 validates the obtained expression with detailed simulation models.

8.2 Model description

Figure 8.1 (a) shows the considered system: a ground source heat pump extracts heat from a borefield with average ground temperature $\bar{T}_b$. Thermal power $\dot{Q}_{cond}$ is supplied to a building at a supply temperature $T_{cond,out}$. The mass flow rate of the heat carrier fluid (HCF) at the source side is $\dot{m}$, resulting in an inlet and outlet evaporator temperature $T_{eva,in}$ and $T_{eva,out}$. The considered electrical power are compressor power (P_{comp}) and source circulation pump power (P_{pump}). The mass flow rate at the sink side is assumed to be constant. Figure 8.1 (c) shows that such a system has an optimal mass flow rate due to the increase of the heat pump COP (see section 8.2.1) and the increase of P_{pump} with $\dot{m}$.

The following sections describe the heat pump model (section 8.2.1), the borefield model (section 8.2.2) and the pump model (section 8.2.3) that are used to derive an analytical solution for the optimal HCF mass flow rate $\dot{m}$.

8.2.1 Heat pump model

A heat pump is a device that converts heat from a low temperature source to heat at a higher temperature, by compressing a refrigerant using a compressor

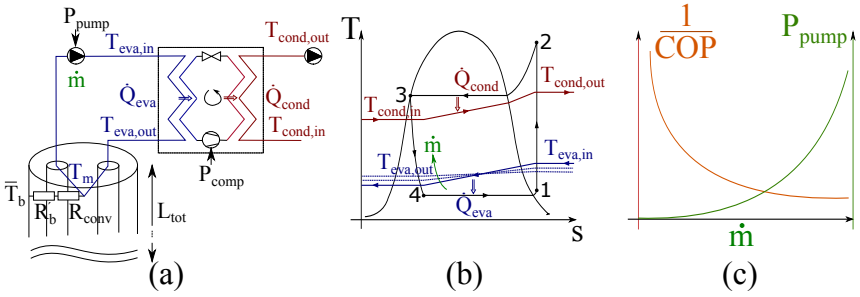

Figure 8.1: System description: (a) Schematic presentation of a ground-source heat pump system, (b) T-s diagram describing the working principle of the heat pump, (c) illustration of the dependency on the HCF mass flow rate for the heat pump COP and the pumping power P_{pump}.

that is typically driven by an electric motor (see section 2.1.2). The refrigerant evaporates in a first heat exchanger (evaporator), which requires heat at a low temperature. This refrigerant is compressed (state 1 in the T-s diagram fig. 8.1 (b)) to a higher pressure and temperature (state 2). The refrigerant then condenses to a liquid state (state 3) while rejecting heat at a higher temperature in the second heat exchanger (condenser). The refrigerant then expands over an expansion valve and enters the evaporator (state 4).

The energy performance of the heat pump depends on the refrigerant pressure difference between the condenser and the evaporator. The pressure difference is determined by the required temperature difference which depends on both the source and sink temperature and on the mass flow rates. The temperature difference is controlled by the expansion valve. While the exact control method of the valve is typically a manufacturer secret, the valve needs to ensure a small amount of superheat in state 1 such that no liquid refrigerant enters the compressor. Furthermore, state 4 should be at a lower temperature than $T_{eva,out}$ and state 2 should be hotter than $T_{cond,out}$. These temperatures are further dependent on the HCF flow rate (see blue lines in fig. 8.1 (b). Therefore, the HCF mass flow rate $\dot{m}$ in the evaporator indirectly influences the heat pump performance as it changes both $T_{eva,in}$ and $T_{eva,out}$.

The heat pump performance data provided by manufacturers are typically the COP and compressor electrical power P_{comp} as a function of the evaporator inlet temperature $T_{eva,in}$, the condenser outlet temperature $T_{cond,out}$ (or inlet $T_{cond,in}$), and (optionally) the evaporator mass flow rate $\dot{m}$. Figure 8.2 shows

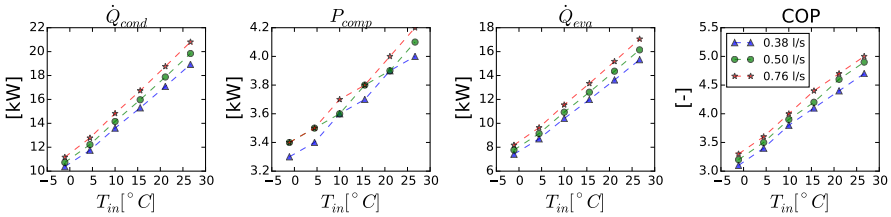

Figure 8.2: Heat pump characteristics for Carrier ground source heat pump type GZ048 (full load) with $T_{cond,in} = 21.11°C$. Characteristics expressed as a function of $T_{eva,in}$ and $\dot{m}$.

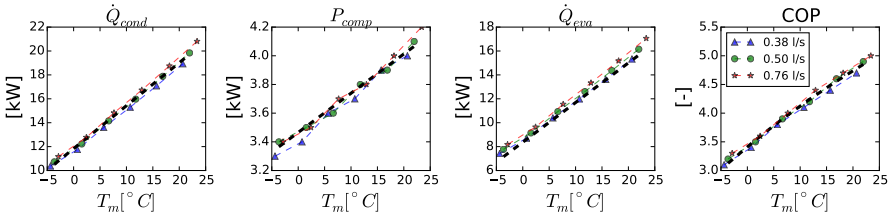

Figure 8.3: Heat pump characteristics for Carrier ground source heat pump type GZ048 (full load) with $T_{cond,in} = 21.11°C$. Characteristics expressed as a function of T_m and $\dot{m}$.

performance data for the Carrier water/air ground source heat pump type GZ048 (full load) for $T_{cond,in} = 21.11°C$ [26]. From fig. 8.2 it is clear that the performance depends on both $T_{eva,in}$ and $\dot{m}$. Based on the reflections in previous paragraphs, a strong relation between $T_m = \frac{T_{eva,out}+T_{eva,in}}{2}$ and the heat pump performance is expected. The heat pump performance is, however, not provided as a function of T_m but it can be computed from the other variables. Transforming fig. 8.2 using $T_m = T_{eva,in} - \frac{\dot{Q}_{eva}}{2c_p\dot{m}}$, with c_p the HCF specific heat capacity, confirms this hypothesis since the curves for the different $\dot{m}$ are now more or less coinciding (see fig. 8.3). This relation has been verified for different $T_{cond,in}$, for Carrier heat pump models G024 to G072 and for Daikin SmartSource 026 [34].

The steady state behaviour of the heat pump can now be modelled using a linear fit of P_{comp} and $\dot{Q}_{eva}$ (assuming full load and constant condenser inlet

temperature):

$$T_m = \frac{T_{eva,in} + T_{eva,out}}{2} \tag{8.1}$$

$$\dot{Q}_{cond} = \alpha + \beta T_m,\ P_{comp} = \gamma + \psi T_m \tag{8.2}$$

$$\Rightarrow \dot{Q}_{eva} = \dot{Q}_{cond} - P_{comp} = \alpha - \gamma + (\beta - \psi) T_m := \eta + \epsilon T_m \tag{8.3}$$

8.2.2 Borefield model

A borefield is a heat exchanger in the ground composed of one or multiple boreholes (see section 2.1.1). If the average temperature of the ground at the borehole wall $\bar{T}_b$ is known, the most simple borehole model is obtained by disregarding the grout dynamics and by assuming a linear variation of the temperature along the pipe length [90]. The ground is assumed to exchange heat $\dot{Q}_{eva}$ at T_m which is the average between the inlet and the outlet HCF temperature. The drawback of this simplification is that $T_{eva,in}$ (which equals the borefield supply temperature) can become higher than $\bar{T}_b$ for low flow rates, which is a violation of the second law of thermodynamics. We therefore assume that $\dot{Q}_{eva}$ is exchanged at $T_{eva,in}$ instead. T_m can now be expressed as a function of $\dot{m}$ by using the energy balance equation in the borefield:

$$R_b^* := \frac{R_b}{L_{tot}} := \frac{R_b' + R_{conv}}{L_{tot}} \tag{8.4}$$

$$\dot{Q}_{eva} R_b^* = \bar{T}_b - T_{eva,in} \tag{8.5}$$

$$\dot{Q}_{eva} = \dot{m} c_p \left(T_{eva,in} - T_{eva,out}\right) \tag{8.6}$$

$$\Leftrightarrow T_m = \bar{T}_b - \left(R_b^* + \frac{1}{2\dot{m} c_p}\right) \dot{Q}_{eva} \tag{8.7}$$

with the HCF heat capacity c_p and the total borehole(s) length L_{tot}. R_b' is the borehole resistance between the pipe inner wall and borehole wall. The flow dependent convective resistance R_{conv} is calculated separately. R_b is usually obtained experimentally by means of a *thermal response test*. If the thermal properties of the grout and ground, and the exact geometry of the borehole are known, R_b' can be computed using the multipole method [69]. R_{conv} in a

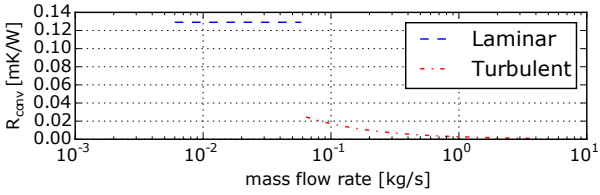

Figure 8.4: Convective thermal resistance of water in a circular pipe (PN10 32mm).

circular pipe is computed from eq. (8.8) [2]:

$$R_{conv} = \frac{1}{\pi \lambda_f \mathrm{Nu}} \quad \text{with} \quad \begin{cases} \mathrm{Nu} = 0.023 \mathrm{Re}^{0.8} \mathrm{Pr}^{0.35} & \text{if turbulent} \\ & \text{(Dittus-Boelter correlation)} \\ \mathrm{Nu} = \frac{3.66+4.36}{2} & \text{if laminar [152]} \end{cases} \tag{8.8}$$

with the HCF thermal conductivity λ_f , the Reynolds number $\mathrm{Re} = \frac{v_f d_{p,in}}{\nu_f}$, the Prandtl number $\mathrm{Pr} = \frac{\nu}{\alpha}$, the HCF velocity v_f, the inner pipe diameter $d_{p,in}$, the HCF dynamic viscosity ν_f and thermal diffusivity α. Figure 8.4 shows that R_{conv} is only weakly dependent on $\dot{m}$ but that a transition from turbulent to laminar increases the resistivity from about 0.02 to 0.13 m.K/W.

8.2.3 Pressure losses and circulation pump

In this section, the circulation pump and typical pressure losses due to the circulation of the HCF in the heat pump and borefield are discussed.

The pressure drop over the heat exchangers depends on the heat pump type and size and can often be found in the manufacturer data sheets. Typically, small units have a pressure drop in the order of 4 kPa at minimal flow ($\theta_{eva,max} := T_{eva,in} - T_{eva,out} \simeq 5$K). Larger units have a pressure drop in the order of 13 kPa at minimal flow ($\theta_{eva,max} = 4$ K). The pressure losses associated to the borefield occur in the borehole, the horizontal connection pipes, the collector and the various bends, valves and connection elements. Typically, the total pressure drop is in the range of 0.5 to 1 bar, but it can widely vary and detailed pressure drop calculations should be carried out for more accurate results.

[2] For the laminar case, the average value between the correlation for constant heat flux and correlation for constant wall temperature is taken.

A circulation pump has an efficiency η_{pump} that varies between 55 and 85% at nominal speed [17], depending on its size. Since the pump load has a quadratic pressure drop characteristic, similarity laws predict that the efficiency is not a function of the pump speed. In this study we therefore assume η_{pump} to be constant.

Assuming a constant pump efficiency η_{pump} and a cubic relation between pump power and flow rate, and using a reference volumetric flow rate $\dot{V}_0$ and corresponding pressure drops, P_{pump} can be expressed as

$$a_p = \frac{\Delta p_{\mathrm{BF}} + \Delta p_{\mathrm{HP}}}{\eta_{pump} \dot{V}_0^2} \tag{8.9}$$

$$P_{pump} = a_p \left(\frac{\dot{m}}{\rho} \right)^3 \tag{8.10}$$

with the borefield and the heat pump pressure drops $\Delta p_{\mathrm{borefield}}$ and $\Delta p_{\mathrm{heat\ pump}}$.

8.3 Optimal solution

In this section, an analytical solution for the optimal HCF mass flow rate is derived by maximizing the system coefficient of performance (COP_2) (eq. (8.11)). Constant condenser inlet temperature and full load condition are assumed for the heat pump.

$$\frac{1}{COP_2} = \frac{P_{\mathrm{pump}} + P_{\mathrm{comp}}}{\dot{Q}_{\mathrm{cond}}} \tag{8.11}$$

The optimization problem can be re-written by substituting the model equations in eq. (8.11). First T_m is obtained as a function of $\dot{m}$ and some parameters using eqs. (6.13) and (8.7):

$$T_m = \bar{T}_b - \left(R_b^* + \frac{1}{2\dot{m} c_p} \right) (\eta + \epsilon T_m) \tag{8.12}$$

$$\Leftrightarrow T_m = \frac{\dot{m} \left(\bar{T}_b - R_b^* \eta \right) - \frac{\eta}{2c_p}}{\dot{m} \left(R_b^* \epsilon + 1 \right) + \frac{\epsilon}{2c_p}} := \frac{\dot{m}\kappa - \lambda}{\dot{m}\xi + \nu} \tag{8.13}$$

with $\xi := R_b^* \epsilon + 1$, $\nu := \frac{\epsilon}{2c_p}$, $\kappa := \bar{T}_b - R_b^* \eta$, $\lambda := \frac{\eta}{2c_p}$.

By inserting eqs. (8.2), (8.3) and (8.10) in eq. (8.11) and developing it with eq. (8.13), following optimization problem is obtained:

$$\frac{1}{COP_2} = \frac{\frac{a_p}{\rho^3}\dot{m}^3 + \gamma + \psi T_m}{\alpha + \beta T_m} = \frac{a_p\xi\dot{m}^4 + a_p\nu\dot{m}^3 + \left(\gamma\rho^3\xi + \kappa\psi\rho^3\right)\dot{m} + \gamma\nu\rho^3 - \lambda\psi\rho^3}{\rho^3\left(\left(\alpha\xi + \beta\kappa\right)\dot{m} + \alpha\nu - \beta\lambda\right)} \tag{8.14}$$

$$= \frac{a_1\dot{m}^4 + a_2\dot{m}^3 + a_3\dot{m} + a_4}{a_5\dot{m} + a_6} \tag{8.15}$$

with $a_1 = a_p\xi$, $a_2 = a_p\nu$, $a_3 = \gamma\rho^3\xi + \kappa\psi\rho^3$, $a_4 = \gamma\nu\rho^3 - \lambda\psi\rho^3$, $a_5 = \rho^3\left(\alpha\xi + \beta\kappa\right)$, $a_6 = \rho^3\left(\alpha\nu - \beta\lambda\right)$.

The optimal solution is computed from the roots of the derivative of this function (the denominator is removed from the equation):

$$0 = \frac{\partial \frac{1}{COP_2}}{\partial\dot{m}} \tag{8.16}$$

$$\Leftrightarrow 0 = 3a_1a_5\dot{m}^4 + \left(4a_1a_6 + 2a_2a_5\right)\dot{m}^3 + 3a_2a_6\dot{m}^2 + a_3a_6 - a_4a_5 \tag{8.17}$$

which becomes after substitution:

$$\begin{aligned} 0 =& 12a_pc_p^2\left[R_b^{*2}\alpha\epsilon^2 - R_b^{*2}\beta\epsilon\eta + R_b^*\bar{T_b}\beta\epsilon + 2R_b^*\alpha\epsilon - R_b^*\beta\eta + \bar{T_b}\beta + \alpha\right]\dot{m}^4 + \\ & 4a_pc_p\left[3R_b^*\alpha\epsilon^2 - 3R_b^*\beta\epsilon\eta + \bar{T_b}\beta\epsilon + 3\alpha\epsilon - 2\beta\eta\right]\dot{m}^3 + \\ & 3a_p\left[\alpha\epsilon^2 - \beta\epsilon\eta\right]\dot{m}^2 + \\ & 2\rho_f^3c_p\left[\bar{T_b}\alpha\epsilon\psi - \bar{T_b}\beta\epsilon\gamma + \alpha\eta\psi - \beta\eta\gamma\right] \end{aligned} \tag{8.18}$$

Equation (8.18) has possibly 4 solutions ($x_{1,2,3,4}$) for the optimal mass flow rates, which can be computed analytically by solving the root-problem for

polynomial $p(x) = ax^4 + bx^3 + cx^2 + e$:

$$\Delta = 256a^3e^3 - 128a^2c^2e^2 + 144ab^2ce^2 + 16ac^4e - 27b^4e^2 - 4b^2c^3e \quad (8.19a)$$

$$p = \frac{8ac - 3b^2}{8a^2} \quad , \quad q = \frac{b^3 - 4abc}{8a^3} \quad (8.19b)$$

$$\Delta_1 = 2c^3 + 27b^2e - 72ace \quad , \quad \Delta_0 = c^2 + 12ae \quad (8.19c)$$

$$Q = \left(\frac{\Delta_1 + \sqrt{-27\Delta}}{2}\right)^{\frac{1}{3}} \quad , \quad S = \frac{1}{2}\sqrt{-\frac{2}{3}p + \frac{1}{3a}\left(Q + \frac{\Delta_0}{Q}\right)} \quad (8.19d)$$

$$x_{1,2} = \frac{-b}{4a} - S \pm \frac{1}{2}\sqrt{-4S^2 - 2p + \frac{q}{S}} \quad (8.19e)$$

$$x_{3,4} = \frac{-b}{4a} + S \pm \frac{1}{2}\sqrt{-4S^2 - 2p - \frac{q}{S}} \quad (8.19f)$$

Even though we cannot prove it formally, we expect the problem to have only one feasible solution. For a practical implementation, the optimal solution can also be obtained by plotting eq. (8.14) or by using a line search method to find the roots of eq. (8.18).

8.4 Results, validation, and discussion

The optimal analytical solution is validated using a simulation model based on an existing GSHP system. The system consists of a borefield with 99 boreholes of 30 m deep (double U-tube), a Wilo Cronoline IL 80/220 4-4 circulation pump, and heat pumps. The total GSHP system pressure drop at nominal flow rate (14.85 kg/s) is 170 kPa. The borefield is connected to 14 Carrier GZ048 heat pumps that are operated at nominal condenser flow rate with an inlet temperature of 21.1 °C. All parameter values used for the simulation and for the analytical solution are summarized in table 8.1. The system is modelled in Modelica using the borefield model from Picard and Helsen [113] and the pump model from Wetter et al. [168]. The heat pump model uses a 3 dimensional linear table interpolation of the manufacturer performance data [26], fig. 8.3. The Modelica model is simulated using Dymola 2017.

The goodness of the linear fits $\dot{Q}_{cond,lin}$ and $P_{comp,lin}$ for resp. $\dot{Q}_{cond}$ and P_{comp} for the considered heat pump are shown in fig. 8.3 (black dashed line). $\dot{Q}_{eva,lin}$ and $\mathrm{COP}_{\mathrm{lin}}$ are computed from $\dot{Q}_{cond,lin}$ and $P_{comp,lin}$. Figure 8.3

Table 8.1: Parameter values used for the validation.

Borefield			Pump		
$\bar{T}_b$	8.7	[°C]	efficiency	0.675	[-]
R_b	0.085	[mK/W]	type	Wilo Cronoline-IL	
R_{conv}	0.0148	[mK/W]	Δp_{BF} *1	170	[kPa]
$n \times H_{bor}$	99 x 30	[m]		*1 $\dot{m}$=14.85 kg/s in BF	
L_{tot}	329	[m]	Δp_{HP} *2	27.6	[kPa]
R_b^*	0.0003	[K/W]		*2 m=0.76 kg/s in HP	
HCF: 20% glycol			Heat pump		
ρ	1033	[kg/m^3]	type	Carrier - GZ048	
c_p	3880	[J/kgK]	Characteristics	see Figure 8.3	
ν	$2.4 * 10^{-6}$	[m^2/s]	$T_{cond,in}$	21.11	[°C]
λ	0.505	[W/mK]	$\dot{m}_{cond}$	0.85	[kg/s]

shows that $\dot{Q}_{cond,lin}$ is a good approximation of $\dot{Q}_{cond}$ but $P_{comp,lin}$ shows a less linear behaviour. This results in a slight underestimation of $\dot{Q}_{eva}$ but a good estimation of the COP.

The following experiment is carried out: the borefield is initialised by assuming a uniform ground temperature of 15 °C and then operating the pump and the heat pump at nominal mass flow rate for 17.4 days. The borefield cools down to around 8.7°C. The mass flow rate is then changed to a different fixed value (see fig. 8.5). Once the heat pump has generated 200 kWh of thermal energy, the COPs are reported. The reason for this approach is to allow objective comparison of a transient system. The analytical solution is obtained by using the same parameter values and a borehole wall temperature of 8.7 °C.

Figure 8.5 compares the results from the simulation model (blue dashed line) and the analytical model (red dotted line) for different mass flow rates. Figure 8.5 (a) and (b) are expressed as a function of the system mass flow rate $\dot{m}_{bf}$ while fig. 8.5 (c) and (d) correspond to a single heat pump. Figure 8.5 (a) shows that the analytical model underestimates the HCF temperatures. This is caused by the assumption that the HCF exchanges heat with the borefield at $T_{eva,in}$ instead of using an exponential HCF temperature variation [90]. The error gets amplified by the decrease of $\dot{Q}_{cond}$, $\dot{Q}_{eva}$ and P_{comp} for smaller T_m resulting in an underestimation of COP_1 (see fig. 8.5 (b),(c),(d)). Despite this underestimation, the optimal mass flow rate obtained by the analytical solution (7.38 kg/s) is close to the optimal mass flow rate obtained from the simulation (7.03 kg/s). The optimal mass flow rate is close to (but lower than) the maximum mass flow rate for which heat pump performance data is provided.

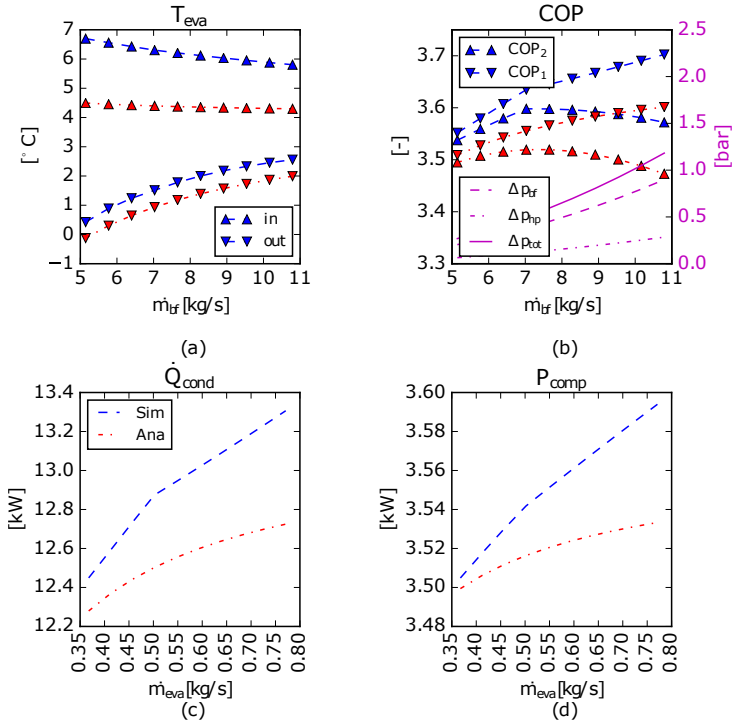

Figure 8.5: Results comparison between analytical model (dotted red) and simulation (dashed blue) model: (a) in and outlet evaporator HCF temperatures; (b) (left axis) heat pump COP_1 and system COP_2, (right axis) head losses; (c) condenser thermal power; (d) compressor electrical power.

It should be noted that the optimal COP_2 is generally found at lower flow rate as illustrated by Southard et al. [137] where the GSHP COP_2 was increased by 18% when the differential pressure set point on the ground loop was reduced from 1.4 to 0.6 bar. The fact that the optimal flow rate for the validation exercise is rather high is explained by its assumptions: i) the heat pumps operate at full load, ii) a relatively small head loss of the ground heat exchanger was used. Running the heat pumps at part load would lead to a lower optimal flow rate as the relative influence of the pumping energy on the COP_2 increases. Other assumptions for the validation are i) constant $T_{\text{cond,in}} = 21.11$ °C, and ii) a cubic relation between pumping power and mass flow rate is assumed.

Further work should experimentally validate the proposed analytical solution for different heat pump load ratio's and different GSHP systems and it should

confirm that the optimal flow rate of a GSHP system depends on the heat pump load, the ground temperature, and borefield and heat pump characteristics. Notice that eq. (6.13) needs to be re-computed for each heat pump part load ratio as the heat pump characteristics change accordingly. The optimal mass flows can then be derived for each part load ratio.

8.5 Conclusion

This study shows that there exists an optimal heat carrier fluid flow rate for GSHP systems that maximizes its total energy (including pumping power) performance. The study proposes an analytical solution for computing the optimal flow rate as a function of measurable variables and system parameters and data that can be obtained from manufacturer data sheets. The optimal solution is based on a steady-state approximation of the borehole and a linear approximation of the thermal and electrical power of the heat pump as a function of the average evaporator temperature. It was found that expressing the heat pump powers and COP as a function of the average evaporator temperature instead of its inlet temperature reduces their mass flow rate dependencies. The obtained analytical solution shows good agreement with the optimal solution obtained by a detailed simulation model representing an existing GSHP system of 99 x 30 m boreholes.

Chapter 9

MPC performance for hybrid GEOTABS buildings

Based on the emulator models of the office building, the school, the retirement home and the block of flats developed in chapter 5 and using the MPC toolchain as described in chapter 6, this chapter investigates the performance of hybrid *GEOTABS* systems in the different buildings when controlled by a current practice rule-based-controller (RBC) and it compares this performance to the performance achieved by Model Predictive Controllers (MPC) which optimize both the heat flow rates to the TABS and to the supplementary systems, and the supply ventilation temperature.

The structure of this chapter is as follows: firstly, section 9.1 gives an overview of current research about GEOTABS buildings and their control, and section 9.2 describes the goals of this study and its methodology. Subsequently, section 9.3 compares the different building models and section 9.4 describes the different MPC formulations. Finally, section 9.5 analyses the results and section 9.6 draws the conclusions.

9.1 Introduction

Hybrid *GEOTABS* buildings can be energetically very efficient but they are difficult to control due to the slow reaction of TABS [71, 82, 20, 134, 133] and their potentially conflicting behaviour with the fast reacting emission systems such as ventilation, radiators, etc. [153, 156, 135]. TABS control using a rule-

based-controller (RBC) has been extensively studied in the past. Typically, TABS are kept at a relatively constant temperature close to the lower thermal comfort temperature bound [132, 106]. Its supply temperature should depend on the running mean ambient temperature over several days by using a heating and cooling curve [154, 82, 155]. Direct room temperature feedback results in a poor control performance [105] and slower changing temperatures such as the concrete core temperature [154] should be used instead. Despite the extensive research on TABS control, the potential of *GEOTABS* buildings cannot be fully used by existing RBCs, as they are not able to optimally exploit the thermal storage capacity of TABS or to fully exploit solar and internal gains as well as changes in thermal comfort constraints due to a variable occupancy. Optimal controllers such as Model Predictive Controller (MPC) are therefore particularly suited for such buildings.

The energy use and energy cost saving potential of MPC in buildings has been widely studied and demonstrated, and several companies already propose commercial products [120]. Hilliard et al. (2015) [72] compared in their review paper 19 different case studies where MPC was applied. They concluded that 15 to 30% of the energy used to heat and cool the building could be saved when the building is controlled by MPC instead of a traditional RBC. Hilliard et al. (2015) [72] distinguished several building features for which MPC has a high saving potential: high building inertia (heavy walls and floors) and possibilities for thermal storage, highly predictable loads (internal and solar gains, etc.), broad thermal comfort ranges, slow HVAC systems, and a low infiltration and a high building insulation level. *GEOTABS* buildings are typically characterized by these features.

In the literature, two types of MPC can be distinguished based on the type of HVAC and the type of building: MPC for light buildings with an air-based HVAC system and high cooling load, and MPC for heavy buildings with a water based HVAC system (e.g. *GEOTABS* building). The former MPC focuses on saving energy by running the cooling machines at their optimal working points by optimizing the supply air temperature and mass flow rates to the machines and to the zones. The MPC also saves cost by exploiting variable electricity prices and by shaving peak loads. The building controller model is typically very simplified and obtained by black or grey-box system identification and the MPC formulation is often non-linear. Due to the low mass content of the building and the fast reaction of the HVAC, optimal load shifting is not done at the building level but rather at a central storage tank level when available. Examples can be found in [15, 96, 124, 64, 22, 23, 5, 172]. The latter MPC type focuses on saving energy and improving thermal comfort by using the inertia of the building optimally. The thermal comfort range and the building inertia are used to shift thermal loads, to maximize the use of *free* energy sources like solar

gains or passive cooling, and to use slow reacting HVAC systems like TABS in an efficient way. The following paragraphs focus on this second type of MPC applied to (hybrid) *GEOTABS* buildings.

The energy use, energy cost and thermal discomfort saving potential of MPC for *GEOTABS* buildings has been investigated both in simulation environments and in real buildings. Sourbron et al. (2013) [136] considered two zones of a typical office building conditioned by a TABS and a ventilation system for which they developed an MPC controlling the TABS supply temperature while the ventilation was controlled by RBC. The MPC controller model was a second order resistive-capacitive model (TRCM) whose parameters had been obtained by grey-box system identification and the building model was developed in TRNSYS. Simulation results showed a savings of 15% of the energy use compared to RBC. Sourbron and Helsen (2013) [135] extended their previous work by adding the ventilation supply temperature as an optimization variable to the MPC while the ventilation on-off flow was prescribed by the hygienic building requirements. The new MPC formulation was still linear and the on-off control of the ventilation was taken into account by using a time dependent matrix coefficient for the ventilation power. Such formulation implies the recomputation of the optimal control problem (OCP) at each time step resulting in a large computation overhead. Furthermore, due to a poor model match between the controller and the building model, the resulting TABS and ventilation MPC control performed worse than the RBC. Oldewurtel et al. (2012) [104] and Gyalistras and Gwerder (2009) [66] investigated the MPC saving potential for office buildings by simulating different variants of a 12^{th} order RC white-box model (different orientations, construction types, building standards, window area fractions, internal gains levels, HVAC systems and climates were considered). The MPC optimized the blinds, the ventilation, the TABS and the supplementary emission system. They found that for about 50% of the investigated building variants, MPC could save more than 40% of the non-renewable energy use. These high energy savings are an over-estimation of the real possible savings as the controller and the building models were identical (no model mismatch and perfect disturbance prediction) and they were relatively simplified. Sturzenegger et al. (2013) [140] used a similar white-box controller model to control the HVAC of a real office building of 6000 m^2 floor area. Experiments showed that the implemented MPC could save 17% of the energy use. The MPC optimization variables were the heating and cooling powers of the TABS, the solar transmission through the windows (blinds), the air flow through the recovery wheel or through its by-pass, and the flow through the ventilation heating and cooling coils. The resulting OCP was bi-linear in both its inputs and its states. Váňa et al. (2014) [157] developed an MPC controlling the TABS of a 3000 m^2 real building. Experiments during the winter season showed energy savings of 17%. The controller model was an 8^{th} order model representing

three thermal zones (one per floor) and its parameters were obtained by means of system identification. As the controller model had been identified using only winter measurement data, the MPC was only used for the heating season. Prívara et al. (2011) [118] also proposed an MPC to control the TABS power of a large university building during the heating season. The controller model was obtained by subspace black-box model identification and savings between 17 and 24% were found.

To the author's best knowledge, no previous study has investigated the savings potential of MPC for different types of hybrid *GEOTABS* building and building occupancy while optimizing the TABS, the ventilation and the supplementary systems for heating and cooling simultaneously. All studies mentioned in the previous paragraphs were for office buildings. This chapter demonstrates that *GEOTABS* concepts can be successfully used to condition an office, a retirement home, a school or a block of flats when proper control is used to control the TABS. The study is carried out on simulation models based on four existing Belgian buildings (see chapter 5). This chapter further investigates the energy use, energy cost and thermal discomfort savings obtainable by MPC for each of the four buildings. Different linear MPC formulations are developed which are able to simulaneously optimize the TABS heating and cooling powers, the supply ventilation temperature (while the on-off ventilation flow is defined by the hygienic building requirements), and the thermal powers of the supplementary systems (radiators, fan coil units) while taking into account the operating cost of the different heat and cold production machines (gas boiler, heat pump, ...). Very accurate controller models for MPC are obtained by automatically linearising the building emulator models (see chapter 6) which ensures good control performance thanks to the low model mismatch (see chapter 7). The study further quantifies the extra savings obtainable when not only the TABS but also the ventilation and the supplementary systems are optimized. Finally, control patterns usable to improve RBC algorithms are retrieved from the optimal MPC results for both TABS and ventilation.

9.2 Goals and Methodology

This chapter has four goals: i) to assess the feasibility and performance of (hybrid) *GEOTABS* systems in terms of thermal comfort, energy use and energy cost for different types of building and occupancy, ii) to assess the performance improvements that MPCs can achieve compared to current practice RBCs, iii) to compare the results obtained when only the TABS are optimally controlled with the results when the TABS, the ventilation and (optionally) the supplementary emission system are optimally controlled, and iv) to search for patterns in the

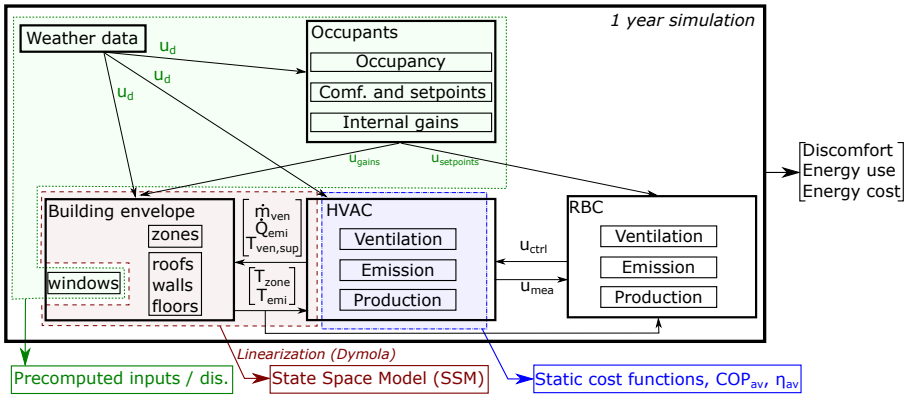

Figure 9.1: Graphical representation of the methodology used to evaluate the performance of the RBC and compute the MPC controller model (SSM), MPC disturbances (dis) and MPC cost function factors.

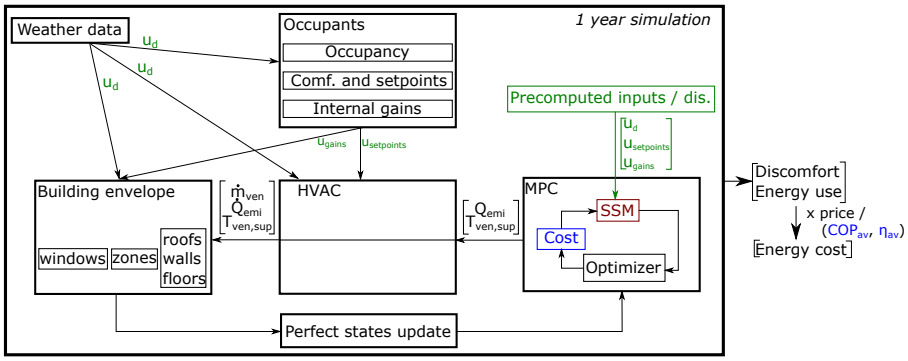

Figure 9.2: Graphical representation of the methodology used to evaluate the performance of the MPC.

optimal control achieved by MPCs that could be used to improve conventional RBCs.

This study is based on the four detailed simulation models (the emulators) presented in chapter 5 and the toolchain developed in chapter 6 is used. For clarity reason, the methodology is here again illustrated in figs. 9.1 and 9.2 specifically applied to this study. Each building model with its RBC is firstly simulated for a full year using typical Belgian weather data [98] and the thermal discomfort, the energy use and the energy cost are evaluated (see fig. 9.1).

Thermal discomfort is expressed as the number of hours during which the operative zone temperatures are lower (resp. higher) than ±0.5K the lower (resp. upper) thermal comfort bound defined by the occupancy model. In order to facilitate the comparison between different buildings which have each a different number of zones, the average thermal discomfort over the zones will be further used (i.e. the sum of the absolute value of discomfort of each zone divided by the number of zones), except where specified differently. The energy use is expressed in kilo-Watt-hour per year per square meter floor area (kWh/y/m^2) and it corresponds to the energy delivered to the emission systems. The energy to the emission systems is used instead of the energy used by the production machines in order to limit the influence of the production machine sub-controllers on the results. Finally, the energy costs are computed using the variable efficiencies of the heat pump and the gas boiler and using the average electricity (P_{el}) and gas (P_{gas}) price of 2015 for Belgian buildings with an energy use between 20 and 500 MWh/year: 0.1466 €/kWh for electricity (computed as energy supply (0.0575 €/kWh) + network (0.0656 €/kWh) + taxes and levies (0.0235 €/kWh)) and 0.0464 €/kWh for gas [47, 46]. A fixed energy prices is chosen as large buildings rarely use a day/night tariff.

The simulation results are then used to generate the MPC precomputed inputs (see green texts and frames in figs. 9.1 and 9.2): the (weather) disturbances u_d including the solar radiation through each window, the internal gains u_{gains}, and the setpoints $u_{\text{setpoints}}$ for thermal comfort, ventilation, ... The yearly average heat pump coefficient of performance (COP_{av}) and gas boiler efficiency (η_{av}) are further computed to be used by the MPC cost function (see blue parts in Fig. 9.1 and 9.2). Using average efficiencies is necessary to keep the MPC formulation linear and the suboptimality it introduces is limited as the efficiencies only slightly vary during the year. The MPC building controller model is obtained by linearising the building envelope into a linear time-invariant state space model (SSM) using the methodology described in section 6.1 (see red parts in figs. 9.1 and 9.2 and see section 9.4.1).

Figure 9.2 shows the MPC framework: the same building model is used as the one used for the RBC simulations except that the RBC is replaced by an MPC and that the HVAC system, which in the case of RBC simulations is composed of hydraulic components (pumps, fans, pipes and valves), production components (heat pumps, heat exchangers, gas boilers) and emission components (water circuits for TABS, radiators, fan coil units, ventilation) (see chapter 5), is here idealized. The MPC simulations assume thus perfect sub-controllers which convert the optimal emission thermal powers and ventilation supply temperature into mass flow rates and water supply temperatures for the different HVAC components such that the optimal control values are respected. The MPC is composed of the linear SSM obtained by linearisation for its controller model

(see section 6.1), of a linear cost function and linear constraints corresponding to the same system constraints as in the RBC simulations (see Section 9.4.2), and of an optimizer (see Section 9.4.3). The annual thermal discomfort and energy use are computed in the same way as for the RBC simulation. The energy costs are computed from the energy use using COP_{av} and η_{av} as using the time varying efficiencies would lead to a non-linear MPC. In this study the linearity of MPC is kept in order to use efficient solvers capable of solving large optimization problems in tractable computational time (see section 6.2). This approximation has the draw-back that peak powers (causing lower COP for GSHP) will not be penalized by the optimization. However, as the borefield of the building is generally oversized, the COP variation is expected to remain limited ($< 1\%$ for short time scales and $< 5\%$ for seasonal time scales in the RBC simulations, except for the block of flat where the COP ranges from 6 to 4.5). Finally, as the controller model originates from the linearisation of the building model and they therefore have the same states, no states observer needs to be used here. The MPC states can thus be updated at each control step using the virtual measurements from the building model (see section 9.4.3).

For each building, an MPC mimizing the energy cost of the TABS and ensuring thermal comfort is set up (further referred as `MPC:T`). In that case, the ventilation is controlled by the same controller as in the RBC case. For all buildings with a ventilation with heating and a cooling coil (all buildings except the block of flats), a second MPC is developed which also optimizes the ventilation supply temperature (`MPC:T+V`). Finally, for the case of the retirement home which also has radiators, an MPC optimizing the TABS and the radiators (`MPC:T+R`) and an MPC optimizing the TABS, the ventilation and the radiators (`MPC:T+V+R`) are set up. For both `MPC:T` and `MPC:T+V` of the retirement home, the radiator powers are kept equal to zero. Based on a comparative analysis of these different MPCs, the necessity or benefits of actively using the heating and cooling power of the ventilation system together with the TABS is investigated. The retirement home `MPC:T+R` and `MPC:T+V+R` further allow assessing the benefits of an additional supplementary (fast reacting) system in a hybrid *GEOTABS* building.

It should be stressed that as the MPC controller models are obtained by linearisation of the building emulator models, as no measurements, weather and heat gains prediction errors are considered, as perfect states update is used and as ideal subcontrollers are assumed, the saving potential found for the MPCs are upper bounds for more realistic cases. The results, however, are very instructive about the physical capabilities and constraints of (hybrid) *GEOTABS* buildings when controlled by optimal controllers. The study allows the isolation of the physical limitations of the building from their limitations due to non-optimal control. Furthermore, the fact that the controller models are an accurate representation of the building models which are themselves

modelled using a detailed BES tool, avoids the sub-optimality that many MPCs encounter due to their simplified controller model and this, without simplifying the building emulator model used for the performance evaluation.

9.3 Building description

In this chapter, four existing Belgian hybrid *GEOTABS* buildings are considered as described in chapter 5: a school (S), an office building (O), a retirement home (R) and a block of flats (F). This section briefly repeats the most important features of the different buildings and compares them to help the reader to understand their main differences.

Table 9.1 gives an overview of the general building parameters. As table 9.1 illustrates, all buildings have a high insulation level(low average U-value), a limited window-to-wall ratio and a good air tightness (see air-change-per-hour (ACH)). The office building is further equipped with solar blinds which automatically shade the windows when the solar radiation on a horizontal plane exceeds 150 W/m^2. The school is composed of two parts: an old existing building and a newly built part. Figure 9.3 shows the hydraulic scheme of each building. All these buildings use TABS and all (except the block of flats) have a ventilation system composed of a heat recovery wheel with by-pass, a heating and cooling coil, a supply and an extraction fan. The ventilation system creates a constant air flow prescribed by the design hygienic requirements during the occupancy periods (see fig. 9.4). The ventilation system of the block of flats is composed of an extraction fan, window slits and it is on/off controlled according to the occupancy. The RBC of each building is similar: based on the 7-days (or 3-days in the case of the office building) running mean average ambient temperature, the HVAC is in *heating*, *neutral*, or *cooling mode*. During the *neutral* mode, the TABS are not used. The water supply temperature changes according to a heating/cooling curve tuned for the specific building. For the office building, the water is circulated in the TABS at the start of each hour for 10 minutes after which the temperature difference between the supply and the return is measured. Depending on the value, water is recirculated for a given amount of time. For the other buildings, a PI-controller keeps the TABS return temperature equal to the thermal comfort lower / upper temperature plus / minus an offset for respectively the heating and cooling modes. For all buildings with a conditioned ventilation, the by-pass, and the heating and the cooling coils are controlled by PI-controllers such that the supply air temperature equals the lower thermal comfort temperature. The different production machines and circulation pumps are also controlled by PI-controllers or on/off.

Table 9.1: General buildings parameters (repeated from chapter 5).

	Floor Area [m^2]	Window to wall [-]	U-value [$W/(m^2.K)$]	ACH (n50) [1/h]
Office	3760	34%	0.22	0.9
School	1800	19.4%	0.49	1 (2.5)*
Elderly home	10135	36%	0.51	1
Block of flats	818	18.4%	0.36	2

* The value between brackets is for the old part of the school.

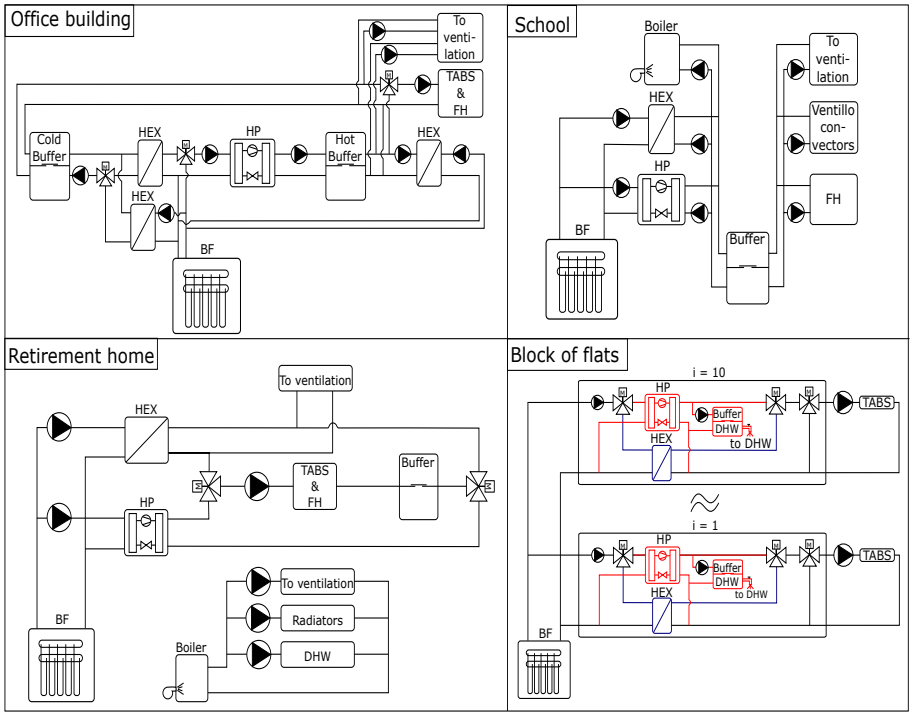

Figure 9.3: Hydraulic scheme of the different buildings. The components are borefields (BF), heat exchangers (HEX), buffers, a heat pump (HP), TABS, floor heating (FH), fan coil units, radiators, domestic hot water (DHW) tap, circulation pumps and threeway valves.

The thermal comfort temperatures, internal gains and ventilation flow rates have a large influence on the total heat and cold consumption of the building. Figure 9.4 shows them for each building for a week in January (the convective and radiative gains are summed in fig. 9.4). Humidity is not modelled and latent gains are therefore not included in the models. For a detailed description per building, see Picard and Helsen (2017) [114]. The thermal comfort range of each building is defined by the standard ISO7730, class B [145] for the heating ([20,24]°C) and the cooling season ([23,26]°C). However, ISO7730 does not specify when the heating and the cooling season start and end. Annex 2 of standard EN15251 [145] is therefore used. According to EN15251 the heating season holds when the running mean ambient temperature T_{rm} is lower than 10°C, and the cooling season when T_{rm} is higher than 15°C. In order to avoid discrete changes, a linear interpolation is used for 10°C$\leq T_{rm} \leq$15°C [132]. When using T_{rm} as defined by EN15251, the thermal comfort range is given by:

$$T_{rm}^{(k)} = \Big(\bar{T}_{e,d}^{(k)} + 0.8\bar{T}_{e,d}^{(k-1)} + 0.6\bar{T}_{e,d}^{(k-2)} + 0.5\bar{T}_{e,d}^{(k-3)} + 0.4\bar{T}_{e,d}^{(k-4)} + 0.3\bar{T}_{e,d}^{(k-5)} + 0.2\bar{T}_{e,d}^{(k-6)}]\Big)/3.8 \tag{9.1}$$

$$[T_{\text{low}}^{(k)}, T_{\text{up}}^{(k)}] = \begin{cases} [20,24]°C & \text{if } T_{rm}^{(k)} < 10°C \\ [23,26]°C & \text{if } T_{rm}^{(k)} > 15°C \\ [20,24]°C + [3,2]\frac{T_{rm}^{(k)}-10}{5} & \text{otherwise} \end{cases} \tag{9.2}$$

with $\bar{T}_{e,d}^{k}$ the average ambient temperature on day k and $T_{\text{low}}^{(k)}$ and $T_{\text{up}}^{(k)}$ the lower and upper comfort temperature bounds. When the building is not occupied, a minimal temperature of 17 °C is kept in order to avoid mold due to condensation.

For the office building, thermal comfort is kept from 7:00AM to 8:00PM during the week and the ventilation is on from 6:00AM to 8:00PM to enable pre-heating of the building. The internal gains profile is taken from the stochastic model of Parys et al. (2011) [109] and the nominal ventilation flow rate from the real building. Figure 9.4 shows that the first occupants arrive around 7:00AM, the last occupants leave before 8:00PM, and the occupancy during lunch time is lower. In the case of the school, thermal comfort is kept from 8:00AM to 4:00PM during the week except during the lunch break from 12:00AM to 1:00PM for the class rooms, on Wednesday afternoon, and during the months of July and August. The internal gains and the ventilation flow rates are taken from Wauman et al. (2015) [163]. Figure 9.4 shows that the internal gains are very high for the class rooms and the teacher rooms. In the case of the retirement home, thermal comfort is kept at all times except for the cafeteria's during the night (11:00PM to 8:00AM). The internal gains and the ventilation flow rates are computed from a detailed description of the appliances in the bedrooms, from

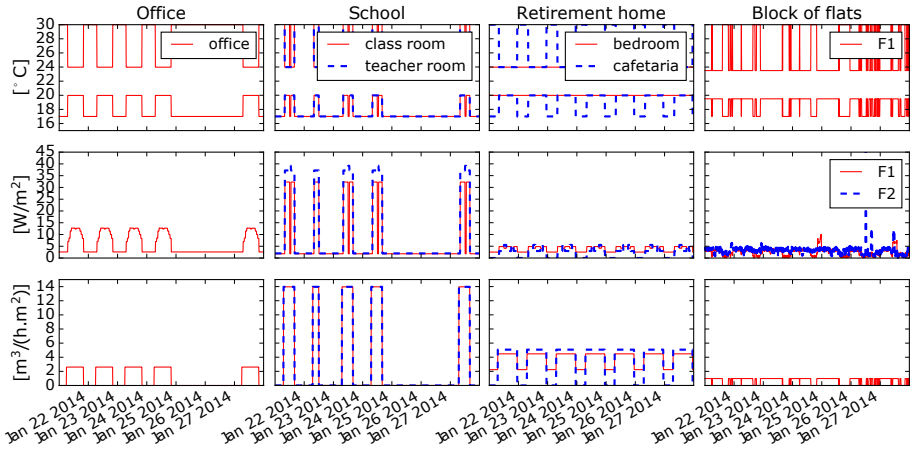

Figure 9.4: Top: thermal comfort ranges, middle: total internal heat gains (convective + radiative) and bottom: ventilation flow rate for a winter week (Tuesday to Monday).

the standard EN13779 [144], and from an assumed schedule of the residents. The EN13779 thermal comfort type IDA1 is used for the bedrooms, type IDA2 for the corridors, and type IDA3 for the cafeteria's. Finally, each flat of the block of flats has its own occupancy and internal gains profile. Each profile is computed using the stochastic model from Baetens and Saelens (2016) [11]. The ventilation is turned on and off based on the occupancy. Figure 9.4 illustrates the case of two different flats (F1 and F2). The internal gains are relatively low but they can have sudden high peak values. The occupancy is also very variable. As clearly illustrated by fig. 9.4, the thermal comfort range, the internal gains and the ventilation flow rates largely vary between the different buildings.

9.4 Model predictive control framework

The building emulator models developed with the Modelica Library `IDEAS` are not well suited for optimization. Even though Modelica is an equation-based language and it can be used directly for gradient-based optimization by using JModelica [1], the complexity of the building models cannot yet be handled by the JModelica compiler. However, gradient based optimization is preferred here over other methods such as *genetic* or *particle swarm* algorithms in order to keep the computation time tractable [166]. In this chapter, only the building envelope is dynamically included in the controller model as its time constants

Table 9.2: Number of states of the SSM of each building.

Bui	O	S	R	F
# states	700	920	941	732

are much larger than those of the HVAC (days/hours compared to minutes) and a linear model is used to enable the use of an efficient solver which ensures a global optimum. As the control time steps of the implemented MPCs vary between 20 to 60 min which is more than twice longer that the longest time constant of the HVAC components and as the constraints of the HVAC system are taken into account by the MPC, it is expected that the HVAC system and its control will be able to reach the set points computed by MPC. However, not including the HVAC system dynamically might conceal unexpected system failures (e.g. oscillatory behaviour of PID controllers for particular reference trackings, etc.) and it also prevents the computation of time-varying efficiencies (e.g. heat pump COP, etc.).

This section describes the controller model (section 9.4.1) and the cost function and the constraints of each MPC (section 9.4.2) as well as the optimization parameters (section 9.4.3).

9.4.1 Controller model

The controller models are obtained automatically from the building emulator models by using the linearisation method described in section 6.2. Figure 9.5a compares the operative temperatures of the linear (controller) and the non-linear (emulator) model of the school building and fig. 9.5b gives the prediction errors on the operative temperature for each zone for an open-loop simulation of 3 days. The simulation includes the same internal gains and ventilation flow rates as for the RBC and MPC simulations. The supply ventilation temperature is kept constant at 22 °C and no TABS or fan coil unit thermal powers are used. The figures show that the SSM approximates the building model very well with errors constrained between $[-0.4, 0.2]$ K for all zones. Similar results are obtained for the other building types. Table 9.2 gives the number of states of the obtained SSMs for each building model.

9.4.2 Cost function and constraints

This section describes the `MPC:T`, `MPC:T+V`, `MPC:T+R`, and `MPC:T+V+R` of the different buildings. The different symbols used in this section are summarized

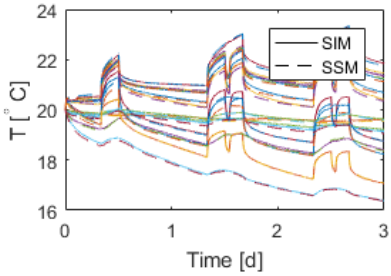

(a) Zone operative temperatures as a function of time for the school simulation model (SIM) and the state space model (SSM).

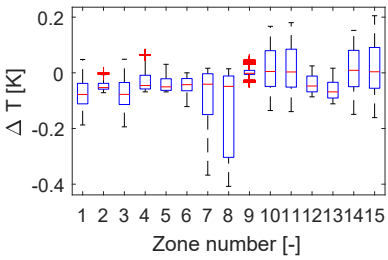

(b) Boxplot of the school zone operative temperature errors made by the SSM compared to the SIM model for each zone for a 3-days open-loop simulation.

Figure 9.5: Controller model open-loop prediction errors for the school.

in table 9.3. Each MPC of each building is characterized by its own specific cost function and constraints. However, due to their similarities, the MPCs share most of their equations. The common equations for the MPCs are summarized in tables 9.4 and 9.5 and the building specific equations are given by tables 9.7 and 9.8. The following paragraphs list the assumptions and approximations made in order to keep the cost function linear and describes each set of equations. For each cost function, an *instantaneous* cost $C_i^{(k)}$ is defined as the thermal power divided by the efficiency of the machine which delivers it and times the energy price. The cost function minimizes then the sum of all *instantaneous* costs of all circuits (with the number of circuits given by N_T, N_R, N_{FCU} with T for TABS, R for radiator and FCU for fan coil unit) for all discrete time steps of the horizon (N_{steps}) times the size of each time step $\Delta_t^{(k)}$. Notice that $\Delta_t^{(k)}$ of different sizes are used within the MPC horizon (see section 9.4.3).

Assumptions and limitations The linear MPC formulation introduces some approximations and assumptions:

1. The different MPCs optimize the heating and cooling powers of each TABS circuit, radiator, and fan coil unit and the unique ventilation supply temperature. It assumes that as long as its power and temperature constraints are respected, the production machines are able to deliver the required power perfectly (see section 9.2). However, despite the fact that all powers computed by MPC are constrained by the subsystem nominal values, this assumption can lead to an overestimation of the

Table 9.3: List of symbols used in section 9.4.2

Roman letter			**Subscripts**	
$\dot{Q}$	thermal power	[W]	T	TABS
T	temperature	[K]	R	radiator
P	energy price	[€/J]	FCU	fan coil unit
$\mathcal{C}$	cost	[€]	V	ventilation
N	number of ...	[-]	H	heating
$\dot{m}$	mass flow rate	[kg/s]	C	cooling
$\mathcal{S}$	slac	[K]	S	supply
c_p	specific heat capacity	[J/(kg.K)]	P	production unit
Greek letter			Z	zone
η	efficiency	[-]	N	night
δ	temperature difference	[K]	DHW	domestic hot water
ϵ	recuperator efficiency	[-]	e	ambient
β	fraction return air	[-]	com	comfort
Δ_t	sampling time	[s]	hp	heat pump
ξ	large positive number	[-]	hex	heat exchanger
μ	small positive number	[-]	boi	boiler
Ξ	ON ($\Xi = 1$) / OFF ($\Xi = 0$)	[-]	el	electricity
Superscripts and accents			gas	gas
(k)	discrete time index		av	average
$\overline{(\cdot)}$	nominal value (upper bound)		steps	steps in MPC horizon
$\underline{(\cdot)}$	lower bound			

MPC performance as several TABS circuits are usually fed by a single circulation pump and they can therefore not be individually controlled in reality.

2. Equations 9.14c and 9.14d takes into account the recovery wheel and the fraction of return ventilation air flow but they do not include the by-pass as the authors could not easily formulate its behaviour by linear equations. The MPCs are therefore not able to use the by-pass. The impact of this approximation is, however, limited as the by-pass is rarely used by `RBC` in the considered simulations.

3. No constraints on simultaneous heating and cooling could be formulated while none of the building HVAC systems are able to simultaneously heat and cool through the TABS and only the retirement home can heat with its radiators and its ventilation while the TABS are cooling. This causes an overestimation of the MPCs capabilities. However, simultaneous active heating and cooling is rarely optimal and the effect of this approximation

Table 9.4: Different cost functions and constraints used in the different MPCs and to be coupled to tables 9.7 and 9.8. Bold style is used for arrays.

	Opt. var.	Cost function and constraints	
TABS	$\begin{bmatrix} \dot{\mathbf{Q}}_{\mathrm{T,H}} \\ \dot{\mathbf{Q}}_{\mathrm{T,C}} \end{bmatrix} =$	$\operatorname{argmin} \sum_{k=0}^{N_{\mathrm{steps}}-1} \sum_{i=1}^{N_{\mathrm{T}}} \mathcal{C}_{\mathrm{T},i}^{(k)}$	(9.3)
	s.t.	$\mathcal{C}_{\mathrm{T},i}^{(k)} = \left[P_{\mathrm{el}} \mathrm{COP}_{av}^{-1} \dot{Q}_{\mathrm{T,H},i}^{(k)} + P_{\mathrm{el}} \mathrm{EER}_{\mathrm{hex}}^{-1} \dot{Q}_{\mathrm{T,C},i}^{(k)} \right] \Delta_t^{(k)}$	(9.4)
		$\overline{\dot{Q}}_{\mathrm{T,H},i}\ ,\ \overline{\dot{Q}}_{\mathrm{T,C},i} \ \geq\ \dot{Q}_{\mathrm{T,H},i}^{(k)}\ ,\ \dot{Q}_{\mathrm{T,C},i}^{(k)} \geq 0$	(9.5)
Radiators	$\left[\dot{\mathbf{Q}}_{\mathrm{R}} \right] =$	$\operatorname{argmin} \sum_{k=0}^{N_{\mathrm{steps}}-1} \mathcal{C}_{\mathrm{R}}^{(k)}$	(9.6)
	s.t.	$\mathcal{C}_{\mathrm{R}}^{(k)} = P_{\mathrm{gas}} \eta_{boi,av}^{-1} \sum_{i=1}^{N_{\mathrm{R}}} \dot{Q}_{\mathrm{R},i}^{(k)} \Delta_t^{(k)}$	(9.7)
		$\overline{\dot{Q}}_{\mathrm{R},i} \geq \dot{Q}_{\mathrm{R},i}^{(k)} \geq 0$	(9.8)
Ven. Con.	$\begin{bmatrix} \dot{\mathbf{Q}}_{\mathrm{FCU,H}} \\ \dot{\mathbf{Q}}_{\mathrm{FCU,C}} \end{bmatrix} =$	$\operatorname{argmin} \sum_{k=0}^{N_{\mathrm{steps}}-1} \sum_{i=1}^{N_{\mathrm{FCU}}} \mathcal{C}_{\mathrm{FCU},i}^{(k)}$	(9.9)
	s.t.	$\mathcal{C}_{\mathrm{FCU},i}^{(k)} = \Big[P_{\mathrm{el}} \mathrm{COP}_{av}^{-1} \dot{Q}_{\mathrm{FCU,H},i}^{(k)} + \dots$ $P_{\mathrm{el}} \mathrm{EER}_{\mathrm{hex}}^{-1} \dot{Q}_{\mathrm{FCU,C},i}^{(k)} \Big] \Delta_t^{(k)}$	(9.10)
		$\overline{\dot{Q}}_{\mathrm{FCU,H},i}\ ,\ \overline{\dot{Q}}_{\mathrm{FCU,C},i} \ \geq\ \dot{Q}_{\mathrm{FCU,H},i}^{(k)}\ ,\ \dot{Q}_{\mathrm{FCU,C},i}^{(k)} \geq 0$	(9.11)

is limited. The approximation error increases when different zones have strong different thermal needs, e.g. cooling for the south zones while the north zones still need heating.

Table 9.5: Continuation of table 9.4. Bold style is used for arrays.

	Opt. var.	Cost function and constraints	
Ventilation (on/off)	$\begin{bmatrix} T_{\mathrm{V,S}} \\ \mathbf{T}_{\mathrm{V,S}} \\ \dot{Q}_{\mathrm{V,S,H}} \\ \dot{Q}_{\mathrm{V,S,C}} \end{bmatrix} =$	$\operatorname{argmin} \sum_{k=0}^{N_{\mathrm{steps}}-1} \mathcal{C}_{\mathrm{V}}^{(k)}$	(9.12)
	s.t.	$\mathcal{C}_{\mathrm{V}}^{(k)} = \Big[P_{\mathrm{P,V,H}}\eta_{\mathrm{P,V,H}}^{-1}\dot{Q}_{\mathrm{V,S,H}}^{(k)} + \cdots P_{\mathrm{el}}\mathrm{EER}_{\mathrm{hex}}^{-1}\dot{Q}_{\mathrm{V,S,C}}^{(k)}\Big]\Delta_t^{(k)}$	(9.13)
	if $\dot{m}_{V,i} = \overline{\dot{m}}_{V,i}$	$\overline{T}_{\mathrm{Z}}^{(k)} + \delta \geq T_{\mathrm{V,S}}^{(k)} \geq \underline{T}_{\mathrm{Z}}^{(k)} - \delta$	(9.14a)
		$T_{\mathrm{V,S},i}^{(k)} = T_{\mathrm{V,S}}^{(k)}$	
		$\dot{Q}_{\mathrm{V,Z},i}^{(k)} = \overline{\dot{m}}_{V,i} c_p \left(T_{\mathrm{V,S},i}^{(k)} - T_{\mathrm{Z},i}^{(k)}\right)$	(9.14b)
		$\dot{Q}_{\mathrm{V,S,H}}^{(k)} = \sum_{i=1}^{N_z} \max\left(0, \overline{\dot{m}}_{V,i} c_p \left(\cdots T_{\mathrm{V,S},i}^{(k)} - \epsilon\beta T_{\mathrm{Z},i}^{(k)} - (1-\epsilon\beta)T_e\right)\right)$	(9.14c)
		$\dot{Q}_{\mathrm{V,S,C}}^{(k)} = \sum_{i=1}^{N_z} \min\left(0, \overline{\dot{m}}_{V,i} c_p \left(\cdots T_{\mathrm{V,S},i}^{(k)} - \epsilon\beta T_{\mathrm{Z},i}^{(k)} - (1-\epsilon\beta)T_e\right)\right)$	(9.14d)
	if $\dot{m}_{V,i} = 0$	$\left\{ \dot{Q}_{\mathrm{V,Z},i}^{(k)}\ ,\ \dot{Q}_{\mathrm{V,S},i}^{(k)} \right\} = 0$	(9.15)
Comfort	$\left[\ \mathbf{S}_{\mathrm{com}}\ \right] =$	$\operatorname{argmin} \sum_{k=0}^{N_{\mathrm{steps}}-1} \sum_{i=1}^{N_{\mathrm{Z}}} \mathcal{S}_{\mathrm{com,i}}^{(k)} \Delta_t^{(k)}$	(9.16)
	s.t.	$\overline{T}_{\mathrm{Z}}^{(k)} + \mathcal{S}_{\mathrm{com,i}}^{(k)} \geq T_{\mathrm{Z},i}^{(k)} \geq \underline{T}_{\mathrm{Z}}^{(k)} - \mathcal{S}_{\mathrm{com,i}}^{(k)}$	(9.17)

TABS, radiators and fan coil units The TABS optimization is described by eqs. (9.3) to (9.5). The optimization variables are the TABS heating ($\dot{Q}^{(k)}_{\mathrm{T,H},i}$) and cooling ($\dot{Q}^{(k)}_{\mathrm{T,C},i}$) power of each circuit i, for each discrete time (k) of the MPC horizon. Equation (9.4) assumes that the TABS are fed by the heat pump and the HEX with efficiencies equal to $\mathrm{COP}_{\mathrm{av}}$ and energy efficiency ratio $\mathrm{EER}_{\mathrm{hex}}$. Each TABS power is constrained by its nominal value (temperature difference between its in- and outlet of 5 K at nominal flow rate). The radiators and the fan coil units are optimized in a similar way (see eqs. (9.6) to (9.8) and eqs. (9.9) to (9.11)) but for the radiator heat is produced by the gas boiler instead of the heat pump (eq. (9.7)) as foreseen in the real building.

Ventilation The optimal operation of the ventilation system with heating and cooling coil is described by eqs. (9.14a) to (9.15) The optimization variables are the unique supply ventilation temperature $T_{\mathrm{V,S}}$ for all zones and the heating ($\dot{Q}^{(k)}_{\mathrm{V,S,H}}$) and cooling ($\dot{Q}^{(k)}_{\mathrm{V,S,C}}$) powers used by the coils necessary to obtain $T_{\mathrm{V,S}}$, while the cost function minimizes the cost related to these thermal powers. Equation (9.13) assumes that the ventilation is fed by the HEX for cooling and by a heat source with energy price and efficiency $P_{\mathrm{P,V,H}}\eta^{-1}_{\mathrm{P,V,H}}$ for heating. The type of heat source is defined for each building in tables 9.7 and 9.8. $\dot{Q}^{(k)}_{\mathrm{V,S,H}}$, $\dot{Q}^{(k)}_{\mathrm{V,S,C}}$ and the ventilation thermal power to each zone i ($\dot{Q}^{(k)}_{\mathrm{V,Z},i}$) are computed using eqs. (9.14a) to (9.14d) when the ventilation is ON and by eq. (9.15) when the ventilation is OFF. Equation (9.14a) ensures that the supply temperature is the same for all zones and that $T_{\mathrm{V,S}}$ stays within the lower and upper bounds of the thermal comfort zone temperature ($\underline{T}^{(k)}_{\mathrm{Z}}, \overline{T}^{(k)}_{\mathrm{Z}}$) with a maximum deviation of $\delta = 1$ K to avoid thermal discomfort caused by too cold or too warm air flows. Equations (9.14c) and (9.14d) compute $\dot{Q}^{(k)}_{\mathrm{V,S,H}}$, $\dot{Q}^{(k)}_{\mathrm{V,S,C}}$ by taking the heat recovery efficiency $\epsilon = 70\%$ and the fraction of return ventilation air flow $\beta = 95\%$ into account. $\overline{\dot{m}}_{V,i}$ and c_p stand for the nominal ventilation air flow rate for zone i and the specific heat capacity of air, respectively. Finally, eq. (9.14b) computes $\dot{Q}^{(k)}_{\mathrm{V,Z},i}$ for each zone.

The ON-OFF behaviour of the ventilation system can be modelled without losing the linearity of the cost function by introducing extra optimization variables and constraints. Firstly, $\dot{Q}^{(k)}_{\mathrm{V,Z},i}$ is forced to zero when the ventilation is OFF by

replacing eq. (9.14b) by:

$$\dot{Q}^{(k)}_{\mathrm{V,Z},i} = \overline{\dot{m}}_{V,i} c_p \left(T^{(k)}_{\mathrm{V,S},i} - T^{(k)}_{\mathrm{Z},i} \right) \tag{9.18}$$

$$\Xi^{(k)}\ \xi - \dot{Q}^{(k)}_{\mathrm{V,Z},i} + \mu_1 \geq 0 \tag{9.19}$$

$$\Xi^{(k)}\ \xi + \dot{Q}^{(k)}_{\mathrm{V,Z},i} + \mu_1 \geq 0 \tag{9.20}$$

with $\Xi^{(k)} = 1$ when the ventilation is ON and $\Xi^{(k)} = 0$ when the ventilation is OFF. Notice that $\Xi^{(k)}$ is defined by the ventilation schedule, it is thus not optimized but imposed. ξ is a large number and μ_1 is a small positive number which relaxes the constraint for numerical robustness. Secondly, the minimum and maximum functions of eqs. (9.14c) and (9.14d) are replaced by eqs. (9.21) and (9.22). Notice that $\dot{Q}^{(k)}_{\mathrm{V,S,H}}$ and $\dot{Q}^{(k)}_{\mathrm{V,S,C}}$ are new optimization variables and that eqs. (9.21) and (9.22) can be used because $\dot{Q}^{(k)}_{\mathrm{V,S,H}}$ and $\dot{Q}^{(k)}_{\mathrm{V,S,C}}$ are minimized by eq. (9.13).

$$\dot{Q}^{(k)}_{\mathrm{V,S,H}} - \dot{Q}^{(k)}_{\mathrm{V,S},i} \geq 0 \quad , \quad \dot{Q}^{(k)}_{\mathrm{V,S,H}} \geq 0 \tag{9.21}$$

$$\dot{Q}^{(k)}_{\mathrm{V,S,C}} + \dot{Q}^{(k)}_{\mathrm{V,S},i} \geq 0 \quad , \quad \dot{Q}^{(k)}_{\mathrm{V,S,C}} \geq 0 \tag{9.22}$$

Finally, one fictive ventilation supply temperature $T^{(k)}_{\mathrm{V,S},i}$ is introduced per zone. When the ventilation is ON, all $T^{(k)}_{\mathrm{V,S},i}$ must be equal to $T^{(k)}_{\mathrm{V,S}}$ and when the ventilation is OFF, each $T^{(k)}_{\mathrm{V,S},i}$ must be equal to $T^{(k)}_{\mathrm{Z},i}$ such that eqs. (9.19) and (9.20) hold. The former is ensured by eqs. (9.23) and (9.24) while the latter is already implicitly ensured by eq. (9.18) to (9.20).

$$\left(1 - \Xi^{(k)}\right) \xi - \left(T^{(k)}_{\mathrm{V,S},i} - T^{(k)}_{\mathrm{V,S}} \right) + \mu_2 \geq 0 \tag{9.23}$$

$$\left(1 - \Xi^{(k)}\right) \xi + \left(T^{(k)}_{\mathrm{V,S},i} - T^{(k)}_{\mathrm{V,S}} \right) + \mu_2 \geq 0 \tag{9.24}$$

with μ_2 a small number to relax the constraint for numerical stability.

By using eq. (9.18) to (9.24) instead of eqs. (9.14c), (9.14d), and (9.15), the cost function remains linear and the on-off control of the ventilation system is included without approximation.

Thermal comfort The thermal comfort is treated as a soft constraint (see eqs. (9.16) to (9.17)) where $\mathcal{S}^{(k)}_{\mathrm{com,i}}$ is a slack variable and N_Z is the number of zones with thermal comfort constraints.

Table 9.6: Average COPs ($\mathrm{COP_{av}}$) and average boiler efficiencies (η_{av}) used for the MPC cost functions.

	Office	School	Retirement home	Block of flats
$\mathrm{COP_{av}}$	6.46	5.74	6.3	5.06
η_{av}	-	1.09	0.98	-

Building specific equations Tables 9.7 and 9.8 specify all equations of the most complex MPC of each building and table 9.6 lists the average COP and the average boiler efficiencies as obtained by the RBC simulation and used by the MPC cost functions. The simpler MPCs can easily be obtained by removing the obsolete equations. The extra optimization variables and constraints introduced to model the ON-OFF behaviour of the ventilation system are not repeated here, but are included in each MPC case that contains a controllable ventilation system.

For the **office building** the most complex MPC (`MPC:T+V`) optimizes both TABS and ventilation. The ventilation heat is produced by the HP (see eq. (9.25)) and the total thermal production power is constrained by the HP ($\overline{\dot{Q}}_{\mathrm{hp}}^{(k)}$) and the passive heat exchanger ($\overline{\dot{Q}}_{\mathrm{hex}}^{(k)}$) nominal powers (eqs. (9.26) and (9.27)).

For the **retirement home**, the most complex MPC (`MPC:T+V+R`) optimizes TABS, ventilation and radiators. The ventilation heat is produced by the gas boiler (eq. (9.36)). The gas boiler nominal power ($\overline{\dot{Q}}_{\mathrm{boi}}^{(k)}$) further constraints the domestic hot water power $\overline{\dot{Q}}_{\mathrm{DHW}}^{(k)}$, the ventilation and the radiator heating powers (see eq. (9.37)). The TABS heat powers are constrained by $\overline{\dot{Q}}_{\mathrm{hp}}^{(k)}$ and the ventilation and TABS cooling powers are constrained by $\overline{\dot{Q}}_{\mathrm{hex}}^{(k)}$ (see eqs. (9.36) to (9.38)). The ventilation of the retirement home has further a day and a night mode with different mass flow rates which is taken into account by eqs. (9.33) to (9.35d). Notice the subscript N referring to *night* and that eqs. (9.33) to (9.35d) must be coupled to similar equations as eqs. (9.19), (9.20), (9.23) and (9.24). $\Xi^{(k)}$ is then 1 during the day and 0 during the night and a new variable $\Xi_N^{(k)} = 1 - \Xi^{(k)}$ can be defined.

For the **school**, the most complex MPC (`MPC:T+V`) optimizes TABS, ventilation and fan coil units. Notice that the zones with fan coil units do not have TABS. Therefore, no MPC where TABS are optimized while fan coil units are controlled by RBC are considered. For simplicity reason, the MPC for which TABS and

Table 9.7: Building specific additional cost functions and constraints for the office building, the school, and the block of flats.

	Opt. var.	Cost function and constraints
Office MPC:T+V	See eqs. 9.3, 9.12 & 9.16	See eqs. 9.3–9.5, 9.12–9.15, & 9.16–9.17
	s.t.	$P_{\mathrm{P,V,H}}\eta_{\mathrm{P,V,H}}^{-1} = P_{\mathrm{el}}\mathrm{COP}_{av}^{-1}$ (9.25)
		$\overline{\dot{Q}}_{\mathrm{hp}}^{(k)} \geq \dot{Q}_{\mathrm{V,S,H}}^{(k)} + \sum_{i=1}^{N_{\mathrm{Z}}} \dot{Q}_{\mathrm{T,H},i}^{(k)}$ (9.26)
		$\overline{\dot{Q}}_{\mathrm{hex}}^{(k)} \geq \dot{Q}_{\mathrm{V,S,C}}^{(k)} + \sum_{i=1}^{N_{\mathrm{Z}}} \dot{Q}_{\mathrm{T,C},i}^{(k)}$ (9.27)
School MPC:T+V	See eqs. 9.3, 9.9, 9.12, & 9.16	See eqs. 9.3–9.5, 9.9–9.11, 9.12–9.15, & 9.16–9.17 but eqs. 9.3, 9.9 & 9.12 are here replaced by eq. 9.28
	$\begin{bmatrix} \dot{Q}_{\mathrm{hp}} \\ \dot{Q}_{\mathrm{boi}} \end{bmatrix} =$	$\operatorname{argmin} \sum_{k=0}^{N_{\mathrm{steps}}-1} [P_{\mathrm{el}}\mathrm{COP}_{av}^{-1}\dot{Q}_{\mathrm{hp}}^{(k)} + \ldots P_{\mathrm{gas}}\eta_{boi,av}^{-1}\dot{Q}_{\mathrm{boi}}^{(k)}] \Delta_t^{(k)}$ (9.28)
	s.t.	$P_{\mathrm{P,V,H}}\eta_{\mathrm{P,V,H}}^{-1} = P_{\mathrm{el}}\mathrm{COP}_{av}^{-1}$ (9.29)
		$\overline{\dot{Q}}_{\mathrm{hp}}^{(k)} \geq \dot{Q}_{\mathrm{hp}}^{(k)} \quad \& \quad \overline{\dot{Q}}_{\mathrm{boi}}^{(k)} \geq \dot{Q}_{\mathrm{boi}}^{(k)}$ (9.30)
		$\dot{Q}_{\mathrm{hp}}^{(k)} + \dot{Q}_{\mathrm{boi}}^{(k)} \geq \dot{Q}_{\mathrm{V,S,H}}^{(k)} + \ldots \sum_{i=1}^{N_{\mathrm{T}}} \dot{Q}_{\mathrm{T,H},i}^{(k)} + \sum_{i=1}^{N_{\mathrm{FCU}}} \dot{Q}_{\mathrm{FCU,H},i}^{(k)}$ (9.31)
		$\overline{\dot{Q}}_{\mathrm{hex}}^{(k)} \geq \dot{Q}_{\mathrm{V,S,C}}^{(k)} + \sum_{i=1}^{N_{\mathrm{T}}} \dot{Q}_{\mathrm{T,C},i}^{(k)} + \sum_{i=1}^{N_{\mathrm{FCU}}} \dot{Q}_{\mathrm{FCU,C},i}^{(k)}$ (9.32)
Flats MPC:T	See eqs. 9.3,9.16	See eqs. 9.3–9.5, 9.16–9.17.

Table 9.8: Continuation of table 9.7 for the retirement home.

	Opt. var.	Cost function and constraints
Retirement home (`MPC:T+V+R`)	See eqs. 9.3, 9.6, 9.12, 9.16	See eqs. 9.3–9.5, 9.6–9.8, 9.12–9.15, and 9.16–9.17

$$\begin{bmatrix} T_{\mathrm{V,S,N}} \\ \mathbf{T}_{\mathrm{V,S,N}} \\ \dot{Q}_{\mathrm{V,S,H,N}} \\ \dot{Q}_{\mathrm{V,S,C,N}} \end{bmatrix} = \operatorname{argmin} \sum_{k=0}^{N_{\mathrm{steps}}-1} \mathcal{C}_{\mathrm{V,N}}^{(k)} \tag{9.33}$$

$$s.t. \qquad \mathcal{C}_{\mathrm{V,N}}^{(k)} = \left[P_{\mathrm{gas}} \eta_{boi,av}^{-1} \dot{Q}_{\mathrm{V,S,H,N}}^{(k)} + P_{\mathrm{el}} \mathrm{EER}_{\mathrm{hex}}^{-1} \dot{Q}_{\mathrm{V,S,C,N}}^{(k)} \right] \Delta_t^{(k)} \tag{9.34}$$

if $\dot{m}_{V,i} = \overline{\dot{m}}_{V,N,i}$

$$\overline{T}_{\mathrm{Z}}^{(k)} + \delta \geq T_{\mathrm{V,S,N}}^{(k)} \geq \underline{T}_{\mathrm{Z}}^{(k)} - \delta \tag{9.35a}$$

$$T_{\mathrm{V,S,N},i}^{(k)} = T_{\mathrm{V,S,N}}^{(k)}$$

$$\dot{Q}_{\mathrm{V,Z,N},i}^{(k)} = \overline{\dot{m}}_{V,N,i} c_p \left(T_{\mathrm{V,S,N},i}^{(k)} - T_{\mathrm{Z},i}^{(k)} \right) \tag{9.35b}$$

$$\dot{Q}_{\mathrm{V,S,H,N}}^{(k)} = \sum_{i=1}^{N_z} \max \left(0, \overline{\dot{m}}_{V,N,i} c_p \left(\cdots \right. \right. \tag{9.35c}$$

$$\left. \left. T_{\mathrm{V,S,N},i}^{(k)} - \epsilon\beta T_{\mathrm{Z},i}^{(k)} - (1-\epsilon\beta) T_e \right) \right)$$

$$\dot{Q}_{\mathrm{V,S,C,N}}^{(k)} = \sum_{i=1}^{N_z} \min \left(0, \overline{\dot{m}}_{V,N,i} c_p \left(\cdots \right. \right. \tag{9.35d}$$

$$\left. \left. T_{\mathrm{V,S,N},i}^{(k)} - \epsilon\beta T_{\mathrm{Z},i}^{(k)} - (1-\epsilon\beta) T_e \right) \right)$$

$$P_{\mathrm{P,V,H}} \eta_{\mathrm{P,V,H}}^{-1} = P_{\mathrm{gas}} \eta_{boi,av}^{-1} \quad , \quad \overline{\dot{Q}}_{\mathrm{hp}}^{(k)} \geq \sum_{i=1}^{N_{\mathrm{T}}} \dot{Q}_{\mathrm{T,H},i}^{(k)} \tag{9.36}$$

$$\overline{\dot{Q}}_{\mathrm{boi}}^{(k)} - \overline{\dot{Q}}_{\mathrm{DHW}}^{(k)} \geq \dot{Q}_{\mathrm{V,S,H}}^{(k)} + \dot{Q}_{\mathrm{V,S,H,N}}^{(k)} + \sum_{i=1}^{N_{\mathrm{R}}} \dot{Q}_{\mathrm{R},i}^{(k)} \tag{9.37}$$

$$\overline{\dot{Q}}_{\mathrm{hex}}^{(k)} \geq \dot{Q}_{\mathrm{V,S,C}}^{(k)} + \dot{Q}_{\mathrm{V,S,C,N}}^{(k)} + \sum_{i=1}^{N_{\mathrm{Z}}} \dot{Q}_{\mathrm{T,C},i}^{(k)} \tag{9.38}$$

fan coil units are optimized is called `MPC:T` and `MPC:T+V` is used when the ventilation is also optimized. The cost function is here particular because the gas boiler and the heat pump can be used in parallel to load the same storage tank (see section 9.3). Two new optimization variables are introduced ($\dot{Q}_{\text{boi}}^{(k)}$ and $\dot{Q}_{\text{hp}}^{(k)}$) such that both the heat pump and the boiler can be used simultaneously but using a different cost. Equation (9.28) replaces the cost computed by eqs. (9.3), (9.9) and (9.12) by the costs due to $\dot{Q}_{\text{boi}}^{(k)}$ and $\dot{Q}_{\text{hp}}^{(k)}$. Equations (9.31) to (9.32) ensure that the total heating and cooling power can be delivered by the production units.

Finally, the **block of flats** MPC (`MPC : T`) only optimizes TABS as its ventilation system is not equipped with heating or coiling coils.

9.4.3 Optimization parameters

The MPC is generated and the simulations are run using the toolchain as described in section 6.2. The MPCs prediction horizon is 6 days in order to take the TABS (and building) inertia correctly into account. Due to the long horizon, an adaptive step size is chosen in order to keep a reasonable time accuracy without increasing the problem size excessively. For the cases of the retirement home and the block of flats the horizon is divided into 24 control steps consisting of 4 groups of 6 steps of equal size each. The different sizes are 3600, 7200, 14400 and 57600 seconds and the horizon steps can thus be written as: (3600, 3600, ... , 7200, ... , 14400, ..., 57600, ... , 57600) seconds. For each step, the average value of the disturbances is taken. For the office building and the school where the thermal comfort bounds switch sharply between day and night, 6 control steps of 1200 seconds each are added to the horizon steps array. In order to avoid sub-optimality, the MPC states are updated at each control time step.

9.5 Results

This section compares the total thermal discomfort, the energy use and the energy cost achieved by the RBC and MPCs for the different buildings (section 9.5.1) and investigates the patterns present in the optimal control obtained by the MPCs to retrieve guidelines to improve current RBC strategies (section 9.5.2).

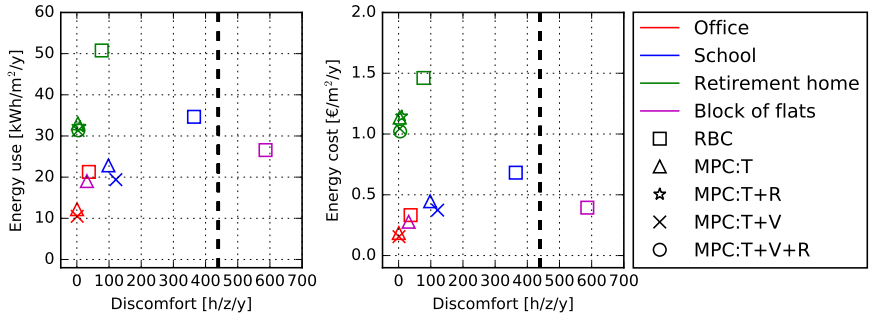

Figure 9.6: Comparison of the thermal discomfort, energy use and energy cost achieved by the RBCs and the different MPCs for the four buildings. The dashed line presents the acceptable limit of thermal discomfort according to EN 15251 [145].

9.5.1 Total thermal discomfort, energy use and energy cost

Figure 9.6 compares the energy use and the energy cost as a function of the thermal discomfort achieved by the RBCs and the MPCs for the four buildings. Each color represents a different building type and each marker a different controller. Table 9.9 summarizes the thermal discomfort, energy and cost savings (reduction) of the different MPCs as:

$$\text{Saving}_{\text{MPC-i}} = \frac{v_{\text{RBC}} - v_{\text{MPC-i}}}{v_{\text{RBC}}} \times 100\% \tag{9.39}$$

with v the thermal discomfort, the energy use or the energy cost achieved by a given MPC-i or by the RBC of the building. Figure 9.7 presents a boxplot of the thermal discomfort of all zones per building and per controller. In both figs. 9.6 and 9.7, the dashed line gives the acceptable thermal discomfort limit according to EN15251.

Thermal comfort: For the block of flats, figs. 9.6 and 9.7 show that its RBC does not achieve an acceptable thermal comfort as it has an average of 589 hours of thermal discomfort per zone per year and up to 1055 hours for one of the flats despite the individual tuning of each flat heating/cooling curve. The slow reaction of TABS is often insufficient to compensate for the intermittent cold flow from the non-conditioned ventilation, for the solar gains through the unshaded windows and for the highly variable internal gains. However, when controlled by MPC, the average thermal discomfort drops to 31 h/z/y

Table 9.9: Thermal discomfort (D), energy use (E) and energy cost (C) savings realized by the different MPCs and expressed in terms of percentage of the RBC results for the different buildings (see eq. (41))

	Office			School			Retir. home			Flats		
[%]	D	E	C	D	E	C	D	E	C	D	E	C
MPC:T	99	43	44	73	34	35	96	35	22	95	28	30
MPC:T+R	-	-	-	-	-	-	88	36	22	-	-	-
MPC:T+V	97	51	53	67	44	45	95	38	29	-	-	-
MPC:T+V+R	-	-	-	-	-	-	94	38	30	-	-	-

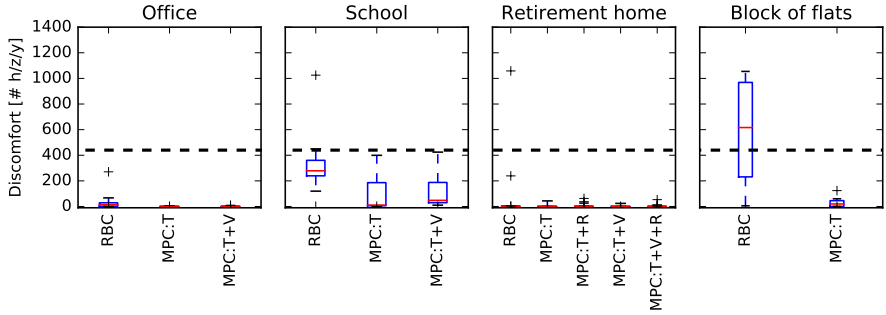

Figure 9.7: Boxplot of thermal discomfort for all zones evaluated for the RBC and the different MPCs for each building. The dashed line presents the acceptable level of thermal discomfort according to EN15251.

which corresponds to a thermal discomfort saving (i.e. a thermal comfort improvement) of 94.7% compared to RBC (see Table 9.9). This indicates that the HVAC system is physically capable of providing thermal comfort and that the bottleneck of the system is its control.

For the school, fig. 9.7 shows that thermal comfort is not guaranteed for all zones when controlled by the RBC and that the average thermal discomfort is relatively high (364 h/z/y). This is mainly due to the zones with fan coil units which are not well insulated and which would still need heating during the neutral and during the cooling season (see figs. 5.32 and 5.33). On the contrary, the renovated zones with floor heating show overheating during the neutral regime and some parts of the heating season (see figs. 3.9 and 3.10 from Picard and Helsen (2017) [114]). As both the fan coil units and the floor heating are connected to the same buffer tank (see fig. 5.27) which is used both for heating

and cooling, the simultaneous need for heating and cooling cannot be met by the production system. This illustrates that supplying different emission system types in rooms with different insulation levels by using a single production system leads to an insufficient controllability of the system. For the MPC simulations, no linear constraints could be formulated to avoid simultaneous cooling with floor heating and heating with fan coil units (see section 9.4.2). The MPC simulations for the school assume therefore that heating and cooling can be provided at any time during the year. Using this system improvement, the MPCs can significantly improve thermal comfort for each zone (thermal comfort improvement of more than 66%, see Table 9.9). The remaining thermal discomfort is mostly occuring in the zones with fan coil units (average thermal discomfort between 186 and 400 K/h/y compared to 1.5 to 20 K/h/y for the zones with FH). This is due to the model mismatch between the MPC controller model and the building emulator model which becomes significant when the air of the zone is strongly excited (high fan coil unit power), often causing undercooling at the start of the day. The effect is worsened by the relatively coarse controller time step of 20 minutes.

For the retirement home, figs. 9.6 and 9.7 show that the thermal comfort realized by the RBC is very high. The two outliers of fig. 9.7 correspond to the corridors of the first and second floor (see fig. 2.11 from Picard and Helsen (2017) [114]) which are overheated due to their high heat gains and very low heat losses (they are not adjacent to any exterior wall). However, this high thermal comfort comes at the cost of the active use of radiators during the cooling season which compensate the undercooling of some zones (see fig. 2.12 from Picard and Helsen (2017) [114]). This undercooling cannot be avoided by a better tuning of the RBC heating/cooling curves because some other rooms show overheating at the same time and because the RBC, as implemented in the model, controls the average water mass flow rate to the TABS instead of each TABS circuit individually. In contrast to RBC, the different MPCs are able to optimize the heat flow rate in each TABS circuit individually which results in an almost perfect thermal comfort (thermal comfort improvement of more than 87%, see table 9.9). The radiators are barely used anymore (see fig. 9.10).

Finally, the office building shows a good thermal comfort when controlled by RBC and nearly no thermal discomfort when MPC is used instead (thermal comfort improvement of more than 96%, see Table 9.9).

Energy use and energy cost: While thermal comfort is considered as a (soft) constraint in the MPC formulation, the actual objective is to minimize the energy cost. Energy *use* differs from energy *cost* due to i) the different efficiencies of the production machines and the different energy prices for electricity and

gas, ii) the cooling energy is considered to be for free as only passive geothermal cooling is used (which leads typically to a very high EER), and iii) for HVAC with a hybrid production system, the same amount of heat or cold can be produced by different machines. Notice that, as passive cooling is almost for free but it is still preferable to minimize the used cooling energy (seasonal storage is here not considered), a fictive cost is still attributed to it.

Table 9.9 shows that when all emission systems are controlled by MPC, the energy cost savings range from 29.4% for the block of flats to 53% for the office building while thermal comfort is significantly improved and energy use decreased. The obtained savings are significantly higher than those found in the literature (15-25%), both when evaluated using BES software and in real buildings (see section 9.1). These substantial savings are mostly due to the ability of MPC to work at the thermal comfort boundaries while RBC is obliged to play safe and as a consequence to remain in the middle of the upper and lower thermal comfort temperature bounds, as illustrated in fig. 9.8. TABS have indeed a too long reaction time to use a feedback controller such as a PID controller and operating closer to the comfort bounds would result in regular overheating or undercooling. When the building controllability is low and the gains and occupancy are highly variable, using MPC can be a necessity to ensure thermal comfort as it is the case for the block of flats where thermal discomfort was reduced from 589 h/z/y to 31 h/z/y. It is interesting to note that thermal comfort improvement did not imply an energy cost increase (the cost was actually reduced from 0.39 to 0.28 €/m^2/y). MPC can further exploit the benefits of hybrid systems. Moreover, table 9.9 shows that optimizing both TABS and ventilation (`MPC:T+V`) increases the cost savings with 6% to 11% compared to `MPC:T` where TABS is optimized but the ventilation is controlled by the RBC algorithm. In the case of the school where the heat pump and the gas boiler can be used in parallel, `MPC:T+V` uses 25 times less the boiler than `RBC`.

9.5.2 Optimal use of TABS, ventilation and supplementary emission systems

In this section, the optimal TABS, ventilation and supplementary emission system behaviours resulting from the MPCs are compared with their respective `RBC` and between the different buildings. The comparison is mainly done qualitatively and aims at assessing the possibility for RBCs to mimic the MPC behaviour.

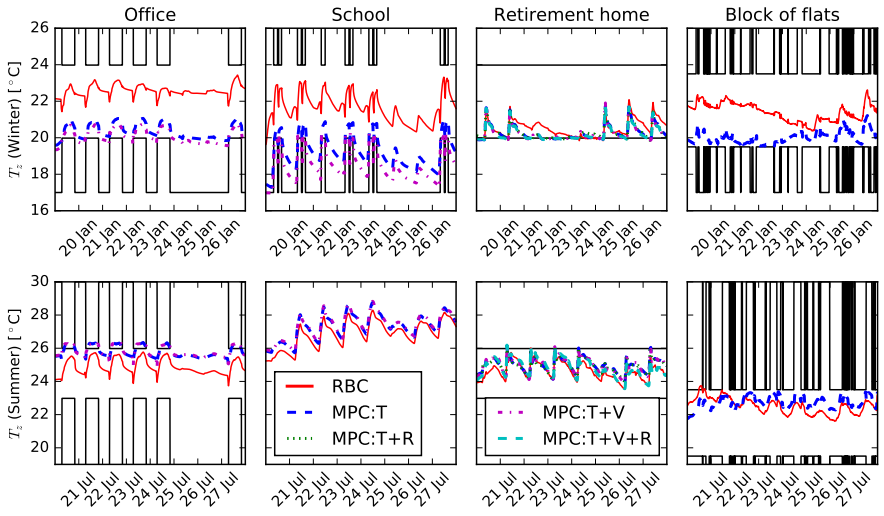

Figure 9.8: Comparison of the zone operative temperature in buildings controlled by RBC and those controlled by MPCs. Top plots represent winter, bottom plots represent summer.

Time dependent behaviour

This section investigates the time patterns for the different MPCs. The time-patterns are investigated using fig. 9.9 which presents a carpet plot of the TABS and ventilation (Ven) heating and cooling energy use for the `RBC`, `MPC:T` and `MPC:T+V` controllers. For each cell of the carpet plot, the sum over the year of all energy used during a given hour (y-axis) of a given week day (x-axis) is given by its color. For example, the sum of all TABS heating energy used on Monday mornings between 6:00 and 7:00AM for the Office building when controlled by `MPC:T` is around 0.24 kWh/m^2/y.

Figure 9.9 shows that MPCs are characterized by clear time-patterns. For all buildings, while RBCs show a relatively constant energy use by both TABS and ventilation, MPCs show a much higher contrast with recurrent *off*-time and periods of intensive use. This is an expected result as both some building disturbances (e.g. solar radiation, internal gains) and the thermal comfort requirements are cyclic. This is most visible for the office building and the school which both have a fixed schedule of occupancy with on the one hand long unoccupied periods and on the other hand high internal gains during occupancy. Table 9.9 shows that the cost savings are also the highest for those buildings

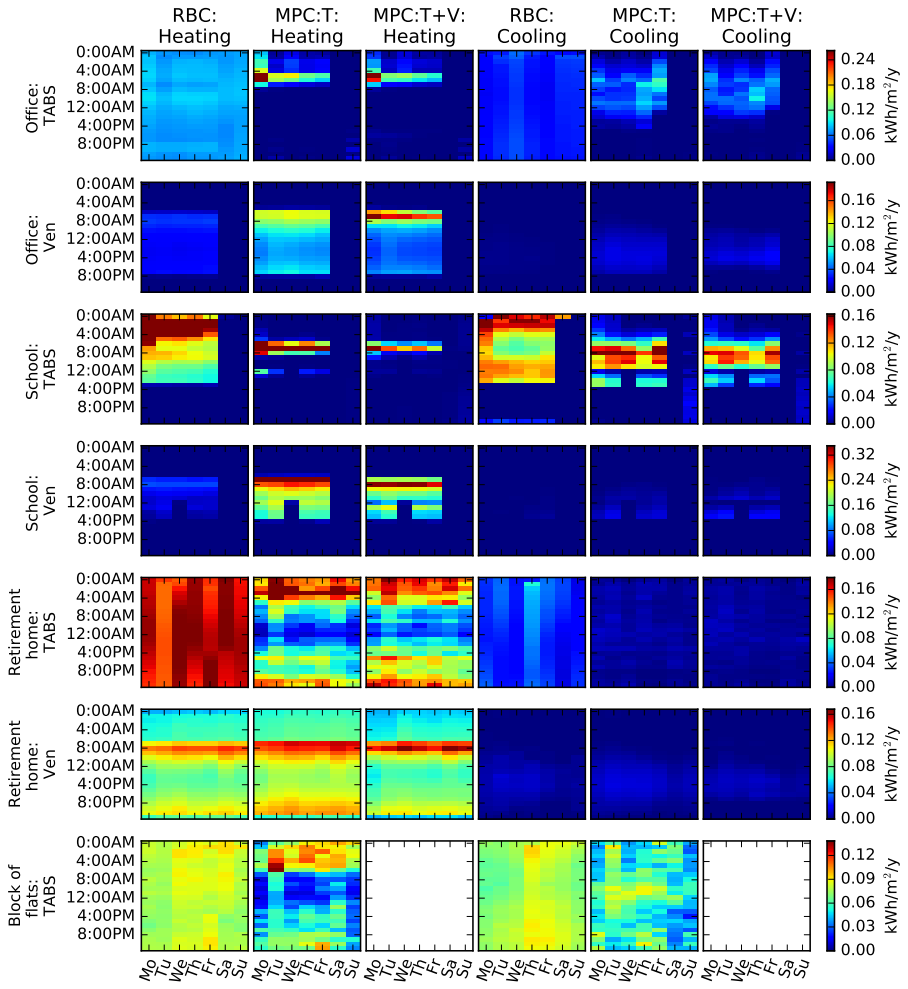

Figure 9.9: Carpet plot of the TABS and ventilation (Ven) heating and cooling energy use for the `RBC`, `MPC:T` and `MPC:T+V` controllers. For each cell of the carpet plot, the sum over the year of all energy used during a given hour (y-axis) of a given week day (x-axis) is given by its color. Within one figure row the same color scale is used.

when `MPC:T+V` is used (resp. 53.2% and 45.2%).

Heating: The most visible contrasts in fig. 9.9 are for heating. For all buildings equipped with a ventilation system with heating coil, the ventilation is intensively

used 1 hour before the thermal comfort switches from night to day. In the case of `MPC:T+V`, the supply ventilation temperature goes to its maximum value in order to reach the thermal comfort requirements by the time the working day starts while the use of TABS is minimized. This is illustrated in fig. 9.8 which shows that the zone temperature is close to its thermal comfort lower bound every winter morning. In the case of `MPC:T`, the ventilation supply temperature is kept at the lower thermal comfort temperature. In this case too, the ventilation energy use is high in the morning due to the cold ambient temperature and the limited power of the recovery wheel as the zone temperature is low after the night. This is in particular visible for the school where the zone temperature can drop significantly for the non-renovated zones (see fig. 9.8). While most of the rooms of the retirement home have constant thermal comfort requirements (no day-night switch), a similar ventilation behaviour is present due to the cafeteria's which do have a day-night thermal comfort range and due to the doubling of the ventilation flow rate between day and night. It should be noted that the zone temperature during the day is higher than the lower thermal comfort bound due to the internal and solar gains. Nevertheless, the ventilation still needs heat to condition the supply air to a temperature at least equal to the lower thermal comfort bound as specified by the MPC constraints. `MPC:T+V+R` can still slightly reduce the energy cost of the retirement home by working closer to the constraints thanks to the fast behaviour of the radiators. However, fig. 9.10 indicates that the radiator energy use is negligible.

In the case of the office building and of the school, the ventilation heat has the same cost as the TABS heat as they are both fed by the heat pump. As a results, `MPC:T` and `MPC:T+V` prefer to use ventilation when it is available rather than the slow reacting TABS. TABS are only activated from 0:00AM to 7:00AM on weekdays, on Sunday late evening for the office building and during the lunch break for the school. The remaining heating needs are fully covered by ventilation. Figure 9.10 shows the energy use per emission system for each building and each controller. For all buildings, both the heating and the cooling TABS energy are drastically decreased while the energy used by the ventilation heating coil increases when replacing RBC by MPC. In the case of the retirement home building where the ventilation heating coil is fed by the more expensive gas-boiler while the TABS are fed by the heat pump, the decrease of the TABS energy is still present but less pronounced than for the other buildings. In the case of the block of flats, no secondary emission system is available. Figure 9.9 shows that still not much TABS energy is used for heating the flats between 8:00AM and 4:00PM.

Finally, the heating energy used by the fan coil units of the school is also reduced by the MPCs (see fig. 9.10). This is mainly due to the fact that all zones are fed by a single ventilation system. As the ventilation is used to heat the rooms

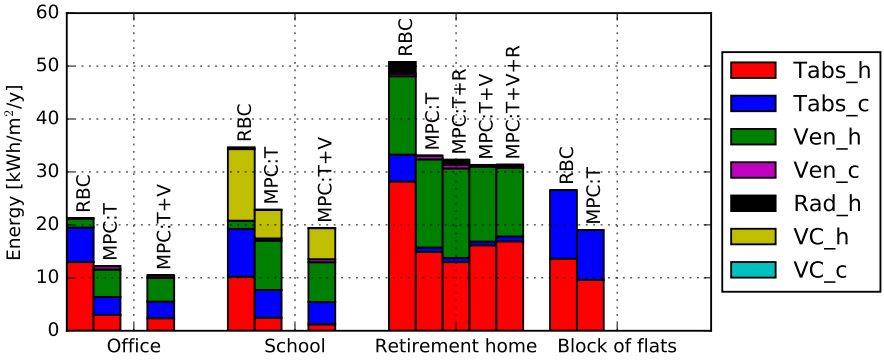

Figure 9.10: Energy use obtained by RBC and MPCs for the different buildings. The energy use is given per emission system: TABS heating (TABS_h) and cooling (TABS_c), ventilation heating (Ven_h) and cooling (Ven_c) coil, radiator (Rad_h), fan coil unit heating (FCU_h) and cooling (FCU_c).

equipped with floor heating, the rooms equipped with fan coil units also benefit from this extra heat.

Cooling: While time-patterns are clearly visible in the MPCs heating behaviour for both TABS and ventilation, the use of TABS and ventilation cooling energy is less contrasted. Figure 9.9 demonstrates that the ventilation air is rarely cooled. The ventilation still cools the zones when the supply air is only conditioned by the recovery wheel but the cooling power is limited (between 1 to 5 W/m^2, see Picard and Helsen (2017) [114]). The ventilation cooling power is not used much due to the different thermal needs of the different zones. Figure 9.11 shows the minimum, maximum and mean temperatures of all zones of the office building and the day thermal comfort boundaries (instead of the time varying (day/night) range which is actually used by the MPC). Therefore the graph looks like thermal comfort violations occur while it is actually not the case. Figure 9.11 confirms that during the summer, some zone temperatures are at the upper thermal comfort bound while other zones are at the lower bound. The MPCs choose therefore to condition the zones separately using the different TABS circuits rather than using the ventilation which has a unique supply temperature. Figure 9.11 also indicates that some simultaneous heating and cooling through TABS occurs (but in different zones).

While no clear ventilation cooling patterns are visible, fig. 9.9 indicates that TABS cooling occurs typically between 4:00AM and 4:00PM and not during the night. This is sufficient to avoid overheating by the end of the afternoon. These

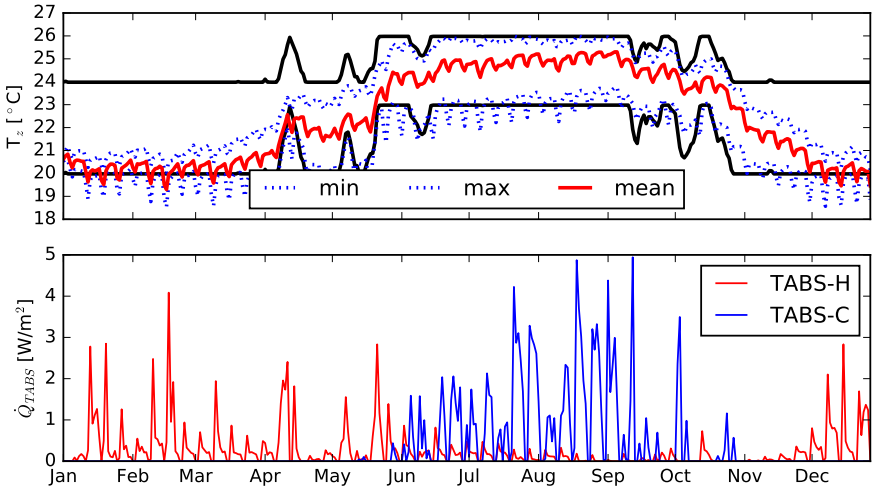

Figure 9.11: Top: Mean, minimum and maximum zone temperatures for the office building and its day thermal comfort bounds. Bottom: heating (H) and cooling (C) TABS average power.

observations in time-patterns may be used as starting points to improve current practice RBCs. In the next section, correlations between weather data and thermal powers are investigated to look for improved heating/cooling curves.

Correlation between weather and control

Section 9.5.2 suggests that the ventilation and TABS activation times when controlled by MPCs are predictable, especially for heating. This section investigates whether the thermal powers can also be predicted by a heating/cooling curve as used by the RBC by looking at the correlation between the TABS thermal powers and the (weighted average) ambient temperature or the building solar gains.

As the best control is achieved by `MPC:T+V`, the correlation analysis is done for that controller except for the block of flats for which `MPC:T` is used instead. Figures 9.12 and 9.13 plot the daily heating and cooling TABS powers of the full year as a function of a weighted average of the ambient temperature of the previous 3 days (Te3d (Past)), 7 days (Te7d (Past)) and future 3 days (Te3d (Pred)), and as a function of the total building solar gains for both the `RBC` (white background) and the `MPC:T+V` (coloured background) simulations.

Only the thermal powers used on Tuesdays, Wednesdays and Thursdays are plotted as the other days are strongly influenced by the different thermal comfort requirements of the weekend. The zero powers (black dots) are further not considered for the linear fit. This is done mainly for the school in order to eliminate the points of the summer months during which the building is not conditioned. A linear fit is then computed on the heating powers occurring when the weighted average temperature is lower than 12° C (red points) and on the cooling powers occuring when the weighted average temperature is higher than 12° C (blue points). The yellow dots on the plots are the heating or cooling TABS powers which occur at the higher and lower side of the 12°C separator. Finally, the R-value of the fit is given for each plot.

Heating: Figure 9.12 indicates that the correlation between the heating TABS power and *Te7d* is very high for all buildings while controlled by `RBC` with R-values above 0.9 (0.7 for the retirement home). This was expected as `RBC`s use a heating curve for the TABS supply temperature based on *Te7d* (or *Te3d* in case of the office building). The correlation for the `MPC:T+V` simulations is lower with R-values between 0.6 and 0.8. In case of the retirement home and of the block of flats, the correlation is significantly improved (R-value of 0.9 and 0.8) when the weighted average ambient temperature of the 3 coming days is used instead of the past. This is, however, not the case for the office building and for the school. Figure 9.12 further shows that the TABS heating powers in the case of the retirement home and of the office building also occur for *Te7d* higher than 12°C. This shows once again that `MPC:T+V` also uses heating during the mid-season and summer. Finally, no real correlation between solar gains and the heating needs is found.

Cooling: Section 9.5.2 suggests that no clear time-pattern could be found for cooling. Figure 9.13 shows that no clear correlation between the cooling TABS powers and the ambient temperature or the solar gains can be found either (R-value between 0.2 and 0.6 for `MPC:T+V` and between 0.3 and 0.8 for `RBC`). In general, `MPC:T+V` appears to use lower cooling powers than `RBC` and to be less predictable.

From these results, and considering that the correlation is worse when including Friday, Saturday, Sunday and Monday, it is clear that a simple RBC based on heating/cooling curve will not be able to have a performance close to what MPC can achieve, even with optimal tuning.

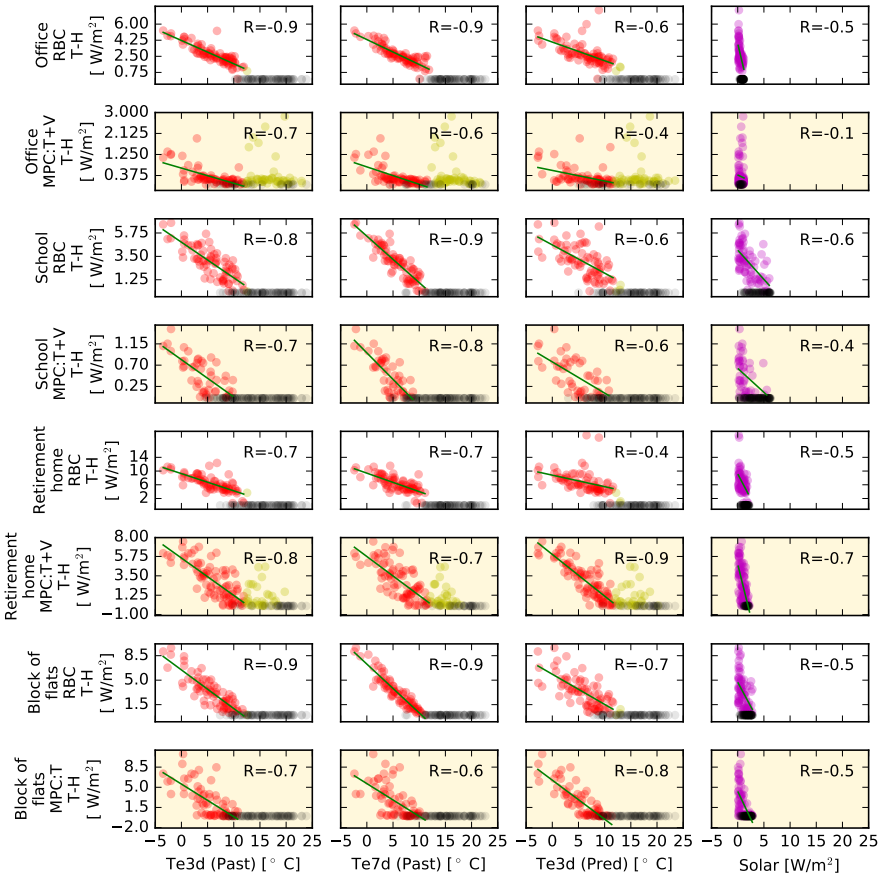

Figure 9.12: Correlations between the TABS heating (T-H) power and weighted average of ambient temperature of the previous 3 days (Te3d (Past)), 7 days (Te7d (Past)) and future 3 days (Te3d (Pred)), and the total solar gains (Solar) for the `MPC:T+V` controller.

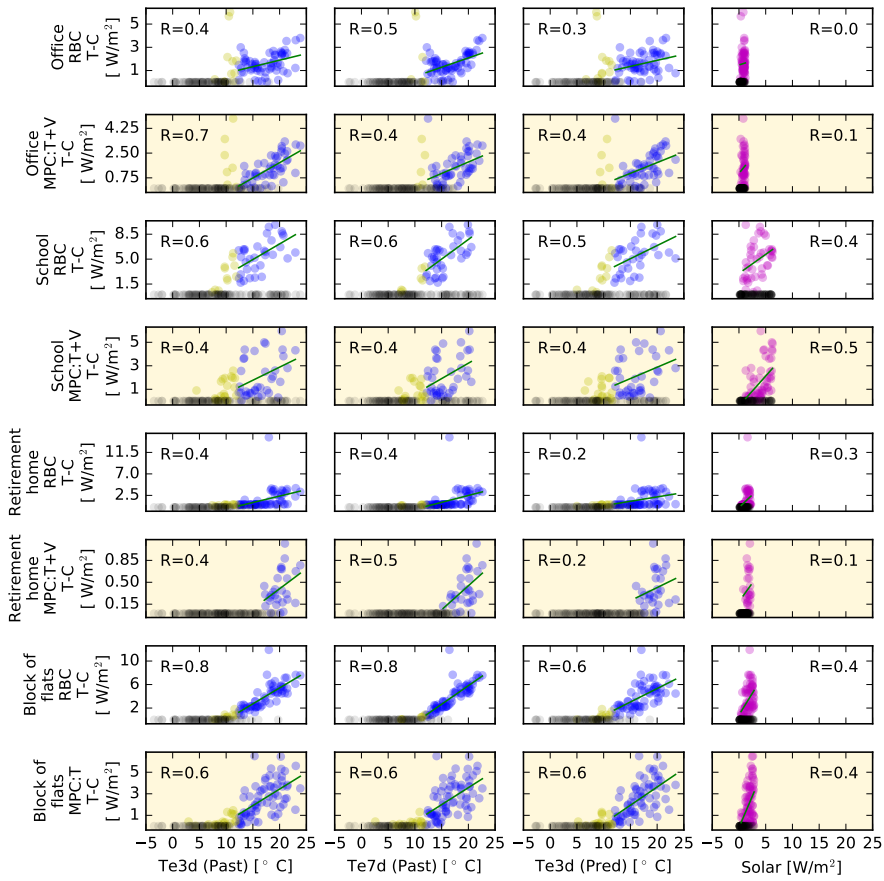

Figure 9.13: Correlations between the TABS cooling (T-C) power and weighted average of ambient temperature of the previous 3 days (Te3d (Past)), 7 days (Te7d (Past)) and future 3 days (Te3d (Pred)), and the total solar gains (Solar) for the `MPC:T+V` controller.

9.6 Conclusions

This chapter had four goals: i) to assess the feasibility and performance of (hybrid) *GEOTABS* systems for different types of buildings and occupancy, ii) to assess the thermal comfort, energy use and energy costs savings that MPCs can achieved compared to current practice RBCs, iii) to compare the results obtained for pure *GEOTABS* buildings where only TABS are optimally controlled with hybrid *GEOTABS* buildings where simultaneously TABS, ventilation and (optionally) supplementary emission systems are optimally controlled, and iv) to search for patterns in the optimal control achieved by MPC which could be used to improve conventional RBCs. This study is carried out using simulation models based on four existing Belgian buildings: an office, a retirement home, a school and a block of flats.

For all buildings, a very high thermal comfort was achieved when controlled by MPC. This means that (hybrid) *GEOTABS* systems can technically be successfully used for a wide variety of building (and occupancy) types when appropriate control is implemented. When a traditional RBC is used, a too low controllability of the building, such as the block of flats with unconditioned ventilation, or a too large difference of thermal needs between the different zones, such as the investigated school, leads to a low thermal comfort satisfaction. If *GEOTABS* is installed in such a building, MPC might be necessary to meet the thermal comfort requirements. The investigated MPCs could further save between 30% to 50% of the energy cost. These high savings contrast with the values found in the literature (between 15% to 25%) both when evaluated in BES software and in real buildings. This is probably due to the excellent predictions of the controller model compared to approaches using a black-box, a grey-box or a low order white-box controller model where significant model mismatch leads to sub-optimality. The implemented MPCs further optimize TABS and ventilation (and the supplementary system) simultaneously which improves the savings with 6 to 11 % compared to the savings obtained by the MPC optimizing TABS only.

In order to mimic the MPC results with heating/cooling curve based RBC, a good correlation between the thermal powers and the past (or future) average ambient temperature or solar gains is necessary. The correlation R-values found between the TABS heating powers and the average past ambient temperature are, however, only between 0.6 to 0.8 for MPC (and above 0.9 for RBC) when evaluated for Tuesdays, Wednesdays and Thursdays and even lower for the other days. Using the predicted average ambient temperature improves the correlation for some buildings (R-value between 0.8 and 0.9) but not for all. The cooling power correlation is even much lower (between 0.2 and 0.6). The heating and cooling power profiles obtained by MPC seem therefore not to be

achievable by RBC using simple heating/cooling curves.

Part IV

Optimal design

Chapter 10

Economic optimal HVAC design for hybrid GEOTABS buildings and CO_2 emissions analysis

In the early design phase, a design engineer will typically firstly estimate the energy profile necessary to heat and cool the future building based on a few parameters such as the building conditioned volume, its floor surface area, the type of occupancy, its windows-to-wall ratio, whether the structure is light or heavy, and typical weather conditions at the given location. Based on the energy profile and optionally some additional constraints set by the client, the design engineer will then propose a combination of properly sized heat and cold production and emission systems (further referred as *HVAC scenario*) able to deliver the required powers and energy loads. Finally, the investment, running, maintenance and replacement costs can be estimated along with the total CO_2 emission or another indicator for environmental impact. Ideally, several alternative HVAC scenarios are compared with each other to choose the most appropriate one. However, since the presented work flow is highly time-consuming, the number of considered alternative scenarios remains (very) limited leading to suboptimal designs. This work presents therefore a python tool which automates the generation of all possible scenarios for given thermal power profiles and energy load and a given database of HVAC components. The tool further sizes each scenario properly, computes its present cost (PC)

based on the investment, running, maintenance and replacement costs, and the total CO_2 emission associated to the building energy use. Finally the different scenarios can be searched and classified to pick to most appropriate scenario. The tool is based on static calculations based on standards, manufacturer data and basic assumptions similar to those made by engineers in the early design phase. It should further be noted that the tool optimizes the HVAC system but not the building envelope while ideally, both should be simultaneously optimized.

This chapter is structured as follows. Firstly, section 10.1 describes common methods used to improve or optimize HVAC systems of buildings. Secondly, section 10.2 introduces the methodology proposed in this work, section 10.3 clarifies its assumptions, and section 10.4 lists the considered HVAC components and summarizes their characteristics. Finally, section 10.5 compares the Present Cost (PC) and the CO_2 emissions of conventional, (pure) GEOTABS, and economic optimal HVAC designs for different boundary conditions, and section 10.6 concludes and proposes some further improvements.

10.1 Introduction

In Europe, buildings are responsible for 40% of the total energy use from which halve is used for heating and cooling [111]. In accordance to the European Union's Directive 2010/31/EN [45], the energy requirements for buildings are becoming increasingly stringent. Not only should the buildings become more energetically efficient through a better design of the building envelope (insulation, shading, etc.) and the use of more efficient HVAC devices, but buildings are also obliged to use a minimum of renewable energy sources (RES) (see section 1.1). Both requirements put building designers and installers under pressure to be innovative and up-to-date with the various and rapidly improving available technologies. Furthermore, systems are becoming increasingly complex. Where a standard gas- or oil-fired boiler and a compression cooling machine connected to radiators and ventilation units used to be installed everywhere, buildings using a combination of production systems such as gas boilers, heat pumps, etc., emission systems such as radiators, fan coil units, chilled beams, TABS, etc. and additional RES such as photovoltaic panels, solar boilers, borefields, etc. are becoming common in Europe. With this increase in system complexity and the lack of knowledge about these new and rapidly improving technologies, design tools are becoming highly necessary to help designers and installers to optimize both the design and the control of buildings. According to Ellis and Mathews (2002) [39], researchers believe that design tools based on an integrated approach where the system efficiency is optimized taking the interactions between the

various factors and their constraints into account could lead to savings around 70%.

According to ASHRAE, three types of equipment related programs exist to help HVAC designers: i) electronic catalogues which simply list available components respecting given constraints, ii) equipment optimizers which propose a range of possible equipment alternatives for given design criteria, and iii) equipment simulation programs which can take the interactions and constraints of different devices connected to each other into account [39]. While only equipment simulation programs can truly help the design engineer to optimize the system, such tool is confronted to an intricate problem. Firstly, the number of design variables (type, size and combination of systems) is usually very high. Secondly, the operation efficiency of each system is very dependent on its components and how they interact, and, finally, the design is heavily based on the building's energy demand which is difficult to predict in the early design phase.

In the literature, building and HVAC designs are typically optimized by heuristic methods such as genetic algorithms. Due to their slow convergence, generally only a limited number of parameters are optimized while the control is fixed or optimized over a short period of time. Another popular approach is to formulate the optimal design problem as a *mixed integer linear programming* (MILP) problem, allowing many variables to be solved in a reasonable computing time. However, a MILP formulation requires linear models which prevents its use in simulation based building design optimization. Nguyen et al. (2014) [100] provide an extensive literature study on building optimization. Examples of optimization using genetic algorithms can be found in e.g. Ooka and Komamura (2009) [107] who used a genetic algorithm to optimize the equipment capacity and operation planning of buildings, and in Seo et al. (2014) [127] who used a multi-island genetic algorithm to optimize the HVAC system of apartments. The MILP approach has been used by, e.g., Ashouri et al. (2013) to simultaneously optimize HVAC equipment, sizing and operation, and by Patteeuw and Helsen (2016) [110] who developed a similar method but also included multiple temperature levels to represent energy storage and conversion efficiencies in a more realistic way, and the explicit modelling of the electricity generation side. Heuristic and MILP optimization methods can also be combined. Evins (2015) [48] simultaneously optimized the building envelope of an office building, its HVAC, and its control, using a multi-objective, multi-level optimization scheme. At the top level, a genetic algorithm optimizes some building envelope parameters and the choice and size of the HVAC system by running an EnergyPlus model. At the lower level, a MILP algorithm is used to optimally control the HVAC with minimization of the running cost as objective. Due to the huge problem formulation, the author used a combination of a workstation with twin eight-core processors and 64 Gb RAM and additional 960 computing cores each with 4

Gb RAM to solve the MILP problems in parallel.

On the more practical and political sides, EU's Directive 2010/31/EN compels the EU countries to limit the energy used by the building sector but leaves each country the freedom to develop its own legislative framework to reach the energy goals. In Belgium, a software called EPB (in Dutch and PEB in French) is used to compute an energy level indicator. The energy level is evaluated based on quasi static energy loss computations and on a point table to grade different HVAC systems. The Flemisch Energy Agency (VEA) publishes every second year a report which investigates for which energy level the building would also be cost optimal with respect to the sum of the investment, running and replacement costs [158]. While the results are very instructive for decision makers of Flanders, the method is not practical for designers as it is difficult to relate the energy indicator to real energy use and the designer is restricted to the initial assumptions made by the program. Furthermore, the EPB software is not able to calculate dynamic aspects, system integration and control correctly.

The drawback of the presented methods is that they require intensive computer power, specialized software, and intensive modelling and set up work. The results are further difficult to analyse as they are influenced by numerous optimization parameters and assumptions/approximations made by the tools. Therefore, this work proposes to go back to the straight-forward but time consuming method used by engineering offices and to automate it. The method should be based on a limited set of parameters and it should remain intuitive to be usable in the early design phase. The starting point of the method is the heating and the cooling *load duration curves* (LDC) of the building which represent the thermal powers required to condition the building. The thermal powers are furthermore ordered and each power is plotted with a width equal to the sum of hours that it is used, such that the integral of the LDC represents the yearly energy load of the building. The developed method proposes then all possible HVAC scenarios composed of the devices present in the database which can provide the powers and the energy load of the LDC and computes the scenarios PC (including the investment, running, maintenance and replacement costs) and CO_2 emissions (see section 10.2). The method has the main advantage to automatically generate and size, and to return the necessary information about each possible HVAC scenario such that design engineers can make the optimal choice, while the method complexity is sufficiently low such that the results can be easily manually verified.

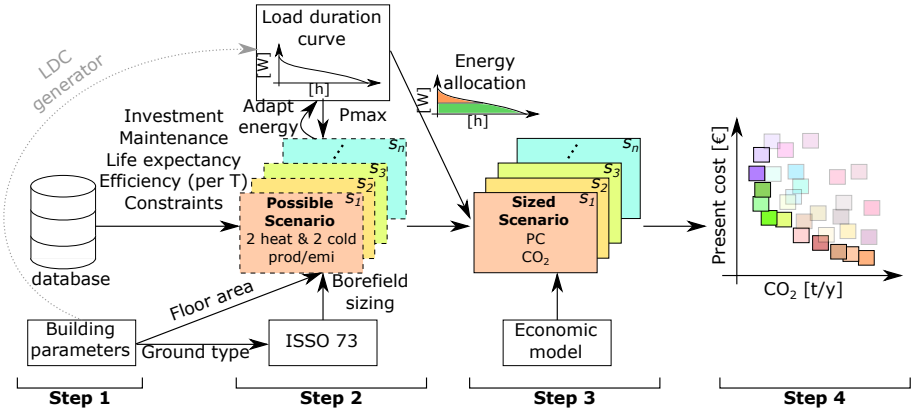

Figure 10.1: Schematic representation of the optimal HVAC design methodology splitted in four consecutive steps. The generation of load duration curves (LDC) based on a limited set of building parameters is not yet implemented and is therefore represented as a dotted grey arrow.

10.2 Methodology

The methodology used by the developed tool to optimize the HVAC system for a given building is schematically represented in fig. 10.1 which shows the four steps that are consecutively carried out.

Step 1 Firstly, a database of HVAC components is created containing for each component (see section 10.4): its cost function returning its price as a function of its size (kW, m^2, etc.), its maintenance cost, and its life expectancy (see table 10.1 and fig. 10.3). If the component is a production device, the energy efficiency is given for different temperatures (for heat production: 30, 45, 60°C, and for cold production: 10, 15, 20°C, see table 10.2) and if the component is an emission device, its nominal supply and return temperatures are specified (see table 10.3). The database also contains the component constraints (e.g. ground source passive cooling (GSPC) cannot deliver water colder than 15°C). Additionally, a number of building parameters are required such as its total floor area (used to size the CCA system) and the ground characteristics which influence the borefield design. In its final state, the tool should also be able to estimate the energy profile of the building based on its parameters in the form of load duration curves (LDC). However, this is not yet implemented and the building's LDCs are thus now assumed to be given.

Step 2 The second step is to generate all possible HVAC scenarios composed of the devices present in the database which can deliver the energy and thermal powers of the given LDC using the HVAC components of the database. In order to limit the number of possible scenarios, a scenario can contain a maximum of two heat and two cold production systems, each coupled to its own emission system. Note that reversible components count for two: one for heating, one for cooling. Figure 10.2 illustrates how the different scenarios are generated. Firstly, a set of production and emission systems is taken from the available components of the database. Secondly, the production systems are sorted by decreasing efficiency and the heat (cold) emission system with the lowest (highest) supply temperature is coupled to the most efficient heat (cold) production system. The maximum heating (cooling) power present in the LDC can now be divided between the two heat (cold) systems according to predefined hybrid fractions (currently set as [0,25,50,75,100]%). Note that both the heating and the cooling hybrid fractions can vary independently, that coupled production and emission systems are sized together, and that when a 0% hybrid fraction is allocated, this means that the component is not installed. When a reversible system is installed, it will be sized by the maximum of its heating and cooling powers, taking its cooling to heating power conversion factor (see table 10.3) into account. This is necessary as, for example, the cooling power of a high temperature 4 pipes fan coil unit (FCP4P-HT) at its nominal conditions is only 60% of its heating power due to the smaller temperature difference between the air of the zone and the fan coil supply water for cooling than for heating.

While most of the components are sized according to their nominal power, CCA and FH are sized to a realistic fixed 80% of the building floor surface area and the ground heat exchanger (i.e. the borefield) is automatically designed according to the standard ISSO73 [77]. Standard ISSO73 returns the number of boreholes and their depth necessary to deliver a given maximum thermal power and a given amount of yearly energy and it takes into account the regeneration level, the ground and grout characteristics, the borefield configuration, the borehole type, the maximum borehole depth, and the minimum allowed ground temperature ($T_{\min}$). The standard was originally developed to size heating dominated borefields based on the results returned by the Energy Earth Design (EED) software [70] with an accuracy of $\pm 10\%$. In this work, the work flow proposed by the standard has been translated in the python tool to automatically size the borefield and the method is extended as follows to allow cooling dominated cases. When the borefield is heating dominated, its sizing depends on the temperature difference between the initial ground temperature (T_0) and $T_{\min}$. In Belgium, this temperature difference is typically around 10°C as T_0 is typically around 10°C and $T_{\min}$ is here chosen equal to 0°C to avoid freezing of the ground. When the borefield is cooling dominated, the borefield is sized such that the ground temperature does not exceed a maximum value ($T_{\max}$) which is chosen

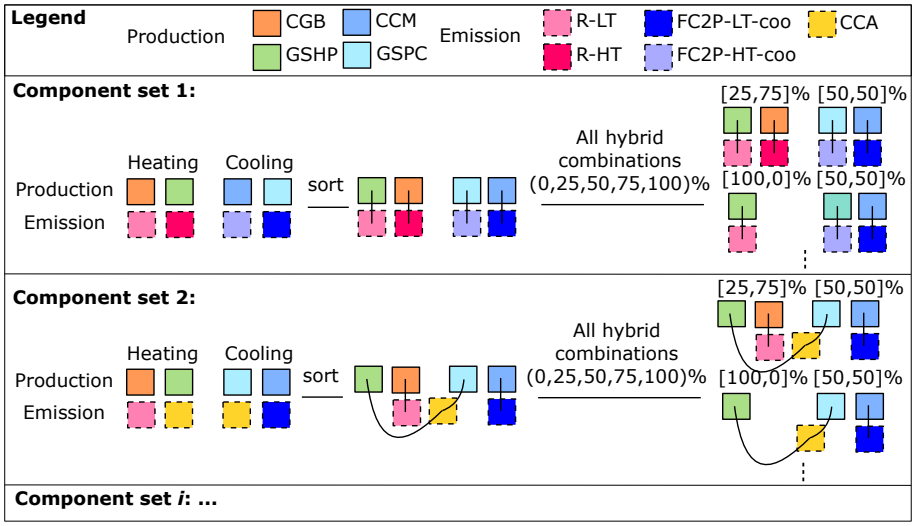

Figure 10.2: Illustration of how different HVAC scenarios composed of two heat and two cold production devices, each coupled to its own emission component.

in this work to be 17°C, to ensure that passive cooling with the ground can always be used. The same work flow can then be applied to size cooling dominated borefields by simply using the cooling energy and power instead of the heating ones and by choosing $T_{\min}$ so that $T_0 - T_{\min} = T_{\max} - T_0$ which means $T_{\min} = 3°\text{C}$ for the mentioned assumptions.

Finally, the original energy of the LDC which corresponds to the building energy needs for space heating and cooling is corrected to include the emission system efficiency as specified by the standard NBN EN15316-2-1:2007 [149] (see section 10.4 and table 10.3).

Step 3 Once the type and the size of each HVAC component of a scenario are defined, the energy from the LDC can be allocated to the different production components such that the most efficient component delivers the base load. Notice that fig. 10.1 shows only one LDC while actually two LDCs are needed: one for heating, one for cooling. The scenario present cost (PC) can now be computed as:

$$\text{PC} = I_0 + \sum_{j}^{N} \left[\left(C_\text{e} + C_\text{m} + C_\text{r} \right) R_j \right] - V_\text{r} R_n \tag{10.1}$$

with I_0 the initial investment cost calculated as the sum of the different component cost functions (see table 10.1), N the number of years during which the system will be used (in this work, 20 years is assumed), C_e, C_m, and C_r the energy, maintenance, and replacement costs computed using the efficiencies, maintenance percentages, and life expectancies of tables 10.1 to 10.3 and a given electricity and gas price of 0.1466 and 0.0534 €/kWh [47, 46], and V_r the remaining value of the system after N years. Note that the investment cost of the components and the energy prices are assumed to stay constant over the years and no inflation is considered. This assumptions are chosen due to the too high uncertainty on those factors and in order to keep the computations more transparent. However, the different costs are discounted with discount factor $R_j = \frac{1}{(1+i)^j}$ with j the number of years counted from the investment time and i the discount rate. An interest rate of 4% is used in this work. V_r is further calculated linearly with the number of years the device can still be used except for radiators, CCA and the ground heat exchanger (GHEX-V) for which V_r is zero as they cannot be easily dismantled and re-used.

Beside the PC, the total CO_2 emissions caused by the energy use of the building are computed using the primary energy conversion factor of 0.056 kg/MJ for gas and 0.179 kg/MJ for electricity [158].

Step 4 The final step compares the PC and the total CO_2 emission of each scenario over a realistic 20 years life time of the building such that the design engineer can make the most appropriate choice.

10.3 Assumptions and limitations

The main assumption/limitation of the presented methodology is that the LDC of the building is assumed given and therefore no dynamic simulations have been carried out. In the future, the method should include an LDC generator. The powers and energy of the LDC furthermore depend on the chosen HVAC scenario which is taken into account by the emission efficiencies from NBN EN 15316-2-1:2007 [149]. However, the accuracy of such efficiencies should be investigated by dynamic simulations.

The following assumptions are also made:

- While different efficiencies for different supply temperatures are used, the nominal power of production devices does not depend on their supply temperature. This might cause an over or underestimation of the device investment cost when it is used in different nominal conditions.

- For geothermal systems, only the most common vertical ground heat exchangers (GHEX-V) are considered. Furthermore, it is assumed that GSHPs are not reversible and that cooling can only be done passively using a GSPC. This assumption might cause an overestimation of the investment cost of GSHP systems.
- If CCA or FH is installed, it is assumed that it will be installed for the whole building and cover a fixed 80% of the building floor surface area.
- So far, the ventilation system and the building climate controller are not included in the HVAC design optimization. Also, the number of considered HVAC components is limited (see table 10.1).
- No inflation is taken into account due to its large uncertainty but all costs are discounted as described in section 10.2.

10.4 Components information

As described in section 10.2, the first step to optimize the HVAC system is to gather the necessary information about its components. The nomenclature, the cost function, the maintenance cost, and the life expectancy of each considered HVAC component are listed in table 10.1 and the cost functions are also represented in fig. 10.3. The cost functions are derived from the (installed) cost data of 18 recently built buildings from two different Belgian engineering offices, as described in appendix A. The maintenance costs, expressed as a percentage of the investment cost, and the life expectancies are retrieved from the standard NBN EN 15459 [146]. The database can easily be extended with new components and the required parameters are known.

Table 10.2 contains the assumed energy conversion efficiencies of the different heat and cold production components for different supply temperatures, based on the average of values found in technical sheets of different manufacturers and in the Annex 48 report [19]. When the efficiency is not given, it means that the component cannot supply water at that particular temperature. For the emission components, table 10.3 indicates their nominal conditions for heating and cooling, the ratio between their cooling and their heating power and their efficiency. The emission system effiencies are taken from NBN EN15316-2-1:2007 and they represent the system additional heat losses. These heat losses are due to the non-uniform internal temperature distribution in the conditioned zones (caused by stratification, heat emitters along outside wall/window, differences between air temperature and mean radiant temperature), the non-ideality of the operative temperature control (causing temperature variations and drift)

Table 10.1: Abbreviation, name, cost function with its lower and upper bounds (∞ means that extrapolation is allowed), maintenance cost in percentage per year of the investment cost and life expectancy of each HVAC component, currently included in the database.

Abb.	Component	Cost function [€] (*1)	Maint. Cost [%/y]	Life. exp. [y]
CGB	Condensing gas boiler	$85.405x + 9451$ $x \in [25,\ 800]$ kW	1.5%	20
GSHP	Ground source heat pump	$83.368x + 11725$ $x \in [34,\ 300]$ kW	3.0 %	20
CCM	Compression cooling machine	$80.084x + 12456$ $x \in [21,\ 1335]$ kW	4.0%	15
GSPC	Plate HEX for passive ground source cooling	$14.421x + 1814$ $x \in [28,\ 472]$ kW	2% (*2)	20 (*2)
GHEX-V	Vertical ground heat exchanger	$32.0x$ (*3) $x \in [0,\ \infty]$ m	0.25%	50
R-HT	High temperature radiator	$134.100x$ $x \in [0, \infty]$ kW	1.5%	35
R-LT	Low temperature radiator	$287.791x$ $x \in [0, \infty]$ kW	1.5%	35
FC2P-HT-coo	High temperature 2-pipes fan coil unit (cooling)	$456.621x$ $x \in [0, \infty]$ kW	4.0%	15
FC2P-LT-coo	Low temperature 2-pipes fan coil unit (cooling)	$267.142x$ $x \in [0, \infty]$ kW	4.0%	15
FC4P-HT	High temperature 4-pipes fan coil unit (reversible)	$223.814x$ $x \in [0, \infty]$ kW	4.0%	15
FC4P-LT	Low temperature 4-pipes fan coil unit (reversible)	$397.417x$ $x \in [0, \infty]$ kW	4.0%	15
CCA	Concrete core activation	$21.650x$ $x \in [0, \infty]$ m^2	2.0 %	50

(*1) Based on cost data from real buildings, see appendix.
(*2) Assumption based on VEA2013 because no data in NBN EN 15459 [146].
(*3) Data provided by Boringen Verheyden [160].

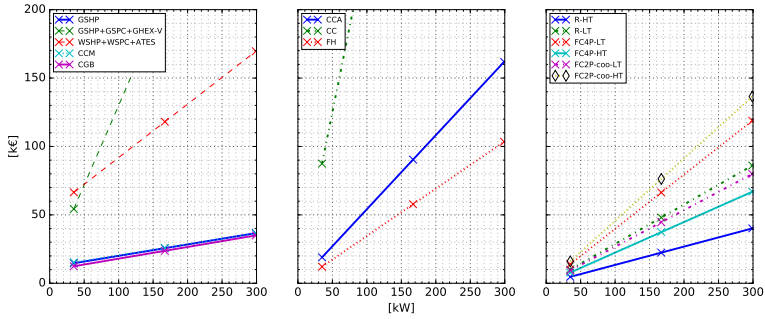

Figure 10.3: Cost function of each component included in the database. 30 W/m for the borefield and 40 W/m^2 (heating) for CCA are assumed to convert the cost function variable to kW. All powers correspond to the nominal heating power of the device, except for *FC2P-coo-LT* and *FC2P-coo-HT* for which the nominal cooling power is used instead. The meaning of the legend entries can be found in table 10.1 and the data used to derive the cost functions are presented in appendix A.

Table 10.2: Efficiencies of production components based on values from technical datasheets (TS) and Annex 48 [19]. In case of GSHP, the given efficiency corresponds to the SPF assuming a circulation pump power of 2.5% of the heat pump thermal power. The COP is given in brackets and it is evaluated for a source temperature of 5°C.

	Efficiencies [-]								
	30	35	45	60	10	15	20	[°C]	
CGB	1.06	1.06	1.02	0.98	-	-	-		(*1)
GSHP	4.91	4.44	3.55	2.62	-	-	-		(*2)
	(5.60)	(5.00)	(3.90)	(2.80)					
GSPC	-	-	-	-	-	20.00	20.00		
CCM	-	-	-	-	3.90	4.30	4.70		(*3)

(*1) from TS: Riello [123]. (*2) from TS: AlphaInnoTec [2], Carrier [27], Viessmann [161], Daikin, Stiebel-Eltron.
(*3) from Annex 48 [19].

and the extra heat losses of heat emitters embedded in the building structure towards the outside.

Table 10.3: Parameters of emission components. Nominal conditions are given as $T_s/T_r/T_a$ with T_s, T_r and T_a the supply, return and zone air temperatures. The power ratio column indicates the ratio between cooling and heating powers for reversible systems and the last column introduces a correction factor for the energy use of the emission system to represent the suboptimality of its control.

	Nominal conditions (°C)		Power ratio	η_{HVAC}
	Heating	Cooling	Cooling/heating	(*3)
CCA	30/-/-	20/-/-	125% (*1)	0.83
FH	35/-/-	20/-/-	30% (*2)	0.83
HTR	60/50/20	-	-	0.91
LTR	45/35/20	-	-	0.91
FC4P-HT	60/50/20	10/15/25	60%	1
FC4P-LT	45/35/20	15/20/25	63%	1
FC2P-coo-HT	-	15/20/25	-	1
FC2P-coo-LT	-	10/15/25	-	1

(*1) It is assumed that CCA can provide a maximum of 40 W/m^2 for heating and 50 W/m^2 for cooling
(*2) It is assumed that FH can provide a maximum of 100 W/m^2 for heating and 30 W/m^2 for cooling
(*3) Taken from NBN EN15316-2-1:2007 [149]

10.5 Results

In this section, two types of scenarios are considered: i) the so-called *minimum scenarios* (`M-Sce`) which are composed of one single production system for heating and one for cooling, each coupled to its own emission system (see section 10.5.1), and ii) so-called *hybrid scenarios* (`H-Sce`) composed of two heating and two cooling systems (see section 10.5.2). For both `M-Sce` and `H-Sce`, their PC over 20 years and their yearly CO_2 emissions are compared for different parameter values. In the case of `M-Sce`, the PC only depends on the maximum heating ($P_{\text{h,max}}$) and cooling ($P_{\text{c,max}}$) powers, and on the total yearly amount of heating (E_h) and cooling energy (E_h) delivered to the building. Additionally, the building floor surface area (A_{floor}) and the ground thermal conductivity (λ_g) can influence the scenarios PC if it uses CCA and a GSHP. In the case of `H-Sce`, the shape of the LDC is also important as it defines the ratio between the energy covered by the base load system and the energy covered by the peak load system.

In order to limit the degrees of freedom, the parametric space is represented in this work by five parameters: $P_{\text{h,max}}$, FLH_h, α, P_{spe}, and λ_g. FLH_h is the number of full load hours that the heat production system runs per year.

Multiplying $\mathrm{FLH_h}$ with $P_{\mathrm{h,max}}$ gives thus E_h. The parameter α is defined as $\alpha = E_c/E_h$ and its value indicates whether the building is heating ($\alpha < 100\%$) or cooling dominated ($\alpha > 100\%$) or in thermal balance ($\alpha = 100\%$). Note that a GEOTABS-scenario (`GEOTABS-M-Sce`) (i.e. a scenario only composed of a GSHP, a GSPC and CCA) with $\alpha = 100\%$ does not have a borefield with a balanced heating and cooling load as a fraction of the heat comes from the electricity use of the GSHP and not from the ground. In this work, α is varied by changing the ratio $P_{\mathrm{c,max}}/P_{\mathrm{h,max}}$ while the number of full load hours of the cold production device (FLH_c) is always kept equal to $\mathrm{FLH_h}$. The influence of A_{floor} is represented by the maximum specific power per unit floor area: $P_{\mathrm{spe,h}} = P_{\mathrm{h,max}}/A_{\mathrm{floor}}$. Finally, λ_g is used as an indicator of the ground suitability for GSHP systems. The values of these five parameters are taken from realistic ranges for large Belgian buildings (see table 10.4). The range for $P_{\mathrm{h,max}}$ is further chosen such that the cost functions of the production components are always evaluated within their validity ranges, even when hybrid systems are installed (see section 10.5.2), and $P_{\mathrm{spe,h}}$ is kept equal to 27 W/m^2 for `M-Sce` to ensure that the maximum heating and cooling powers can be provided by CCA without auxiliary emission systems, even for the maximum value of $\alpha = 150\%$.

For the reader's convenience, the meaning of the different symbols and abbreviations used thoroughout this chapter are summarized in tables 10.1, 10.4 and 10.5. Figures 10.5-10.10 furthermore use the following convention for the legend entries: each keyword separated by '/' represents an HVAC component installed in the scenario, and the number following the keyword indicates its nominal power as a fraction of $P_{\mathrm{h,max}}$ for heating devices and $P_{\mathrm{c,max}}$ for cooling devices. For example, for a LDC with $P_{\mathrm{h,max}} = P_{\mathrm{c,max}} = 150$ kW, GSHP0.75/CGB0.25/GSPC1/R-HT0.25/CCA means that the scenario is composed of a GSHP of 112.5 kW, a CGB of 37.5 kW, R-HT with a total power of 37.5 kW and CCA (for which no fraction is given as CCA is assumed to always cover the whole building floor surface area).

10.5.1 Results for single production/single emission scenarios

In this section, scenarios (`M-Sce`) composed of a single heat and single cold production system, each coupled to its own emission system, are considered.

Figure 10.4 plots the PC of each `M-Sce` for the different parameter values of table 10.4. Each row assumes a different $\mathrm{FLH_h}$ and λ_g, each column a different α while the x-axes specify $P_{\mathrm{h,max}}$, and each line represents a different `M-Sce`. The lines representing `GEOTABS-M-Sce` are plotted in *green* with *square* markers and the lines referring to the most conventional scenario type (`Conv-M-Sce`) (composed of a CGB, a CCM and FC4P-HT) are plotted in *red* with *diamond*

Table 10.4: Symbol, units, description and possible values of the different parameters used in section 10.5.

Symbol	Units	Description	Considered values
$P_{\mathrm{h,max}}$	$[kW]$	Maximal heating power	$[150, 250]$
$\mathrm{FLH_h}$	$[h]$	Full load hours (heating)	$[500, 1750, 2500]$
α	[%]	Cooling to heating energy ratio	$[0, 50, 80, 100, 150]$
λ_g	$[W/(m.K)]$	Ground conductivity	$[1.8, 2.4]$
$P_{\mathrm{spe,h}}$	$[W/m^2]$	Maximum heating power per floor surface area	$[27,70^{(*1)}]$

(*1) this value is only used in section 10.5.2, not in section 10.5.1.

Table 10.5: Description of the abbreviations used in section 10.5. When the abbreviation is followed by a star (*), it indicates that the scenario is cost optimal compared to the scenarios of the same type.

Abbr.	**Description**
`Sce`	HVAC scenario(s) containing some heat/cold production and emission systems.
`M-Sce`	Minimal `Sce`: `Sce` containing only one heat, one cold production system, each coupled to its own emission system. (*1)
`H-Sce`	Hybrid `Sce`: `Sce` containing max two heat and max two cold production systems, each coupled to its own emission system. (*1)
`GEOTABS-M-Sce`	`M-Sce` only composed of GSHP/GSPC/CCA.
`Conv-M-Sce`	Conventional `M-Sce` only composed of CGB/CCM/ FC4P-HT.
`Geo-Sce`	`Sce` with at least one geothermal production system.

(*1) In case of reversible emission system, one heat and one cold production system can be coupled to the same emission system.

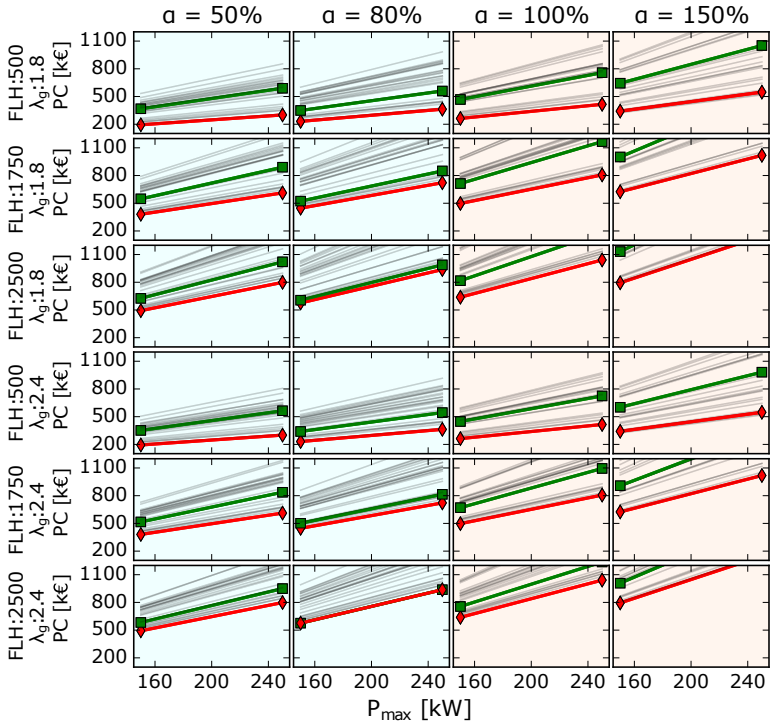

Figure 10.4: PC of `M-Sce` for the different parameter values of table 10.4. The blue backgrounds indicate that borefield of the `Geo-Sce` is heating dominated (more energy extracted than injected). The lines representing `GEOTABS-M-Sce` are plotted in *green* with *square* markers and the lines referring to the most conventional scenario type (`Conv-M-Sce`) are plotted in *red* with *diamond* markers.

markers. Finally, the background of the graphs is set in blue if `GEOTABS-M-Sce` extract more heat from the ground than they inject (i.e. the borefield is heating dominated) and in orange otherwise.

From fig. 10.4, it appears that, in general, `Conv-M-Sce` are the most cost efficient `M-Sce` that can be installed. When only a low cooling load is required ($\alpha = 50\%$), `Conv-M-Sce` are a factor 1.0 to 1.7 cheaper than `GEOTABS-M-Sce` and for cooling dominated buildings ($\alpha = 150\%$), the factor varies between 1.2 to 1.8. Only the cases when the cooling and heating loads of the borefield are in balance (i.e.

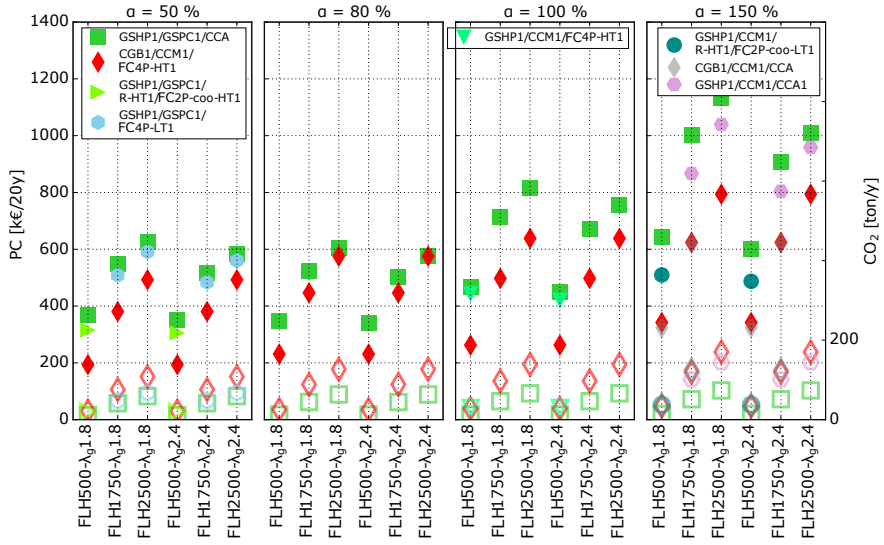

Figure 10.5: PC (filled markers) and CO_2 emissions (unfilled markers) of `GEOTABS-M-Sce`, `Conv-M-Sce`, `Geo-Sce`*, and `M-Sce`*.

$\alpha = 82\%$ for a COP=5.6) and when the building uses a minimum of 1750 FLHs, `GEOTABS-M-Sce` are financially advantageous (up to a factor 1.1 for the highest λ_g and FLH). Interestingly, the lines representing the different `M-Sce` do not cross each other for different $P_{\text{spe,h}}$ which means that the cost optimal `M-Sce` (`M-Sce`*) for the investigated parameter values do not depend on $P_{\text{spe,h}}$. The cooling dominated columns of fig. 10.4 ($\alpha \geq 100\%$) further indicate that other `M-Sce` than `Conv-M-Sce` can be cost optimal. This is illustrated in fig. 10.5.

Figure 10.5 contains the same information as fig. 10.4 evaluated at $P_{\text{h,max}} = 150$ kW but the CO_2 emissions are added to the figure. The left y-axis represents the PC (filled markers) of the `M-Sce` (in €/20y) and the right y-axis returns the CO_2 emissions (unfilled markers) in ton/1y, the x-axes indicate the number of FLH_h and λ_g, and each subplot corresponds to a different α value. For each condition, the `GEOTABS-M-Sce` and the `Conv-M-Sce` are plotted with *green square* markers and *red diamond* markers, respectively. Additionally, `M-Sce`* and the cost optimal geothermal scenario (`Geo-Sce`*) are also included if they differ from `GEOTABS-M-Sce` and `Conv-M-Sce`. Finally, the CO_2 emissions of each plotted scenario are represented by the same (but unfilled) marker and their value is to be read on the right axis.

Figure 10.5 shows that when a large amount of cooling is required (α is high),

`GEOTABS-M-Sce` are systematically (much) more expensive than `Conv-M-Sce` despite the fact that cooling with `GEOTABS-M-Sce` is more energy efficient (EER=20) than with `Conv-M-Sce` (EER=3.9). This is due to the fact that the borefields of `GEOTABS-M-Sce` with $\alpha \geq 100\%$ are sized according to the cooling load which leads to larger, thus (much) more expensive, borefields. By sizing the borefield only for the heating load and covering the cooling load with a CCM (GSHP1/CCM1/CCA1 markers in fig. 10.5), the scenario price could be decreased by a factor up to 1.3. The cost of the `Geo-Sce` can further be reduced by allowing a hybrid design such that the borefield would deliver only a fraction of the cooling load (see section 10.5.2). Similarly, the FC4P-HT are becoming very expensive when they are used for unbalanced loads. The scenarios GSHP1/CCM1/CCA1 and those combining GSHP, GSHPC, R-HT, and FC2P-coo-HT can therefore become cheaper as the use of the expensive FC4P-HT can then be avoided. In the case of a thermally balanced borefield ($\alpha = 80\%$), the `GEOTABS-M-Sce` become very advantageous and their PC drops below those of `Conv-M-Sce` for buildings using at least 1750 FLH while they emit 58% less CO_2. Finally, the use of R-LT and FC4P-LT instead of their high temperature equivalent appears not to be advantageous to be coupled to the condensing gas boiler and cooling machine as their additional investment costs are not compensated by the realized energy savings.

While `GEOTABS-M-Sce` are in general more expensive than `Conv-M-Sce`, fig. 10.5 also shows that `GEOTABS-M-Sce` emit between 64% (for $\alpha = 150\%$) and 55% (for $\alpha = 50\%$) less CO_2 than `Conv-M-Sce`.

10.5.2 Results for hybrid scenarios

This section is similar to section 10.5.1 but hybrid scenarios (`H-Sce`) are now allowed with a maximum of two heat and two cold production systems, each coupled to its own emission system (see section 10.2). `H-Sce` depend on the same parameters as `M-Sce` (see table 10.4), but the shape of the LDC now also influences their PC and CO_2 emissions. Therefore, two types of LDC are used, i.e. triangular and logarithmic, as represented in fig. 10.6. Furthermore, two different values of $P_{\text{spe,h}}$ are considered in this section (27 and 70 W/m^2, see table 10.4), as the CCA can now be complemented with a second emission system both for heating and cooling.

The following figures representing the PCs and CO_2 emissions of `H-Sce` for the different boundary conditions contain the following information. Firstly, as `H-Sce` can become a `M-Sce` if only 0% and 100% hybrid factions are used, green squares and red diamonds still represent `GEOTABS-M-Sce` and `Conv-M-Sce`, respectively. Note, however, that when $P_{\text{spe,h}} = 70$ W/m^2, `H-Sce` will not

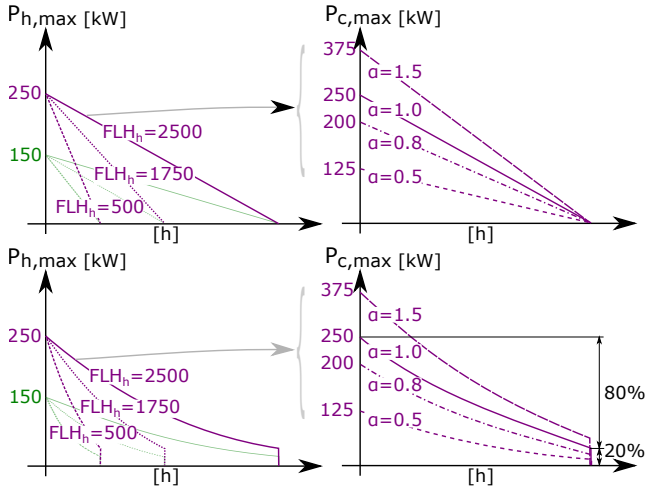

Figure 10.6: Heating (left) and cooling curves (right) with triangular (top) and logarithmic (bottom) shapes. The represented cooling curves correspond to the heating curve with $P_{\mathrm{h,max}} = 250$ kW for different α values.

contain any `GEOTABS-M-Sce` as the CCA cannot provide the thermal power without an auxiliary emission system. Secondly, the cost optimal geothermal scenario (`Geo-Sce*`) is also plotted in each figure. Finally, if the overall cost optimal `H-Sce` (`H-Sce*`) does not coincide with an already plotted scenario, `H-Sce*` is added to the figure.

Triangular LDCs The shapes of the triangular LDCs are chosen such that they correspond to the $P_{\mathrm{h,max}}$, $\mathrm{FLH_h}$, and α values of table 10.4. Figures 10.7 and 10.8 assume a P_{spe} of 27 W/m^2 and 70 W/m^2, respectively, resulting in different optimal scenarios as the CCA (if installed) is a factor 2.6 cheaper for the latter (CCA are assumed to cover a fixed 80% of the building floor surface area) but it needs to be complemented with an auxiliary emission system to provide enough thermal power.

In the case when $P_{\mathrm{spe}} = 27$ W/m^2, the results for `Conv-M-Sce` and `GEOTABS-M-Sce` are the same as in section 10.5.1. Figure 10.7 shows that, for heating dominated buildings, `Geo-Sce*` are generally composed of a combination of a GSHP (25%) and a GSPC (25%) coupled to FC4P-LT and of a CGB (75%) and a CCM (75%) coupled to FC4P-HT. Here, the `Geo-Sce*` remain a factor 1.03 to 1.28 more expensive than the `Conv-M-Sce` but emit 20% less CO_2 than `Conv-M-Sce`. For cooling dominated cases, installing a GSPC covering only a

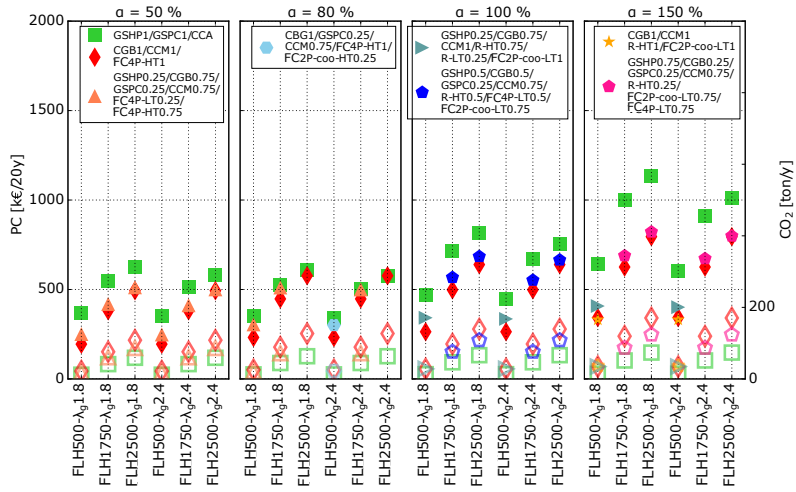

Figure 10.7: Triangular, $P_{\text{spe}} = 27$ W/m^2.

fraction of the required cooling power (25 to 50%) significantly reduces the PC cost differences between `Conv-M-Sce` and `Geo-Sce`* to such an extent that `Geo-Sce`* become the `H-Sce`* for buildings with large energy loads (2500 FLH). Furthermore, `Geo-Sce`* systematically reduce the CO_2 emission by more than 50% compared to `Conv-M-Sce`.

As illustrated by fig. 10.8, in the case when $P_{\text{spe}} = 70$ W/m^2, `Geo-Sce` coupled to CCA and FC4P-HT are the optimal scenarios `H-Sce`* when $\alpha \geq 80$ and have similar cost as `Conv-M-Sce` for $\alpha = 50\%$. For example, `Geo-Sce`* can be up to 1.1 cheaper than `Conv-M-Sce` when $\alpha = 80\%$ and up to 1.2 when $\alpha = 100\%$ while `Geo-Sce`* save in both situations around 50% of the CO_2 emissions.

Logarithmic LDCs LDCs have rather an (inverted) logarithmic shape than a triangular shape and this paragraph therefore investigates the cost optimality of HVAC scenarios for LDCs described by $f(x) = \gamma - \beta(x - \xi)$ with x the number of hours and $f(x)$ the heating power. The parameter ξ influences the steepness of the curve and γ and β are calculated such that the different LDCs correspond to the parameter values of table 10.4, and such that the LDCs tail is cut at $P = 0.2P_{\text{max}}$ (see fig. 10.6). The results are again analysed for $P_{\text{spe}} = 27$ and 70 W/m^2(see figs. 10.9 and 10.10).

The results for logarithmic LDCs are very similar to those for the triangular LDCs. However, where the `Geo-Sce`* from the triangular LDCs would most of

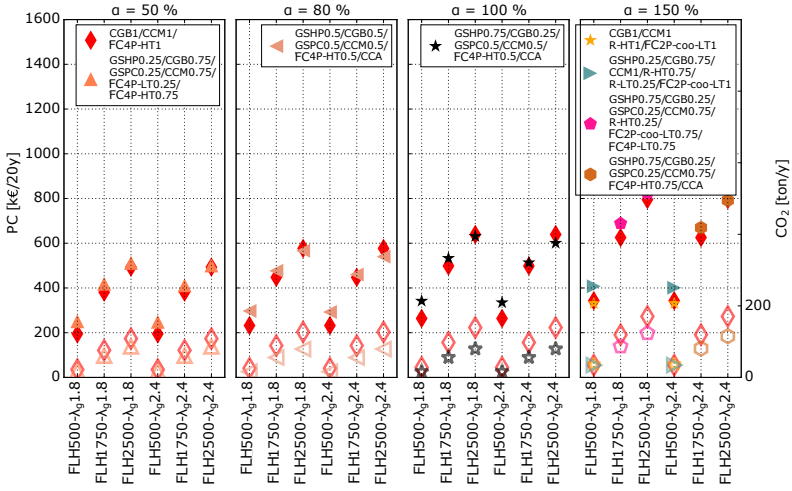

Figure 10.8: Triangular, $P_{\text{spe}} = 70$ W/m^2.

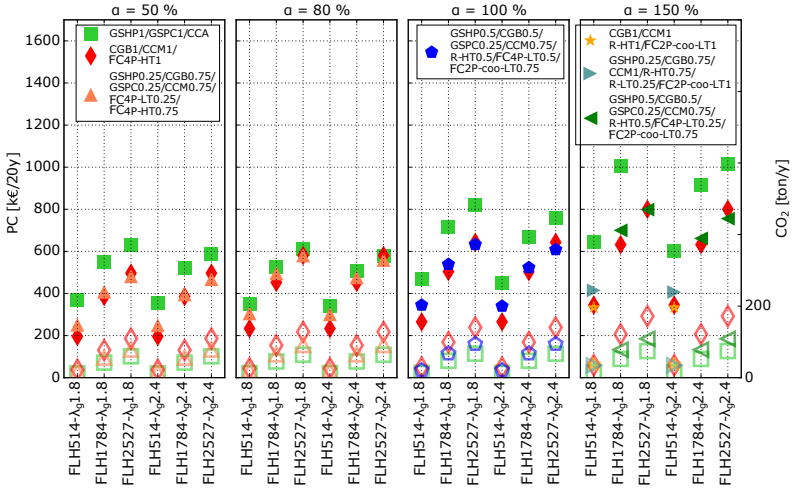

Figure 10.9: Logarithmic, $P_{\text{spe}} = 27$ W/m^2.

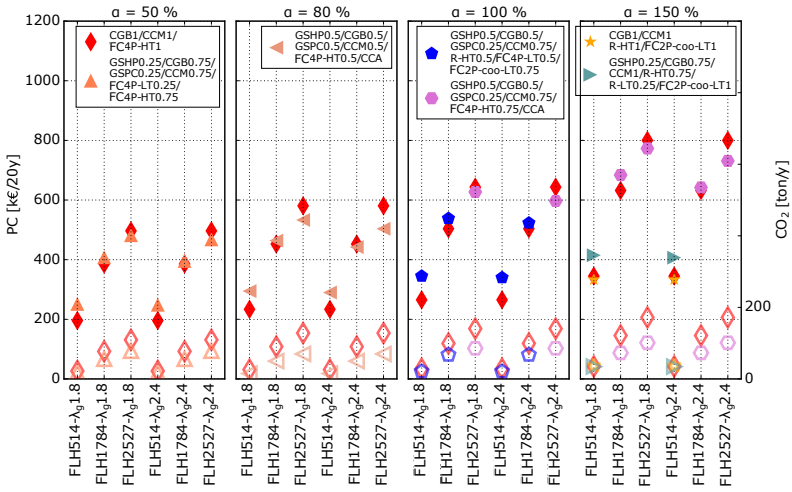

Figure 10.10: Logarithmic, $P_{\text{spe}} = 70$ W/m^2.

the time size its GSHP to 75% and its GSPC to 50 or 25%, the `Geo-Sce*` from the logarithmic LDCs would rather size them to 50% and 25%, respectively. This is a logical result as the number of FLH for the higher thermal powers decreases faster for logarithmic LDCs than for triangular ones. This also results in a lower PC for the `Geo-Sce` with logarithmic LDC while `Conv-M-Sce` and `GEOTABS-M-Sce` remain the same. For example, the `Geo-Sce*` is 1.25 times cheaper than `Conv-M-Sce` when FLH=2527 h, $\lambda_g = 2.4$ W/(m.K) and $P_{\text{spe}} = 70$ W/m^2 and still saves 50% of the CO_2 emissions.

10.6 Conclusion

This chapter presents a tool developed in Python to automatically compute the present cost (PC) and CO_2 emissions of all possible HVAC designs of a given building composed of the devices contained in the database. The tool was used to investigate when HVAC systems using a vertical ground heat exchanger (GHEX-V) become economically interesting and to compare their CO_2 emissions to those of a conventional HVAC system which uses a condensing gas boiler, a compression cooling machine and reversible high temperature four pipes fan coil units.

It was found that pure GEOTABS systems (i.e. an HVAC system composed of

a GSHP system coupled to CCA) are generally 1.0 to 1.8 times more expensive than a conventional HVAC system when the GHEX-V is not in thermal balance but that pure GEOTABS systems have the lowest PC of all possible scenarios when ground thermal balance is reached and the building uses its GSHP system for at least 1750 full load hours (FLH) per year. For all cases, pure GEOTABS systems save more than 50% of CO_2 emissions compared to a conventional one.

It was further shown that, instead of installing pure GEOTABS systems, combining a GSHP system with TABS to cover the base load of the building and a condensing gas boiler and a cooling machine with fan coil units and/or radiators, results in hybrid GEOTABS systems with an PC that is lower than or similar to the PC of a conventional system, while still between 20% to more than 50% of CO_2 emissions are saved. Hybrid GEOTABS concepts are thus very advantageous both economically and for the environment. Therefore, it is advised to always consider their installation for large buildings.

Part V

Conclusion and further research

Chapter 11

Conclusion

The main objective of this work was:

> *To improve the thermal comfort, the energy efficiency and the economic viability of large hybrid GEOTABS buildings.*

To this end, different models and new tools have been developed in order to reach the objective and to answer the related research questions using an integrated approach where the building envelope, its HVAC system, its occupancy and its control were all taken into account simultaneously.

Firstly, a model for borefields with arbitrary configuration has been developed and validated for both short-term (minutes) and long-term (decades) accuracy. The model is also computationally very efficient and modelled in Modelica based on the `Fluid` and `Media` packages of the Modelica Standard Library. It can therefore be coupled to full building energy simulation (BES) models developed with the Modelica library `IDEAS`. Four building models were further developed with `IDEAS` representing an existing office, retirement home, school, and block of flats and the building envelope model of the office building was successfully validated against measurements from the real building. The different building models are therefore considered to be a realistic representation of the thermal behaviour of real buildings. While the four buildings are all low energy and massive buildings and all equipped with a GSHP and TABS, their HVAC and building envelope design and their occupancy profiles vary widely which allows the generalization of the conclusions of this work to a wide range of (large) buildings. As the tools and libraries to model these buildings in Modelica with the required level of complexity were not available, this work contributed

to the development of the KU Leuven open-source library `IDEAS`, and to the open-source library `Annex60` (which is now further developed under the new name `IBPSA`). Secondly, this work developed a new method to linearise the building envelope of the developed Modelica models in order to obtain highly accurate controller models for model predictive controllers (MPC). The method automatically precomputes the non-linear equations which do not depend on the model states and linearises the other equations. The obtained controller models are then used by a toolchain which semi-automatically generates a linear MPC for the considered building. The generated MPC optimizes the thermal powers to TABS and auxiliary systems and the ventilation supply temperature, assuming thus the existence of subcontrollers controlling the different HVAC devices. Therefore, as the control of individual HVAC components is not optimized by the MPC, a analytical solution for the optimal mass flow rate in borefields was proposed. The solution maximizes the total energy efficiency of GSHP systems (i.e. the energy used by the circulation pump and by the heat pump compressor) as a function of measurable variables and system parameters available from typical manufacturer datasheets. Finally, a python tool was created to optimize both the choice and the size of the HVAC components based on the total net present cost (PC) of the HVAC system or the total CO_2 emissions.

The novelties of the developed models and tools are the following. Firstly, while many borefield models exist and while the model in this PhD work is itself based on different models from the literature, it is the first to combine state-of-the-art short- and long-term borefield models and aggregation technique (which speeds up the computations) into one single, practical model and to program it in Modelica such that it can be coupled to different BES Modelica libraries. Secondly, while different methods exist to linearise BES models, the methodology developed in this work goes several steps further by: i) being integrated in the BES `IDEAS` library allowing the user to easily switch between the most accurate but non-linear model formulation to the linear one, ii) being part of a whole toolchain which largely automates the generation and simulation of linear MPCs for buildings, and iii) going to a, so far unachieved, level of details in the linearisation and pre-computations of the non-linear equations resulting in very accurate linear models. Thirdly, thank to the automation of the toolchain, this work is the first to investigate in details the saving potential of MPC for hybrid GEOTABS systems not only for one building type but several while using a unique methodology, making the inter-comparison more meaningful. Furthermore, the developed MPCs can simultaneously control both the thermal powers to the TABS and to the auxiliary system and the supply temperature of the on/off controlled ventilation, which is rarely the case of MPCs presented in the literature. Fourthly, this work is one of the very few ones proposing an optimal flow rate in borefields which maximizes the GSHP

system effiency. Finally, the introduced tool to optimize HVAC designs is novel in its simple and easy-to-understand approach while the generated results are very informative and helpful for design engineers.

Based on the main objective, seven specific research questions were formulated focussing on the *feasibility* of hybrid *GEOTABS* systems, on their *control* and on their *design* (see section 1.2). Each research question is answered in the following paragraphs using the models and tools developed.

The **feasibility of (hybrid) GEOTABS systems** for office buildings, schools, retirement homes, and block of flats was assessed by evaluating the thermal comfort of the different building models provided that controlled by a RBC and by different MPCs. It was found that, for all investigated buildings, a very high thermal comfort was achieved when controlled by MPC. This means that (hybrid) *GEOTABS* systems can technically be successfully used for a wide variety of building (and occupancy) types when appropriate control is implemented. When a traditional RBC is used, a too low controllability of the building, such as the block of flats which was only equipped with TABS and with an unconditioned air handling system, or a too large difference of thermal needs between the different zones, such as the investigated school with a renovated and a non renovated building part, leads to a low thermal comfort satisfaction. If *GEOTABS* is installed in such a building, MPC might be necessary to meet the thermal comfort requirements.

The **control of GEOTABS buildings** was an important part of the research in this work. The RBC and MPC simulations were analysed to estimate how much energy use and energy cost can be saved and how much thermal comfort can be gained in (hybrid) GEOTABS buildings when the building is controlled by MPC instead of RBC. Savings between 30% to 50% for the energy cost and between 28 and 53% for the energy use were found. These high savings contrast to the values found in the literature (between 15% to 25%) both for studies carried on BES software and for studies on real buildings. This is probably due to the excellent predictions of the controller model compared to approaches using a black-box, a grey-box or a low order white-box controller model where significant model mismatch leads to sub-optimality and to the fact that perfect disturbance predictions were used.

The minimum controller model accuracy required to avoid MPC to be significantly suboptimal was also investigated. To this end, the accuracy of the controller model was artificially decreased by applying model order reduction to transform the model into reduced order models (ROM) of different orders. It was found that the controller model should contain a minimum of states to model each zone separately, and that the walls and floors separating the zones should also have enough states to act as a low pass filter with correct cut-off

frequency. The minimum number of states further increases with the building mass content. In the case of the investigated 6-room house, the thermal comfort achieved by MPC using a controller model with a minimum of 30 states instead of 20 states was improved with a factor 2 to 6 without significant increase of the energy use, showing that good MPC performances require controller models with a significantly higher number of states than the order used by most of the black- and grey-box system identification techniques. It was further shown that the computational effort required to solve the optimization problem becomes independent on the number of states of the controller model when a dense approach is used. The controller model can thus be as complex as necessary to generate accurate predictions without increasing the solving time.

Developing an MPC to control the climate of a building is usually more time consuming and requires more expert knowledge than the implementation of a typical RBC. However, more complex and hybrid HVAC systems turn also the tuning of RBC into a challenge that requires time and expert knowledge. In order to investigate whether ideally tuned, heating/cooling curves based RBCs could score (nearly) as well as MPC, it was checked whether the correlation between the thermal powers computed by MPC and the past (or future) average ambient temperature or solar gains was high. The correlation R-values found between the TABS heating powers and the average past ambient temperature were, however, only between 0.6 to 0.8 for MPCs (and above 0.9 for RBCs) when evaluated for Tuesdays, Wednesdays and Thursdays and even lower for the other days. Using the predicted average ambient temperature improved the correlation for some buildings (R-value between 0.8 and 0.9) but not for all. The cooling power correlation was even much lower (between 0.2 and 0.6). The heating and cooling power profiles obtained by MPC seemed therefore not to be achievable by RBC using simple heating/cooling curves.

Finally, this work also looked into the **HVAC design of GEOTABS building**. The different MPC simulations showed that when the building is optimally controlled, a pure GEOTABS concept (i.e. no auxiliary emission system beside the TABS and no conditioned ventilation) is capable of maintaining good thermal comfort. However, when MPC could optimize both the ventilation supply temperature and the thermal powers to the TABS and the auxiliary system simultaneously, additional energy cost savings of 6 to 11% were realised compared to the case where only TABS were optimized. When RBCs are used instead, controlling the ventilation supply temperature might also substantially increase the achieved thermal comfort as it fast reaction time can complement the slow reacting TABS well, and it is therefore highly recommended to install an air handling unit with heating and cooling coils in GEOTABS buildings. However, using auxiliary emission systems such as radiators showed no added value when the building was optimally controlled since the ventilation was

sufficient to assist the TABS, even when the supply ventilation temperature was constrained conservatively to ±1 °C the comfort bounds.

From the CO_2 emissions and the economic (using the present cost (PC) of the system of 20 years with a discount factor of 4%) analysis of HVAC systems, it was found that pure GEOTABS systems (i.e. an HVAC system composed of a GSHP system coupled to CCA) are generally 1.0 to 1.8 times more expensive than a conventional HVAC system when the GHEX-V is not in thermal balance but that pure GEOTABS systems have the lowest PC of all possible scenarios when ground thermal balance is reached and the building uses its GSHP system for at least 1750 full load hours (FLH) per year. For all cases, pure GEOTABS systems save more than 50% of CO_2 emissions compared to a conventional one. It was further shown that, instead of installing pure GEOTABS systems, combining a GSHP system with TABS to cover the base load of the building and a condensing gas boiler and a cooling machine with fan coil units and/or radiators, results in hybrid GEOTABS systems with an PC that is lower than or similar to the PC of a conventional system, while still between 20% to more than 50% of CO_2 emissions are saved. Hybrid GEOTABS concepts are thus very advantageous both economically and for the environment. Therefore, it is advised to always consider their installation for large buildings.

Chapter 12

Further research

Research is rarely closed at the end of a PhD but it rather opens new paths for further studies. This chapter proposes a series of improvements and possible tracks to continue this work.

First of all, this work has demonstrated the high savings potential of MPC for (hybrid) GEOTABS buildings and it proposes a novel methodology to design such controllers. The developed MPCs should now be applied to real buildings to confirm the promising simulation results. However, the practical implementation gives rise to several challenges which have not been handled in this work. Beside the technical challenges such as the communication between the optimization algorithm and the building sensors and actuators, the first challenge to tackle is robustness. The MPC needs to be able to run uninterruptedly for long periods of time and to be robust against sensors and actuators inaccuracy or failure, weather predictions inaccuracy, uncertainties about the occupancy gains and the occupant behaviour, and potentially a non-negligible model mismatch. Secondly, subcontrollers translating the high level MPC control variable such as thermal powers into low level control variables such as mass flow rates, valve positions or modulation ratios need to be developed. Finally, a state estimator needs to be added and the MPC could be made adaptive. These different challenges will be tackled by the GEOTABS$^{\text{hybrid}}$ project [56].

Beside the demonstration of the developed framework, the automation of the toolchain should also be improved in order to make MPC commercially interesting. While the current toolchain allows a rapid generation of MPCs once the Modelica building model based on the `IDEAS` library is available, creating such Building Energy Simulation (BES) model remains a highly time consuming task. This obstacle could be alleviated by the increasingly popular Building

Information Modelling (BIM) standard. BIM contains all geometrical and thermal information from the architectural drawings of the building as well as the technical information necessary for the heating, cooling and ventilation system and BIM is usually available from the architect company. The BIM data can then be used to automatically generate BES models [4]. Additionally, the current toolchain, which only allows the creation of linear MPCs, should be extended to allow non-linear cost functions in order to take the behaviour of the HVAC system better into account. Furthermore, a library of HVAC component models suitable for optimization could be added to the framework to further automate the creation of MPCs. Finally, the development and improvement of the `IDEAS` library, which is used both to simulate BES models and to retrieve controller models should be continued with particular attention to the modelling of air flows and ventilation units in buildings.

At the component level, the user friendliness of the borefield model can be improved. In its current implementation, simulating a borefield requires a one-time manual initialization by the user who has to run a script. The script is used to precompute the short-term temperature step response of the ground directly surrounding the boreholes by running a separate modelica model with the same parameters as those of the borefield model. The use of this second modelica model can be avoided by replacing it by a infinite cylindrical source model [28] which can be automatically computed at the initialization time of the borefield. The improved borefield model should then be added to the `IBPSA` library.

At the component control level, the optimal solution found for the mass flow rate in borefields which maximizes the GSHP system performance should be tested in an actual system. A sensitivity analysis should also be added as well as guidelines helping designers to choose an appropriate flow rate for the installed system.

Finally, the HVAC design tool should be extended to include more components and to enable the generation of load duration curves of the building thermal needs based on a small number of parameters.

Appendix A

Cost function for HVAC components

In this appendix, cost data of 18 recently built buildings (10 offices, 7 retirement homes, and 1 school) from two different engineering companies (Boydens Engineering [21] and Ingenium n.v. [75]) are transformed into cost functions for HVAC components. The cost functions return the component (installed) price as a function of its nominal power or size and the function is derived from an optimal linear fit on the available data. For the production components (see appendix A.1), the fit uses a slope and an offset ($f(x) = \alpha x + \beta$) and extrapolation is not allowed (except for the vertical ground heat exchanger). Instead, several components of the same size are installed if the requested size is larger than the largest size used for the fit and the minimum size is installed if the requested power is too small. For the emission components (see appendix A.2), the fit does not have an offset ($f(x) = \alpha x$) and extrapolation is permitted.

The following sections give the cost functions of all production and emission components used in chapter 10. For each component, a figure is given containing all data points, the linear fit, the cost function, and the component price per kW evaluated at 100 kW. Furthermore, two different types of marker are used to refer to the different engineering offices (EO) but it is left unspecified which marker refers to which EO, as requested by the companies. Finally, only the data of typical components are used to avoid a too high uncertainty on the cost. For example, only flat plate steel radiators are included, as decorative radiators may cost twice as much for the same nominal power.

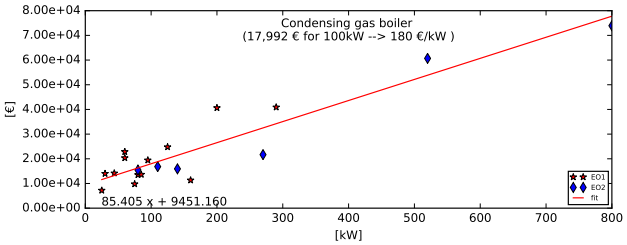

Figure A.1: Cost of condensing gas boilers with respect to the nominal power.

A.1 Production systems

Production components are in this work HVAC components which transform electricity or gas into thermal energy. This section includes condensing gas boilers (appendix A.1.1), components for GSHP systems (appendix A.1.2), and compression cooling machines (appendix A.1.3).

A.1.1 Condensing gas boiler (CGB)

Figure A.1 shows the fit for condensing gas boilers including their additional costs such as the connection to tap water and gas network, the ventilation of the fireplace, the piping work, the security measures, and the inspection of the gas company.

A.1.2 Ground source heat pump system (GSHP and GSPC)

A ground source heat pump system is typically composed of a ground source heat pump (GSHP), a vertical ground heat exchanger (or borefield, GHEX-V), and a plate heat exchanger used for passive cooling with the ground (GSPC). Figure A.2 gives the fit for GSHPs. No additional costs are included. Notice that the price variation is high. This is probably due to the different COP of the GSHPs which were, unfortunately, often not specified in the cost data. Figure A.3 depicts the fit for GHEX-V including the following costs: the drilling and filling of the boreholes, the piping work and a Thermal Response Test. The cost function returns the cost with respect to the total borehole(s) length. Finally, fig. A.4 contains the cost function of GSPC (single wall). No additional costs are included.

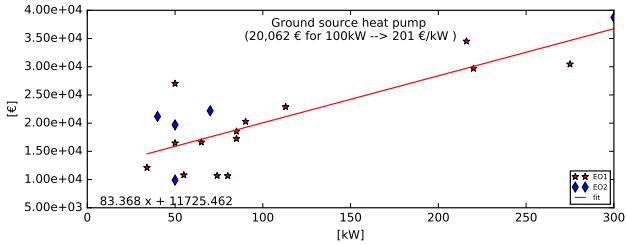

Figure A.2: Cost of ground source heat pumps with respect to the nominal power.

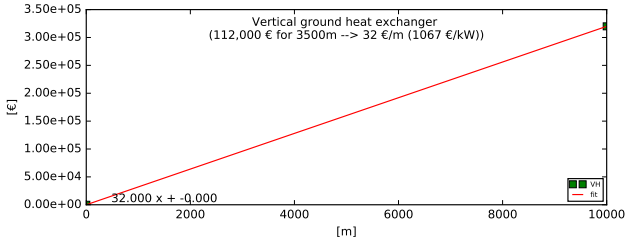

Figure A.3: Cost of vertical ground heat exchangers with respect to the total borehole(s) length.

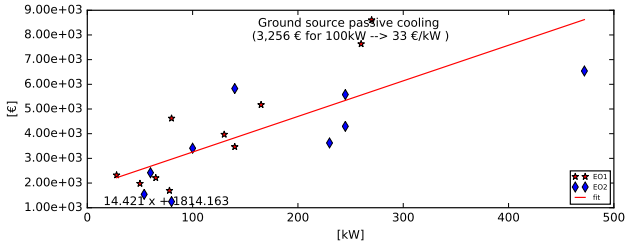

Figure A.4: Cost of plate heat exchangers with respect to the nominal power.

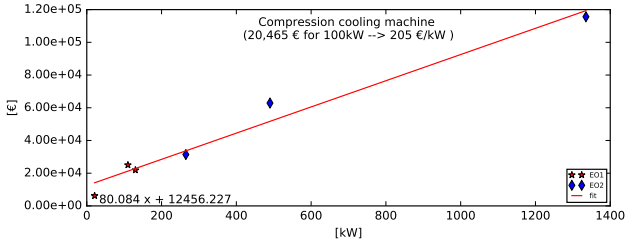

Figure A.5: Cost of compression cooling machines with respect to the nominal power.

A.1.3 Compression cooling machine (CCM)

Figure A.5 plots the fit for compression cooling machines (air/water) with no additional costs included.

A.2 Emission systems

Emission components are HVAC components which deliver the thermal energy to the building. This section includes radiators (appendix A.2.1), fan coil units (appendix A.2.2) and CCA (appendix A.2.3).

A.2.1 Low and high temperature radiators (R-LT and R-HT)

Figures A.6 and A.7 present the cost functions for high (60/50/20) and low (45/35/20) temperature radiators with $T_s/T_r/T_a$ referring to the nominal supply water (T_s), return water (T_r) and room air temperature (T_a). Both cost functions are based on the same cost data expressed according to the standard EN 442 [148] (75/65/20) and the powers P at nominal condition $T_s/T_r/T_a$ are rescaled using:

$$P_{T_s/T_r/20} = P_{75/65/20} \left(\frac{\delta_{T_s/T_r/20}}{\delta_{75/65/20}} \right)^n \quad \text{with} \quad \delta_{T_s/T_r/20} = \frac{T_s - T_r}{\ln \frac{T_s - 20}{T_r - 20}} \tag{A.1}$$

with $n = 1.3$ for radiators.

Each data point represents a steel plate heat exchanger without special features (such as decorative, etc.). No additional costs are included to be consistent with the fan coil units for which no additional costs were available.

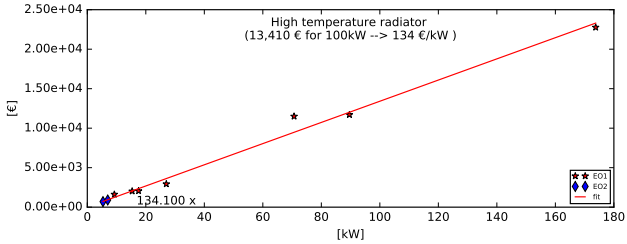

Figure A.6: Cost of high temperature flat steel plate radiators with respect to the nominal power (60/50/20).

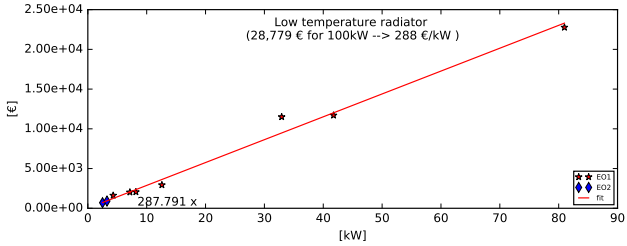

Figure A.7: Cost of low temperature flat steel plate radiator with respect to the nominal power (45/35/20).

A.2.2 Fan coil units (FCU)

The price of fan coil units does not strongly depend on the nominal power of a single FCU but rather on its type and the number of FCU installed per square meter floor area. Figures A.8 and A.9 show the cost functions of respectively high temperature (heating: 60/50/20, cooling: 10/15/25) and low temperature (heating: 45/35/20, cooling: 15/20/25) four pipes fan coil units (FCU4P-HT, FCU4P-LT). The cost functions are based on the assumption that FCU units of 2000 W (sensible cooling) at the nominal conditions 16/20/25.5 are installed, each costing 1250 €. The nominal sensible cooling power is then converted to heating power at nominal condition 75/65/20 using conversion factors found in FCU datasheets. Finally, the heating (cooling) power is converted to different nominal heating (cooling) conditions using eq. (A.1) with $n = 1$. The prices of 2 pipes cooling fan coil units are given by figs. A.10 and A.11 for respectively high temperature (FCU2P-coo-HT) and low temperature (FCU2P-coo-LT) devices. Similarly to FCU4Ps, it is assumed that units of 2000 W (sensible cooling) at the nominal conditions 16/20/25.5 are installed, each costing 900 €. The cooling power is then converted to different nominal cooling conditions using

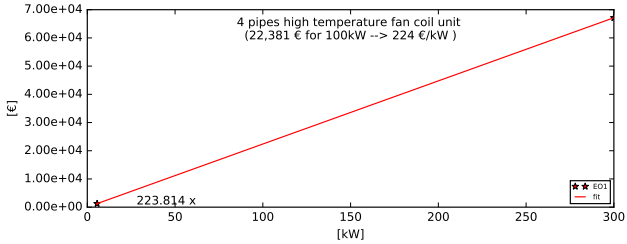

Figure A.8: Cost of high temperature 4-pipes fan coil unit with respect to the nominal heating power (60/50/20).

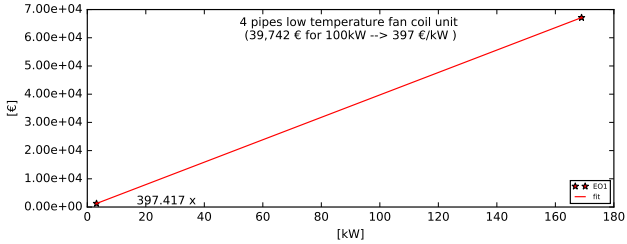

Figure A.9: Low temperature 4-pipes fan coil unit with respect to the nominal heating power (45/35/20).

eq. (A.1) with $n = 1$. Notice that the prices of FCU2P-coo are seemingly higher than those of FCU4P due to the fact that the former is expressed w.r.t. cooling power while the latter is expressed w.r.t. to heating power.

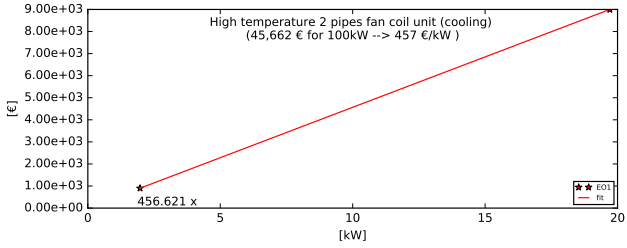

Figure A.10: Cost of high temperature 2-pipes cooling fan coil unit with respect to the nominal cooling power (15/20/25).

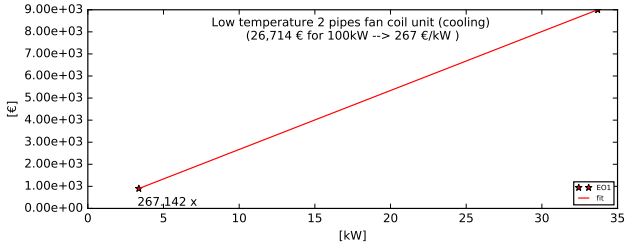

Figure A.11: Low temperature 2-pipes cooling fan coil unit with respect to the nominal cooling power 10/15/20).

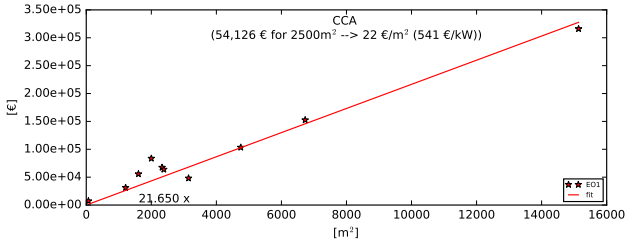

Figure A.12: Cost of concrete core activation with respect to the covered floor surface area.

A.2.3 Concrete core activation (CCA)

Figure A.12 presents the fit for concrete core activation as a function of the covered floor surface area.

Bibliography

[1] Åkesson, J., Årzén, K.-E., Gäfvert, M., Bergdahl, T., and Tummescheit, H. Modeling and optimization with optimica and JModelica.org—languages and tools for solving large-scale dynamic optimization problems. *Computers & Chemical Engineering 34*, 11 (nov 2010), 1737–1749.

[2] AlphaInnoTec. Brine/water warmtepompen, warmtecentrale brine – instalatlatie- en gebruikshandleiding. `http://www.nathan.be/uploads/public/83053100bNL_BA_WZS_1.pdf`, 2017. [Online; accessed 16-Februar-2017].

[3] Andersson, J. *A General-Purpose Software Framework for Dynamic Optimization*. PhD, Dep. of Electrical Engineering, KU Leuven, Leuven, Belgium, October 2013.

[4] Andriamamonjy, A., Klein, R., and Saelens, D. Sensor handling in Building Information Models. Development of a method and application on a case study. In *Proceedings of Building Simulation 2015* (Hyderabad, India, 2015).

[5] Armstrong, P. R., Leeb, S. B., and Norford, L. K. Control with building mass-part ii: Simulation. *Transactions-American Society of Heating Refrigerating and Air Conditioning Engineers 112*, 1 (2006), 462.

[6] ASHRAE. AHSRAE handbook – HVAC application, chap 32, geothermal energy. *American Society of Heating, Refrigerating and Air Conditioning Engineers, Atlanta* (2007).

[7] Awbi, H., and Hatton, a. Natural convection from heated room surfaces. *Energy and Buildings 30*, 3 (August 1999), 233–244.

[8] Bacher, P., and Madsen, H. Identifying suitable models for the heat dynamics of buildings. *Energy and Buildings 43*, 7 (2011), 1511–1522.

[9] Baetens, R. *On externalities of heat pump-based low-energy dwellings at the low-voltage distribution grid.* PhD thesis, Dep. of Civil Engineering, KU Leuven, 2015.

[10] Baetens, R., De Coninck, R., Jorissen, F., Picard, D., Helsen, L., and Saelens, D. OpenIDEAS - An open framework for integrated district energy simulations. In *Proceedings of Building Simulation 2015* (Hyderabad, India, 2015).

[11] Baetens, R., and Saelens, D. Modelling uncertainty in district energy simulations by stochastic residential occupant behaviour. *Journal of Building Performance Simulation 9*, 4 (2016), 431–447.

[12] Bauer, D., Heidemann, W., Müller-Steinhagen, H., and Diersch, H.-J. G. Thermal resistance and capacity models for borehole heat exchangers. *International Journal of Energy Research 35* (2011), 312–320.

[13] Beier, R. A. Transient heat transfer in a U-tube borehole heat exchanger. *Applied Thermal Engineering 62*, 1 (2014), 256–266.

[14] Beier, R. A., Smith, M. D., and Spitler, J. D. Reference data sets for vertical borehole ground heat exchanger models and thermal response test analysis. *Geothermics 40* (2011), 79–85.

[15] Bengea, S. C., Kelman, A. D., Borrelli, F., Taylor, R., and Narayanan, S. Implementation of model predictive control for an HVAC system in a mid-size commercial building. *HVAC and Research 20*, 1 (2014), 121–135.

[16] Bennet, J., Claesson, J., and Hellstrom, G. Multipole method to compute the conductive heat transfer to and between pipes in a composite cylinder. Notes on Heat Transfer 3-1987. Department of Building Physics, Lund Institute of Technology, Lund, Sweden.

[17] Bernier, M. A., and Bourret, B. Pumping energy and variable frequency drives. *ASHRAE Journal 41*, 12 (1999), 37–40.

[18] Bertagnolio, S., Bernier, M., and Kummert, M. Comparing vertical ground heat exchanger models. *Journal of Building Performance Simulation 1* (2012), 1–15.

[19] Bertagnolio, S., Stabat, P., Caciolo, M., and Corgier, D. *IEA ECBCS Annex 48 Reversible Air-Conditioning: Review of heat recovery and heat pumping solutions.* Annex, 2011.

[20] Bockelman, F., Plesser, S., and Soldaty, H. *Advanced system design and operation of GEOTABS buildings.* Rehva, 2013.

[21] Boydens Engineering. Building services and sustainable engineering office. http://www.boydens.be/en/home-2.html. [Online; accessed 19-May-2016].

[22] Braun, J. E. Load control using building thermal mass. *Transactions-American Society of Mechanical Engineers Journal of Solar Energy Engineering 125*, 3 (2003), 292–301.

[23] Braun, J. E., and Lee, K.-H. An experimental evaluation of demand limiting using building thermal mass in a small commercial building. *ASHRAE Transactions 112*, 1 (2006a), 559–571.

[24] Brinsfield, R., Yaramanoglu, M., and Wheaton, F. Ground level solar radiation prediction model including cloud cover effects. *Solar Energy 33*, 6 (1984), 493–499.

[25] Brugeo. La géothermie - Un potentiel énergétique à mieux exploiter bruxelles. http://geothermie.brussels/. [Online; accessed 30-May-2017].

[26] Carrier. GZ Infinity Series, Geothermal Split Heat Pump. http://www.utcccs-cdn.com/hvac/docs/1009/Public/00/GZ-02PD.pdf, 2016. [Online; accessed 12-August-2016].

[27] Carrier. Water-sourced liquid chillers/heat pumps with or without integrated hydronic module. 61 WG/30WG. http://carrierab.se/media/49347/16121_psd_02_2012_61wg_30wg_lr.pdf, 2017. [Online; accessed 16-Februar-2017].

[28] Carslaw, H. S., and Jaeger, J. C. *Conduction of Heat in Solids*. Oxford University Press, UK, 1959.

[29] Cheap GSHPs. Cheap and efficient - Application of reliable ground source heat exchangers and pumps. http://cheap-gshp.eu/. [Online; accessed 30-May-2017].

[30] Chiasson, A. *Simulation and design of hybrid geothermal heat pump systems*. PhD, Dep. Civil and Architectural Engineering, University of Wyoming, Laramie, USA, 2007.

[31] Cigler, J., Siroky, J., Korda, M., and Jones, C. On the selection of the most appropriate MPC problem formulation for buildings. In *Proceedings of the 11th REHVA World Congress CLIMA 2013* (Prague, Czech Republic, 2013).

[32] Claesson, J., and Javed, S. An analytical method to calculate borehole fluid temperatures for time-scales from minutes to decades. *ASHRAE Transactions 117, Part 2* (2011), 279–288.

[33] Claesson, J., and Javed, S. A load-aggregation method to calculate extraction temperatures of borehole heat exchangers. *ASHRAE Transactions 118, Part 1* (2012), 1–10.

[34] Daikin. Smartsource two-stage horizontal & vertical water heat pumps, unit size 026-072. `http://lit.daikinapplied.com/bizlit/DocumentStorage/WaterSourceHeatPump/Catalogs/CAT_1114-6_HR_WS_SS_Two_Stage_GTH_GTV_LR.pdf`, 2016. [Online; accessed 12-August-2016].

[35] De Coninck, R. *Grey-Box Based Optimal Control for Thermal Systems in Buildings-Unlocking Energy Efficiency and Flexibility.* PhD, KU Leuven, Leuven, Belgium, 2015.

[36] De Coninck, R., Magnusson, F., Åkesson, J., and Helsen, L. Toolbox for development and validation of grey-box building models for forecasting and control. *Journal of Building Performance Simulation 9*, 3 (2016), 288–303.

[37] Defraeye, T., Blocken, B., and Carmeliet, J. Convective heat transfer coefficients for exterior building surfaces: Existing correlations and CFD modelling. *Energy Conversion and Management 52*, 1 (2011), 512 – 522.

[38] Dynasim, A. Dymola-dynamic modeling laboratory. Tech. rep., Lund, Sweden, 2017.

[39] Ellis, M., and Mathews, E. Needs and trends in building and HVAC system design tools. *Building and Environment 37*, 5 (2002), 461–470.

[40] Elmqvist, H. *Modelica - A unified object-oriented language for physical systems modeling*, 1997.

[41] Eskilson, P. *Thermal analysis of heat extraction boreholes.* PhD, Dep. of Mathematical Physics, University of Lund, Lund, Sweden, 1987.

[42] ESTMAP. Energy storage mapping and planning. `http://www.estmap.eu/`. [Online; accessed 30-May-2017].

[43] European Geothermal Energy Council. 2016 EGEC geothermal market report. Tech. rep., 2016.

[44] European Parliament. Directive 2010/31/EU of the European Parliament and of the council of 19 May 2010 on the energy performance of buildings, 2010.

[45] European Parliament. Directive 2010/31/EU of the European Parliament and of the Council of 19 May 2010 on the energy performance of buildings (recast). *Official Journal of the European Union 18*, 06 (2010), 2010.

[46] Eurostat. Gas prices for industrial consumers - bi-annual data (from 2007 onwards). Tech. rep., 2016. [Online; accessed 21-February-2017].

[47] Eurostat. Electricity prices components for industrial consumers - annual data (from 2007 onwards). Tech. rep., 2017. [Online; accessed 8-March-2017].

[48] Evins, R. Multi-level optimization of building design, energy system sizing and operation. *Energy 90* (2015), 1775–1789.

[49] Finlayson, E. U., Arasteh, D. K., Huizenga, C., Rubin, M. D., and Reilly, M. S. WINDOW 4.0: Documentation of calculation procedures. Tech. rep., Berkeley, CA, USA, 1993.

[50] Foucquier, A., Brun, A., Faggianelli, G. A., and Suard, F. Effect of wall merging on a simplified building energy model: accuracy vs number of equations. In *Proceedings of the 13th Conference of International Building Performance Simulation Association* (Chambéry, France, August 2013).

[51] Fraisse, G., Viardot, C., Lafabrie, O., and Achard, G. Development of a simplified and accurate building model based on electrical analogy. *Energy and buildings 34*, 10 (2002), 1017–1031.

[52] François, L., Van den Bossche, P., and Van Lysebetten, G. *Note d'information technique 259: Géothermie peu profonde. Conception et mise en oeuvre de systèmes avec échangeurs en forme de U.* 2016.

[53] Frison, G., and Jorgensen, J. A fast condensing method for solution of linear-quadratic control problems. In *Proceedings of 52nd IEEE Conference on Decision and Control* (December 2013), pp. 7715–7720.

[54] GEO.POWER. Geothermal project. `http://www.geopower-i4c.eu/`. [Online; accessed 30-May-2017].

[55] Geotabs. Towards optimal design and control of geothermal heat pumps combined with thermally activated building systems in offices. `https://www.geotabs.eu/`. [Online; accessed 30-May-2017].

[56] GEOTABS HYBRID. Controlling the power of the ground by integration. http://www.hybridgeotabs.eu/. [Online; accessed 30-May-2017].

[57] GEOTECH. The challenge: increasing deployment of shallow geothermal technology. http://www.geotech-project.eu/project/. [Online; accessed 30-May-2017].

[58] GEOTRAINET. European wide training and certification programme for shallow geothermal installers. http://geotrainet.eu/. [Online; accessed 30-May-2017].

[59] GLHEPRO. *GLHEPro 5.0 for Windows. Users Guide.*, 2016.

[60] GORECKI, T. T., QURESHI, F. A., AND JONES, C. N. OpenBuild: An integrated simulation environment for building control. In *Proceedings of IEEE Conference on Control Applications (CCA)* (Sydney, Australia, 2015), pp. 1522–1527.

[61] GOUDA, M., DANAHER, S., AND UNDERWOOD, C. Building thermal model reduction using nonlinear constrained optimization. *Building and Environment 37*, 12 (2002), 1255–1265.

[62] GRANRYD, E. Analytical expressions for optimum flow rates in evaporators and condensers of heat pumping systems. *International Journal of Refrigeration 33*, 7 (2010), 1211–1220.

[63] GROUNDMED. Advanced ground source heat pump systems for heating and cooling in mediterranean climate. http://groundmed.eu/about_ground_med/. [Online; accessed 30-May-2017].

[64] GRUBER, M., TRÜSCHEL, A., AND DALENBÄCK, J.-O. Model-based controllers for indoor climate control in office buildings–complexity and performance evaluation. *Energy and Buildings 68* (2014), 213–222.

[65] GUROBI OPTIMIZATION, I. Gurobi optimizer reference manual, 2012.

[66] GYALISTRAS, D., AND GWERDER, M. Use of weather and occupancy forecasts for optimal building climate control (Opticontrol), two years progress report. Tech. rep., Terrestrial Systems Ecology ETH Zurich, Zurich, Switzerland, 2009.

[67] HARISH, V., AND KUMAR, A. Reduced order modeling and parameter identification of a building energy system model through an optimization routine. *Applied Energy 162* (2016), 1010–1023.

[68] Hazyuk, I., Ghiaus, C., and Penhouet, D. Optimal temperature control of intermittently heated buildings using model predictive control: Part I – Building modeling. *Building and Environment 51* (2012), 379 – 387.

[69] Hellström, G. *Ground heat storage: thermal analyses of duct storage systems (Theory).* Dep. of Mathematical Physics, University of Lund, Lund, Sweden, 1991.

[70] Hellström, G., and Sanner, B. *Earth Energy Designer, User manual, Version 2.0.* Lund, Sweden, 2000.

[71] Henze, G. P., Felsmann, C., Kalz, D. E., and Herkel, S. Primary energy and comfort performance of ventilation assisted thermo-active building systems in continental climates. *Energy and Buildings 40*, 2 (2008), 99–111.

[72] Hilliard, T., Kavgic, M., and Swan, L. Model predictive control for commercial buildings: trends and opportunities. *Advances in Building Energy Research 2* (2015), 172–190.

[73] Huber, A. Program EWS, version 4.7, Calculation of borehole heat exctraction. Tech. rep., Huber Energietechnik AG, Zürich, 2011.

[74] Huchtemann, K., and Müller, D. Advanced simulation methods for heat pump systems. In *Proceedings of the 7th International Modelica Conference* (Como, Italy, 2009).

[75] Ingenium n.v. Experts in sustainable buildings. `http://www.ingenium.be/BENL/site/index.aspx`. [Online; accessed 29-May-2017].

[76] Iolova, N., and Bernier, M. A. Quantifying the energy impact of a variable flow pump in a ground-coupled heat pump system. In *Proceedings of Conference ESIM 2006 : IBPSA-Canada's 4. Biennial Building Performance Simulation Conference* (2006), pp. 260–267.

[77] ISSO. *ISSO73: Ontwerp en uitvoering van verticale bodemwarmtewisselaar.* Rotterdam, The Netherlands, 2005.

[78] Javed, S. *Thermal modelling and evaluation of borehole heat transfer.* PhD, Dep. Energy and Environment, Chalmers University of Technology, Göteborg, Sweden, 2012.

[79] Jorissen, F., and Helsen, L. Towards an automated toolchain for MPC in multi-zone buildings. In *Proceedings of International High Performance Buildings Conference* (West-Lafayette, Indiana, USA, 2016), pp. 1–10.

[80] Jorissen, F., Reynders, G., Baetens, R., Picard, D., Saelens, D., and Helsen, L. Implementation and verification of the IDEAS building energy simulation library. *Journal of Building Performance Simulation - submitted* (May, 2017).

[81] Jorissen, F., Wetter, M., and Helsen, L. Simulation speed analysis and improvements of Modelica models for building energy simulation. In *Proceedings of the 11th International Modelica Conference* (Versailles, France, September 2015), no. 118, pp. 59–69.

[82] Kalz, D. E. *Heating and Cooling Concepts Employing Environmental Energy and Thermo-Active Building Systems, System Analysis and Optimization.* PhD, University of Karlsruhe. Fraunhofer IRB Verlag, Stuttgart, Germany, 2011.

[83] Kim, D., and Braun, J. E. Reduced-order building modeling for application to model-based predictive control. In *Proceedings of the 5th National Conference of IBPSA-USA* (Madison, USA, August 2012), vol. 5/1, pp. 554–561.

[84] Klein, S. Trnsys 17, a transient system simulation program. Tech. rep., Solar Energy Laboratory, University of Wisconsin, Madison, USA, 2010.

[85] Koschenz, M., and Lehmann, B. *Handbuch thermoaktive Bauteilsysteme TABS.* EMPA, Dübendorf, Switzerland, 2000.

[86] Kramer, R., Van Schijndel, J., and Schellen, H. Simplified thermal and hygric building models: a literature review. *Frontiers of Architectural Research 1*, 4 (2012), 318–325.

[87] Kummert, M. *Contribution to the application of modern control techniques to solar buildings. Simulation-based approach and experimental validation.* PhD, Fondation Universitaire Luxembourgeoise, Luxembourg, 2001.

[88] Lamarche, L., and Beauchamp, B. A new contribution to the finite line-source model for geothermal boreholes. *Energy and Buildings 39* (2007), 188–198.

[89] Lamarche, L., and Beauchamp, B. New solutions for the short-time analysis of geothermal vertical boreholes. *Heat and Mass Transfer 50* (2007), 1408–1419.

[90] Lamarche, L., Kajl, S., and Beauchamp, B. A review of methods to evaluate borehole thermal resistance in geothermal heat-pump systems. *Geothermics 39* (2010), 187–200.

[91] Lehmann, B., Gyalistras, D., Gwerder, M., Wirth, K., and Carl, S. Intermediate complexity model for model predictive control of integrated room automation. *Energy and Buildings 58*, 0 (2013), 250 – 262.

[92] Li, M., and Lai, A. C. Thermodynamic optimization of ground heat exchangers with single U-tube by entropy generation minimization method. *Energy Conversion and Management 65* (2013), 133–139.

[93] Li, X., and Wen, J. Review of building energy modeling for control and operation. *Renewable and Sustainable Energy Reviews 37* (2014), 517–537.

[94] Liesen, R., and Pedersen, C. *An evaluation of inside surface heat balance models for cooling load calculations*. American Society of Heating, Refrigerating and Air-Conditioning Engineers, Inc., Atlanta, GA, USA, Dec 1997.

[95] Löfberg, J. YALMIP: A toolbox for modeling and optimization in Matlab. In *Proceedings of the CACSD Conference* (Taipei, Taiwan, 2004).

[96] Ma, Y., Kelman, A., Daly, A., and Borrelli, F. Predictive control for energy efficient buildings with thermal storage: Modeling, simulation, and experiments. *IEEE Control Systems 32*, 1 (Feb 2012), 44–64.

[97] Malayappan, V., and Spitler, J. Limitations of using uniform heat flux assumptions in sizing vertical borehole heat exchanger fields. In *Proceedings of the Clima Conference* (Prague, Czech Republic, June 2013).

[98] Meteotest. METEONORM version 6.1 - edition 2009. Tech. rep., Meteotest, 2009.

[99] Müller, D., Lauster, M., Constantin, A., Fuchs, M., and Remmen, P. Aixlib – An open-source Modelica library within the IEA-EBC Annex 60 framework. In *Proceedings of Central European Symposium on Building Physics / BauSIM* (Dresden, Germany, September 2016).

[100] Nguyen, A.-T., Reiter, S., and Rigo, P. A review on simulation-based optimization methods applied to building performance analysis. *Applied Energy 113* (2014), 1043–1058.

[101] Nowak, T., Jaganjacova, S., and Westring, P. European heat pump market and statistics report 2014. *European Heat Pump Association, Brussels* (2014).

[102] Nytsch-Geusen, C., Huber, J., Ljubijankic, M., and Rädler, J. Modelica BuildingSystems, eine Modellbibliothek zur Simulation komplexer energietechnischer Gebäudesysteme. *Bauphysik 35(1)* (2013), 21–29.

[103] OCMW Brugge. WZC De Vliedberg. `https://www.ocmw-brugge.be/wzc-de-vliedberg-2`. [Online; accessed 06-March-2017].

[104] Oldewurtel, F., Parisio, A., Jones, C. N., Gyalistras, D., Gwerder, M., Stauch, V., Lehmann, B., and Morari, M. Use of model predictive control and weather forecasts for energy efficient building climate control. *Energy and Buildings 45* (2012), 15–27.

[105] Olesen, B. W. Radiant heating and cooling by embedded water-based systems. In *Proceedings of Congreso Climaplus 2011* (Madrid, Spain, 2011).

[106] Olesen, B. W., and Liedelt, D. Cooling and heating of buildings by activating their thermal mass with embedded hydronic pipe systems. In *Proceedings of CIBSE conference* (Dublin, Ireland, 2000).

[107] Ooka, R., and Komamura, K. Optimal design method for building energy systems using genetic algorithms. *Building and Environment 44*, 7 (2009), 1538–1544.

[108] Otter, M. Modelica_linearsystems2. Tech. rep., 2014.

[109] Parys, W., Saelens, D., and Hens, H. Coupling of dynamic building simulation with stochastic modelling of occupant behaviour in offices–a review-based integrated methodology. *Journal of Building Performance Simulation 4*, 4 (2011), 339–358.

[110] Patteeuw, D., and Helsen, L. Combined design and control optimization of residential heating systems in a smart-grid context. *Energy and Buildings 133* (2016), 640–657.

[111] Perez-Lombard, L., Ortiz, J., and Pout, C. A review on buildings energy consumption information. *Energy and Buildings 40*, 3 (2008), 394–398.

[112] Petitclerc, E. Overview of European geothermal projects in Belgium. `http://geothermie.brussels/uploads/files/petitclerc-tour-dhorizons-des-projets-europeens.pdf`, 2016. [Online; accessed 30-May-2017].

[113] Picard, D., and Helsen, L. A new hybrid model for borefield heat exchangers performance evaluation. In *Proceedings of the American Society of Heating, Refrigeration and Air Conditioning Engineers, Inc.* (Seattle, USA, 2014), vol. 120.

[114] Picard, D., and Helsen, L. Report on the building energy simulation models of an office building, a retirement home, a school, and a block of flats. Tech. rep., KU Leuven, Leuven, Belgium, May 2017.

[115] Picard, D., Jorissen, F., and Helsen, L. Methodology for obtaining linear state space building energy simulation models. In *Proceedings of the 11th International Modelica Conference* (Paris, France, 2015), pp. 51–58.

[116] Picard, D., Sourbron, M., Jorissen, F., Cigler, J., Ferkl, L., and Helsen, L. Comparison of model predictive control performance using grey-box and white-box controller models. In *Proceedings of the 4th International High Performance Buildings Conference* (West-Lafayette, Indiana, USA, 2016), pp. 1–10.

[117] Privara, S., Cigler, J., Vana, Z., Oldewurtel, F., Sagerschnig, C., and Zacekova, E. Building modeling as a crucial part for building predictive control. *Energy and Buildings 56* (January 2013), 8–22.

[118] Prívara, S., Široký, J., Ferkl, L., and Cigler, J. Model predictive control of a building heating system: The first experience. *Energy and Buildings 43*, 2-3 (Feb. 2011), 564–572.

[119] PyEphem. Astronomical computations for the python programming language. `http://rhodesmill.org/pyephem/`, 2016. [Online: accessed: 28-April-2016].

[120] Qin, S. J., and Badgwell, T. A. A survey of industrial model predictive control technology. *Control Engineering Practice 11*, 7 (2003), 733–764.

[121] REGEOCITIES. Implementing geothermal in cities. `http://regeocities.eu/results/`, 2015. [Online; accessed 22-May-2017].

[122] Reynders, G., Diriken, J., and Saelens, D. Quality of grey-box models and identified parameters as function of the accuracy of input and observation signals. *Energy and Buildings 82* (2014), 263–274.

[123] Riello. Systèmes à condensation: Riello tau n, riello tau premix. `http://sos-express.be/wp-content/uploads/2015/11/Riello-RIELLO-TAU-PREMIX.pdf`, 2017. [Online; accessed 16-Februar-2017].

[124] Risbeck, M. J., Maravelias, C. T., Rawlings, J. B., and Turney, R. D. Cost optimization of combined building heating/cooling equipment via mixed-integer linear programming. In *Proceedings of the American Control Conference (ACC), 2015* (Chicago, IL, USA, 2015), pp. 1689–1694.

[125] Ruano, A., Crispim, E., Conceicao, E., and Lucio, M. Prediction of building's temperature using neural networks models. *Energy and Buildings 38*, 6 (2006), 682–694.

[126] Schmidt, T., and Hellström, G. Superposition borehole model, working paper on usable tools and methods. Tech. rep., Nordon, Nordic Energy Research, February 2005.

[127] Seo, J., Ooka, R., Kim, J. T., and Nam, Y. Optimization of the HVAC system design to minimize primary energy demand. *Energy and Buildings 76* (2014), 102–108.

[128] SIA. *SIA384/6:2010: Sondes géothermiques.* Switzerland, 2010.

[129] Široký, J., Oldewurtel, F., Cigler, J., and Prívara, S. Experimental analysis of model predictive control for an energy efficient building heating system. *Applied Energy 88*, 9 (2011), 3079–3087.

[130] Sliwa, T., and Rosen, M. A. Natural and artificial methods for regeneration of heat resources for borehole heat exchangers to enhance the sustainability of underground thermal storages: a review. *Sustainability 7*, 10 (2015), 13104–13125.

[131] Smartgeotherm. Towards energy neutral buildings by the integration of geothermal concepts, concrete core activation and other techniques. `http://smartgeotherm.be/`. [Online; accessed 30-May-2017].

[132] Sourbron, M. *Dynamic Thermal Behaviour of Buildings with Concrete Core Activation.* PhD, Dep. of Mechanical Engineering, KU Leuven, Leuven, Belgium, 2013a.

[133] Sourbron, M., De Herdt, R., Van Reet, T., Van Passel, W., Baelmans, M., and Helsen, L. Efficiently produced heat and cold is squandered by inappropriate control strategies: A case study. *Energy and Buildings 41*, 10 (2009), 1091–1098.

[134] Sourbron, M., and Helsen, L. Thermally activated building systems in office buildings: impact of control strategy on energy performance and thermal comfort. In *Proceedings of International Conference on System Simulation in Buildings* (Liege, Belgium, December 2010).

[135] Sourbron, M., and Helsen, L. Slow thermally activated building system and fast air handling unit join forces through the use of model based predictive control. In *Proceedings of the CLIMA 2013 Congress* (Prague, Czech Republic, 2013c), pp. 1–10.

[136] Sourbron, M., Verhelst, C., and Helsen, L. Building models for model predictive control of office buildings with concrete core activation. *Journal of Building Performance Simulation 6*, 3 (2013b), 175–198.

[137] Southard, L. E., Liu, X., and Spitler, J. Performance of HVAC systems at ASHRAE HQ. *ASHRAE Journal 56*, 12 (2014), 12.

[138] Stober, I., and Bucher, K. *History of Geothermal Energy Use*. Springer Berlin Heidelberg, Berlin, Heidelberg, Germany, 2013.

[139] Strand, R., Winkelmann, F., Buhl, F., Huang, J., Liesen, R., Pedersen, C., Fisher, D., Taylor, R., Crawley, D., and Lawrie, L. Enhancing and extending the capabilities of the building heat balance simulation technique for use in Energyplus. In *Proceedings of Building Simulation Conference* (Kyoto, Japan, 1999), vol. 2, pp. 653–660.

[140] Sturzenegger, D., Gyalistras, D., Gwerder, M., Sagerschnig, C., Morari, M., and Smith, R. S. Model predictive control of a swiss office building. In *Proceedings of the 11th REHVA World Congress Clima* (Prague, Czech Republic, 2013).

[141] Sturzenegger, D., Gyalistras, D., Morari, M., and R., S. Semi-automated modular modeling of buildings for model predictive control. In *Proceedings of BuildSys 2012 - Workshop of ACM SenSys Conference* (Toronto, Canada, 2012).

[142] Sturzenegger, D., Gyalistras, D., Semeraro, V., Morari, M., and Smith, R. BRCM Matlab toolbox: Model generation for model predictive building control. In *Proceedings of the American Control Conference* (Portland, USA, June 2014), pp. 1063–1069.

[143] Technical Committee CEN/TC 156. *NBN EN442-2:1996: Radiators and convectors - Part 2: Test methods and rating*. 1996.

[144] Technical Committee CEN/TC 156. *EN 13779:2004: Ventilation for non-residential buildings - Performance requirements for ventilation and room-conditioning systems*. 2004.

[145] Technical Committee CEN/TC 156. *EN 15251:2007: Indoor environmental input parameters for design and assessment of energy performance of buildings addressing indoor air quality, thermal environment, lighting and acoustics*. 2007.

[146] Technical Committee CEN/TC 156. *NBN EN 15459:2007: Energy performance of buildings - Economic evaluation procedure for energy systems in buildings.* 2007.

[147] Technical Committee CEN/TC 156. *NBN EN15450:2008: Heating systems in buildings - Design of heat pump heating systems.* 2008.

[148] Technical Committee CEN/TC 156. *NBN EN 442:2014: Radiators and convectors.* 2014.

[149] Technical Committee CEN/TC 228. *NBN EN 15316-2-1:2007: Heating systems in buildings - Method for calculation of system energy requirements and system efficiencies - Part 2-1: Space heating emission systems.* 2007.

[150] Technical Committee ISO/TC 159. *ISO 7730:2005: Ergonomics of the thermal environment - Analytical determination and interpretation of thermal comfort using calculation of the PMV and PPD indices and local thermal comfort criteria.* 2005.

[151] ThermoMap. Fostering the information environment on shallow geothermal potential across europe. `http://www.thermomap-project.eu/`. [Online; accessed 30-May-2017].

[152] Thirumaleshwar, M. *Fundamentals of heat and mass transfer.* Pearson Education India, 2009.

[153] Tian, Z., and Love, J. A. Energy performance optimization of radiant slab cooling using building simulation and field measurements. *Energy and Buildings 41*, 3 (2009), 320–330.

[154] Tödtli, J., Güntensperger, W., Gwerder, M., Haas, A., Lehmann, B., and Renggli, F. Control of concrete-core conditioning systems. In *Proceedings of the 8th REHVA World Congress* (Lausanne, Switzerland, 2005).

[155] Tödtli, J., Gwerder, M., Lehmann, B., Renggli, F., and Dorer, V. TABS-control: Steuerung und regelung von thermoaktiven bauteilsystemen. *Faktor Verlag Zurich (Switzerland) 86*, 9 (2009).

[156] Treiber, M. *Nutzenübergabe thermoaktiver Decken.* PhD, University of Stuttgart, Stuttgart, Germany, 2007.

[157] Váňa, Z., Cigler, J., Širokỳ, J., Žáčeková, E., and Ferkl, L. Model-based energy efficient control applied to an office building. *Journal of Process Control 24*, 6 (2014), 790–797.

[158] Vergaert, V., Parys, W., and Marten, D. Studie naar kostenoptimale niveaus van de minimumeisen inzake energieprestaties van niet-residentiële gebouwen, December 2015.

[159] Verhelst, C. *Model predictive control of ground coupled heat pump systems for office buildings*. PhD, Dep. Mechanical engineering, KU Leuven, Leuven, Belgium, 2012.

[160] Verheyden. Boringen verheyden bvba. `http://www.boringenverheyden.be`, 2017. [Online; accessed 14-August-2017].

[161] Viessmann. Installation and service instruction, vitocal 300-g. `http://www.viessmann.com/vires/product_documents/5600161VSA00002_1.PDF`, 2017. [Online; accessed 16-Februar-2017].

[162] Vlaamse Energie Agenschap. EPB-eisen voor EPN-eenheden, 2016.

[163] Wauman, B., Saelens, D., and Breesch, H. The definition of representative boundary conditions for Flemish schools for use in energy assessment methods. *Energy and Buildings 87* (2015), 1–13.

[164] Wetter, M. *Simulation-based building energy optimization*. PhD, University of California, Berkeley, USA, 2004.

[165] Wetter, M. Fan and pump model that has a unique solution for any pressure boundary condition and control signal. In *Proceedings of the 13-th IBPSA Conference* (2013), pp. 3505–3512.

[166] Wetter, M., Bonvini, M., and Nouidui, T. S. Equation-based languages – A new paradigm for building energy modeling, simulation and optimization. *Energy & Buildings 117* (2016), 290–300.

[167] Wetter, M., Bonvini, M., Nouidui, T. S., and Zuo, W. Modelica Buildings library 2.0. In *Proceedings of Building Simulation 2015* (Hyderabad, India, 2015).

[168] Wetter, M., Fuchs, M., Grozman, P., Helsen, L., Jorissen, F., Lauster, M., Dirk, M., Nytsch-geusen, C., Picard, D., Sahlin, P., and Thorade, M. IEA EBC Annex 60 Modelica library - an international collaboration to develop a free open-source model library for buildings and community energy systems. In *Proceedings of the 14th Conference of International Building Performance Simulation Association* (Hyderabad, 2015), J. Mathur and V. Garg, Eds., International Building Performance Simulation Association, pp. 395–402.

[169] Wetter, M., Zuo, W., Nouidui, T., and Pang, X. Modelica buildings library. *Journal of Building Performance Simulation 7*, 4 (2014), 253–270.

[170] Xu, X., and Wang, S. Optimal simplified thermal models of building envelope based on frequency domain regression using genetic algorithm. *Energy and Buildings 39*, 5 (2007), 525–536.

[171] Yun, K., Luck, R., Mago, P. J., and Cho, H. Building hourly thermal load prediction using an indexed ARX model. *Energy and Buildings 54* (2012), 225–233.

[172] Zaheer-Uddin, M., and Zheng, G. Optimal control of time-scheduled heating, ventilating and air conditioning processes in buildings. *Energy conversion and Management 41*, 1 (2000), 49–60.

Curriculum

Damien Picard
Born on 14 May 1989 in Uccle
Personal email address damien.picard@gmail.com

Experience

2012 - 2017: PhD-student at KU Leuven (Smartgeotherm project). July 2013: Intership at Boydens Engineering. August 2011: Design of solar panel installation at Elsingor.

Education

2010-2012: Master in Mechanical Engineering, KU Leuven
2007-2010: Bachelor in Engineering (Mechanics and electrotechnics), KU Leuven

International exchange

2010-2011: first Master Mechanical Engineering, TU Graz, Austria

Languages

French (C2), Dutch (C1), English (C1), German (B2), Hungarian (B1), Spanish (A2).

Interest and skills

Building design, modeling, control and optimization. Geothermal energy and renewable energy for buildings. Programming (Modelica, Python, Matlab, C) and automatisation. Optimization. Literature, culture, religion, music, photography, wood work, nature, parenthood, travelling, and friends.

List of publications

Picard D. and Helsen L. Report on the building energy simulation models of an office building, a retirement home, a school, and a block of flats. Tech. rep., KU Leuven, Leuven, Belgium, May 2017.

Picard, D., Drgoňa, J., Kvasnica, M. and Helsen, L. Impact of the controller model complexity on model predictive control performance for building. *Energy and Buildings* (August, 2017).

Picard, D., Jorissen, F. and Helsen, L. Analytical solution for optimal mass flow rate in primary circuit of ground-coupled heat pump systems. In *Proceedings of the International Ground Source Heat Pump Association* (Denver, CO, USA, March 2017).

Picard, D., Sourbron, M., Jorissen, F., Cigler, J., Ferkl, L. and Helsen, L. Comparison of model predictive control performance using grey-box and white-box controller models. In *Proceedings of the 4th International High Performance Buildings Conference* (West-Lafayette, Indiana, USA, 2016), pp. 1–10.

Baetens R., De Coninck R., Jorissen F., Picard D., Helsen L., Saelens D. (2015). OpenIDEAS - An Open Framework for Integrated District Energy Simulations. In *Proceedings of Building Simulation 2015* (Hyderabad, India, December 2015).

Wetter M., Fuchs M., Grozman P., Helsen L., Jorissen F., Müller D., Nytsch-Geusen C., Picard D., Sahlin P., Thorade M. IEA EBC Annex 60 Modelica Library - An international collaboration to develop a free open-source model library for buildings and community energy systems. In *Proceedings of Building Simulation 2015* (Hyderabad, India, December 2015).

Picard, D., Jorissen, F., Helsen, L. Methodology for obtaining linear state space building energy simulation models. In *11th International Modelica Conference* (Paris, France, 2015), pp. 51–58.

Picard, D. and Helsen, L. A new hybrid model for borefield heat exchangers

performance evaluation. In *Proceedings of the American Society of Heating, Refrigeration and Air Conditioning Engineersm, Inc.* (Seattle, USA, 2014), vol.120.

Picard, D. and Helsen, L. Advanced hybrid model for borefield heat exchanger performance evaluation, an implementation in Modelica. In *Proceedings of the 10th International Modelica Conference.* (Lund, Sweden, 2014).

FACULTY OF ENGINEERING SCIENCE
DEPARTMENT OF MECHANICAL ENGINEERING
THERMAL SYSTEM SIMULATION
Celestijnenlaan 200A box 2402
B-3001 Leuven
damien.picard@kuleuven.be
http://www.mech.kuleuven.be